Optimization and Energy Maximizing Control Systems for Wave Energy Converters

(Article begins on next page)

24 April 2024

$$\Omega_j = \begin{bmatrix} diag(\omega_{wj}) & 0 \\ 0 & \omega_{mj} \end{bmatrix} \tag{25}$$

where $\omega_{wj} \in \mathbb{R}^{n_W}$ stores the n_W harmonics to model the WEF components. The number of frequencies in Ω, have to be chosen in order to have a compromise between the accuracy of the estimation for each excitation force component and the computational effort. The matrices (25) include a term at low frequency to represent the contribution of the mooring forces for each DoF.

Let us consider the following linear time-invariant stochastic discrete model representing the discrete-time version of the augmented System (17):

$$\begin{aligned} \hat{X}_{ad}(k+1) &= A_{ad}\hat{X}_{ad}(k) + B_{ad}F_g(k) + \Gamma w(k) \\ Y_d(k) &= C_{ad}\hat{X}_{ad}(k) + D_{ad}F_g(k) + v(k) \\ w(k) &\sim \mathcal{N}(0,Q) \\ v(k) &\sim \mathcal{N}(0,R) \end{aligned} \tag{26}$$

where $\hat{X}_{ad}(k)$ represents the system estimated states, $F_g(k)$ is the known input and $Y_d(k)$ contains the measurements of the system dynamics. $w(k)$ and $v(k)$ are zero mean white noise sequences with known covariance, uncorrelated with each other and with the initial state of the system. A_{ad}, B_{ad}, C_{ad} and D_{ad} stand for the discretised versions of the matrices A_a, B_a, C_a and D_a. Γ is the weighting matrix for the process disturbances. Q and R are the covariance matrices of the process and measurements noise. The KF algorithm performs the estimation in the form of a feedback control: the filter estimates the process state at some time and then obtains feedback in the form of (noisy) measurements. As such, the equations for the KF fall into two groups: time-update equations and measurement-update equations [43]:

Time Update:

$$\begin{aligned} P^-(k) &= A_{ad}P(k-1)A_{ad}^T + \Gamma Q \Gamma^T \\ \hat{X}_a^-(k) &= A_{ad}\hat{X}_a(k-1) + B_{ad}F_g(k-1) \end{aligned} \tag{27}$$

Measurement Update:

$$\begin{aligned} K(k) &= P_k^- C^T \left(C_{ad}P^-(k)C_{ad}^T + R \right)^{-1} \\ P(k) &= (I + K(k)C_{ad}) P^-(k) \\ \hat{X}_{ad}(k) &= \hat{X}_{ad}^-(k) + K(k) \left(Y(k) - C_{ad}\hat{X}_{ad}^-(k) - D_{ad}F_g(k) \right) \end{aligned} \tag{28}$$

The time update equations can also be thought of as predictor equations, while the measurement update equations can be thought of as corrector equations. In this framework, the KF algorithm can be implemented to estimate the unknown WEF vector $\hat{F}_w(k)$ by measured system dynamics $Y_d(k)$ and known input $F_g(k)$ at any instant k.

4. Wave Excitation Force Estimation with Neural Network

Despite its simplicity and efficacy, the KF filter observer may suffer from several drawbacks: the non-linear effects emerging in sever sea-states conditions as well as the reliabiliy of the WEC model could negatively affect the estimation performances. For example, the slack-mooring of the ISWEC is modelled with a quasi-static approach (developed in-house). The main advantage consists in reducing the computational burden of the simulation at the expense of model accuracy. More accurate mooring models are presented in [44] considering two dynamic lumped-mass approaches (the open source MoorDyn [45] and the commercial OrcaFlex 11.0e [46]) where mooring actions are resolved coupling both the hydrodynamics and gyroscope model of the WEC in the MoorDyn and Orcaflex enviorments. When the system model is not reducible to a series of analytical equations or, even more,

is based only on observed data the implementation KF model is not trivial. This argument can be extended to any other complex aspect of WEC modelling that cannot be analytically formulated with acceptable accuracy. In this context, artifical NNs represents powerful tools to map the non-linear relations from sets of input-output data. In NN models the parameters are tuned to fit the input-output data, without reference to the physical background and no information about the model architecture.

In general mathematical terms, WEFs acting on the ISWEC can be expressed as a non-linear function $f(\bullet)$ of the system known inputs and measurements as follows [14]:

$$\hat{F}_w(k) = f(F_g(k), \ldots, F_g(k - k_N + 1), Y_d(k), \ldots, Y_d(k - k_N + 1)) \tag{29}$$

Equation (29) shows that the estimation of the WEF at instant k is, at least in principle, addressed combining a series of known system inputs and measurements collected from discrete time $k - k_N + 1$ to k where k_N represents the delay steps of the available data. More in detail, the WEF could be obtained from the set of WEC motion measurements from the ISWEC on-board sensors and the gyroscopic reaction. In [14] the same approach is considered including the measures provided by the IMU and encoders mounted on the ISWEC adding the velocity $\dot{z}_d(k)$ and position $z_d(k)$ obtained by numerical integration of the acceleration $\ddot{z}_d(k)$. These two inputs were included to improve the estimation accuracy. However, this measurements framework does not consider the effect of the sensor noise: in practice, accelerometer signals are often very noisy, hence velocity and position integration from acceleration are likely to be unreliable, resulting in unreliable estimations in practice. In this work, the NN is evaluated for all the configurations of Table 2 and the sensitiveness and roubustness analysis is extended to all the wave domain of the installation site. The input-output architecture of the NN is shown in Figure 8. The feedforward NN is composed of linked neurons arranged in three layers. The input layer collects a set of inputs I_I multiplying them by a set of weights, assigned to the data on the basis of their relative importance to other inputs. The hidden neurons apply a non-linear activation function σ to the weighted sum of their inputs. Then, the outputs of each hidden neuron are linearly combined by the output functions Σ to produce the network outputs O_O. The use of delays in the input variables is considered to increase the reliability of the estimate. For a generic dynamic system, one way to consider its dynamic behaviour using static neurons is to employ past values of the inputs [47], resulting in good performances in term of estimation accuracy and robustness to different wave conditions as demonstrated in [14].
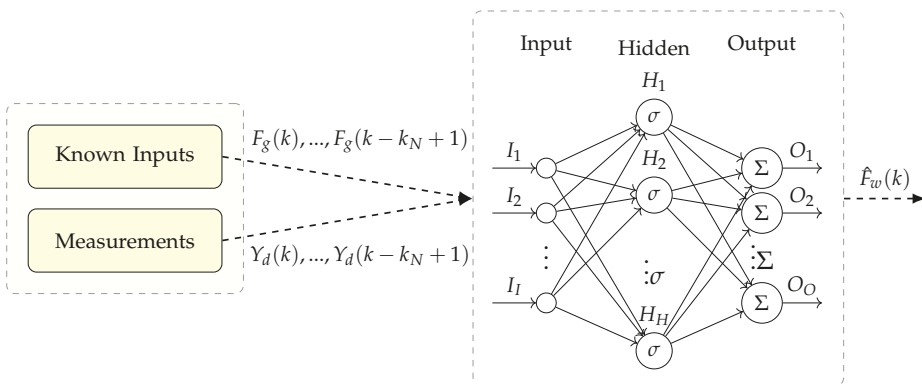

Figure 8. Neural Network architecture for ISWEC.

5. Kalman Filter and Neural Network Tuning

The matrix Ω containing the frequencies to model the WEFs as well as Q and R are tuned for the system under study. A sensitivity analysis has been performed to tune the number of frequencies. Then, through an iterative process the diagonal coefficients of Q and R are identified in order to have the

best estimation performances for each measurement framework considered. Numerical experiments are conduced considering the four wave profiles of Table 1. The estimation performances are valuated considering the Goodness-of-Fit (*GoF*) proposed by [48]:

$$GoF_j = 1 - \frac{\sqrt{\sum_{k=1}^{T_s} \left(F_{wj}(k) - \hat{F}_{wj}(k) \right)^2}}{\sqrt{\sum_{k=1}^{T_s} F_{wj}(k)^2}} \tag{30}$$

In Equation (30), $F_{wj}(k)$ and $\hat{F}_{wj}(k)$ are the true and estimated WEF for the *j*-th DoF at discrete time instant *k*, respectively. T_s is the total number of samples.

5.1. Kalman Filter Parameters

For the presented case, 1, 3, 6 and 9 frequencies are tested in order to find a compromise between the accuracy of the estimation process and the KF complexity. The interval is chosen between period 3 s and period 9 s, linearly spaced. Each point refers to the mean of each GoF_j obtained from four tuning sea-states. The mooring components are modelled with only one period: 100 s for $F_{mx}(t)$ and 2000 s for $F_{mz}(t)$ and $F_{m\delta}(t)$, considered as low frequency contributions (Figure 7). The FM framework has been considered for this tuning process. Table 3 sets out the results obtained from each tuning wave gruped in respect to the number of frequencies n_W.

Table 3. *GoF* results of the KF observer for each tuning wave for different number of frequencies n_W. The last row stores the mean values.

Id	$n_W = 1$			$n_W = 3$			$n_W = 6$			$n_W = 9$		
	GoF_x	GoF_z	GoF_δ	GoF_x	GoF_z	GoF_δ	GoF_x	GoF_z	GoF_δ	GoF_x	GoF_z	GoF_δ
1	0.665	0.640	0.675	0.901	0.956	0.898	0.917	0.962	0.894	0.917	0.965	0.899
2	0.747	0.846	0.706	0.931	0.968	0.919	0.942	0.986	0.919	0.943	0.987	0.925
3	0.771	0.899	0.642	0.911	0.974	0.927	0.924	0.988	0.927	0.925	0.988	0.930
4	0.785	0.933	0.537	0.914	0.970	0.925	0.930	0.990	0.927	0.930	0.991	0.928
	0.755	0.824	0.685	0.917	0.962	0.913	0.928	0.981	0.917	0.928	0.982	0.921

Increasing the number of harmonics from $n_W = 1$ to $n_W = 3$ leads to a significant improvement of all *GoF*. On average, an advance of 0.162 is obtained for GoF_x, 0.138 for GoF_z and 0.228 for GoF_δ. Passing from $n_W = 3$ to $n_W = 6$ shows a slight increase of GoF_x and GoF_z, enchancing the quality of the $\hat{F}_{wx}(t)$ and $\hat{F}_{wz}(t)$ estimation of 0.011 and 0.021, respectively. Further enlarge of n_W results in a minimal or null upgrade of any *GoF*. In this regard, $n_W = 6$ is considered a good trade-off between accuracy and complexity of the observer.

For what concerns the covariance matrices, repeated simulations are conduced to tune the diagonal elements of *Q* and *R* for each mesurement framework. They are chosen to guarantee an accurate estimation of the unknown states without amplifying the noise level. Figure 9a–c compare the *Q* coeffcients relative to the WEF components for each measurement framework. From the chart, it can be seen that the *Q* coeffcients are reduced as the magnitude of the noise increases and are tuned in respect to the energy content of the WEF. In this way, the most relevant frequency components are amplified more than the others, resulting in a more accurate estimation. Figure 9d provides the *R* coefficients, balanced in order to penalize the most inaccurate measurements (e.g., DGPS positions) giving less importance to the related signals. Data indicate that the *R* coefficients grow as the noise magnitudes increase. Missing markers mean that the measurements are not available for that framework.
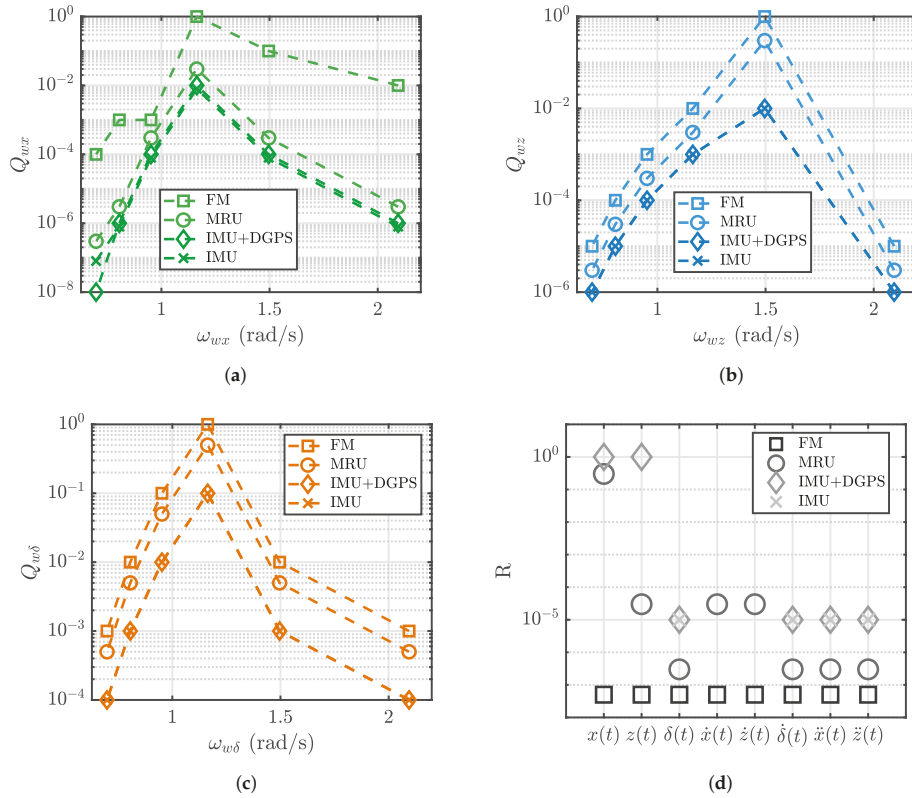
Figure 9. *Q* and *R* coefficients for each measurement framework and WEF compoenents: *Q* values for $\hat{F}_{wx}$ (**a**), *Q* values for $\hat{F}_{wz}$ (**b**), *Q* values for $\hat{F}_{w\delta}$ (**c**) and *R* values. (**a**) *Q* coefficients of surge components; (**b**) *Q* coefficients of heave components; (**c**) *Q* coefficients of pitch components; (**d**) *R* coefficients.

5.2. Neural Network Parameters

The NN training aims to obtain the weights and bias of the network evaluating the sensitivity of the model to both the delay steps k_N and neurons n_N. The four wave profiles of Table 1 are used to obtain the training data for each measurement framework. The time-series of the WEFs are concatenated to generate a long training set applied to the ISWEC numerical model obtaining the WEC motion measurements. Then, all the time-series are normalized in the $[-1, 1]$ range to avoid problems due to different magnitude between input-output signals. Since the system is non-linear, the data normalization could negatively affect the trainign process if, for example, saturations of the PTO appear. To avoid saturations, the training data are chosen to cover the operating range of the ISWEC. However, in sever sea-states the WEC motion could overcome the normalization range causing estimation errors but, in such extreme conditions, the WEC is shut-down for safety purposes and no control is applied. In order to address over-fitting problem the data are randomly divided into three parts: 50% for training purposes, 30% for validation and 20% for performance evaluation. The performance function is the Mean Squared Error (MSE) normalized between −1 and 1, ensuring that the relative accuracy of output elements of different magnitude are treated as equally important. Then, 1, 3, 5, and 7 delay steps are tested while the number of neurons is fixed to 10; 5, 10, 15 and 20 neurons are evaluated with 3 delay steps. Specific tuning processes are applied for

each framework with the same number of delay steps and neurons, considering noisy signals. The FM framework has been considered for tuning the network hyperparameters.

The sensitivity analysis on the delay steps is reported in Table 4. The mean value of each GoF reveals that increasing the number of delay steps from $k_N = 1$ to $k_N = 3$ results in a revelant increase of estimation accuracy, expecially for the GoF_δ that passes from 0.880 to 0.977. A similar behaviour is obtained for the GoF_x, where the mean estimation performance grows of 0.053 points. On the other hand, no relevant improvements are obtained for the GoF_z as well as for the other DoFs employing 5 and 7 delay steps. In this regard, 3 unit delays are chosen for the NN architecture.

Table 4. GoF results of the NN model for each tuning wave for different delay steps k_N. The number of neurons are fixed to 10. The last row stores the mean values.

Id	$k_N = 1$			$k_N = 3$			$k_N = 5$			$k_N = 7$		
	GoF_x	GoF_z	GoF_δ	GoF_x	GoF_z	GoF_δ	GoF_x	GoF_z	GoF_δ	GoF_x	GoF_z	GoF_δ
1	0.900	0.935	0.839	0.963	0.938	0.966	0.969	0.939	0.966	0.978	0.951	0.973
2	0.922	0.967	0.891	0.977	0.970	0.980	0.980	0.972	0.978	0.985	0.978	0.978
3	0.927	0.969	0.889	0.979	0.976	0.980	0.980	0.977	0.978	0.985	0.982	0.982
4	0.933	0.968	0.903	0.979	0.978	0.981	0.978	0.977	0.978	0.985	0.985	0.982
	0.921	0.960	0.880	0.974	0.965	0.977	0.977	0.966	0.975	0.983	0.974	0.980

Table 5 reports the estimation results obtained for different values of neurons. 10 neurons represents the best choise ensuring the good estimation performances with acceptable network complexity. Surprisingly, increasing the number of neurons over 10 leads to a slight degradation of performances, suggesting that the learning algorithm is not able to converge properly during the learning process over-fitting noisy data.

Table 5. GoF results of the NN model for each tuning wave for different neurons n_N. The delay steps are fixed to 3. The last row stores the mean values.

Id	$n_N = 5$			$n_N = 10$			$n_N = 15$			$n_N = 20$		
	GoF_x	GoF_z	GoF_δ	GoF_x	GoF_z	GoF_δ	GoF_x	GoF_z	GoF_δ	GoF_x	GoF_z	GoF_δ
1	0.952	0.929	0.947	0.963	0.938	0.966	0.958	0.937	0.964	0.956	0.934	0.964
2	0.969	0.967	0.964	0.977	0.970	0.980	0.972	0.971	0.980	0.972	0.969	0.978
3	0.968	0.972	0.964	0.979	0.976	0.980	0.974	0.976	0.980	0.972	0.975	0.979
4	0.970	0.974	0.963	0.979	0.978	0.981	0.976	0.976	0.981	0.973	0.976	0.981
	0.965	0.961	0.959	0.974	0.965	0.977	0.970	0.965	0.976	0.970	0.964	0.975

6. Numerical Results and Discussions

In this section, several results are carried out for a comprehensive analysis of the KF and NN performances. An exhaustive evaluation in different wave conditions as well as a robustness evaluation to different measurements and plant inaccuracies is provided. Both the KF and NN are tested and compared extending the wave domain to the 35 waves represented in Figure 4. Each GoF_j is weighted on the annual energy of the specific site in analysis:

$$\overline{GoF_j} = \frac{\sum_{v=1}^{V} GoF_j(v)E(v)}{\sum_{v=1}^{V} E(v)} \tag{31}$$

In Equation (31), $E(v)$ is the annual energy associated to v-th wave and V the total number of waves considered. Then, the percentage difference between the KF and NN results is defined as follows:

$$\Delta\overline{GoF}_j = \frac{\overline{GoF}_j\big|_{NN} - \overline{GoF}_j\big|_{KF}}{\overline{GoF}_j\big|_{KF}}100 \tag{32}$$

where $\overline{GoF}_j\big|_{KF}$ and $\overline{GoF}_j\big|_{NN}$ are the weighted *GoF* obtained with KF and NN, respectively.

6.1. Influence of the Measurement Framework

The available measurements and their accuracy play an important role in the estimation process. The main question concerns the influence of the available signals and how missing data can affect the estimation performances. The three measurement configurations MRU, IMU+DGPS and IMU are compared considering noisless data. In order to improve readability, some of the bulky figures are placed in the Appendix A.

Focusing on the KF results, Figure A1 is quite revealing in several ways. Overall, maximum estiamtion performances are found near the tuning waves (marked with black squares) except for the GoF_z provided by the IMU framework. In particular, best performances are achieved in the range $[4, 8]$ seconds as the period interval is chosen between 3 s and 9 s. In a practical setup, an accurate analysis the dominant periods is crucial to achieve the best performances from the KF. Moreover, promising results are obtained in all the sea-states considered, suggesting a good versatility of the observer where the system is not tuned. The accuracy is almost the same for the force components in surge and pitch directions. Despite the configuration IMU+DGPS does not provide the $\dot{x}(t)$ signal, the IMU+DGPS equipment is able to estimate the $\hat{F}_{wx}(t)$ component with the same accuracy as the MRU one. The same argument can be applied considering the IMU results. In spite of the IMU does not provide both $x(t)$ and $\dot{x}(t)$, its accuracy of the pitch force estimation equals the MRU and IMU+DGPS one. Since surge and pitch DoFs are coupled due to the device geometry, the surge force can be succesfully estimated from the pitching motion of the device (available in all the frameworks). Morevoer, the effect of the damping is negligible and the hydrostatic stiffness is null in the surge direction, not affecting the estimate of $\hat{F}_{wx}(t)$. For what concern the heave component, there is a significant difference between the GoF_z of the IMU and the other two frameworks. The absence of both $z(t)$ and $\dot{z}(t)$ leads a decrease of performances since, as illustrated in Figure 10, the KF is not able to estimate correctly the position $z(t)$ resulting in a loss of estimation accuracy.
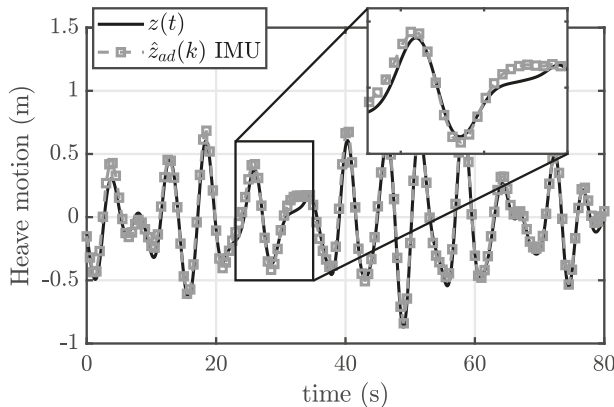

Figure 10. Heave motion compared with its estimation obtained with the IMU framework (Wave Id 2).

Considering the NN, Figure A2 demonstrates that the NN performance is maximized with a MRU measurement framework and near the tuning waves. In agreement with the KF, removing the absolute velocities $\dot{x}(t)$ and $\dot{z}(t)$ leads to a minimal decrease in estimation accuracy for all the DoFs. This finding is expected for both surge and pitch DoFs since the measurements that influence the $\hat{F}_{wx}(t)$ and $\hat{F}_{w\delta}(t)$

estimation ($\delta(t)$, $\dot{\delta}(t)$ and $\ddot{x}(t)$) are provided both in MRU and IMU+DGPS configurations. The lack of performance increase for the IMU framework, especially for the heave DoF where the goodness of estimation significantly reduces for all the waves, suggesting that the NN is not able to obtain an appropriate fit of the $F_{wz}(t)$ if a full measurement framework is not provided. On the other hand, $\delta(t)$, $\dot{\delta}(t)$ and $\ddot{x}(t)$ are adequate to succesfully estimate the $\hat{F}_{wx}(t)$ and $\hat{F}_{w\delta}(t)$ components, as demonstrated for the KF observer.

6.2. Sensor Noise Effect

Once the influence of the available measurements is evaluated, realistic data are applied both to the KF and NN to assess the effect of the sensor disturbances. Starting with the KF observer, Figure A3 highlights that the MRU framework gives almost the same precision compared to the noiseless case, especially for the surge and pitch excitation forces. MRU units are affected by minimal disturbances and offer an accurate measures of angular rates, orientations, accelerations, velocities and positions. The use of IMU+DGPS intruduces higher estimation errors due to the increase of noise. In particular, the positions are the most polluted due to a noise RMS equal to 0.5 m (Table 2) as depicted in Figure 11. The errors introduced by the DGPS are the same order of manitude of the heave motion $z(t)$ providing a significant decrease in performance of the $\hat{F}_{wz}(t)$ estimation. The performances of the IMU framework almost equalize the IMU+DGPS one for all the DoF. As demonstrated for the noiseless case, it is apparent that removing the DPGS noisy measurements does not affect the quality of the estimation. Having a good quality in $\delta(t)$, $\dot{\delta}(t)$ and $\ddot{x}(t)$ acquisitions allows to effectively handle the estimation of the coupled DoF since they mutually influence each other. For what concern the GoF_z value, the error introduced by the DGPS forces to increase R coefficient associated to $z(t)$ to such an extent that its measurements are not taken into account. This demonstrate why IMU+DGPS and IMU have similar performances for the heave component.
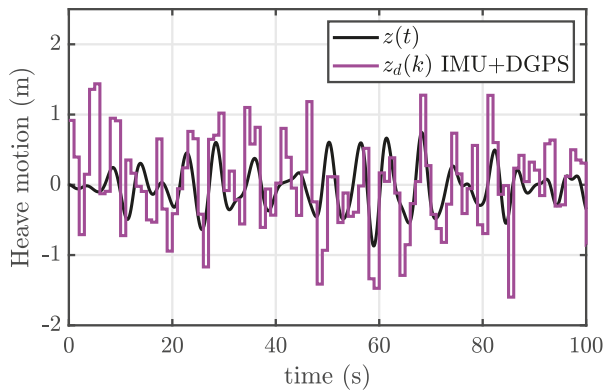

Figure 11. Heave motion compared with its DGPS acquired signal (Wave Id 2).

As shown in Figure A4, the introduction of noisy measurements negatively affects the estimation accuracy of the NN, expecially for the heave DoF. A relevant degradation of performance is shown for the IMU+DGPS and IMU framework estimating the wave exctitation force along the heave direction. As demostrated in Figure 11, the heave motion provided by the DGPS is heavily polluted by sensor noise making the NN unable to estimate the heave component with acceptable accuracy. In this context, the KF implementing the IMU+DGPS or IMU unit exploits the heave acceleration to estimate the $\hat{F}_{wz}(t)$ component with almost double precision than the NN.

6.3. Sensitivity to Plant Variations

In order to evaluate the effectiveness of KF and NN, the architectures are tested considering a typical case may happen in practice: variation of the physical properties of the floater. In fact, the WEC model may differ from its built version passing from the theoretical design to its construction in the shipyard and, even more, during its life cycle due to wear and biofouling. A further analysis is performed, testing the behavior of the frameworks modifying the mass matrix M and stiffness matrix K. An iterative method is proposed varying both the mass and stiffness matrix in respect to the nominal value as follows:

$$M_c = \overline{M}M$$
$$K_c = \overline{K}K$$

(33)

where $\overline{M}$ and $\overline{K}$ are the correction coefficients and M_c and K_c the corrected values. $\overline{M}$ and $\overline{K}$ span from 0.85 to 1.15. At this point, the performances of the KF are shown in Figure 12 in term of $\overline{GoF}$. The decrease of performances is limited for the surge component. The variation of the mass matrix results in a decay of almost 0.1 of $\overline{GoF}_x$ for all the measurement frameworks. The stiffness matrix does not influence the estimation of the $\hat{F}_{wx}(t)$ since the hydrostatic stiffness is null in the x direction. In this regard, no variation of $\overline{GoF}_x$ is detected in Figure 12d. The degradation of performance is quite sensitive to the mass and the stiffness variation for heave and pitch DoFs. As to the mass matrix, the $\overline{GoF}_{delta}$ in Figure 12c shows an higher decrease since pitch-surge modes are coupled and the estimation is influenced both by the diagonal and off-diagonal terms of M; as demonstrated in [14], the pitch force estimation is more influenced than the heave one because more terms of M are modified at once. The K variation results in a decay of almost 0.2 in both $\overline{GoF}_z$ and $\overline{GoF}_\delta$ for all the measurement frameworks as depicted in Figure 12e,f.
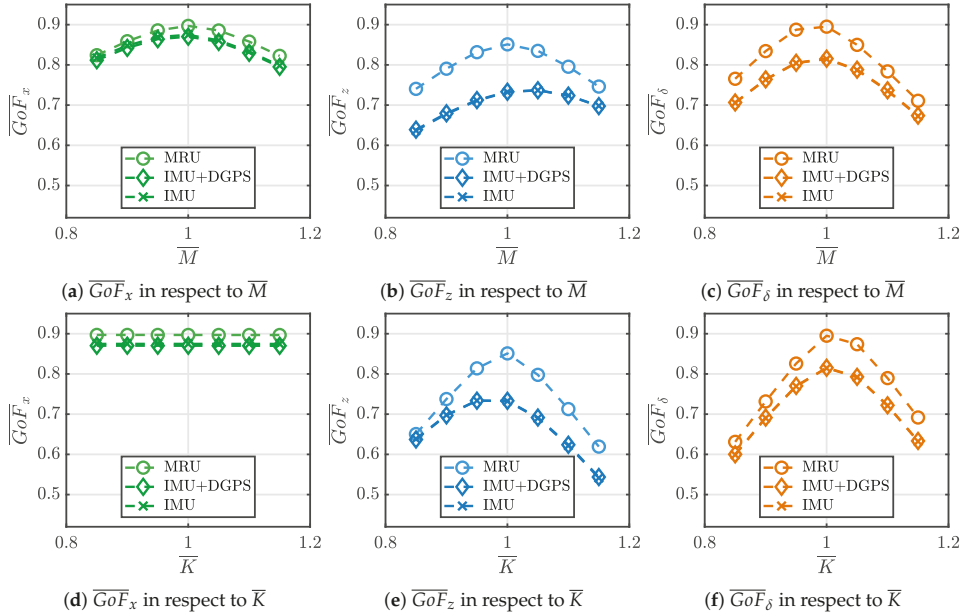
Figure 12. $\overline{GoF}$ results obtained with the KF varying $\overline{M}$ and $\overline{K}$. The first column refers to the x DoF (**a,d**), the second to the z DoF (**b,e**) and the third to the δ DoF (**c,f**).

Figure 13 illustrates the influence of $\overline{M}$ and $\overline{K}$ for the NN framework.
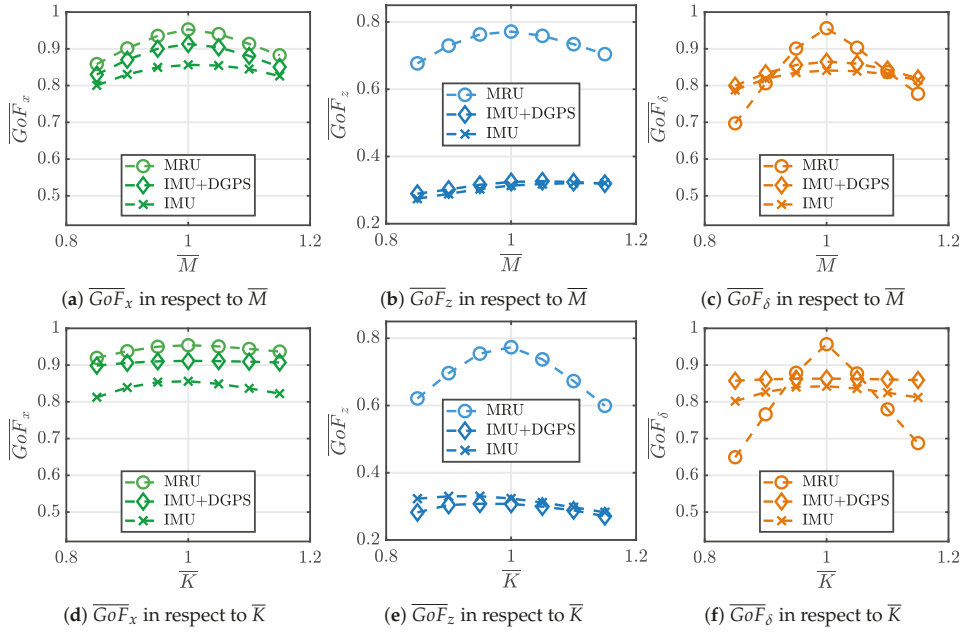
Figure 13. $\overline{GoF}$ results obtained with the NN varying $\overline{M}$ and $\overline{K}$. The first column refers to the x DoF (**a**,**d**), the second to the z DoF (**b**,**e**) and the third to the δ DoF (**c**,**f**).

A mean decrease of 0.1 is shown for all the measurement frameworks in presence of mass matrix variations, except for a high reduction of GoF_δ with the MRU configuration. The NN is merely a non-linear function that maps a serie of input-output arguments regardless of any phisical background. The training algorithm considers all the measurements available from the MRU to train the NN and a variation of the mass matrix influences all the measurements data provided to the network leading to a lower estimation accuracy. On the other hand, IMU+DGPS and IMU consider few measurements and appear to be less sensitive to plant variations. In particular, the GoF_δ suffers of a decrease up to 0.3 for a $\overline{K}$ of 0.85 and almost 0.25 for a $\overline{K}$ equal to 1.15, suggesting again that the MRU framework is less robust in presence of plant variations with the NN model. Likewise, a stiffness matrix variation negatively affects the estimation accuracy of $\hat{F}_{wx}$ despite its estimation is influenced only by $\delta(t)$, $\dot{\delta}(t)$ and $\ddot{x}(t)$ acquisitions as demostrated for the KF observer.

6.4. Comparison and Summary

The weighted GoFs and percentage differences of the KF and NN results are summarized in Table 6. The apex * means that no disturbances are considered. Starting from noiseless results, the $\overline{GoF}_x$ and $\overline{GoF}_\delta$ values confirm that the measurements of an IMU* unit are sufficient to estimate the surge and pitch components with acceptable accuracy. In detail, excluding absolute displacements and velocity measurements the $\overline{GoF}_x|_{KF}$ decreases from 0.910 to 0.893, the $\overline{GoF}_\delta|_{KF}$ from 0.901 to 0.899, the $\overline{GoF}_x|_{NN}$ from 0.951 to 0.931 and the $\overline{GoF}_\delta|_{KF}$ from 0.961 to 0.940. $\overline{GoF}_z$ follows the same behaviour, especially from the IMU+DGPS* to IMU* framework where a decrease of 0.229 and 0.397 appear for the KF and NN, respectively. Comparing the two techniques, the performance of the NN model surpasses the KF perfromance for surge and pitch DoFs, especially for the pitch DoF where an increment of 6.65%, 6.31% and 5.73% is achieved. However, the estimation of the heave force is not reliable with the NN, where a difference of −28.5% is obtained. Interestingly, the NN is able to handle noisy data better than the KF for both surge and pitch DoF, except for the IMU case. Specifically, a minimal difference of 2.73% is

obtained with the IMU framework in surge direction. The NN always overcomes the $\overline{GoF}_\delta$ of the KF with a peak of 6.70% with a MRU unit. On the other hand, poor performances are carried out for the heave DoF with the NN, obtaining a weighted GoF almost equal to 0.3 for both IMU+DGPS and IMU.

Table 6. $\overline{GoF}$ and $\Delta\overline{GoF}$ results of the KF observer and NN model for each measurement frameworks. The measurements are considered with and without noise.

Framework	Noise	Kalman Filter			Neural Network			$\Delta\overline{GoF}_x$ (%)	$\Delta\overline{GoF}_z$ (%)	$\Delta\overline{GoF}_\delta$ (%)
		$\overline{GoF}_x$	$\overline{GoF}_z$	$\overline{GoF}_\delta$	$\overline{GoF}_x$	$\overline{GoF}_z$	$\overline{GoF}_\delta$			
MRU*	×	0.910	0.971	0.901	0.951	0.941	0.961	4.50	−3.08	6.65
IMU+DGPS*	×	0.910	0.967	0.902	0.950	0.939	0.959	4.39	−2.89	6.31
IMU*	×	0.893	0.758	0.889	0.913	0.542	0.940	2.23	−28.5	5.73
MRU	✓	0.898	0.873	0.895	0.950	0.771	0.955	5.79	−11.6	6.70
IMU+DGPS	✓	0.875	0.744	0.824	0.912	0.327	0.863	4.22	−56.1	4.73
IMU	✓	0.878	0.744	0.819	0.854	0.322	0.839	−2.73	−56.7	1.82

Surprisingly, the sensitivity of the KF in presence of plant inaccuracies is evident compared to the NN. In particular, Figure 14 highlight a relevant decrease in performance for $\hat{F}_{w\delta}(t)$ estimation with a $\overline{M}$ and $\overline{K}$ variation when the KF is employed (IMU framework). Using the KF, the results show a decrease of performances up to 0.18 points varying $\overline{M}$ and 0.20 varying $\overline{K}$. In contrast, the NN guarantee a weighted $\overline{GoF}_\delta$ always greater than 0.77 suggesting low sensitivity when plant variations appear. In all likelihood, the sensitivity of the KF could be diminished tuning the matrix Q in order to give less importance to the model in favor of measurements. However, more research on this topic needs to be undertaken before the association between Q and KF sensitivity is more clearly understood.

(**a**) $\overline{GoF}_\delta$ in respect to $\overline{M}$ (**b**) $\overline{GoF}_\delta$ in respect to $\overline{K}$
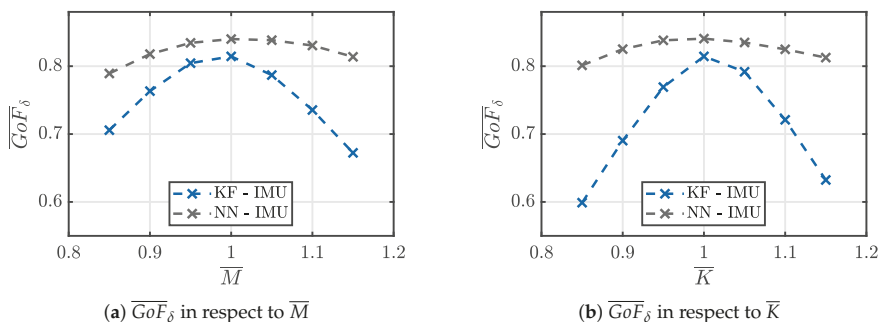
Figure 14. $\overline{GoF}_\delta$ comparison varying $\overline{M}$ (**a**) and $\overline{K}$ (**b**) for the IMU framworks.

The real ISWEC system is equipped with the MTi unit presented in Section 2.2.7. Unlike the MRU, the IMU unit does not provide positioning data and the measurement noise are one order of magnitude higher than the MRU ones. Although more information are available with the MRU, the IMU framework provide acceptable accuracy for both surge and pitch wave forces, directly involved in the power extraction. In detail, in case of noisy measurements and KF observer, the weighted accuracy approaches 0.88 and 0.82 for $\overline{GoF}_x$ and $\overline{GoF}_\delta$, respectively; with the NN the accuracy is about 0.85 and 0.84 for $\overline{GoF}_x$ and $\overline{GoF}_\delta$, respectively. Moreover, the MRU units are (usually) one order of magnitude more expensive than the IMU ones, and the precision provided does not justify the little increase of performances, expecially in the KF case. Despite the low performances obtained for the WEF in heave direction (not directly involted in the power extraction), the IMU sensor is considered reliable for the estimation.

7. Conclusions

The purpose of this work is to estimate the WEFs of a non-linear WEC employing a KF observer and a NN model. This study proposes a methodology for tuning both estimators and compares them for a wide range of sea-states in presence of noise disturbances and plant variations. Four different measurement frameworks are proposed, one ideal (full measurements available without noise) and three real frameworks composed by three different sensors commercially available. The main aim is to assess the estimation performances in term of GoF for different sensor equipments in all the operating conditions of the ISWEC device. The non-linear 3-DoF model of the ISWEC is considered as the plant of reference. A linear 3-DoF hydrodynamic model is used in the KF assuming linear wave theory and linear viscous damping along the pitch DoF. Moreover, the filter model assumes no viscous damping in both surge and heave directions and the mooring forces are considered as an unknow state to be estimated. The key of the KF is to approximate the expression of the WEFs as a linear superposition of finite harmonic components with variable amplitudes and fixed frequencies. Hence, it is possible to include the excitation forces into the state vector of the system model and perform an unknown state estimation. This method restricts the bandwidth of the estimated disturbance as it can only estimate at the specified discrete frequencies. This makes it more robust to other external disturbances such as unmodelled hydrodynamic forces outside from the frequency range considered. The feedforward NN is designed according to the hydrodynamic equation of the ISWEC. The WEFs are expressed as a function of the system dynamics at current and past time instants taking into account the dynamic memory of the plant using static neurons with no feedback data.

First, the KF parameters are tuned according to the frequency range, stating the WEF frequencies and the mooring frequencies. The wave energy matrix of the sea-site of interest has been considered to identify the principal wave periods of the incoming sea-states to decouple them from the mooring actions. Moreover, according to the noise magnitudes of the sensors, matrices Q and R have been balanced to obtain the best GoF from each measurement framework. The NN has been tuned with the same intent, chosing both delay steps and number of neurons guaranteeing the best compromise between network complexity and estimation accuracy. Second, numerical simulations are performed to investigate the influence of the measurement framework and sensors accuracy. Overall, it is demonstrated that the 3-DoF KF performs well when applied to a non-linear WEC model. The KF shows best performances with the MRU* and IMU+DGPS* frameworks, expecially in surge and pitch directions where a $\overline{GoF}_x$ and $\overline{GoF}_\delta$ greater than 0.9 are guaranteed. The IMU* framework gives the worst performances along the heave direction performing a $\overline{GoF}_z$ almost equal to 0.75. The same argument applies for the NN, where the estimation performances are maximized in surge and pitch. Adding noisy measurements results in an acceptable decrease of accuracy for $\overline{GoF}_x$ and $\overline{GoF}_\delta$. In detail, the comparison shows that the estimation accuracies of NN and KF are approximately the same and a $\overline{GoF}_x$ and $\overline{GoF}_\delta$ greater than 0.83 is obtained. However, both the KF and NN are considered not reliable for the WEF estimation along the heave DoF if DGPS and IMU are employed. Then, intersting results are obtained comparing the estimation performances under plant variations. Contrary to expectations, the KF is affected by plant variations more than the NN. Despite the KF can handle inaccuracies of the numerical model tuning on the Q matrix, the NN shows good performances when these inaccuracies become relevant. Further work is required to establish the underlying cause of this outcome, acting on the Q matrix to improve the mean performances of the KF observer. Sections 6.1–6.3 demonstrated the good reliability of the IMU framework for the WEF estimation in surge and pitch directions for both KF and NN. However, it is evident how the estimation of the heave component is affected by the absence of the heave motion in the KF and both heave motion and velocity in NN. Despite this outcome, the use of the IMU unit is encourageed since the $\hat{F}_{wz}(t)$ is not directly involved in the power extraction of the ISWEC.

In conclusion, the main advantage of the model-based approach is that in presence of a real plant, it is possible to tune the observer on a small number of waves to obtain accurate estimation performances for a large number of sea states. The main strength of the KFHO is to consider only the

frequency bandwidth specified; the knowlegde of the spectral properties of the signal to estimate allow to exclude all the undesired components and disturbance from the estimation (e.g., Mooring forces). On the other hand, a model-free non-linear approach should be more suitable to model complex hydrodynamic phenomena when their analytical expression are not available. Future work will approach the problem of the WEF estimation using more non-linear approaches (e.g., Recurrent Neural Networks and Extended Kalman Filter). The non-linear approach is expected to be more accurate in presence of strong non-linearity (e.g., PTO saturations and non-linear mooring models) in respect to a linear model-based observer. The aim will be elaborate on the estimation results between a model-based and model-free approach in term of estimation performances for a broad range of sea states. The best estimation approach will be used for the implementation of the MPC strategy on ISWEC.

Appendix A Figures

Appendix A.1. GoF with Noiseless Data and KF Observer

(**a**) *GoF$_x$* of MRU   (**b**) *GoF$_z$* of MRU   (**c**) *GoF$_\delta$* of MRU

(**d**) *GoF$_x$* of IMU+DGPS   (**e**) *GoF$_z$* of IMU+DGPS   (**f**) *GoF$_\delta$* of IMU+DGPS

Figure A1. *Cont.*

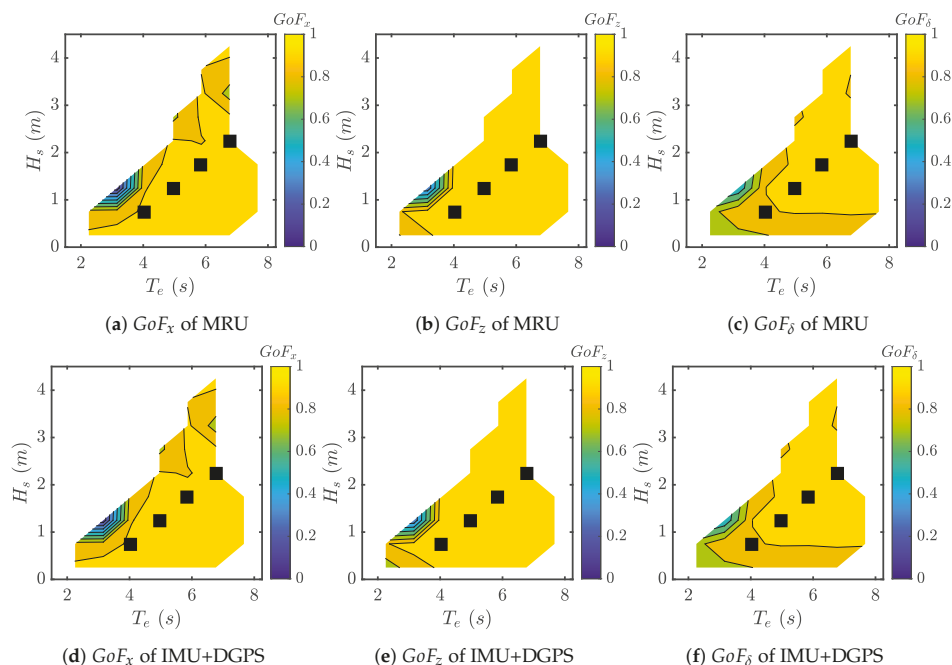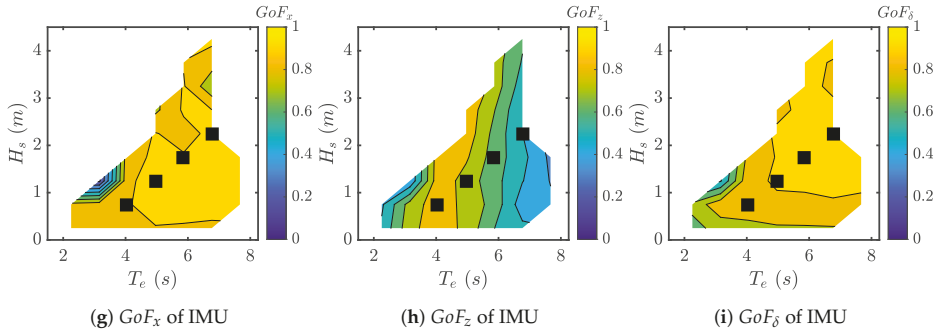(**g**) *GoF_x* of IMU　　　　　　　(**h**) *GoF_z* of IMU　　　　　　　(**i**) *GoF_δ* of IMU
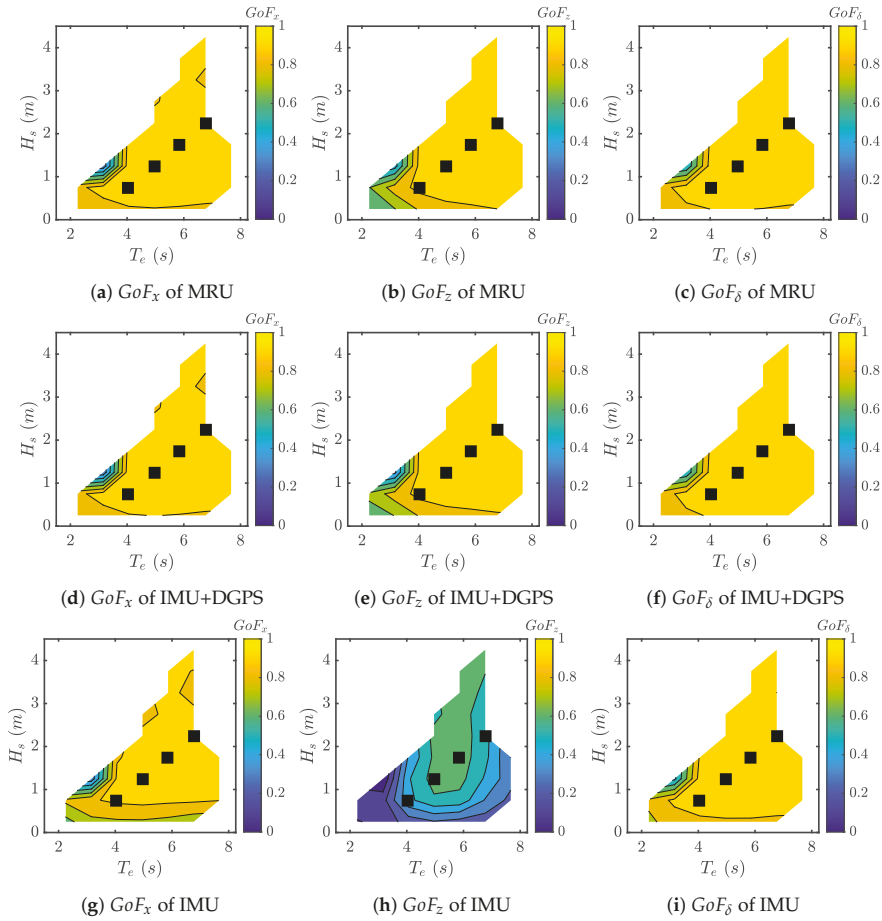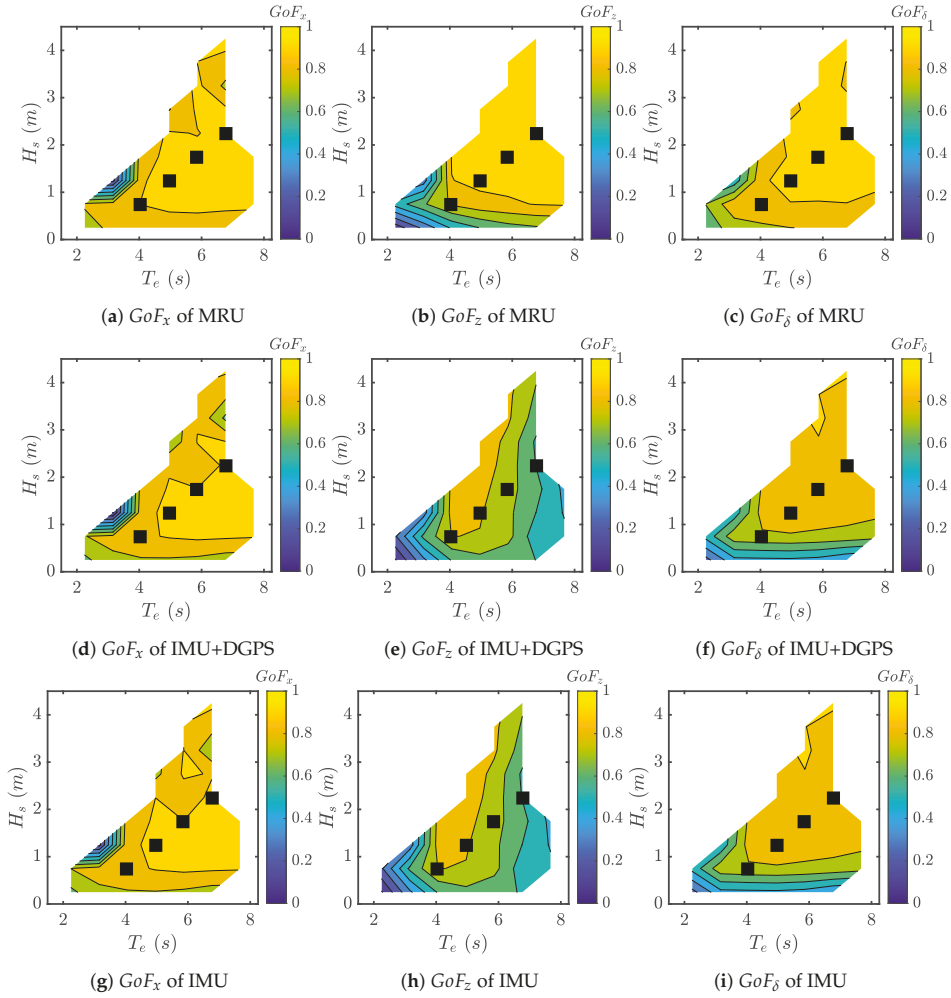
Figure A1. *GoF* results with noisless measurements for each measurement framework obtained with the KF. The first row refers to the MRU framework (**a–c**), the second to the IMU+DGPS framework (**d–f**), the thrid to the IMU framework (**g–i**).

Appendix A.2. GoF with Noiseless Data and NN Model

(**a**) *GoF_x* of MRU　　　　　　　(**b**) *GoF_z* of MRU　　　　　　　(**c**) *GoF_δ* of MRU

(**d**) *GoF_x* of IMU+DGPS　　　　(**e**) *GoF_z* of IMU+DGPS　　　　(**f**) *GoF_δ* of IMU+DGPS

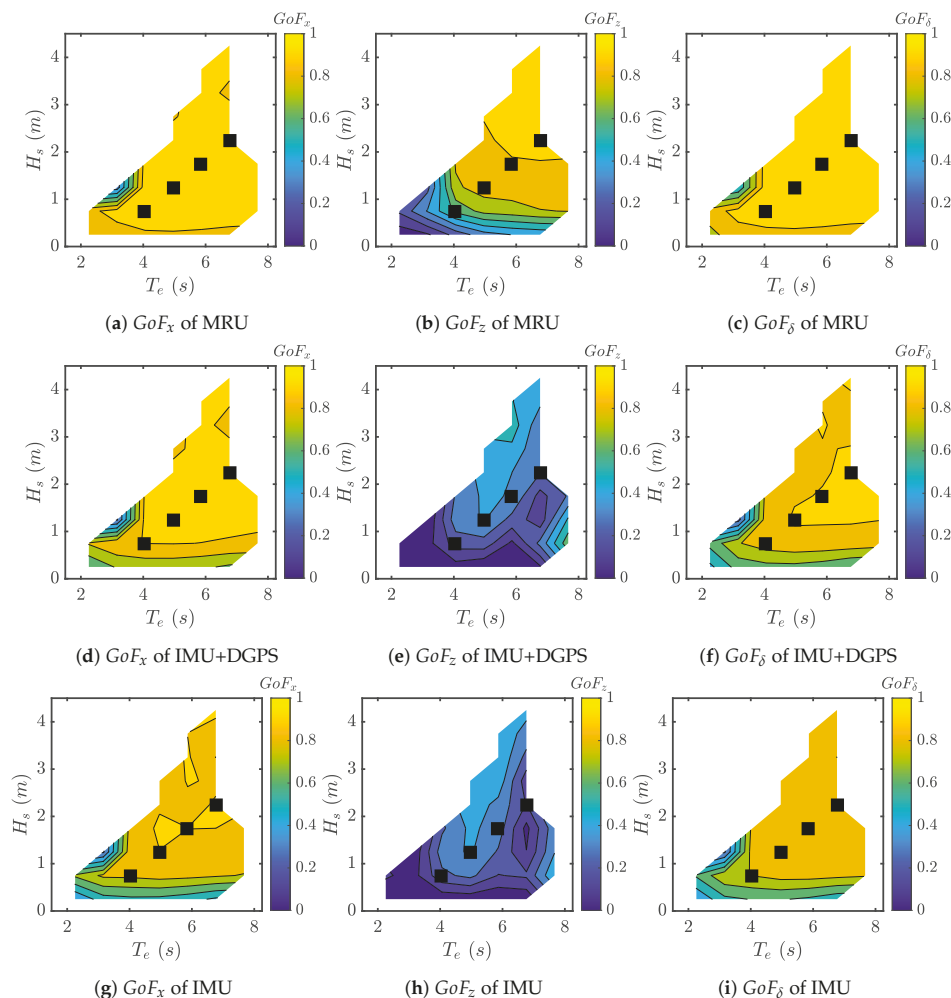(**g**) *GoF_x* of IMU　　　　　　　(**h**) *GoF_z* of IMU　　　　　　　(**i**) *GoF_δ* of IMU

Figure A2. *GoF* results with noisless measurements for each measurement framework obtained with the NN. The first row refers to the MRU framework (**a–c**), the second to the IMU+DGPS framework (**d–f**), the thrid to the IMU framework (**b–i**).

Appendix A.3. GoF with Noisy Data and KF Observer

Figure A3. *GoF* results with noisy measurements for each measurement framework obtained with the KF. The first row refers to the MRU framework (**a**–**c**), the second to the IMU+DGPS framework (**d**–**f**), the thrid to the IMU framework (**g**–**i**).

Appendix A.4. GoF with Noisy Data and NN Model

(**a**) *GoF$_x$* of MRU (**b**) *GoF$_z$* of MRU (**c**) *GoF$_\delta$* of MRU

(**d**) *GoF$_x$* of IMU+DGPS (**e**) *GoF$_z$* of IMU+DGPS (**f**) *GoF$_\delta$* of IMU+DGPS

(**g**) *GoF$_x$* of IMU (**h**) *GoF$_z$* of IMU (**i**) *GoF$_\delta$* of IMU

Figure A4. *GoF* results with noisy measurements for each measurement framework obtained with the NN. The first row refers to the MRU framework (**a**–**c**), the second to the IMU+DGPS framework (**d**–**f**), the thrid to the IMU framework (**g**–**i**).

References

1. Faedo, N.; Olaya, S.; Ringwood, J.V. Optimal control, MPC and MPC-like algorithms for wave energy systems: An overview. *IFAC J. Syst. Control* **2017**, *1*, 37–56. [CrossRef]
2. Pena-Sanchez, Y.; Windt, C.; Davidson, J.; Ringwood, J.V. A Critical Comparison of Excitation Force Estimators for Wave-Energy Devices. *IEEE Trans. Control Syst. Technol.* **2019**, 1–13. [CrossRef]
3. Ling, B.A.; Batten, B.A. Real Time Estimation and Prediction of Wave Excitation Forces on a Heaving Body. In Proceedings of the International Conference on Offshore Mechanics and Arctic Engineering, St. John's, NL, Canada, 31 May–5 June 2015.
4. Garcia-Abril, M.; Paparella, F.; Ringwood, J.V. Excitation force estimation and forecasting for wave energy applications. *IFAC Pap.* **2017**, *50*, 14692–14697. [CrossRef]

5. Pena-Sanchez, Y.; Garcia-Abril, M.; Paparella, F.; Ringwood, J.V. Estimation and Forecasting of Excitation Force for Arrays of Wave Energy Devices. *IEEE Trans. Sustain. Energy* **2018**, *9*, 1672–1680. [CrossRef]
6. Nguyen, H.N.; Tona, P. Wave Excitation Force Estimation for Wave Energy Converters of the Point-Absorber Type. *IEEE Trans. Control Syst. Technol.* **2018**, *26*, 2173–2181. [CrossRef]
7. Abdelrahman, M.; Patton, R.; Guo, B.; Lan, J. Estimation of wave excitation force for wave energy converters. In Proceedings of the 2016 3rd Conference on Control and Fault-Tolerant Systems (SysTol), Barcelona, Spain, 7–9 September 2016; pp. 654–659.
8. Abdelkhalik, O.; Zou, S.; Robinett, R.; Bacelli, G.; Wilson, D. Estimation of excitation forces for wave energy converters control using pressure measurements. *Int. J. Control* **2017**, *90*, 1793–1805. [CrossRef]
9. Hillis, A.J.; Brask, A.; Whitlam, C. Real-time wave excitation force estimation for an experimental multi-DOF WEC. *Ocean Eng.* **2020**, *213*, 107788. [CrossRef]
10. Li, L.; Gao, Z.; Yuan, Z.M. On the sensitivity and uncertainty of wave energy conversion with an artificial neural-network-based controller. *Ocean Eng.* **2019**. [CrossRef]
11. Desouky, M.A.A.; Abdelkhalik, O. Wave prediction using wave rider position measurements and NARX network in wave energy conversion. *Appl. Ocean Res.* **2019**, *82*, 10–21. [CrossRef]
12. Genuardi, L.; Bracco, G.; Sirigu, S.; Bonfanti, M.; Paduano, B.; Dafnakis, P.; Mattiazzo, G. An application of model predictive control logic to inertial sea wave energy converter. *Adv. Mech. Mach. Sci.* **2019**. [CrossRef]
13. Sirigu, S.A.; Bracco, G.; Bonfanti, M.; Dafnakis, P.; Mattiazzo, G. On-board sea state estimation method validation based on measured floater motion. In Proceedings of the 11th IFAC Conference on Control Applications in Marine Systems, Robotics, and Vehicles CAMS 2018, Opatija, Croatia, 10–12 September 2018.
14. Bonfanti, M.; Carapellese, F.; Sirigu, S.A.; Bracco, G.; Mattiazzo, G. Excitation Forces Estimation for Non-linear Wave Energy Converters: A Neural Network Approach. Unpublished work.
15. Vissio, G. ISWEC toward the Sea-Development, Optimization and Testing of the Device Control Architecture. Ph.D. Thesis, Politecnico di Torino, Torino, Italy, 2018.
16. Bracco, G.; Casassa, M.; Giorcelli, E.; Giorgi, G.; Martini, M.; Mattiazzo, G.; Passione, B.; Raffero, M.; Vissio, G. Application of sub-optimal control techniques to a gyroscopic Wave Energy Converter. *Renew. Energies Offshore* **2014**, 265–269. [CrossRef]
17. Bonfanti, M.; Bracco, G.; Dafnakis, P.; Giorcelli, E.; Passione, B.; Pozzi, N.; Sirigu, S.; Mattiazzo, G. Application of a passive control technique to the ISWEC: Experimental tests on a 1:8 test rig. In Proceedings of the NAV International Conference on Ship and Shipping Research, Trieste, Italy, 20–22 June 2018.
18. Bracco, G.; Giorcelli, E.; Giorgi, G.; Mattiazzo, G.; Passione, B.; Raffero, M.; Vissio, G. Performance assessment of the full scale ISWEC system. In Proceedings of the 2015 IEEE International Conference on Industrial Technology (ICIT), Seville, Spain, 17–19 March 2015; pp. 2499–2505.
19. Bracco, G.; Cagninei, A.; Giorcelli, E.; Mattiazzo, G.; Poggi, D.; Raffero, M. Experimental validation of the ISWEC wave to PTO model. *Ocean. Eng.* **2016**, *120*, 40–51. [CrossRef]
20. Cagninei, A.; Raffero, M.; Bracco, G.; Giorcelli, E.; Mattiazzo, G.; Poggi, D. Productivity analysis of the full scale inertial sea wave energy converter prototype: A test case in Pantelleria Island. *J. Renew. Sustain. Energy* **2015**, *7*, 61703. [CrossRef]
21. Raffero, M.; Martini, M.; Passione, B.; Mattiazzo, G.; Giorcelli, E.; Bracco, G. Stochastic control of inertial sea wave energy converter. *Sci. World J.* **2015**, *2015*. [CrossRef]
22. Wendt, F.; Nielsen, K.; Yu, Y.H.; Bingham, H.; Eskilsson, C.; Kramer, M.; Babarit, A.; Bunnik, T.; Costello, R.; Crowley, S.; et al. Ocean energy systemswave energy modelling task: Modelling, verification and validation ofwave energy converters. *J. Mar. Sci. Eng.* **2019**, *7*, 379. [CrossRef]
23. Ransley, E.; Yan, S.; Brown, S.; Hann, M.; Graham, D.; Windt, C.; Schmitt, P.; Davidson, J.; Ringwood, J.; Musiedlak, P.H.; et al. A blind comparative study of focused wave interactions with floating structures (CCP-WSI blind test series 3). *Int. J. Offshore Polar Eng.* **2020**, *30*, 1–10. [CrossRef]
24. Faltinsen, O.M. *Sea Loads on Ships and Offshore Structures*; Cambridge University Press: Cambridge, UK, 1993.
25. Cummins, W.E. *The Impulse Response Function and Ship Motions*; Technical Report 1661; Department of the Navy: Port Hueneme, CA, USA, 1962.
26. Perez, T.; Fossen, T.I. Joint identification of infinite-frequency added mass and fluid-memory models of marine structures. *Model. Identif. Control* **2008**, *29*, 93–102. [CrossRef]
27. Pérez, T.; Fossen, T.I. Time-vs. frequency-domain Identification of parametric radiation force models for marine structures at zero speed. *Model. Identif. Control* **2008**, *29*, 1–19. [CrossRef]

28. Fontana, M.; Casalone, P.; Sirigu, S.A.; Giorgi, G. Viscous Damping Identification for a Wave Energy Converter Using CFD-URANS Simulations. *J. Mar. Sci. Eng.* **2020**, *8*, 355. [CrossRef]

29. Pozzi, N.; Bracco, G.; Passione, B.; Sirigu, S.A.; Mattiazzo, G. PeWEC: Experimental validation of wave to PTO numerical model. *Ocean. Eng.* **2018**, *167*, 114–129. [CrossRef]

30. Newman, J.N. Second-order, slowly-varying Forces on Vessels in Irregular Waves. In *International Symposium on the Dynamics of Marine Vehicles and Structures in Waves*; IME: London, UK, 1974; pp. 182–186.

31. Sirigu, S.A.; Bonfanti, M.; Begovic, E.; Bertorello, C.; Dafnakis, P.; Giorgi, G.; Bracco, G.; Mattiazzo, G. Experimental investigation of the mooring system of a wave energy converter in operating and extreme wave conditions. *J. Mar. Sci. Eng.* **2020**, *8*, 180. [CrossRef]

32. Pozzi, N.; Bonfanti, M.; Mattiazzo, G. Mathematical Modeling and Scaling of the Friction Losses of a Mechanical Gyroscope. *Int. J. Appl. Mech.* **2018**, *10*, 1–21. [CrossRef]

33. Ochi, M.K. *Ocean Waves: The Stochastic Approach*; Cambridge Ocean Technology Series; Cambridge University Press: Cambridge, UK, 1998.

34. Mei, C.; Stiassnie, M.; Yue, D. *Theory and Applications of Ocean Surface Waves*; Technion-Israel Institute of Technology: Haifa, Israel, 2005; Volume 23, p. 503.

35. Merigaud, A. A Harmonic Balance Framework for the Numerical Simulation of Non-Linear Wave Energy Converter Models in Random Seas. Ph.D. Thesis, National University of Ireland Maynooth, Kildare, Ireland, 2018.

36. Sirigu, S.A. Development of A Resonance-Tunable Wave Energy Converter. Ph.D. Thesis, Politecnico di Torino, Torino, Italy, 2019.

37. Hasselmann, K.; Barnett, T.; Bouws, E.; Carlson, H.; Cartwright, D.; Enke, K.; Ewing, J.; Gienapp, H.; Hasselmann, D.; Kruseman, P.; et al. Measurements of wind-wave growth and swell decay during the Joint North Sea Wave Project (JONSWAP). *Deut. Hydrogr. Z.* **1973**, *8*, 1–95.

38. MTi User Manual. 2020. Available online: https://www.xsens.com/hubfs/Downloads/usermanual/MTi_usermanual.pdf (accessed on 20 October 2020)

39. *ECN 413, ECN 425, ERN 487, Product Information ECN*; HEIDENHAIN: Traunreut, Germany, 2017.

40. NI cRIO-9030 User Manual. 2020. Available online: https://www.ni.com/pdf/manuals/376260a_02.pdf (accessed on 20 October 2020)

41. Khaleghi, B.; Khamis, A.; Karray, F.O.; Razavi, S.N. Multisensor data fusion: A review of the state-of-the-art. *Inf. Fusion* **2013**, *14*, 28–44. [CrossRef]

42. Fung, M.L.; Chen, M.Z.; Chen, Y.H. Sensor fusion: A review of methods and applications. In Proceedings of the 29th Chinese Control and Decision Conference, Chongqing, China, 28–30 May 2017; pp. 3853–3860.

43. Crassidis, J.L.; Junkins, J.L. *Optimal Estimation of Dynamic Systems (Chapman & Hall/CRC Applied Mathematics & Nonlinear Science)*, 2nd ed.; Chapman & Hall/CRC: Boca Raton, FL, USA, 2011.

44. Paduano, B.; Giorgi, G.; Gomes, R.P.; Pasta, E.; Henriques, J.C.; Gato, L.M.; Mattiazzo, G. Experimental validation and comparison of numerical models for the mooring system of a floating wave energy converter. *J. Mar. Sci. Eng.* **2020**, *8*, 565. [CrossRef]

45. Hall, M. MoorDyn User's Guide. 2015. Available online: http://www.matt-hall.ca/ (accessed on 20 October 2020).

46. Orcina-Ltd. OrcaFlex Software. 2014. Available online: http://orcina.com/ (accessed on 20 October 2020).

47. Ablameyko, S.; Goras, L.; Gori, M.; Piuri, V. *Neural Networks for Instrumentation, Measurement and Related Industrial Applications*; IOS Press: Amsterdam, The Netherlands, 2003.

48. Laurent, Q. Estimation and Prediction of Wave Input and System States Based on Local Hydropressure and Machinery Response Measurements. Ph.D. Thesis, KTH, Optimization and Systems Theory, Stockholm, Sweden, 2016. Available online: http://urn.kb.se/resolve?urn=urn:nbn:se:kth:diva-191995 (accessed on 20 October 2020).

Article

Towards Real-Time Reinforcement Learning Control of a Wave Energy Converter

**Enrico Anderlini [1,*], Salman Husain [2], Gordon G. Parker [2], Mohammad Abusara [3]
and Giles Thomas [1]**

[1]   Department of Mechanical Engineering, University College London, London WC1E 6BT, UK;
       giles.thomas@ucl.ac.uk
[2]   Department of Mechanical Engineering—Engineering Mechanics, Michigan Technological University,
       Houghton, MI 49931, USA; shusain@mtu.edu (S.H.); ggparker@mtu.edu (G.G.P.)
[3]   College of Engineering, Mathematics and Physical Sciences, University of Exeter, Penryn Campus, Penryn,
       Cornwall TR10 9FE, UK; M.Abusara@exeter.ac.uk
*   Correspondence: e.anderlini@ucl.ac.uk

Abstract: The levellised cost of energy of wave energy converters (WECs) is not competitive with fossil fuel-powered stations yet. To improve the feasibility of wave energy, it is necessary to develop effective control strategies that maximise energy absorption in mild sea states, whilst limiting motions in high waves. Due to their model-based nature, state-of-the-art control schemes struggle to deal with model uncertainties, adapt to changes in the system dynamics with time, and provide real-time centralised control for large arrays of WECs. Here, an alternative solution is introduced to address these challenges, applying deep reinforcement learning (DRL) to the control of WECs for the first time. A DRL agent is initialised from data collected in multiple sea states under linear model predictive control in a linear simulation environment. The agent outperforms model predictive control for high wave heights and periods, but suffers close to the resonant period of the WEC. The computational cost at deployment time of DRL is also much lower by diverting the computational effort from deployment time to training. This provides confidence in the application of DRL to large arrays of WECs, enabling economies of scale. Additionally, model-free reinforcement learning can autonomously adapt to changes in the system dynamics, enabling fault-tolerant control.

Keywords: wave energy converter; control; reinforcement learning; deep reinforcement learning; deep learning; adaptive control

---

1. Introduction

Ocean wave energy is a type of renewable energy with the potential to contribute significantly to the future energy mix. Despite an estimated global resource of 146 TWh/yr [1], the wave energy industry is still in its infancy. In 2014, there were less than 10 MW of installed capacity worldwide due to the high levellised cost of energy (LCoE) of approximately EUR 330–630/MWh [1]. The main operational challenge is the maximisation of energy extraction in the common, low-energetic sea states, whilst ensuring the survival of the wave energy converters (WECs) in storms [2]. Two major contributors to the lowering of the LCoE to EUR 150/MWh by 2030 are expected to be the achievement of economies of scale and the development of effective control strategies [3].

Over the past decade, model predictive control (MPC) has attracted much research interest, as it can offer improved performance over the control strategies developed in the 1970s and 1980s, based on hydrodynamic principles. Assuming knowledge of the wave excitation force, MPC computes the control action, typically the force applied by the power take-off system (PTO), that results in optimal energy absorption over a future time horizon using a model of the WEC dynamics. The controller

applies only the first value of the PTO force, recomputing the optimal control action at the next time horizon. The iterative procedure enables the controller to reduce the negative impact of inaccuracies in the prediction of the future excitation force and modelling errors. Additionally, the MPC framework enables the inclusion of constraints on both the control action and the system dynamics. A good review of MPC for WEC control can be found in [4]. Li and Belmont first proposed a fully convex implementation, which trades off the energy absorption, the energy consumed by the actuator and safe operation [5]. An even more efficient implementation cast in a quadratic programming form has been proposed by Zhong and Yeung [6]. Fundamentally, the convex form enables the strategy to be generalised to the control of multiple WECs in real-time [7,8]. However, linear MPC relies on a linear model of the WEC dynamics. In energetic waves, nonlinearities in the static and dynamic Froude–Krylov forces (i.e., the hydrostatic restoring and wave incidence forces) and viscous drag effects can become significant [9]. Although nonlinear MPC strategies have been proposed [10,11] and even tested experimentally [12], achieving a successful real-time, centralised control implementation for multiple WECs is expected to be challenging [13].

As described in [14,15], alternative strategies have been developed for the control of WECs. Some, like simple-and-effective control [16], present similar performance to MPC at a much lower computational cost. Alternative solutions based on machine learning have been recently considered thanks to the advancements in the field of artificial intelligence. Most commonly, the neural networks are used to provide a data-based, nonlinear model of the system dynamics, i.e., for system identification. After training, the identified model is coupled with standard strategies used for the control of WECs, e.g., resistive or damping control in [17], reactive or impedance-matching in [18] and latching control in [19,20]. On the one hand, some studies have proposed the use of neural networks to find the optimal parameters for impedance-matching control on a time-averaged basis [21], thus being readily applicable to the centralised control of multiple WECs [22]. On the other hand, other works have focused on real-time control [19,20,23], exploiting the capability of neural networks to handle the predicted wave elevation over a future time horizon, similar to MPC. The main advantage of machine learning models for the system identification of WECs is that the same method can be used for different WEC technologies and is potentially adaptive to changes in the system dynamics, e.g., to subsystem failures or biofouling.

A promising solution to developing an optimal, real-time nonlinear controller for WECs inclusive of constraints on both the state and action is to cast the problem in a dynamic programming framework, similarly to MPC for WEC problems. In non-linear dynamic programming solutions, a neural network is used as a critic to approximate the time-dependent optimal cost value expressed as a Hamilton–Jacobi–Bellman equation. Numerical studies have shown the effectiveness and robustness of this approach for the control of a single WEC [24–26]. In particular, dynamic programming, also classified as model-based reinforcement learning (RL), is much more data-efficient than model-free RL [27]. Using a machine learning model trained on the collected data, such as Gaussian processes [27] or neural networks [24–26], enables the controller to plan off-line, thus significantly speeding up the learning of a suitable control policy even from a small set of samples. Conversely, model-free RL methods which learn from direct interactions with the environment require a much larger number of samples (in order of 10^8 as opposed to 10^4 for complex control tasks [28]). For this reason, to date model-free RL has been applied only to the time-averaged resistive and reactive control of WECs with discrete PTO damping and stiffness coefficients [29–31], with lower level controllers necessary to ensure constraints abidance [32]. However, model-free RL schemes are known to find the optimal control policy, even for real-time applications and very complex systems [28].

This paper introduces the world-first deep reinforcement learning (DRL) control method for WECs. The novel approach enables the real-time, nonlinear optimal control of WECs based on model-free RL. Deep learning allows the method to treat continuous control input and output features efficiently at deployment time.

To avoid unpredictable behaviour during the initial learning stage, WECs are expected to be controlled with model-based, robust methods once first deployed in the future. For a real-time implementation on complex WECs, these are likely to rely on linear models considering current technologies. After sufficient data samples are collected, the controller can move to the proposed data-driven model, whose computational cost at deployment does not increase if nonlinearities are present and can adapt to changes in the system dynamics or noncritical faults if retrained regularly. Hence, first of all, the WEC is operated in a range of representative sea states under the convex MPC proposed in [6,8]. Data samples are collected from 15-minute-long wave traces in each sea state. Subsequently, the dataset is used to train a deep neural network (DNN), defined as a neural network with more than one hidden layer according to [33], which mimics the controller behaviour. The DNN thus corresponds to the actor of an actor-critic RL strategy. The actor will be then used to initialise a model-free RL controller, as in [28]. The agent will then be further trained to optimise its behaviour as in [34].

In this article, the analysis is limited to the simulation of a standard spherical point absorber constrained to heaving motions [9]. The simulation environment is currently based on a linear model as presented in Section 2. The new DRL-based control method for WECs is described in Section 3. Finally, the performance of the trained actor is assessed directly against the original linear MPC developed in [6] in Section 4, with conclusions drawn in Section 5.

2. Linear Model of a Heaving Point Absorber

A heaving point absorber is shown schematically in Figure 1. Assuming linear potential wave theory, the equation of motion of a heaving point absorber can be expressed in the time domain as [35]

$$m\ddot{z}(t) = f_e(t) + f_r(t) + f_h(t) + f_m(t) + f_{PTO}(t), \tag{1}$$

where t indicates time, z the heave displacement, f_e the wave excitation force inclusive of wave incidence and diffraction effects (or dynamic Froude–Krylov and scattering forces), f_r the wave radiation force, f_h the hydrostatic restoring force (or static Froude–Krylov), f_m the mooring force, f_{PTO} the PTO or control force, and m is the mass of the buoy. In this study, the mooring forces are ignored for simplicity.
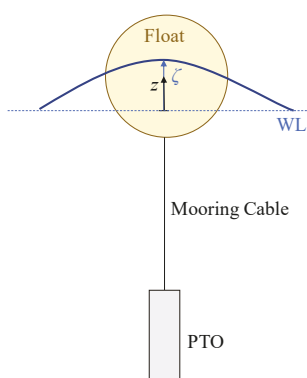
Figure 1. Heaving point absorber.

The linear excitation wave force can be obtained using the excitation impulse response function $H(t)$ as

$$f_e(t) = \int_{-\infty}^{\infty} H(t-\tau)\zeta(t)d\tau, \tag{2}$$

where ζ is the wave elevation. Similarly, the linear hydrostatic restoring force is

$$f_h(t) = -\rho g A_w z(t), \tag{3}$$

where ρ is the water density, g the gravitational acceleration and A_w the waterplane area. Using Cummins' equation [36], the radiation force can be expressed as

$$f_r(t) = -A(\infty)\ddot{z}(t) - \int_{-\infty}^{t} K(t-\tau)\dot{z}(\tau)d\tau, \tag{4}$$

where $A(\infty)$ is the heave added mass at infinite wave frequency and K is the radiation impulse response function. The convolution integral in (4) causes significant challenges for control tasks. Hence, it is common practice to approximate the convolution integral with a state-space model to improve the computational performance and ensure controllability. Here, the approach based on moment matching proposed in [37] is followed. Hence, (4) is reformulated as

$$\dot{x}_{ss}(t) = A_{ss}x_{ss} + B_{ss}\dot{z}, \tag{5a}$$

$$\int_{-\infty}^{t} K(t-\tau)\dot{z}(\tau)d\tau \approx C_{ss}x_{ss} + D_{ss}\dot{z}. \tag{5b}$$

Substituting (3)–(5) into (1) allows the equation of motion of the heaving point absorber to be expressed in state space form:

$$\dot{x}(t) = Ax(t) + B_u u(t) + B_v v(t), \tag{6a}$$

$$y = Cx, \text{ where} \tag{6b}$$

$$x = \begin{bmatrix} z & w & x_{ss}^T \end{bmatrix}^T, \tag{6c}$$

$$u = f_{PTO}, \tag{6d}$$

$$v = f_e, \tag{6e}$$

$$B_u = B_v = \begin{bmatrix} 0 & M^{-1} & \mathbf{0}^T \end{bmatrix}^T, \tag{6f}$$

$$A = \begin{bmatrix} 0 & 1 & \mathbf{0} \\ -M^{-1}C & 0 & -M^{-1}C_{ss} \\ \mathbf{0} & B_{ss} & A_{ss} \end{bmatrix}, \tag{6g}$$

$$C = \begin{bmatrix} 1 & 1 & \mathbf{0}^T \end{bmatrix}^T, \tag{6h}$$

with $M = m + A(\infty)$. The net useful energy that can be absorbed from the waves between times t_0 and t_f is given by

$$E = -\int_{t_0}^{t_f} f_{PTO}(t)\dot{z}(t)dt. \tag{7}$$

3. Real-Time Reinforcement Learning Control of a Wave Energy Converter

RL is a decision-making framework in which an agent learns a desired behaviour, or policy π, from direct interactions with the environment [38]. As shown in Figure 2, at each time step, the agent is in a state s and takes and action a, thus landing in a new state s' while receiving a reward r. A Markov decision process is used to model the action selection depending on the value function

$Q(s, a)$, which represents an estimate of the future reward. By interacting with the environment for a long time, the agent learns an optimal policy, which maximises the total expected reward.

Figure 2. Block diagram of reinforcement learning (RL) control.

3.1. Problem Formulation

As a decision-making framework, RL is typically used to train an agent, or system, to perform a task that is particularly challenging to express in a standard control setting, e.g., walking for a legged robot. These tasks are usually described as episodic, i.e., the experience can be subdivided into discrete trials whose end is determined by either success in achieving the desired task, e.g., the robot has correctly made a walking step, or failure, e.g., the robot has fallen over and needs to start again. However, WEC control is clearly continuous, which will require a reformulation of the RL schemes as shown in [29–32].

In a feedforward configuration, the control of WECs is dependent on the wave excitation force and its predicted value over a future time horizon. Here, a simple state space is selected, which includes only the WEC displacement and velocity and capture the wave excitation information from the wave elevation and its rate. Therefore, the RL state space for a heaving point absorber is defined as

$$s = \begin{bmatrix} z & \dot{z} & \zeta & \dot{\zeta} \end{bmatrix}^T. \tag{8}$$

The action space is identical to the control input u:

$$a = f_{\text{PTO}}. \tag{9}$$

Although RL originated with the treatment of discrete actions, as for instance shown in [29–32], successful strategies with continuous action spaces have been recently proposed [34,39,40]. With either solution, constraints on the action can be easily imposed, so that $|a| < f_{\max}$.

Specifying an appropriate reward function is fundamental to have the agent learn the desired behaviour. Note that in RL, the optimisation problem is typically cast as a maximisation rather than a minimisation. Taking inspiration from [24–26], the reward function can be defined as

$$r = -f_{\text{PTO}}\dot{z} - w_u f_{\text{PTO}}^2 - w_z p_z, \tag{10}$$

where the weights w_u and w_z can be used to tune the penalty on the control action and heave displacement, respectively. Whilst a constraint can be placed on the PTO force, as it coincides with the control action, it is not possible to impose proper limits on the heave displacement. Therefore, a discontinuous function is used to determine the penalty term p_z to produce an aggressive controller:

$$p_z = \begin{cases} 0 & \text{if } |z| \le z_{\max}, \text{ (11a)} \\ 1 & \text{if } |z| > z_{\max}, \text{(11b)} \end{cases}$$

where $z_{\max}$ defines the displacement limit.

Another difference between the RL and MPC frameworks consists of the way the information on the future incoming waves is treated, i.e., the prediction step. In feedforward MPC, an external method, e.g., autoregressive techniques and the excitation impulse response function [41], is used to predict the incoming wave force and the information is included in the cost function to select the control action. In the RL framework, the agent learns an optimal policy for the maximisation of the total reward, which is a function of the current reward as well as discounted future rewards deriving from following either the current or the optimal policy. This means that the reward function should be specified for the current time step rather than include information from predicted future time steps. The prediction step is embedded within the RL system in a probabilistic setting.

3.2. RL Real-Time WEC Control Framework

Although trust region policy optimisation is used in [28] for a model-free controller initialised with samples obtained from an MPC controller, here actor-critic strategies are considered for the real-time control of a WEC. An example of a successful scheme with continuous state and action spaces, which are necessary for improved control performance, is soft actor-critic (SAC) [34]. In particular, SAC [34], which is the most advanced actor-critic DRL algorithm at the time of writing, is selected here for the control framework for the point absorber.

As shown in Figure 3, the controller would be split into an actor and a critic. The function of the critic is to evaluate the policy, thus updating the action-value function, which is a measure of the total discounted reward, using the samples collected from observations of the environment. The discounted reward estimated by the critic is then fed to the actor. Using the estimated action-value function, the actor selects an action based on the current state, directly interacting with the environment. The policy is then improved by learning from the collected observations. As SAC is an off-line, off-policy algorithm, the critic and actor can be updated using batches of data samples, known as experience replay buffer.
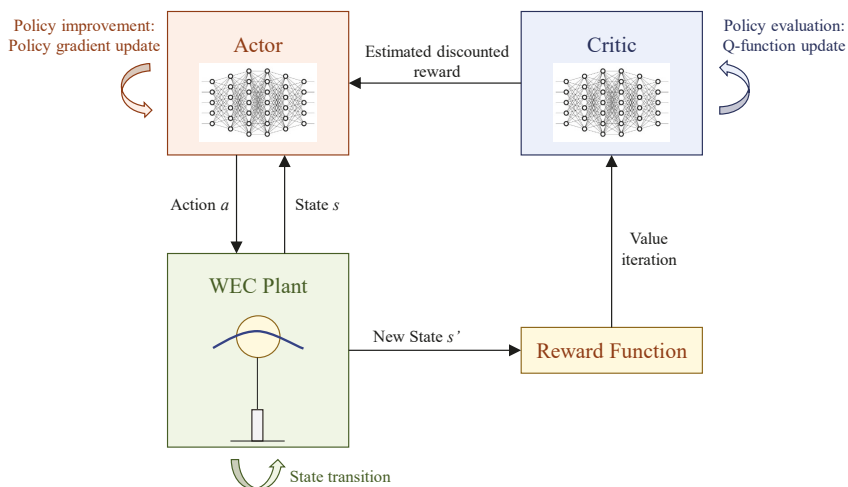
Figure 3. Diagram of the soft actor-critic (SAC) algorithm for the real-time control of a wave energy converter (WEC).

The agent seeks to maximise not only the environment's expected reward, but also the policy's entropy. The concept of entropy ensures that the agent selects random actions to explore the environment through a parameter α defined as the entropy temperature. The parameter is automatically adjusted with gradient descent to ensure sufficient exploration at the start of learning,

and subsequently a greater emphasis on the maximisation of the expected reward. A DNN is used to model the mean of the log of the standard deviation of the policy. For the policy improvement step, the policy distribution is updated towards the softmax distribution for the current Q function by minimizing the Kullback–Leibler divergence.

In SAC, two DNNs are used to approximate the critic's policy evaluation to mitigate positive bias in the policy evaluation step. The DNNs are trained off-line using batches of data collected by the actor during deployment. The minimum value of the two soft Q-functions is used in the gradient descent during training, which has been found to significantly speed up convergence. Additionally, target networks that are obtained as an exponentially moving average of the soft Q-function weights are used to smooth out the effects of noise in the sampled data.

The SAC algorithm is summarised in Algorithm 1. For a full explanation, the reader is referred to [34].

Algorithm 1: SAC algorithm taken from [34].

Result: Optimised actor and critic DNNs
initialise policy, two soft Q and two target soft Q DNNs;
initialise experience replay buffer with MPC samples;
for *each episode* **do**
    for *each step* **do**
        sample actions from the policy;
        sample transition from the environment;
        store the transition in the replay buffer;
    end
    for *each gradient update step* **do**
        update the soft Q DNN weights;
        update the policy DNN weights;
        adjust the entropy temperature;
        update the target DNN weights;
    end
end

As compared with the RL solutions presented in [29–32], once trained the new DRL implementation can be implemented in real time, with a control time step similar to the one used by other control methods, e.g., MPC.

4. Results and Discussion

4.1. Case Study

A spherical point absorber as shown in Figure 1 is selected as a case study for the development of the real-time RL WEC control scheme. The spherical buoy represents a standard case study based on the Wavestar prototype WEC, which has also been used in [9,37,42] among other studies. Additionally, the simple geometry enables the inclusion of computationally efficient nonlinear Froude–Kryolv and viscous forces in the future. The properties of the point absorber in the simulation environment can be found in Table 1. The hydrodynamic coefficients have been computed in the panel-code WAMIT. However, the same matrices as in [37] have been used for the state-space approximation of the radiation convolution integral. The problem has been programmed in the Python/Pytorch framework for the SAC controller.

In addition, the robust and computationally efficient MPC strategy described in [6,8] is selected to initialise the training and benchmark the results of the DRL scheme. The method is implemented in the MATLAB/Simulink framework using the quadratic-programming solver quadprog, after discretising the matrix equation in (6) with a zero-order hold. Similarly to [6,8], the future wave elevation is

assumed here to be known exactly, as prediction methods with 90% accuracy up to 10 s into the future have been proposed [41,43].

For both control methods, a first-order Euler scheme is used for the time integration of the simulations with a time step of 0.01 s.

Table 1. Properties of the spherical point absorber in the simulation environment.

Property	Value
Buoy diameter [m]	5
Buoy mass [kg]	32.725
Buoy resonant period [s]	3.17
Water depth [m]	∞
ρ [kg/m^3]	1000
g [m/s^2]	9.81

Typical ocean waves have an energy wave period approximately ranging from 5 s to 20 s [44]. Hence, it is clear that the selected point absorber will need significant control effort to extract energy from realistic ocean waves, since its resonant period is lower, as shown in Table 1. In this work, the peak wave period is considered to range from 4 s to 10 s, which is expected to be realistic for the small point absorber. Additionally, as the simulation environment is based here on a linear model, only small wave amplitudes up to 1 m are analysed. As a result, no constraints on either the buoy displacement or the PTO force are set on the MPC controller. The penalty on the slew rate is expected to be sufficient for the achievement of a suitable WEC response, by setting $r_{\text{MPC}} = 10^{-5}$ to ensure convexity according to [8].

Zhong and Yeung [6] have shown that, in regular waves, the mean absorbed power does not increase with time horizon duration after the horizon is one wave period long. Hence, here we set $H = 10$ s, since it corresponds to the longest wave period that is analysed and corresponds to realistic prediction timeframes [41,43]. The control time step length is set to $\delta t = 0.2$ s.

A maximum PTO force $f_{\text{max}} = 10^5$ N and displacement $z_{\text{max}} = 2.5$ m are selected. Additionally, the weights of (10) are set to $w_u = 10^{-5}$ and $w_z = 10^6$. The hyperparameters used for the SAC agent are the same as in [34] and are reported in Table 2 for greater clarity.

Table 2. Hyperparameters of the SAC agent.

Parameter	Value
optimizer	Adam
learning rate	3×10^{-4}
discount factor	0.99
replay buffer size	10^6
number of hidden layers (all networks)	2
number of hidden units per layer	256
number of samples per minibatch	256
entropy target	-1
activation function	ReLU
target smoothing coefficient	0.005
target update interval	2
gradient steps	1

4.2. Results in Irregular Waves

To generate sufficient data samples for the training of the actor DNN, 28 wave traces of irregular waves lasting 15 min each are produced, with the significant wave height ranging from 0.5 m to 2 m in steps of 0.5 m and the peak wave period from 4 s to 10 s in steps of 1 s. A Bretschneider spectrum is used [44]. The controller is started only after 100 s from the start of the wave trace to avoid numerical instabilities during the initial transient. The wave trace is logged after an additional 50 s for 900 s.

4.2.1. Training

The sampled data is used to initialise the experience replay buffer of the SAC agent. Each episode consists of a randomly initialised wave trace whose significant wave height and peak wave period are randomly selected in the 1.5–2 m and 6–8 s range, respectively. The wave trace lasts for 200 s and is initialised with no control force for the first 100 s to avoid numerical instabilities. Hence, each episode lasts a total of 2001 steps for the selected control time step of 0.2 s. The same control time step is selected for the DRL controller. To ensure the robustness of the algorithm, the agent is trained with five different seed values to the random number generator.

As can be seen in Figure 4, after the initialisation with the samples collected by the MPC controller, the agent learns a policy to maximise the expected reward after approximately 50 episodes (or approximately 10^5 steps). Note that in Figure 4, the total reward per episode is highly dependent on the randomly selected significant wave height and peak period; hence, large variations are possible even after training, due to the different level of energy in the waves.
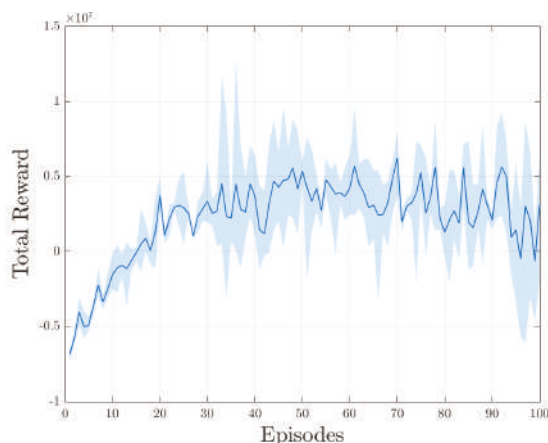

Figure 4. Total reward per episode during training.

The convergence time corresponds to approximately 5000 s of experience in addition to the previous 25,200 s with MPC control for a total of approximately 8.4 h. This is a really short time over the life time of the WEC and provides confidence in the controller being able to deliver adaptive control in practical implementations. However, the negative absorbed powers shown during the first episodes are highly worrying. At the start of learning, the agent is preferring random actions to ensure exploration. However, during exploration the device, and in particular the PTO, may fail. Therefore, in the future, a fixed entropy temperature may reduce exploration at the start and thus its associated risks if the controller is already initialised with data from a robust controller. This solution is however likely to slow down the training time.

4.2.2. Comparison between SAC and MPC

To assess the performance of the DRL control, MPC and SAC are tested in unseen waves. The traces have a Bretschneider spectrum in the same range of significant wave height and peak wave period, but different seed numbers to the random number generator from the training set. They last 1050 s, with the controller initialised after 100 s and the averaging to compute the mean power started after a further 50 s.

The mean useful or net absorbed power is shown in the dashed lines in Figure 5 for MPC. The reactive power, P_{rea}, is defined as the power transferred from the PTO to the point absorber, whilst the active or resistive power, P_{act}, is the power transferred from the absorber to the PTO. The net useful power is thus $P_u = P_{act} - P_{rea}$. For the MPC, the extracted power at higher wave periods is curtailed by the penalty on the slew rate. In Figure 6, the ratio of the reactive and active power for the MPC can be seen in the dashed lines. Reactive power is primarily used to speed the WEC up in shorter waves, i.e., when the wave period is shorter than the resonant period, whereas passive damping can be used to slow the device down for longer wave periods. The steady increase in the ratio of the reactive and active power for higher wave periods for the MPC is thus unexpected. The greater control effort the further from the resonance period (3.17 s for the point absorber) is however visible also in [6] and can be explained with the decrease of the absolute value of the active power for longer waves. Furthermore, a comparison with the case studies in [6,8] shows that the selected value of r_{MPC} is providing a stronger influence in this example.
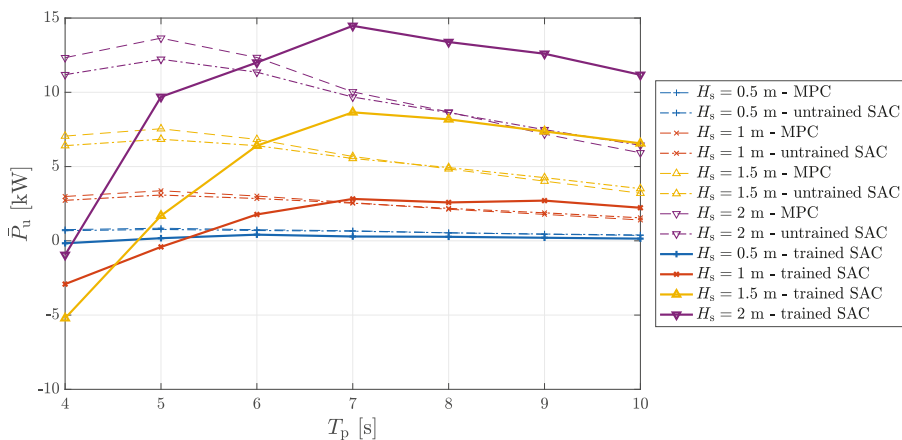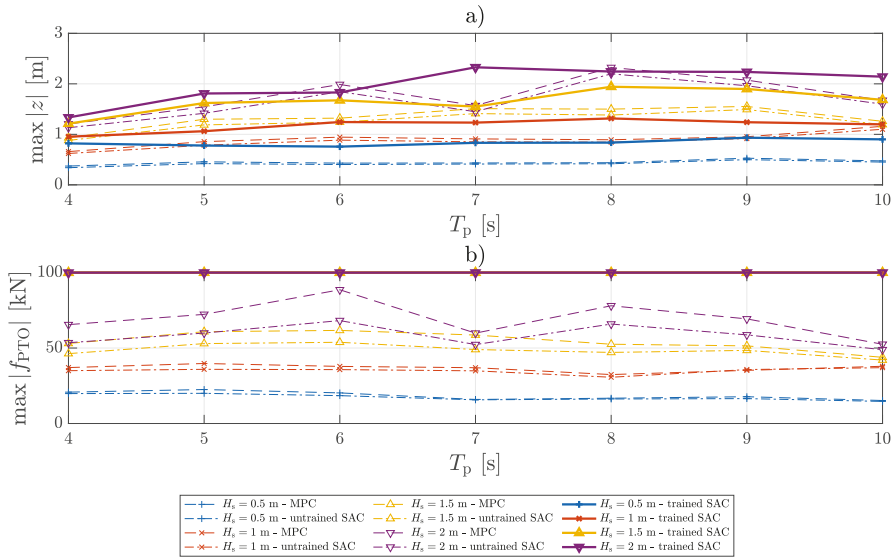

Figure 5. Variation with peak wave period of the mean useful power absorbed by the heaving sphere for the considered range of significant wave height.
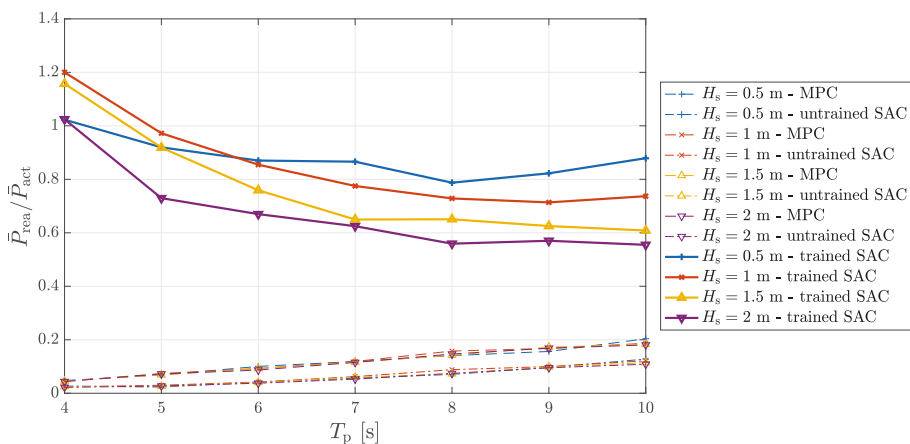
Figure 6. Variation with peak wave period of the ratio of the mean reactive and active power absorbed by the heaving sphere for the considered range of significant wave height.

Figures 5 and 6 also display the performance of the SAC agent before and after training. The dot-dash lines correspond to the SAC agent before training, with the entropy set to zero. In this case, the agent replicates closely the MPC behaviour, even though there are differences in the actual time-domain response. After training, the SAC agent (shown with thick continuous lines) improves the energy absorption for the higher peak wave period values ($T_P > 6$ s) and the higher significant wave height values ($T_P > 1$ m). These ranges correspond with the ranges used during training and show poor generalisation ability. The negative mean absorbed power values for the lower periods close to the WEC's resonant period are particularly worrying. From Figure 6, it is clear that the main cause for this behaviour is the aggressive policy that the SAC agents selects. The large flows of reactive power are useful for periods smaller than the resonant period, i.e., in shorter waves, but unhelpful close to the resonant period or for long wave periods, where damping is more useful to slow the WEC down. The problem may be caused by the low resonant period of the point absorber. A larger device whose resonant period is within the typical ocean waves period range should be selected in the future to assess the behaviour of the controller for both short and long waves.

In Figure 7, the magnitude of the maximum heave displacement and PTO force can be seen. Although the SAC algorithm presents higher displacements than MPC, the maximum value of 2.5 m is not exceeded. This hints at the efficacy of the discontinuous penalty term in (10). However, designing a method to guarantee the constraint handling for the displacement is critical for the DRL controller to find an industrial application in the future. The aggressive behaviour of the SAC agent is further underlined in Figure 7b, where the peak PTO force is hit in all sea states.

Figure 7. Variation with peak wave period of the maximum absolute displacement (**a**) and PTO force (**b**) for the heaving sphere for the considered range of significant wave height.

The response of the MPC and SAC algorithms in the time domain can be seen in Figure 8. The figure shows an extract of one of the simulations used to verify the performance of the SAC scheme against MPC ($H_s = 2$ m and $T_p = 6$ s). From the figure, it is clear that the SAC converges onto an aggressive bang-bang control policy.
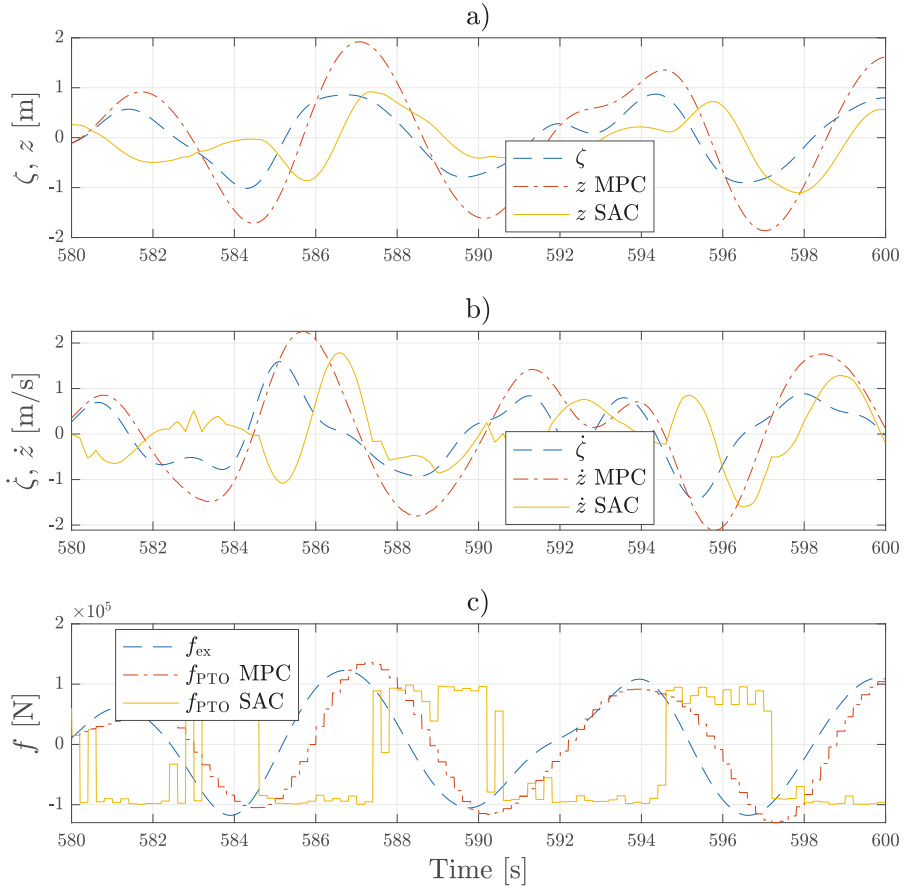
Figure 8. Time variation of the wave elevation and float heave displacement (**a**), wave and heave velocity (**b**) and wave excitation and PTO force (**c**) for the simulation of the WEC in an irregular wave trace with $H_s = 2$ m and $T_P = 6$ s.

The aggressiveness of the controller can be reduced by increasing the penalty on the PTO force (through w_u). The poor ability of the SAC agent to generalise to unseen wave conditions is problematic and symptomatic of a possibly over-simplistic selection of the state-space. In [34], the information from a number of past time steps is captured in the state-space to ensure convergence for the control of a walking robot. A similar approach will be needed for the control of a WEC to capture the oscillatory nature of gravity waves, similar to MPC. Furthermore, it is clear that the experience replay buffer should include data samples from a broad range of sea states, in particular with regards to period both below and above the resonance period of the device. Currently, the memory buffer is updated with new samples by removing the oldest sample if the memory is full. This technique will be changed by binning the data by wave period and height and ensuring a minimum number of samples per bin.

Table 3 shows the computational time required to train the SAC controller (over 100 episodes) and to run a simulation of the WEC lasting 1050 s using the MPC and trained SAC schemes. The mean from the 28 simulations employed to compare the two strategies is used. Note that the first 150 s are needed to initialise the WEC dynamics and power averaging and that the control time step is 0.2 s for both algorithms. Hence, there are 4501 control time steps per simulation, leading to the values for

the computational time per time step shown in Table 3. The simulations are run on a laptop with an Intel 5, 2.3 GHz, dual-core processor and 16 GB RAM.

Table 3. Training time (if applicable), mean total simulation time and time per control time step for the simulations used to verify and compare the MPC and SAC control algorithms.

Scheme	Training Time [s]	Total Simulation Time [s]	Time Per Control Time Step [s]
MPC	-	11.798	2.6×10^{-3}
SAC	869	2.607	5.8×10^{-4}

As can be seen in Table 3, the SAC algorithm requires approximately 15 min to train over 100 episodes for analysed point absorber. The large computational time prevents an on-line application, although training can happen regularly off-line in practice, once significantly large new batches of data are collected. Conversely, once trained, the computational effort is 40 times lower than the simulation control time step, thus enabling a real-time implementation with ease. Additionally, the computational effort associated with SAC is one order of magnitude smaller than for linear MPC. In fact, the computational time per control time step shown in Table 3 is overly conservative for SAC, as it includes the overhead from the dynamic simulation in Python. Conversely, the linear MPC code is implemented in a very efficient MALTAB/Simulink script with C-coded S-functions. Therefore, a gain in performance as high as one additional order of magnitude is expected from compiled solutions if the system has to be implemented on an actual WEC [45].

For reproducibility, the results of the SAC algorithm in the unseen test wave traces can be accessed on Github[1], including the wave elevation, vertical velocity and excitation force.

5. Conclusions

In this article, an established convex MPC has been used to generate observations for a heaving point absorber in a range of irregular waves in a linear simulation environment. The samples have been used to initialise a DRL agent, which learns an optimal policy from direct interactions with with the environment for the maximisation of the energy absorption. By being off-line and off-policy, the SAC algorithm enables the training to be decoupled from deployment, thus shifting the computational effort on the training. This is a fundamental trait, as the control of large groups of WECs in the future to achieve economies of scale is reliant on having an effective, real-time centralised strategy.

The DRL control improves the energy absorption of the point absorber over convex MPC for wave periods higher than the resonant period of the device, whilst meeting the displacement and force constraints. This is achieved by adopting a more aggressive policy with higher slew rate. However, poorer performance is shown for lower wave height and period values. These problems will be addressed by reformulating the state-space, updating the reward function and the sampling of data for the experience replay. Additionally, the exploration will be reduced from the start of training to prevent the controller from taking actions that damage the PTO. Furthermore, the DRL controller will be tested in a simulation environment inclusive of nonlinear effects, e.g., nonlinear static and dynamic Froude–Krylov forces as in [42] and viscous drag. A sensitivity analysis will be run to assess the impact of modelling errors on the performance of the DRL and MPC algorithms.

---

[1]   https://github.com/enricoande/Results-for-jmse-967614

Abbreviations

The following abbreviations are used in this manuscript:

DNN   Deep Neural Network
DRL   Deep Reinforcement Learning
LCoE   Levellised Cost of Energy
MPC   Model Predictive Control
PTO   Power Take-Off
RL   Reinforcement Learning
SAC   Soft Actor-Critic
WEC   Wave Energy Converter

References

1. Kempener, R.; Neumann, F. *Wave Energy: Technology Brief 4*; International Renewable Energy Agency Technical Report; International Renewable Energy Agency: Abu Dhabi, UAE, 2014.
2. Sgurr Control; Quoceant. *Control Requirements for Wave Energy Converters Landscaping Study: Final Report*; Technical report; Wave Energy Scotland: Inverness, Scotland, 2016.
3. Luis Villate, J.; Ruiz-Minguela, P.; Berque, J.; Pirttimaa, L.; Cagney, D.; Cochrane, C.; Jeffrey, H. *Strategic Research and Innovation Agenda for Ocean Energy*; Technical report; ETIPOCEAN: Bruxelles, Belgium, 2020.
4. Faedo, N.; Olaya, S.; Ringwood, J.V. Optimal control, MPC and MPC-like algorithms for wave energy systems: An overview. *IFAC J. Syst. Control.* **2017**. [CrossRef]
5. Li, G.; Belmont, M.R. Model predictive control of sea wave energy converters—Part I: A convex approach for the case of a single device. *Renew. Energy* **2014**, *69*, 453–463. [CrossRef]
6. Zhong, Q.; Yeung, R.W. An efficient convex formulation for model predictive control on wave-energy converters. In Proceedings of the 36th International Conference on Ocean, Offshore and Arctic Engineering, Trondheim, Norway, 25–30 June 2017. [CrossRef]
7. Li, G.; Belmont, M.R. Model predictive control of sea wave energy converters—Part II: The case of an array of devices. *Renew. Energy* **2014**, *68*, 540–549. [CrossRef]
8. Zhong, Q.; Yeung, R.W. Model-Predictive Control Strategy for an Array of Wave-Energy Converters. *J. Mar. Sci. Appl.* **2019**, *18*, 26–37. [CrossRef]
9. Giorgi, G.; Ringwood, J.V. Nonlinear Froude-Krylov and viscous drag representations for wave energy converters in the computation/fidelity continuum. *Ocean Eng.* **2017**, *141*, 164–175. [CrossRef]
10. Richter, M.; Magana, M.E.; Sawodny, O.; Brekken, T.K.A. Nonlinear Model Predictive Control of a Point Absorber Wave Energy Converter. *IEEE Trans. Sustain. Energy* **2013**, *4*, 118–126. [CrossRef]
11. Li, G. Nonlinear model predictive control of a wave energy converter based on differential flatness parameterisation. *Int. J. Control* **2017**, *90*, 68–77. [CrossRef]
12. Son, D.; Yeung, R.W. Optimizing ocean-wave energy extraction of a dual coaxial-cylinder WEC using nonlinear model predictive control. *Appl. Energy* **2017**, *187*, 746–757. [CrossRef]
13. Oetinger, D.; Magaña, M.E.; Sawodny, O. Centralised model predictive controller design for wave energy converter arrays. *IET Renew. Power Gener.* **2015**, *9*, 142–153. [CrossRef]
14. Ringwood, J.V.; Bacelli, G.; Fusco, F. Energy-Maximizing Control of Wave-Energy Converters: The Development of Control System Technology to Optimize Their Operation. *IEEE Control Syst. Mag.* **2014**, *34*, 30–55. [CrossRef]
15. Korde, U.A.; Ringwood, J.V. *Hydrodynamic Control of Wave Energy Devices*; Cambridge University Press: Cambridge, UK, 2016.
16. Fusco, F.; Ringwood, J.V. A simple and effective real-time controller for wave energy converters. *IEEE Trans. Sustain. Energy* **2013**, *4*, 21–30. [CrossRef]

17. Gaspar, J.F.; Kamarlouei, M.; Sinha, A.; Xu, H.; Calvário, M.; Faÿ, F.X.; Robles, E.; Soares, C.G. Speed control of oil-hydraulic power take-off system for oscillating body type wave energy converters. *Renew. Energy* **2016**, *97*, 769–783. [CrossRef]
18. Valério, D.; Mendes, M.J.G.C.; Beirão, P.; Sá da Costa, J. Identification and control of the AWS using neural network models. *Appl. Ocean Res.* **2008**, *30*, 178–188, [CrossRef]
19. Li, L.; Yuan, Z.; Gao, Y. Maximization of energy absorption for a wave energy converter using the deep machine learning. *Energy* **2018**, *165*, 340–349. [CrossRef]
20. Li, L.; Gao, Z.; Yuan, Z.M. On the sensitivity and uncertainty of wave energy conversion with an artificial neural-network-based controller. *Ocean Eng.* **2019**, *183*, 282–293. [CrossRef]
21. Anderlini, E.; Forehand, D.I.; Bannon, E.; Abusara, M. Reactive control of a wave energy converter using artificial neural networks. *Int. J. Mar. Energy* **2017**, *19*, 207–220. [CrossRef]
22. Thomas, S.; Giassi, M.; Eriksson, M.; Göteman, M.; Isberg, J.; Ransley, E.; Hann, M.; Engström, J. A Model Free Control Based on Machine Learning for Energy Converters in an Array. *Big Data Cogn. Comput.* **2018**, *2*, 36. [CrossRef]
23. Tri, N.M.; Truong, D.Q.; Thinh, D.H.; Binh, P.C.; Dung, D.T.; Lee, S.; Park, H.G.; Ahn, K.K. A novel control method to maximize the energy-harvesting capability of an adjustable slope angle wave energy converter. *Renew. Energy* **2016**, *97*, 518–531. [CrossRef]
24. Na, J.; Li, G.; Wang, B.; Herrmann, G.; Zhan, S. Robust Optimal Control of Wave Energy Converters Based on Adaptive Dynamic Programming. *IEEE Trans. Sustain. Energy* **2019**, *10*, 961–970. [CrossRef]
25. Na, J.; Wang, B.; Li, G.; Zhan, S.; He, W. Nonlinear constrained optimal control of wave energy converters with adaptive dynamic programming. *IEEE Trans. Ind. Electron.* **2019**, *66*, 7904–7915. [CrossRef]
26. Zhan, S.; Na, J.; Li, G. Nonlinear Noncausal Optimal Control of Wave Energy Converters via Approximate Dynamic Programming. *IEEE Trans. Ind. Infor.* **2019**, *15*, 6070–6079. [CrossRef]
27. Kamthe, S.; Deisenroth, M.P. Data-Efficient Reinforcement Learning with Probabilistic Model Predictive Control. In Proceedings of the Machine Learning Research, Lanzarote, Spain, 9–11 April 2018; Volume 84, pp. 1701–1710.
28. Nagabandi, A.; Kahn, G.; Fearing, R.S.; Levine, S. Neural Network Dynamics for Model-Based Deep Reinforcement Learning with Model-Free Fine-Tuning. *arXiv* **2017**, arXiv:1708.02596v2.
29. Anderlini, E.; Forehand, D.I.M.; Stansell, P.; Xiao, Q.; Abusara, M. Control of a Point Absorber using Reinforcement Learning. *IEEE Trans. Sustain. Energy* **2016**, *7*, 1681–1690. [CrossRef]
30. Anderlini, E.; Forehand, D.I.; Bannon, E.; Abusara, M. Control of a Realistic Wave Energy Converter Model Using Least-Squares Policy Iteration. *IEEE Trans. Sustain. Energy* **2017**, *8*, 1618–1628. [CrossRef]
31. Anderlini, E.; Forehand, D.I.; Bannon, E.; Xiao, Q.; Abusara, M. Reactive control of a two-body point absorber using reinforcement learning. *Ocean Eng.* **2018**, *148*, 650–658. [CrossRef]
32. Anderlini, E.; Forehand, D.I.; Bannon, E.; Abusara, M. Constraints Implementation in the Application of Reinforcement Learning to the Reactive Control of a Point Absorber. In Proceedings of the 36th International Conference on Ocean, Offshore and Arctic Engineering, Trondheim, Norway, 25–30 June 2017. [CrossRef]
33. LeCun, Y.; Bengio, Y.; Hinton, G. Deep learning. *Nature* **2015**, *521*, 436–444. [CrossRef]
34. Haarnoja, T.; Zhou, A.; Hartikainen, K.; Tucker, G.; Ha, S.; Tan, J.; Kumar, V.; Zhu, H.; Gupta, A.; Abbeel, P.; et al. Soft Actor-Critic Algorithms and Applications. *arXiv* **2018**, arXiv:1812.05905.
35. Falnes, J. *Ocean Waves and Oscillating Systems*, paperback ed.; Cambridge University Press: Cambridge, UK, 2005. [CrossRef]
36. Cummins, W.E. The impulse response function and ship motions. *Schiffstechnik* **1962**, *47*, 101–109.
37. Faedo, N.; Peña-Sanchez, Y.; Ringwood, J.V. Finite-order hydrodynamic model determination for wave energy applications using moment-matching. *Ocean Eng.* **2018**, *163*, 251–263. [CrossRef]
38. Sutton, R.S.; Barto, A.G. *Reinforcement Learning*, hardcover ed.; MIT Press: Cambridge, MA, USA, 1998; p. 344.
39. Lillicrap, T.P.; Hunt, J.J.; Pritzel, A.; Heess, N.; Erez, T.; Tassa, Y.; Silver, D.; Wierstra, D. Continuous control with deep reinforcement learning. In Proceedings of the International Conference on Learning Representations, San Juan, PR, USA, 2–4 May 2016. [CrossRef]
40. Haarnoja, T.; Zhou, A.; Abbeel, P.; Levine, S. Soft Actor-Critic: Off-Policy Maximum Entropy Deep Reinforcement Learning with a Stochastic Actor. In Proceedings of the 35th International Conference on Machine Learning, Stockholm, Sweden, 10–15 July 2018.

41. Fusco, F.; Ringwood, J. Short-Term Wave Forecasting for time-domain Control of Wave Energy Converters. *IEEE Trans. Sustain. Energy* **2010**, *1*, 99–106. [CrossRef]

42. Giorgi, G.; Ringwood, J.V. Computationally efficient nonlinear Froude–Krylov force calculations for heaving axisymmetric wave energy point absorbers. *J. Ocean. Eng. Mar. Energy* **2017**, *3*, 21–33. [CrossRef]

43. Paparella, F.; Monk, K.; Winands, V.; Lopes, M.F.; Conley, D.; Ringwood, J.V. Up-wave and autoregressive methods for short-term wave forecasting for an oscillating water column. *IEEE Trans. Sustain. Energy* **2015**, *6*, 171–178. [CrossRef]

44. Holthuijsen, L.H. *Waves in Oceanic and Coastal Waters*; Cambridge University Press: Cambridge, UK, 2007. [CrossRef]

45. Fourment, M.; Gillings, M.R. A comparison of common programming languages used in bioinformatics. *BMC Bioinform.* **2008**, *9*, 82. [CrossRef] [PubMed]

Spectral Control of Wave Energy Converters with Non-Ideal Power Take-off Systems

Alexis Mérigaud * and Paolino Tona

IFP Energies Nouvelles, 1-4 Avenue du Bois Préau, 92852 Rueil-Malmaison, France; paolino.tona@ifpen.fr
* Correspondence: alexis.merigaud@ifpen.fr

Abstract: Spectral control is an accurate and computationally efficient approach to power-maximising control of wave energy converters (WECs). This work investigates spectral control calculations with explicit derivative computation, applied to WECs with non-ideal power take-off (PTO) systems characterised by an efficiency factor smaller than unity. To ensure the computational efficiency of the spectral control approach, it is proposed in this work to approximate the discontinuous efficiency function by means of a smooth function. A non-ideal efficiency function implies that the cost function is non-quadratic, which requires a slight generalisation of the derivative-based spectral control approach, initially introduced for quadratic cost functions. This generalisation is derived here in some detail given its practical interest. Two application case studies are considered: the Wavestar scale model, employed for the WEC control competition (WECCCOMP), and the 3rd reference model (RM3) two-body heaving point absorber. In both cases, with the approximate efficiency function, the spectral approach calculates WEC trajectory and control force solutions, for which the mean electrical power is shown to lie within a few percent of the true optimal electrical power. Regarding the effect of a non-ideal PTO efficiency upon achievable power production, and concerning heaving point-absorbers, the results obtained are significantly less pessimistic than those of previous studies: the power achieved lies within 80–95% of that obtained by simply applying the efficiency factor to the optimal power with ideal PTO.

Keywords: wave energy converters; spectral control; optimal control; power take-off

1. Introduction

Power-maximising control is a promising path to improve the economic competitiveness of WECs [1]. Various control methods have been proposed, of which the most basic are simple parametric control strategies, whereby one or two scalar control parameters are adjusted on a sea state-by-sea state basis. Recent years have witnessed a growing interest for model predictive control (MPC) strategies [2], whereby an optimisation problem is solved in real-time to update a prescribed control input, or a reference trajectory to be followed by the WEC. MPC strategies take profit from wave excitation predictions. They can, in theory, handle nonlinear WEC models, through the use of nonlinear optimisation algorithms, as well as constraints on the WEC dynamics, control force or instantaneous power.

First introduced in [3] for WEC control applications, spectral and pseudo-spectral MPC methods discretise the wave inputs and optimisation variables by means of basis functions, typically Fourier [4,5] (when a periodic wave input is considered), or Chebyshev-like [6] (to handle directly the non-periodic wave signal, seen within the receding-horizon control window). In terms of signal approximation (i.e., when it comes to approximate a given function by means of a finite number of "spectral" basis functions), spectral techniques are said to have *superlinear convergence* properties [7], which means that the approximation error decreases more than linearly with the number of basis functions employed,

provided that the function approximated is continuous (with a geometric convergence rate for functions with a finite degree of smoothness, and an exponential convergence rate for infinitely-smooth functions such as linear functions). As a consequence, spectral methods require a small number of coefficients to describe the control inputs or WEC dynamics with a prescribed accuracy, thus reducing the number of optimisation variables, and the associated computation cost. Spectral methods can thus handle relatively long control horizons. In addition, the "aggressiveness" of the control solution, i.e., how abruptly the solution oscillates, can be tuned, by adjusting the number of basis functions.

In [5], a computationally efficient spectral control formulation for nonlinear, 1-DoF WEC models is introduced in which, using the dynamical equation, the control variable is eliminated in the expression of the objective function, thus resulting in a problem where the only variables to optimise are those, corresponding to the WEC motion. The approach in [5], combined with the explicit computation of the first- and second-order derivatives of the objective function, is shown to be orders of magnitude faster than usual spectral control formulations, whereby the dynamical equations are considered as a set of equality constraints. Although the proposed approach is based on Fourier basis functions, it has been successfully implemented in a receding-horizon set-up [8,9]. Also note that combining spectral control (for optimal reference generation) with tracking control entails a certain degree of robustness to modelling errors, in contrast to direct computation of the optimal control force, which requires accurate modelling of all the WEC dynamics. Indeed, the controller presented in [9] is shown to be little affected by tracking loop imperfection as well as by estimation and forecast errors.

In all references previously mentioned, like in the vast majority of the wave energy control literature, only hydrodynamic power absorption is considered. From an optimal control perspective, the objective function, here denoted as f, is generally the raw mechanical power absorbed by the PTO system [2]. For a WEC with one mechanical degree of freedom, the raw absorbed power is written as follows,

$$f(x,u) = -\frac{1}{T}\int_{t=0}^{T}\dot{x}u\,dt \qquad (1)$$

where T is the length of the control horizon, x denotes the WEC generalised position and u the PTO force (which is the control input).

However, in practical applications, the PTO system is not ideal, so that the electrical power, P_e, is not equal to the absorbed mechanical power, $P_a = -u\dot{x}$, as highlighted by a number of authors [10–17]. More specifically, when power is mechanically absorbed from the waves, the electrical power P_e, actually available at the end of the mechanical-to-electrical conversion stage, is smaller than the absorbed power P_a, because of the losses occurring in the conversion stage ($0 \leq P_e \leq P_a$). Conversely, if a reactive control strategy is adopted [1], at times some power must be returned from the electromechanical system back into the ocean ($P_a \leq 0$). At those instants, because of the losses in the PTO system, the electrical power provided by the grid to the PTO system must be greater than $|P_a|$, so that $P_e \leq P_a \leq 0$. PTO losses should be taken into account when designing the WEC control strategy [10–17]. In fact, a reactive control strategy, obtained without modelling losses in the objective function, can yield negative average generated power when applied to the true system, where losses occur (see, for example, in [13]).

Therefore, it is of high practical interest to extend the methodology proposed in [5] to more general objective functions of the form

$$f(x,u) = \frac{1}{T}\int_{t=0}^{T}\alpha(x,\dot{x},u)\,dt \qquad (2)$$

where α is some scalar function of x, $\dot{x}$ and u (while the control calculations presented in [5] can only deal with cost functions in the form $-u\dot{x}$, quadratic in the problem variables). P_e, being modelled as a function of $P_a = -u\dot{x}$, is a special case of the formulation in Equation (2). Such a formulation can also include, for example, quadratic terms introduced to penalise the WEC excursions or control effort.

This work, like that in [5], is concerned with the calculation of optimal control solutions in an "off-line" fashion (as opposed to receding-horizon implementations such as in [6,8,9]), taking into account the totality of a relatively long, simulated irregular wave input signal comprising a few tens of wave periods. Therefore, the insight provided, regarding the effect of a non-ideal PTO system onto optimal control results, is reasonably general, and remains free of the many effects, which interact when considering a particular receding-horizon implementation [9]. Furthermore, the optimal control solution, obtained off-line, and the corresponding generated power, provide a reference to assess the performance of real-time, receding-horizon control algorithms (which cannot, in theory, outperform the optimal solution obtained off-line). The present study is restricted to WECs with one degree of freedom.

The rest of this paper is organised as follows.

- Section 2 revisits the method presented in [5], for an objective function of the form of Equation (2).
- Section 3 introduces the simple non-ideal PTO model retained in this work, and two numerical case studies: the Wavestar model used in the WECCCOMP challenge [18], and the RM3 two-body heaving point absorber [19].
- For both case studies, numerical results are shown and discussed in Section 4;
- Finally, conclusions are presented in Section 5.

2. An Efficient Spectral Control Method for a 1-DoF, Non-Linear WEC Model

2.1. WEC Dynamical Model

Consider a WEC, modelled with one degree of freedom, denoted x. Newton's second law, which describes the WEC motion, typically takes the following mathematical form (see in [5], and detailed justifications in Chapter 4 of the work in [20]):

$$\mathcal{L}\{x\} + n(x, \dot{x}) = u + e \tag{3}$$

where the dependence in the time variable t has been omitted to alleviate notations, and

- $\mathcal{L}$ represents a linear integro-differential operator, containing some of, or all the terms of the well-known Cummins' equation [21]:

$$\mathcal{L}\{x\}(t) := (I + I_\infty)\ddot{x}(t) + C\dot{x}(t) + \int_{\tau=0}^{\infty} k_r(\tau)\dot{x}(t-\tau)d\tau + Sx(t) \tag{4}$$

where I represents the system inertia; I_∞ and k_r are the radiation infinite-frequency added inertia and damping convolution kernel, respectively; C models some linear damping term (for example, to take friction effects into account); and S is the hydrostatic restoring force (resulting from the balance between gravity and Archimede's force);
- n represents some nonlinear function, with the aim of modelling nonlinear dynamical effects, not accounted for by a linear modelling approach. If n includes effects, usually modelled linearly in Cummins' Equation (4), then the corresponding linear coefficients in Equation (4) can be assumed equal to zero;
- $e(t)$ is the wave excitation force; and
- $u(t)$ is the control force, exerted by the PTO system onto the WEC's moving part.

The operator $\mathcal{L}$ is represented by a frequency-response mapping $z(\omega) = S - \omega^2(I + A_r(\omega)) - j\omega(C + B_r(\omega))$, where the radiation frequency-dependent added mass $A_r(\omega)$ and damping $B_r(\omega)$ are related to I_∞ and k_r through Ogilvie's relation [22].

2.2. Spectral Control Problem Formulation

Consider an optimal control problem of the following form,

$$
\begin{cases}
\max_{x,u} f(x,u) \\
\text{s.t. } \mathcal{L}\{x\} + n(x,\dot{x}) = u + e
\end{cases}
\tag{5}
$$

where $f(x,u) := \frac{1}{T}\int_{t=0}^{T}\alpha(x,\dot{x},u)dt$; T is the control time horizon; the equality constraint expresses the fact that the dynamical Equation (3) must be satisfied at every instant; and the function α, as mentioned in the introduction, represents the "instantaneous" objective function. Given the particular form of the dynamical equation, u can be expressed as a function of the other variables, so that Problem (5) can be recast as follows,

$$
\max_{x} f(x)
\tag{6}
$$

where $f(x) = \frac{1}{T}\int_{t=0}^{T}\alpha(x,\dot{x},\mathcal{L}\{x\} + n(x,\dot{x}) - e)dt$, while the variable u, as well as the equality constraint, are eliminated, so that only the device trajectory is now optimised.

Assume a periodic, polychromatic excitation signal with period T, of the form

$$
e(t) = \frac{1}{\sqrt{2}}\hat{e}_1 + \sum_{n=1}^{N}\hat{e}_{2n}\cos(\omega_n t) + \hat{e}_{2n+1}\sin(\omega_n t)
\tag{7}
$$

where the frequencies ω_n are defined harmonically with $\Delta\omega = \frac{2\pi}{T}$ and $\forall n \in \{1...N\}$, $\omega_n = n\Delta\omega$. In the following, consistently with a periodic excitation signal, solutions x are searched among periodic signals with period T, and the WEC motion is assumed of the form

$$
x(t) = \frac{1}{\sqrt{2}}\hat{x}_1 + \sum_{n=1}^{N}\hat{x}_{2n}\cos(\omega_n t) + \hat{x}_{2n+1}\sin(\omega_n t)
\tag{8}
$$

Note that, in Equations (7) and (8), the number N of harmonics being formally identical does not imply any loss of generality: for example, the number of harmonics in x can be considered larger than that in e, by setting to zero higher frequency components of e. In the extreme case of a zero-mean, monochromatic wave input, all components $\hat{e}_n$, except for $\hat{e}_2$ and $\hat{e}_3$, are zero, while the solution x can have an arbitrarily large number of components N.

The next step consists of discretising the integral in objective function, using a set of M equally-spaced points t_m, spanning the interval $[0; T]$, with typically $M \geq 2N + 1$, so that the maximisation problem becomes

$$
\max \tilde{f}(x) := \sum_{m=1}^{M}\alpha(t_m)
\tag{9}
$$

where, for the sake of conciseness, $\alpha(t_m)$ denotes the value of α when its arguments are evaluated at time t_m.

Define the matrix $\Phi \in \mathbb{R}^{M\times(2N+1)}$ as

$$
\forall i \in \{1...M\}, j \in \{1...N\},
\begin{cases}
\Phi_{i,1} = \frac{1}{\sqrt{2}} \\
\Phi_{i,2j} = \cos(\omega_j t_i) \\
\Phi_{i,2j+1} = \sin(\omega_j t_i)
\end{cases}
\tag{10}
$$

and the matrix

$$
\Omega = \begin{pmatrix}
\Omega_0 & \cdots & 0 \\
\vdots & \ddots & \vdots \\
0 & \cdots & \Omega_N
\end{pmatrix}
\tag{11}
$$

where $\Omega_0 = 0$ and, $\forall n \geq 1$, $\Omega_n = \begin{pmatrix} 0 & \omega_n \\ -\omega_n & 0 \end{pmatrix}$.

Define vectors $\hat{\mathbf{x}} := \left(\hat{x}_1 \cdots \hat{x}_N\right)^{\mathsf{T}}$, $\hat{\mathbf{e}} := \left(\hat{e}_1 \cdots \hat{e}_N\right)^{\mathsf{T}}$, $\mathbf{x} := \left(x(t_1) \cdots x(t_M)\right)^{\mathsf{T}}$, $\dot{\mathbf{x}} := \left(\dot{x}(t_1) \cdots \dot{x}(t_M)\right)^{\mathsf{T}}$ and $\mathbf{e} := \left(e(t_1) \cdots e(t_M)\right)^{\mathsf{T}}$. Then, it is easy to see that $\mathbf{x} = \Phi\hat{\mathbf{x}}$, $\dot{\mathbf{x}} = \Phi\Omega\hat{\mathbf{x}}$ and $\mathbf{e} = \Phi\hat{\mathbf{e}}$.

Furthermore, the linear terms of $\mathcal{L}$ evaluated at times $t_1 ... t_M$, $l := \left(\mathcal{L}\{x\}(t_1) \quad \cdots \quad \mathcal{L}\{x\}(t_M)\right)^{\mathsf{T}}$, can be calculated as $l = \mathbf{L}\hat{\mathbf{x}}$, where

$$\mathbf{L} = \begin{pmatrix} L_0 & \cdots & 0 \\ \vdots & \ddots & \vdots \\ 0 & \cdots & L_N \end{pmatrix} \tag{12}$$

with blocks $L_0 = \Re\{z(0)\}$ and $\forall n \in \{1...N\}$, $L_n = \begin{pmatrix} \Re\{z(\omega_n)\} & \Im\{z(\omega_n)\} \\ -\Im\{z(\omega_n)\} & \Re\{z(\omega_n)\} \end{pmatrix}$.

Finally, the objective function can be expressed as a function of $\hat{\mathbf{x}}$, as follows,

$$\tilde{f}(\hat{\mathbf{x}}) = \mathbf{1}_{M \times 1}^{\mathsf{T}} \alpha\left(\Phi\hat{\mathbf{x}}, \Phi\Omega\hat{\mathbf{x}}, \Phi\mathbf{L}\hat{\mathbf{x}} + n(\Phi\hat{\mathbf{x}}, \Phi\Omega\hat{\mathbf{x}}) - \Phi\hat{\mathbf{e}}\right) \tag{13}$$

where $\mathbf{1}_{M \times 1}$ is the unit vector of size $M \times 1$ and, with a slight abuse of notation, the functions α and n are applied component-wise to the vectors used as arguments, i.e., for example, $g(\mathbf{v}) = \left(g(\mathbf{v}_1)...g(\mathbf{v}_M)\right)^{\mathsf{T}}$.

Note that Equation (13) differs from the objective function in [5], as α is, in general, not a quadratic function of its arguments. The calculations which follow constitute a useful generalisation of the results in [5].

2.3. Explicit Calculation of the Objective Function Derivatives

In this section, it is assumed that α and n are continuous in all their arguments, and admit second-order derivatives. Under such an assumption, the first- and second-order derivatives of $\tilde{f}$, with respect to the components of $\hat{\mathbf{x}}$, can be put to good use within a gradient-based optimisation algorithm [5]. In the following, it is shown how to calculate explicitly those derivatives. The calculations do not present any particular difficulty, but they are not detailed here for the sake of brevity.

A useful convention is first introduced. Given a function y defined on $[0; T]$, the notation D_y represents the $M \times M$ diagonal matrix with diagonal entries $y(t_1), ... y(t_M)$. Then, the vector of 1st-order derivatives is given as

$$\frac{\partial \tilde{f}}{\partial \hat{\mathbf{x}}} = \mathbf{1}_{M \times 1}^{\mathsf{T}} \left[D_{v_1}\Phi + D_{v_2}\Phi\Omega + D_{v_3}\Phi\mathbf{L}\right] \tag{14}$$

with

$$\begin{cases} v_1 = \frac{\partial \alpha}{\partial x} + \frac{\partial \alpha}{\partial u} \frac{\partial n}{\partial x} \\ v_2 = \frac{\partial \alpha}{\partial \dot{x}} + \frac{\partial \alpha}{\partial u} \frac{\partial n}{\partial \dot{x}} \\ v_3 = \frac{\partial \alpha}{\partial u} \end{cases}$$

The matrix of second-order derivatives is given as

$$\begin{aligned} \frac{\partial^2 \tilde{f}}{\partial \hat{\mathbf{x}}^2} = &\; \Phi^{\mathsf{T}} D_{w_1}\Phi + \Phi^{\mathsf{T}} D_{w_2}\Phi\Omega + \Omega^{\mathsf{T}}\Phi^{\mathsf{T}} D_{w_2}\Phi \\ &+ \Omega^{\mathsf{T}}\Phi^{\mathsf{T}} D_{w_3}\Phi\Omega + \Phi^{\mathsf{T}} D_{w_4}\Phi\mathbf{L} + \mathbf{L}^{\mathsf{T}}\Phi^{\mathsf{T}} D_{w_4}\Phi \\ &+ \Omega^{\mathsf{T}}\Phi^{\mathsf{T}} D_{w_5}\Phi\mathbf{L} + \mathbf{L}^{\mathsf{T}}\Phi^{\mathsf{T}} D_{w_5}\Phi\Omega \\ &+ \mathbf{L}^{\mathsf{T}}\Phi^{\mathsf{T}} D_{w_6}\Phi\mathbf{L} \end{aligned} \tag{15}$$

with:

$$\begin{cases} w_1 = \frac{\partial^2 \alpha}{\partial x^2} + 2\frac{\partial^2 \alpha}{\partial x \partial u}\frac{\partial n}{\partial x} + \frac{\partial^2 \alpha}{\partial u^2}(\frac{\partial n}{\partial x})^2 + \frac{\partial \alpha}{\partial u}\frac{\partial^2 n}{\partial x^2} \\ w_2 = \frac{\partial^2 \alpha}{\partial \dot{x} \partial x} + \frac{\partial^2 \alpha}{\partial u^2}\frac{\partial n}{\partial x}\frac{\partial n}{\partial \dot{x}} + \frac{\partial^2 \alpha}{\partial \dot{x} \partial u}\frac{\partial n}{\partial x} + \frac{\partial^2 \alpha}{\partial x \partial u}\frac{\partial n}{\partial \dot{x}} + \frac{\partial \alpha}{\partial u}\frac{\partial^2 n}{\partial x \partial \dot{x}} \\ w_3 = \frac{\partial^2 \alpha}{\partial \dot{x}^2} + 2\frac{\partial^2 \alpha}{\partial \dot{x} \partial u}\frac{\partial n}{\partial \dot{x}} + \frac{\partial^2 \alpha}{\partial u^2}(\frac{\partial n}{\partial \dot{x}})^2 + \frac{\partial \alpha}{\partial u}\frac{\partial^2 n}{\partial \dot{x}^2} \\ w_4 = \frac{\partial^2 \alpha}{\partial u \partial x} + \frac{\partial^2 \alpha}{\partial u^2}\frac{\partial n}{\partial x} \\ w_5 = \frac{\partial^2 \alpha}{\partial u \partial \dot{x}} + \frac{\partial^2 \alpha}{\partial u^2}\frac{\partial n}{\partial \dot{x}} \\ w_6 = \frac{\partial^2 \alpha}{\partial u^2} \end{cases}$$

In practice, at each iteration of the optimisation algorithm, the objective function $\tilde{\alpha}$, the nonlinear terms n, and their 1st- and 2nd-order derivatives, are evaluated along the trajectory given by $\mathbf{x} = \Phi\hat{\mathbf{x}}$. $\tilde{f}$ is evaluated; $v_1...v_3$ are built in order to calculate $\frac{\partial \tilde{f}}{\partial \hat{\mathbf{x}}}$ as in Equation (14), and $w_1...w_6$ are built in order to calculate $\frac{\partial^2 \tilde{f}}{\partial \hat{\mathbf{x}}^2}$ as in Equation (15).

2.4. Inequality Constraints

The reader may have noticed that inequality constraints have not been introduced in the problem formulation. Yet, operational limitations, typically on the WEC position or velocity, on the control force or on instantaneous power, are essential for the safe operation of the device.

In particular, constraints which are nonlinear with respect to x (e.g., force or power constraints) are computationally challenging. How their 1st- and 2nd-order derivatives can be explicitly computed, is detailed in [5]. The more general objective function, introduced in the present paper in Equation (5), does not result in any change in the constraint-related calculations, which are therefore not reproduced here.

3. Numerical Case Studies

3.1. Non-Ideal Power Take-Off Systems

The effect of a non-ideal PTO efficiency upon WEC control is specifically addressed in a number of studies [10–15,18]. In most of them [11,12,14–18], the non-ideal PTO system is modelled by means of a non-unity efficiency factor μ verifying $0 \leq \mu \leq 1$, so that the instantaneous electric power is expressed as follows.

$$P_e = \begin{cases} -\mu u\dot{x} & \text{if } -u\dot{x} \geq 0 \\ -\frac{1}{\mu}u\dot{x} & \text{if } -u\dot{x} < 0 \end{cases} \tag{16}$$

The simple model (16) is also retained in the present study, for the two WEC models described in Sections 3.2 and 3.3.

Reactive control techniques (which imply that, at times, P_a is negative) are essential to achieve optimal or near-optimal hydrodynamic power absorption, when the incoming wave frequency is away from the system's resonant frequency. In the case of monochromatic waves, a simple PI control law, of the form $u = -b\dot{x} - kx$, can achieve optimal power absorption, following the principle of impedance matching [1]. In irregular waves, a PI control law also presents significant improvements in absorbed power, with respect to a passive law of the form $u = -b\dot{x}$, although the PI controller is then sub-optimal. A salient point of studies [11,12] is that reactive control is particularly affected by a non-ideal PTO efficiency. In particular, it appears that the smaller μ is, the less reactive control should be performed (i.e., $|k|$ should be smaller).

Overall, all studies [10–15,17,18] are relatively pessimistic, regarding the mean electrical power $\overline{P}_e$ which can be achieved with a non-ideal PTO system: a 10% decrease in efficiency results in a drop in $\overline{P}_e$ of more than 50%, even when control parameters are tuned taking the PTO efficiency into account[1].

Define $h(P_a)$ the efficiency function, so that $h(P_a) = \frac{P_e}{P_a}$. Consistently with Equation (16), h is equal to μ for positive P_a, and $1/\mu$ for negative P_a, as illustrated in Figure 1. Such a discontinuous function is undesirable for the efficient implementation of the spectral control approach, detailed in Section 2, and which requires the explicit calculation of the 1st- and 2nd-order derivatives of the objective function. Therefore, in this work, $h(P_a)$ is approximated by the following function,

$$h_\kappa(P_a) = A \tanh(\kappa P_a) + B \tag{17}$$

where $A = \frac{1}{2}(\mu - 1/\mu)$, $B = \frac{1}{2}(\mu + 1\mu)$ and $\kappa > 0$ is a real parameter, which governs the accuracy of the approximation, as illustrated in Figure 1. Note that in [16], the use of a smoothed approximation of the function (16) is also advocated, in order to avoid issues in gradient-based optimisation for the considered optimal control problems. However, the sensitivity of the results to smoothing has not been investigated.
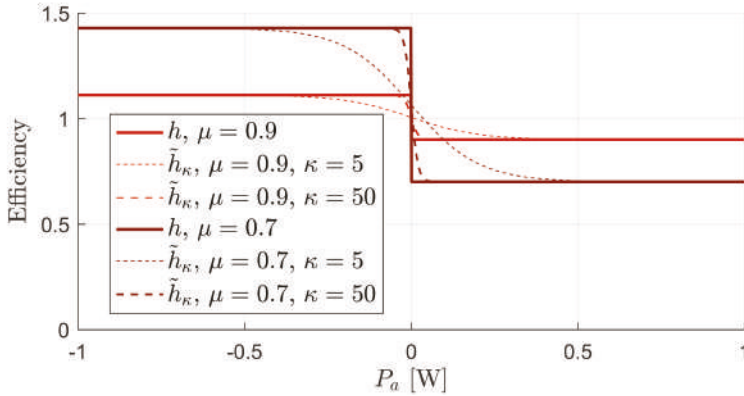
Figure 1. Efficiency function h for $\mu = 0.9$ and $\mu = 0.7$, and their approximations h_κ.

If the *exact* efficiency is considered, the function α in the optimisation problem (5) is $\alpha(\dot{x}, u) := -u\dot{x}\, h(-u\dot{x})$. However, in practice, the problem is solved using the approximate function $\alpha_\kappa(\dot{x}, u) := -u\dot{x}\, h_\kappa(-u\dot{x})$. For all $(\dot{x}, u)$, $\alpha(\dot{x}, u) \leq \alpha_\kappa(\dot{x}, u)$. Therefore, the optimal mean electric power, $\overline{P}^*_{e,\kappa}$, obtained with α_κ, is an upper bound to the optimal exact electric power, $\overline{P}^*_e$, which would be obtained if Problem (1) could be solved using the exact efficiency. Furthermore, for all $\kappa_1 \leq \kappa_2$, for all $(\dot{x}, u)$, $\alpha_{\kappa_2}(\dot{x}, u) \leq \alpha_{\kappa_1}(\dot{x}, u)$, which implies that $\overline{P}^*_{e,\kappa}$ decreases monotonically with κ, and has $\overline{P}^*_e$ as a limit when $\kappa \to \infty$.

$\overline{P}^*_e$ can also be bounded from below: consider the solution x^*_κ, u^*_κ, obtained with the approximate objective function. x^*_κ, u^*_κ is necessarily sub-optimal, with respect to the exact objective function. Therefore, the exact mean electric power, effectively achieved with (x^*_κ, u^*_κ), constitutes a lower bound to $\overline{P}^*_e$, and is calculated as follows.

$$\overline{P}^{\dagger}_{e,\kappa} = \frac{1}{T} \int_{t=0}^{T} \alpha(\dot{x}^*_\kappa, u^*_\kappa)dt \tag{18}$$

---

[1] It should be noted, however, that the control strategies adopted, and the PTO efficiency models, differ across studies, so that accurate comparisons are difficult.

Therefore the following inequality holds.

$$\overline{P}_{e,\kappa}^{\dagger} \leq \overline{P}_e^* \leq \overline{P}_{e,\kappa}^* \tag{19}$$

Even if the true optimal electrical power $\overline{P}_e^*$ cannot be calculated for the exact efficiency, by setting κ to a large enough value, it can be ensured that the electric power $\overline{P}_{e,\kappa}^{\dagger}$, effectively achieved with the solution found, lies within a prescribed percentage of $\overline{P}_e^*$.

Finally, let $(x^*, u^*)|_{\mu}$ be the optimal solution for efficiency $\mu < 1$, and $\overline{P}_e^*|_{\mu}$ (resp. $\overline{P}_a|_{\mu}$) the mean electrical (resp. absorbed) power with the solution $(x^*, u^*)|_{\mu}$. It is easy to show[2] that $\overline{P}_e^*|_{\mu} < \mu \overline{P}_a|_{\mu}$. Define $\overline{P}_{id}^*$ as the optimal power for an ideal PTO (absorbed and electric power are then identical). The solution $(x^*, u^*)|_{\mu}$ is sub-optimal with respect to an ideal PTO, thus $\overline{P}_a|_{\mu} < \overline{P}_{id}^*$. Therefore, the following simple inequality holds.

$$\overline{P}_e^*|_{\mu} < \mu \overline{P}_{id}^* \tag{20}$$

Equation (20) means that the optimal mean electric power, for a non-ideal PTO efficiency, cannot exceed the optimal mean electric power for an ideal PTO efficiency, multiplied by the efficiency factor. In the particular case, where the optimal solution, for an ideal PTO efficiency, is purely passive, then that solution is also the optimal solution for a non-ideal PTO efficiency $\mu < 1$, and the inequality becomes an equality: $P_e^*|_{\mu} = \mu P_e^*|_{id}$. This can happen if the incoming wave frequency coincides with the WEC natural frequency, so that no reactive power is needed to achieve optimal control.

3.2. The WECCCOMP Model

The Wavestar device is a point absorber WEC, primarily operating in heave, rigidly connected to a rotation arm. The power is captured through the arm rotation around a fixed axis. In the WEC control competition (WECCCOMP), a scale model of the Wavestar device is considered. The linearised WEC dynamics can be modelled by expressing Newton's second law around the rotation axis, which results in a dynamical equation, of the form of Equation (3), where the nonlinear terms n are set to zero. The variable x, in this case, corresponds to the angular displacement of the rotation arm. All the linear parameters of Equation (3) are derived from the linear model, provided by the competition organisers [18]. Lower and upper limits on the PTO torque (± 10 N.m) and angular position ($\pm 24°$) are considered as constraints. Six JONSWAP wave spectra [23], proposed by the organisers [18], and with characteristics listed in Table 1, are used to generate random excitation torque time series, with duration $T = 40$s, at least equal to 20 typical wave periods for the sea states considered.

In each random realisation, the optimal solution $\hat{x}_\kappa^*|_{\mu}$, and power $\overline{P}_{e,\kappa}^*|_{\mu}$, with $\mu = 1, 0.9, \ldots, 0.5$, are calculated using the *approximate* efficiency function h_κ. Then, the *exact* power $\overline{P}_{e,\kappa}^{\dagger}|_{\mu}$, obtained with $\hat{x}_\kappa^*|_{\mu}$, is also calculated.

For each pair of sea states (1–4, 2–5, 3–6), the appropriate range of values for κ differs (when typical values for absorbed power are larger, a smaller κ yields a satisfactory approximation). For each pair of sea states, κ is gradually increased, until bounds given by Equation (19) are sufficiently close. Suitable values for κ are indicated in Table 1.

Table 1. List of WECCCOMP JONSWAP sea states.

ID	(H_{m_0}, T_p, γ)	ID	(H_{m_0}, T_p, γ)	κ
1	$(0.0208, 0.988, 1)$	4	$(0.0208, 0.988, 3.3)$	100
2	$(0.0625, 1.412, 1)$	5	$(0.0625, 1.412, 3.3)$	5
3	$(0.1042, 1.836, 1)$	6	$(0.1042, 1.836, 3.3)$	2

---

[2] To see this, decompose $\overline{P}_a$ into its passive and reactive components.

3.3. The RM3 Device

The RM3 device is a self-reacting, two-body point absorber, exploiting the relative heave motion of the two bodies [19]. The RM3 consists of a cylindrical float (B1) which vertically oscillates with waves, relative to a vertical column spar buoy (B2) damped by a subsurface reaction plate. Within the scope of linear hydrodynamics, the heaving mode of motion is decoupled from the other degrees of freedom, and therefore B1 and B2 may be modelled in terms of heave only. Assuming harmonic signals and adopting complex notations (omitting the frequency dependence for conciseness), the position in heave of B1 and B2, x_1 and x_2, can be described by the following two equations [24],

$$\begin{cases} z_1 \hat{x}_1 + z_{21} \hat{x}_2 = \hat{e}_1 + \hat{u} \\ z_{12} \hat{x}_1 + z_2 \hat{x}_2 = \hat{e}_2 - \hat{u} \end{cases} \tag{21}$$

where

- the complex mechanical impedance z_i is built as $z_i(\omega) = S_i - \omega^2(I_i + A_{r,i}(\omega)) - j\omega(C_i + B_{r,i}(\omega))$ from the hydrodynamic coefficients of Body i,
- the coupling terms $z_{ij}(\omega) = z_{ji}(\omega) = -\omega^2 A_{r,i\to j}(\omega) - j\omega B_{r,i\to j}(\omega)$ are due to the radiation interaction between B1 and B2,
- $\hat{e}_i$ denotes the wave excitation force onto Body i and
- the PTO system applies a force u from B2 onto B1.

By rearranging Equation (21), it is easy to obtain a new formulation in terms of the relative motion[3], $x := x_1 - x_2$, sufficient to solve the control problem (see in [24] for more detail):

$$z_{eq} \hat{x} = \hat{e}_{eq} + \hat{u} \tag{22}$$

where $z_{eq} = \frac{z_2 z_1 - z_{12}^2}{z_0}$, $\hat{e}_{eq} = \frac{z_2 + z_{12}}{z_0} \hat{e}_1 + \frac{z_1 + z_{12}}{z_0} \hat{e}_2$ and $z_0 = z_1 + z_2 + 2z_{12}$. The proposed spectral method can thus be applied, using the equivalent impedance z_{eq} to determine the entries of the matrix **L** as in Section 2.2.

Control calculations are carried out in four JONSWAP [23] sea states, inspired by the scatter diagram of the device's design location, given in [19], with $H_{m_0} = 2$m, $\gamma = 3$, and $T_p = 6, 8, 10$ and 12 s. The relative heave x is subject to the constraint $-2\text{m} \leq x \leq 2\text{m}$ [19]. The wave signal duration is set to $T = 300$ s (more than 25 typical wave periods in all sea states). A value κ of the order of 10^{-6} allows for accurate optimal power estimates[4].

4. Numerical Results

All constrained control results were obtained using the interior-point algorithm implemented in the Matlab[5] *fmincon* function. For the WECCCOMP model, the cut-off frequency for the control solution is set to 4 Hz (as the signal duration is $T = 40$s, the order N of the approximation is therefore $N = 4 \times 40 = 160$). The number M of collocation points is set to $M = 3N + 1$. For the RM3 device, the cut-off frequency for the control solution is set to 0.5 Hz (as the signal duration is $T = 300$ s, the order N of the approximation is therefore $N = 0.5 \times 300 = 150$). The number M of collocation points is set to $M = 4N + 1$.

---

3   For the motion to be fully determined, another equation is necessary, for example in terms of $y := x_1 + x_2$, but this does not have any influence in terms of power absorption.

4   The reader may have noted that this value is very different from those, which were found appropriate for the WECCCOMP model. This is because, given the form of Equation (17), the appropriate value for κ depends on the typical magnitude of P_a: in the RM3 case, which is a full-scale model, P_a takes much larger values than in the WECCCOMP case.

5   www.matlab.com.

4.1. The WECCCOMP Model

Figure 2 shows control results obtained with the WECCCOMP numerical model (see Section 3.2), in the six sea states of the competition, and values of μ between 1 and 0.5. In each sea state, power values are normalised by $\overline{P}^*_{id}$, the optimal power obtained with $\mu = 1$. $\overline{P}^*_{id}$ essentially represents the optimal absorbed mechanical power; it is a well-known theoretical limit in the wave energy literature [1], which can be calculated as $\overline{P}^*_{id} = \int_{\omega=0}^{\infty} \frac{-\omega|\hat{e}(\omega)|^2}{2\Im\{z(\omega)\}} d\omega$. As per Equation (19), $\overline{P}^\dagger_{e,\kappa}|_\mu$ and $\overline{P}^*_{e,\kappa}|_\mu$ together provide bounds to $\overline{P}^*_e|_\mu$, the optimal power for the exact efficiency function.
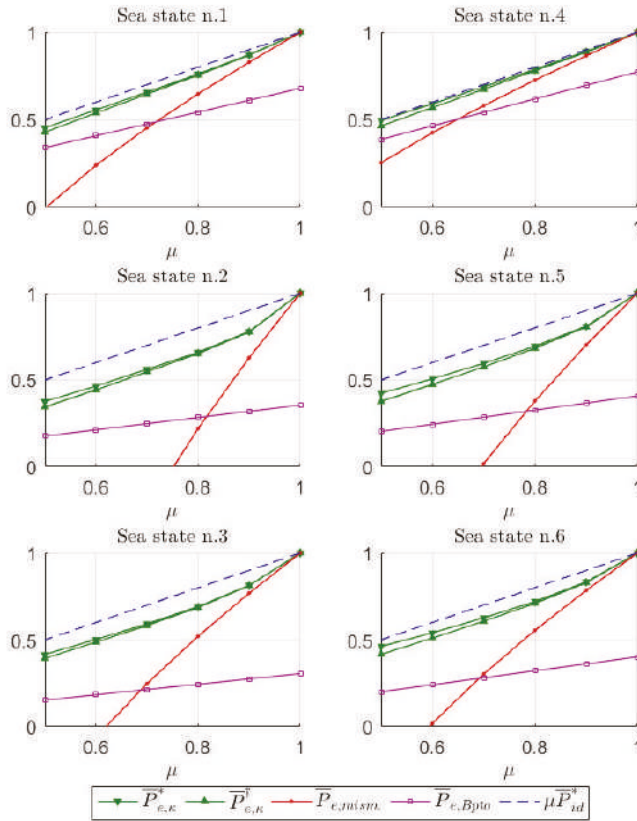
Figure 2. Normalised mean electric power for the model Wavestar device in the six WECCCOMP sea states, over a range of efficiency parameter values.

Also shown in Figure 2, the dotted lines labelled "$\mu\overline{P}^*_{id}$" represent the upper bound of Equation (20), i.e., a hypothetical scenario where $\overline{P}^*_{id}$ would "only" be affected by a factor of μ. $\overline{P}_{mism.}$ is the actual electric power which would be obtained, if the solution $\hat{x}^*_{id}$ to the ideal control problem were followed by a WEC with imperfect PTO efficiency $\mu \leq 1$; in other words, $\overline{P}_{mism.}$ shows the effect of a *mismatch* between the nominal efficiency ($\mu = 1$) and the actual efficiency ($1 > \mu \geq 0.5$). Finally, $\overline{P}_{Bpto}$ represents the power obtained using a simple linear PTO damping, with coefficient B_{pto} optimised for each sea state.

The importance of taking into account the non-ideal PTO efficiency in control calculations is evidenced by $\overline{P}_{mism.}$, which can even take negative values, similarly to the results of [13]. In contrast,

the proposed spectral control approach, with approximate efficiency function, provides a solution for which the mean electric power, $\overline{P}^{\dagger}_{e,\kappa}|_{\mu}$, lies within a few percents of the true optimal power value. Unlike other studies [11–14], the controller's performance, optimised taking μ into account, is reasonably close to the "best-case scenario" $\mu\overline{P}^{*}_{id}$ (in fact, almost identical in sea states 1 and 4). Results also clearly evidence the interest of the proposed spectral control approach, with respect to an optimised linear damper, even in sea states 1 and 4, where the waves are close to the WEC resonant frequency.

Figure 3 shows the effect of a non-ideal PTO efficiency, upon the WEC optimal trajectory (in this case, represented by the WEC angular velocity $\dot{\theta}$, see Section 3.2), control torque, and instantaneous power, in Sea State 3. In the non-ideal case, μ is set to 0.7 as in the WECCCOMP.
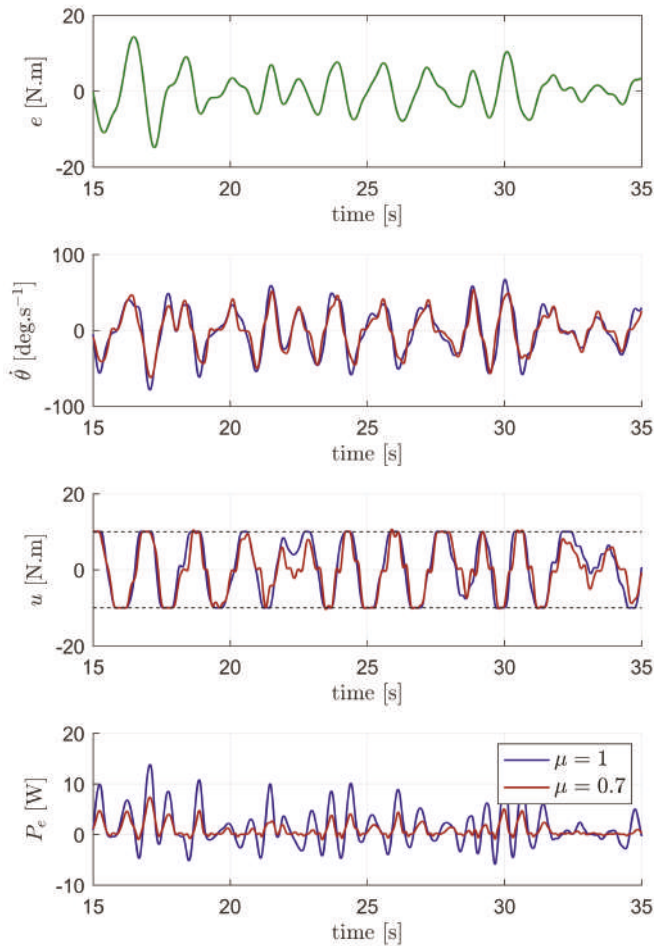
Figure 3. Excitation torque, optimal angular velocity, control torque and instantaneous electric power, with $\mu = 1$ and $\mu = 0.7$.

Although the two optimal velocities and control inputs look qualitatively similar[6], the optimal electric power is fundamentally modified by the non-ideal PTO efficiency. As could be expected, very little reactive power must be employed with $\mu = 0.7$; furthermore, the peaks in instantaneous electric power are reduced by a factor of at least 2 (while the average electric power still exceeds 60% of the ideal one).

4.2. The RM3 Device

Results for the RM3 device (see Section 3.3) are illustrated in a way similar to those of Section 4.1, in Figures 4 and 5. In Figure 4, the two bounds $\overline{P}^*_{e,\kappa}|_\mu$ and $\overline{P}^\dagger_{e,\kappa}|_\mu$ are close enough to indicate that the solution obtained is nearly optimal.
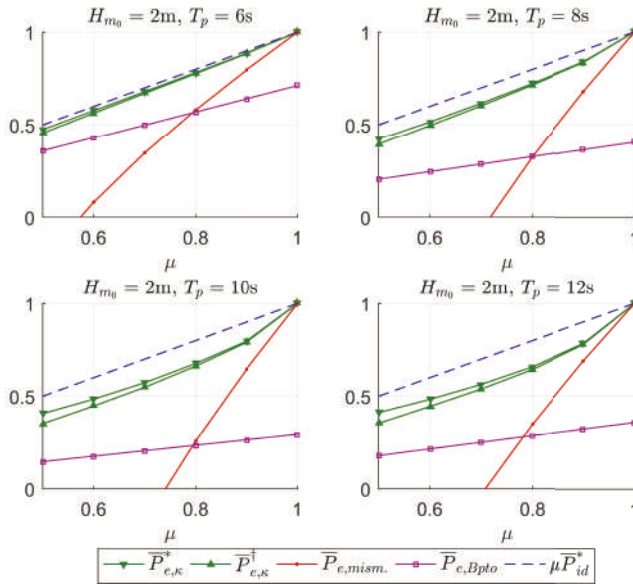
Figure 4. Normalised mean electric power for the RM3 device in four JONSWAP sea states with $\gamma = 3$, over a range of efficiency parameter values.

The RM3 resonant period of the device is of the order of 4.5s, which is shorter than typical waves encountered at the device's design location[7]. As a consequence, from Figure 4, it can be seen that for shorter T_p, less reactive power is used to achieve optimal power absorption, thus making the simple linear damper perform reasonably well with respect to the reactive control strategy. In contrast, when waves are away from the WEC resonant frequencies, more reactive power must be employed, and the control strategy is significantly affected by the non-ideal efficiency; see, in particular, $\overline{P}_{e,mism.}$. However, the efficiency-aware spectral control strongly mitigates such adverse effects, bringing $\overline{P}^\dagger_{e,\kappa}$ close to the hypothetical best-case scenario $\mu\overline{P}^*_{id}$.

Finally, similarly to Figure 3, the effect of a non-ideal efficiency upon the control strategy is examined more closely in Figure 5, for the JONSWAP sea state with $T_p = 8$ s. While the ideal PTO

---

6   In particular, in both cases the optimal velocity is in phase with the excitation torque, which is a classical WEC optimal control result [1]
7   This is typically the case for heaving point absorbers: their dimensions give them a relatively short resonant period, but reactive control can artificially make them resonate in longer wave periods.

yields large reactive power flows, taking into account a non-ideal efficiency $\mu = 0.7$ eliminates most of the reactive power, and spectacularly reduces the peak power amplitude. With the non-ideal PTO efficiency, the optimal relative heave velocity $\dot{x}$ (see Section 3.3) and control force u exhibit visible higher-frequency oscillations. Finally, note that the relative position constraint is successfully implemented within the spectral control strategy, which would not be possible with a simpler control approach, such as a PI controller.
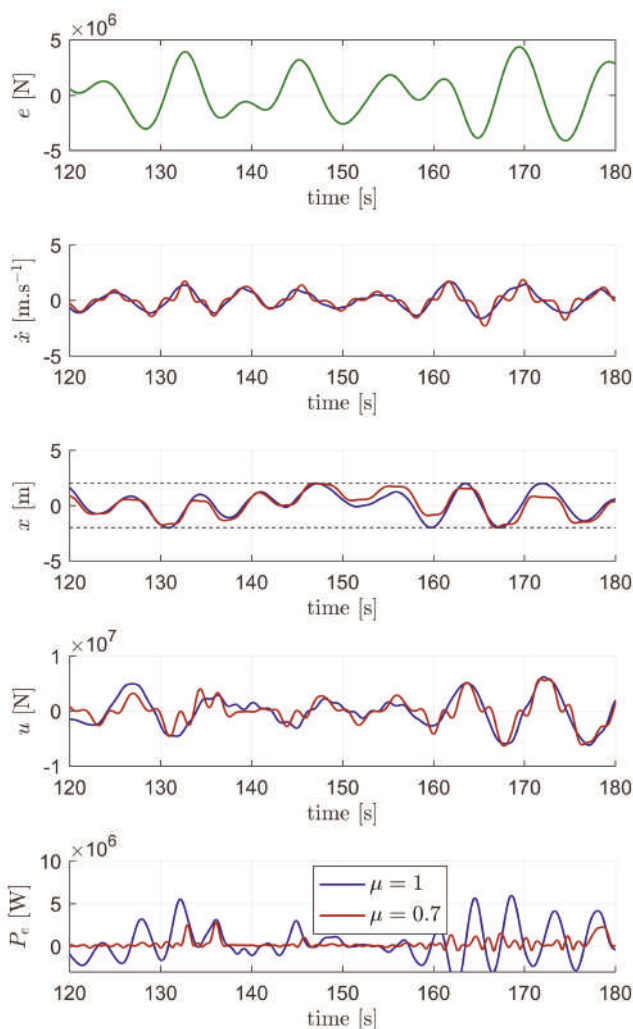
Figure 5. Excitation force, optimal relative velocity, relative position, control force, and instantaneous electric power, with $\mu = 1$ and $\mu = 0.7$, $T_p = 8$ s.

5. Conclusions

This work shows how the spectral control approach in [5] can be extended to handle more general objective functions, of the form outlined in Equation (2). The efficiency of the proposed technique allows optimal control results to be calculated at once in long wave signals, comprising more than

20 wave periods. Such calculations permit a theoretical analysis of WEC optimal control results, under a variety of modelling and control choices. Furthermore, as in [9], they can provide a robust point of comparison to assess the performance of more practical control approaches, typically implemented in a receding-horizon configuration. In fact, the authors have used the optimal spectral control approach proposed in this work, to assess the receding-horizon MPC solution, proposed by their institution for the WECCCOMP. This comparison will be the subject of a future paper.

A particularly important application of the proposed spectral method consists of WEC control with non-ideal PTO efficiency. In this study, a discontinuous efficiency function, given in Equation (16), is considered. A smooth, hyperbolic tangent approximation for the efficiency function allows the calculation of a near-optimal solution, which also provides upper and lower bounds to the exact optimal electric power.

In view of the results of Figures 2 and 4, concerning two different WECs representative of heaving point absorbers (both devices have resonant periods shorter than their design waves), a non-ideal PTO efficiency may not be as detrimental as suggested in previous studies [11,12,14,15], if the control strategy is able to take the non-ideal efficiency into account, which is the case for the proposed optimal spectral approach. In fact, with realistic efficiency values in the range of $0.7 \leq \mu \leq 0.9$ [11], it does not seem unreasonable to approximate the optimal electric power achievable with $\mu \overline{P}_{id}^*$, minus 5 to 15% (reminding that $\mu \overline{P}_{id}^*$ is merely a theoretical limit, that no control strategy can exceed if the PTO has an efficiency factor of μ).

The fact that a non-ideal PTO efficiency necessitates a control strategy with less reactive power, already evidenced in previous studies [11,12], is clearly corroborated by the results of Figures 3 and 5. This is to be expected, irrespective to the WEC technology and the sea states considered. However, the extent of power production degradation when a control strategy neglects the non-ideal PTO characteristics will be, in general, system- and wave climate-dependent. Note, also, that the results of this study depend, to some extent, on the specific model adopted for the PTO efficiency. Other efficiency functions could be investigated, such as those in [10,13], which model the fact that the PTO efficiency drops for small load factors.

The computational speed of the proposed spectral control technique is not a central aspect of the present work; however, it was found that optimal solutions, for irregular wave signals with more than 5 wave periods, could be obtained in less than 1 second, with a Matlab implementation running on a 2.60 GHz, 4-core Intel® processor. A real-time, receding-horizon implementation could be considered in future work, either by employing windowing functions to make the receding-horizon control problem periodic, in the spirit of the works in [8,9], or through the use of non-periodic spectral basis functions [6].

Author Contributions: Conceptualising, A.M.; software, A.M.; writing—original draft preparation, A.M.; writing—review and editing, A.M. and P.T.; supervision, P.T.; project administration, P.T. All authors have read and agreed to the published version of the manuscript.

Conflicts of Interest: The authors declare no conflicts of interest.

References

1. Ringwood, J.V.; Bacelli, G.; Fusco, F. Energy-maximizing control of wave-energy converters: The development of control system technology to optimize their operation. *IEEE Control Syst. Mag.* **2014**, *34*, 30–55.
2. Faedo, N.; Olaya, S.; Ringwood, J.V. Optimal control, MPC and MPC-like algorithms for wave energy systems: An overview. *IFAC J. Syst. Control* **2017**, *1*, 37–56. [CrossRef]
3. Bacelli, G.; Ringwood, J.V.; Gilloteaux, J.C. A control system for a self-reacting point absorber wave energy converter subject to constraints. *IFAC Proc. Vol.* **2011**, *44*, 11387–11392. [CrossRef]
4. Bacelli, G.; Ringwood, J.V. Nonlinear optimal wave energy converter control with application to a flap-type device. *IFAC Proc. Vol.* **2014**, *47*, 7696–7701. [CrossRef]

5. Mérigaud, A.; Ringwood, J.V. Improving the computational performance of nonlinear pseudospectral control of wave energy converters. *IEEE Trans. Sustain. Energy* **2017**, *9*, 1419–1426. [CrossRef]
6. Genest, R.; Ringwood, J.V. Receding horizon pseudospectral control for energy maximization with application to wave energy devices. *IEEE Trans. Control Syst. Technol.* **2016**, *25*, 29–38. [CrossRef]
7. Boyd, J.P. *Chebyshev and Fourier Spectral Methods*; Courier Corporation: North Chelmsford, MA, USA, 2001.
8. Auger, C.; Merigaud, A.P.L.; Ringwood, J.V. Receding-horizon pseudo-spectral control of wave energy converters using periodic basis functions. *IEEE Trans. Sustain. Energy* **2018**, *10*, 1644–1652. [CrossRef]
9. Mérigaud, A.; Ringwood, J.V. Towards realistic nonlinear receding-horizon spectral control of wave energy converters. *Control Eng. Pract.* **2018**, *81*, 145–161.
10. Tedeschi, E.; Carraro, M.; Molinas, M.; Mattavelli, P. Effect of control strategies and power take-off efficiency on the power capture from sea waves. *IEEE Trans. Energy Convers.* **2011**, *26*, 1088–1098. [CrossRef]
11. Genest, R.; Bonnefoy, F.; Clément, A.H.; Babarit, A. Effect of non-ideal power take-off on the energy absorption of a reactively controlled one degree of freedom wave energy converter. *Appl. Ocean. Res.* **2014**, *48*, 236–243. [CrossRef]
12. Falcão, A.F.; Henriques, J.C. Effect of non-ideal power take-off efficiency on performance of single-and two-body reactively controlled wave energy converters. *J. Ocean. Eng. Mar. Energy* **2015**, *1*, 273–286.
13. Bacelli, G.; Genest, R.; Ringwood, J.V. Nonlinear control of flap-type wave energy converter with a non-ideal power take-off system. *Annu. Rev. Control* **2015**, *40*, 116–126. [CrossRef]
14. Sánchez, E.V.; Hansen, R.H.; Kramer, M.M. Control performance assessment and design of optimal control to harvest ocean energy. *IEEE J. Ocean. Eng.* **2014**, *40*, 15–26. [CrossRef]
15. Tom, N.M.; Madhi, F.; Yeung, R.W. Power-to-load balancing for heaving asymmetric wave-energy converters with nonideal power take-off. *Renew. Energy* **2019**, *131*, 1208–1225. [CrossRef]
16. Tona, P.; Nguyen, H.N.; Sabiron, G.; Creff, Y. An Efficiency-Aware Model Predictive Control Strategy for a Heaving Buoy Wave Energy Converter. In Proceedings of the European Wave and Tidal Energy Conference (EWTEC) 2015, Nantes, France, 6–11 September 2015.
17. Saupe, F.; Creff, Y.; Gilloteaux, J.C.; Bozonnet, P.; Tona, P. *Latching Control Strategies for a Heaving Buoy Wave Energy Generator in a Random Sea*; IFAC World Congress: Prague, Czech Republic, 2014; Volume 19, pp. 7710–7716.
18. Ringwood, J.V.; Ferri, F.; Ruehl, K.; Yu, Y.H.; Coe, R.G.; Bacelli, G.; Weber, J.; Kramer, M.M. A competition for WEC control systems. In Proceedings of the 12th European Wave and Tidal Energy ConferencEuropean Wave and Tidal Energy Conference, Cork, Ireland, 27 August–1 September 2017.
19. Neary, V.S.; Lawson, M.; Previsic, M.; Copping, A.; Hallett, K.C.; LaBonte, A.; Rieks, J.; Murray, D. *Methodology for Design and Economic Analysis of Marine Energy Conversion (MEC) Technologies*; Technical Report; Sandia National Lab. (SNL-NM): Albuquerque, NM, USA, 2014.
20. Mérigaud, A. A Harmonic Balance Framework for the Numerical Simulation of Non-Linear Wave Energy Converter Models in Random Seas. Ph.D. Thesis, Maynooth University, Maynooth, Ireland, 2018.
21. Cummins, W. The impulse response function and ship motions. *Schiffstechnik* **1962**, *9*, 101–109.
22. Ogilvie, T. Recent progress toward the understanding and prediction of ship motions. In Proceedings of the Sixth Symposium on Naval Hydrodynamics, Bergen, Norway, 10–12 September 1964.
23. Hasselmann, K.; Barnett, T.; Bouws, E.; Carlson, H.; Cartwright, D.; Enke, K.; Ewing, J.; Gienapp, H.; Hasselmann, D.; Kruseman, P. *Measurements of Wind-Wave Growth and Swell Decay During the Joint North Sea Wave Project (JONSWAP)*; Technical Report; Deutches Hydrographisches Institut: Hamburg, Germany, 1973.
24. Olaya, S. Contribution à la Modélisation Multi-Physique et au Contrôle Optimal d'un Générateur Houlomoteur: Application à un Système 'deux corps'. Ph.D. Thesis, Université de Bretagne occidentale, Brest, France, 2016. (In French)

Article

The Influence of Sizing of Wave Energy Converters on the Techno-Economic Performance

Jian Tan *, Henk Polinder , Antonio Jarquin Laguna , Peter Wellens and Sape A. Miedema

Department of Maritime & Transport Technology, Delft University of Technology,
2628 CD Delft, The Netherlands; H.Polinder@tudelft.nl (H.P.); A.JarquinLaguna@tudelft.nl (A.J.L.);
P.R.Wellens@tudelft.nl (P.W.); S.A.Miedema@tudelft.nl (S.A.M.)
* Correspondence: J.Tan-2@tudelft.nl

Abstract: Currently, the techno-economic performance of Wave Energy Converters (WECs) is not competitive with other renewable technologies. Size optimization could make a difference. However, the impact of sizing on the techno-economic performance of WECs still remains unclear, especially when sizing of the buoy and Power Take-Off (PTO) are considered collectively. In this paper, an optimization method for the buoy and PTO sizing is proposed for a generic heaving point absorber to reduce the Levelized Cost Of Energy (LCOE). Frequency domain modeling is used to calculate the power absorption of WECs with different buoy and PTO sizes. Force constraints are used to represent the effects of PTO sizing on the absorbed power, in which the passive and reactive control strategy are considered, respectively. A preliminary economic model is established to calculate the cost of WECs. The proposed method is implemented for three realistic sea sites, and the dependence of the optimal size of WECs on wave resources and control strategies is analyzed. The results show that PTO sizing has a limited effect on the buoy size determination, while it can reduce the LCOE by 24% to 31%. Besides, the higher mean wave power density of wave resources does not necessarily correspond to the larger optimal buoy or PTO sizes, but it contributes to the lower LCOE. In addition, the optimal PTO force limit converges at around 0.4 to 0.5 times the maximum required PTO force for the corresponding sea sites. Compared with other methods, this proposed method shows a better potential in sizing and reducing LCOE.

Keywords: WECs; size optimization; techno-economic performance; PTO sizing

1. Introduction

Wave energy has been highlighted as a renewable energy resource for decades. However, large scale utilization of wave energy is still far from commercialization [1,2]. An important obstacle in the development of Wave Energy Converters (WECs) is that their techno-economic performance is not competitive with offshore wind and other renewable technologies [3]. Another challenge is the wide variety of WEC types [4], which makes it hard to converge the attention and investment. During the last 40 years, over 200 WEC concepts have been proposed [1]. To select the promising WECs, it is necessary to compare and evaluate their viability at different potential sea sites.

The feasibility of WECs has already been evaluated in existing literature. A set of technical and economic indicators of various WEC concepts have been presented [5]. During the operation of WECs, power production relies not only on the wave resources available but also on the operating principles of the particular device [4]. In Reference [5], a benchmarking of 8 types of WECs was established considering 5 different representative sea sites, and a series of cost-related metrics of different WECs was analyzed and compared. In Reference [6], based on a cost estimation model, a techno-economic evaluation for 6 types of WECs was conducted for different devices. The sensitivity of the Levelized Cost Of Energy (LCOE) to wave resources, array configurations, Capital Expenditure (CAPEX), and Operational Expenditure (OPEX) was also discussed.

Apart from the variation of wave resources and types of WECs, the size determination also has a significant impact on the techno-economic evaluation of WECs. Firstly, the power performance of WECs depends strongly on their size [4]. Secondly, given the variation of operating principles, the sensitivity of power performance to the size of WECs also varies considerably [7]. Thirdly, the cost is highly related to the size of WECs [8]. Thus, the size optimization of WECs is expected to make a difference in the evaluation results. However, the optimization is not widely considered in evaluation studies even though the original sizes of WECs are usually designed to suit only some specific sea sites.

Independently or integrated with evaluation studies, size optimization of WECs has been discussed in existing literature. In Reference [9,10], the theoretical ratio of absorbed power to the buoy volume was derived based on linear wave theory. It was concluded that the smaller the volume of the floating WEC is, the higher this ratio is. In Reference [11], a theoretical method for determining the suitable buoy size of WECs for different sea sites was proposed based on Budal diagram. By means of that method, the volume of the buoy could be selected to guarantee the required working time at full capacity of devices for a certain sea site. In Reference [4,7,12], the optimal characteristic lengths of WECs were demonstrated from the perspective of maximizing Capture Width Ratio (CWR), concluding that the optimal characteristic length depends on sea sites. Furthermore, the effect of sizing of WECs on their techno-economic performance has been investigated [8,13], and the results showed that size optimization is able to reduce the LCOE dramatically. However, above-mentioned literature regarding size optimization of WECs concentrated mainly on buoy sizing without considering Power Take-Off (PTO) sizing. Mostly, the PTO size is simply scaled with the same scaling factor used for the buoy.

As a core component, the PTO system is significantly influential to the techno-economic performance of WECs [14]. On the one hand, its cost normally accounts for over 20% of the total CAPEX [15]. On the other hand, the PTO size is highly related to the rated power and the force constraint, which can directly affect the absorbed power. The affecting factors on PTO sizing have been investigated, as well. In Reference [16,17], a series of studies on the influence of the generator rating and control strategies on the power performance was conducted through simulations and experiments. In Reference [14,18], the impact of the control strategies on the PTO sizing of point absorbers was investigated. Although these studies made a profound contribution to presenting the impact of PTO sizing on the absorbed power, buoy sizing was not taken into account collectively. Recently, the influence of PTO sizes has started to be considered in a few of studies regarding buoy geometry optimization. In Reference [19], the geometry optimization of a cylindrical WEC with only a few of different force constraints was performed. The paper indicates that the PTO force constraint has a notable influence on the optimization results, and this finding is highly valuable for the design optimization of WECs. However, there are some limitations in Reference [19]. Firstly, the force constraint is not treated as an optimization variable and only a limited number of force constraints were included. Secondly, the optimization is conducted to maximize the absorbed power for the specific sea states, which is not necessarily beneficial for improving the techno-economic performance at realistic sea sites.

To the authors' knowledge, there is a lack of studies considering both PTO and buoy sizing of WECs. Thus, the aim of this paper was to investigate the collective influence of PTO sizing and buoy sizing on the LCOE. To achieve this aim, four research questions were addressed. Firstly, what are the optimal buoy sizes and PTO sizes for minimizing the LCOE in different wave resources and control strategies? Secondly, how much reduction in the LCOE can be gained by including PTO sizing? Thirdly, how does PTO sizing interact with buoy sizing from the techno-economic perspective? Fourthly, how much difference on the size determination and the optimized LCOE will there be when using different size optimization methods?

It should be acknowledged that one of the important factors affecting the LCOE is related to the system survivability and safety of WECs. Therefore, the techno-economic performance in practice is strongly related to the recurrence of extreme conditions, such

as the roughest sea state for 50 or 100 years in the deployment site. In this way, the total LCOE could be significantly higher than the optimized value based on the current study, which could mitigate the effects of sizing on the techno-economic performance. However, a better understanding on the collective influence of buoy and PTO sizing of WECs can clearly contribute to a more suitable WEC design. In addition, sizing of a single WEC could make a difference in the total number of units selected for a wave farm or array, where the operation and maintenance costs are directly influenced by the number of WECs. For instance, a wave farm with a large number of small individual WECs is expected to result in the increased number of operation and maintenance activities, leading to higher operation and maintenance costs. On the other hand, larger WECs can reduce the number of units in the wave farm, but their requirements for service operation vessels could be higher [8]. Thus, as stated in Reference [20], estimating an accurate value for OPEX is a difficult task since there is not enough available information in practical projects. For the sake of simplicity this study will be limited to the analysis of a single device using general values of OPEX costs derived from existing literature.

In this paper, a size optimization method considering both buoy and PTO sizing is established, and it is applied to a generic heaving point absorber. The optimization is performed based on an exhaustive search algorithm. Firstly, frequency domain modeling is used to calculate the power performance of WECs with different buoy and PTO sizes. The implementation of the PTO sizing using passive and reactive control is demonstrated, respectively. In addition, a preliminary economic model is described to build a cost function with the aim to minimize the LCOE. Next, based on the proposed method, size optimization of WECs is carried out for three realistic sea sites. The interaction between buoy and PTO sizing is analyzed, and the dependence of size determination on wave resources and control strategies is presented. Furthermore, a comparison between this proposed size optimization method and other methods is performed. Finally, conclusions are drawn based on the obtained results.

2. Methodology

This section starts with the description of the heaving spherical WEC concept and chosen sea sites. Next, the equations of motion and frequency domain modeling of WECs are presented. Finally, the size optimization method is established, in which the approaches to perform PTO sizing, buoy sizing, and the cost estimation of WECs are explained in detail.

2.1. WEC Concept Description

A generic heaving point absorber [21,22] is used in this study as WEC reference. The diameter of the buoy in the original size is 5 m. The average density of the buoy in all sizes is assumed to be identical and with a value of half of the water density (1025 kg/m^3). The schematics of the concept are shown in Figure 1. In practice, the amplitude of the buoy motion has to be limited to protect the mechanical structure, and the displacement limit of this WEC is set as 0.8 times the radius of the buoy. In addition, WECs have to be stopped from operating at severe sea states. Thus, there must be a maximum operational wave height for protection. A similar prototype to the WEC in this work is WaveStar, which is a semi-spherical heaving point absorber [23]. The maximum operational wave height of WaveStar is 6 m and the diameter of WaveStar is 5 m. Therefore, the maximum operational wave height for the original WEC in this case is estimated as $H_s = 5$ m, in a conservative way.
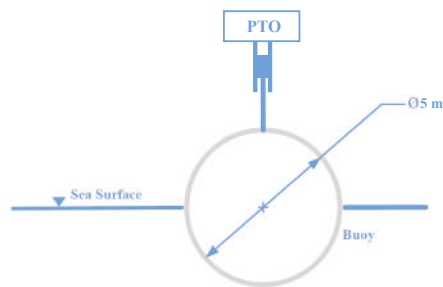
Figure 1. Schematic of the heaving point absorber concept.

Three realistic sea sites are selected to investigate the techno-economic performance of WECs. They are Yeu Island, in the oceanic territory of France, Biscay Marine Energy Park (BIMEP) in Spain, and DK North Sea Point 2 (DK2) in Denmark. The scatter diagrams of these sea sites are taken from Reference [8], which are shown in Tables 1–3. In these scatter diagrams, H_s and T_z represent the significant wave height and the mean zero-crossing wave period, respectively, and the time of the corresponding occurrence are depicted in each cell as the number of occurrence hours in a year for that particular sea state. It should be pointed out that Yeu, BIMEP, and DK2 are geographically far from each other and their most frequent wave heights and periods differ significantly. Hence, these three sea sites are chosen to be the representatives of European wave characteristics.

Table 1. Scatter diagram showing yearly hours of occurrence of sea states in the Yeu Island (Yeu), France.

Hours T_z (s) H_s (m)	2.14	2.86	3.57	4.29	5.00	5.71	6.43	7.14	7.89	8.57	9.29	10.00	10.71	11.43	12.14
0.50	1.27	55.70	79.75	67.09	64.56	62.03	37.98	12.66	1.27						
1.00		56.97	219.00	268.37	337.99	369.64	244.32	135.45	62.03	3.80	1.27	1.27			
1.50		1.27	36.71	163.30	278.50	281.03	215.20	145.58	124.06	86.08	17.72	3.80	2.53		
2.00				69.62	225.33	235.46	175.98	146.84	64.56	62.03	22.79	11.39	6.33		
2.50				81.02	345.59	324.07	272.17	106.34	72.16	43.04	11.39	2.53			
3.00				15.19	281.03	340.53	250.66	112.66	87.35	58.23	31.66	10.13			
3.50					69.62	293.69	192.42	118.99	65.83	51.90	36.71	22.79	7.60	1.27	
4.00					3.80	110.13	127.86	65.83	49.37	27.85	27.85	22.79	15.19	3.80	
4.50						26.58	43.04	60.76	21.52	12.66	6.33	5.06		1.27	
5.00						2.53	20.25	34.18	15.19	7.60	1.27				
5.50							7.60	24.05	12.66	6.33					
6.00							3.80	13.92	8.86		1.27				
6.50								2.53	7.60	1.27					

Table 2. Scatter diagram showing yearly hours of occurrence of sea states in Biscay Marine Energy Park (BIMEP), Spain.

Hours T_z (s) H_s (m)	5.00	7.00	9.00	11.00	13.00	15.00	17.00
0.75	148.92	219.00	78.84	17.52			
1.50	858.48	2664.52	1445.40	508.08	78.84	8.76	
2.50		744.60	560.64	324.12	157.68	35.04	
3.50		87.60	262.80	61.32	52.56	35.04	8.76
4.50			105.12	35.04	8.76	8.76	8.76
5.50			8.76	26.28			

Table 3. Scatter diagram showing yearly hours of occurrence of sea states in DK North Sea Point 2 (DK2), Denmark.

Hours T_z (s) H_s (m)	2.50	3.50	4.50	5.50	6.50	7.50	8.50	9.50
0.25	584.00	634.00	113.00	29.00	7.00	1.00		
0.75	20.00	1552.00	610.00	153.00	56.00	16.00	6.00	2.00
1.25		188.00	1397.00	123.00	25.00	9.00	7.00	3.00
1.75		1.00	621.00	501.00	8.00	2.00	1.00	1.00
2.25			14.00	709.00	18.00	1.00		
2.75				286.00	224.00	1.00		
3.25				10.00	314.00	2.00		
3.75					190.00	34.00		
4.25					17.00	121.00		
4.75						77.00	1.00	
5.25						26.00	11.00	
5.75						2.00	16.00	
6.25							10.00	
6.75							4.00	1.00
7.25								1.00

2.2. Frequency Domain Modeling

In this subsection, the frequency domain model of WECs is presented based on linear wave theory. As the device in this paper is assumed to oscillate only in heave motion, the frequency domain modeling of the WEC is only discussed for the heaving degree of freedom. According to Newton's law, the motion of the WEC as a rigid body can be described through Equation (1).

$$ma(t) = F_{hs}(t) + F_e(t) + F_{pto}(t) + F_r(t), \tag{1}$$

where textitm is the mass of the oscillating body, F_{hs} is the hydrostatic force, F_e is the wave excitation force, F_r is the wave radiation force, F_{pto} is the PTO force, and $a(t)$ is the acceleration. If the body is assumed to perform harmonic motion and a linear PTO model is used to simulate the behavior of the PTO system, (1) could be rewritten in the form of complex amplitudes [10], as

$$\hat{F}_e(\omega) = [R_i(\omega) + R_{pto}]\hat{u} + i\omega\hat{u}[m + M_r(\omega)] + i\hat{u}[-\frac{K_{pto}}{\omega} - \frac{S_{wl}}{\omega}], \tag{2}$$

where $R_i(\omega)$ is the hydrodynamic damping coefficient, R_{pto} is the PTO damping coefficient, ω is the wave frequency, m and $M_r(\omega)$ are the mass and the added mass of the WEC, $\hat{u}$ is complex amplitude of the vertical velocity, K_{pto} is the PTO stiffness coefficient, and S_{wl} is the hydrostatic stiffness. The intrinsic impedance of the heaving buoy and PTO impedance can be introduced as

$$Z_i(\omega) = R_i(\omega) + iX_i(\omega), \tag{3}$$

$$X_i(\omega) = \omega[m + M_r(\omega)] - \frac{S_{wl}}{\omega}, \tag{4}$$

where $Z_i(\omega)$ is the intrinsic impedance of the heaving buoy, and $X_i(\omega)$ is the intrinsic reactance. Similarly, the impedance of PTO can be given as:

$$Z_{pto}(\omega) = R_{pto}(\omega) + iX_{pto}(\omega), \tag{5}$$

$$X_{pto}(\omega) = -\frac{K_{pto}}{\omega}, \tag{6}$$

where $Z_{pto}(\omega)$ is the PTO impendence, and $X_{pto}(\omega)$ is the PTO reactance. So, (2) is rewritten as

$$\hat{F}_e(\omega) = [Z_i(\omega) + Z_{pto}(\omega)]\hat{u}. \tag{7}$$

The hydrodynamic characteristics of WECs, including $M_r(\omega)$, $R_i(\omega)$, and $F_e(\omega)$, are calculated using the Boundary Element Method through the open source software Nemoh [24]. Then, by solving (7), the complex amplitude of velocity $\hat{u}$ could be obtained as

$$\hat{u} = \frac{\hat{F}_e}{Z_i + Z_{pto}}. \tag{8}$$

Then, the complex amplitude of the motion displacement is expressed as

$$\hat{z} = \frac{\hat{F}_e}{i\omega(Z_i + Z_{pto})}. \tag{9}$$

For regular wave conditions, the time averaged absorbed power can be obtained and expressed as

$$P_{ave\_re} = \frac{1}{2}R_{pto}|\hat{u}|^2. \tag{10}$$

The above analysis is based on the assumption of harmonic motion, but incoming waves in real sea states are always irregular. In this work, the calculation of power absorption in irregular waves is conducted based on the superposition of regular waves [25]. So, the power absorption in each sea state is calculated by integrating over frequency the product of the spectrum density with the power absorption in regular waves which can be expressed as

$$P_{ave\_irr} = \int_0^\infty R_{pto}\left(\frac{|\hat{z}|}{\zeta_a}, \omega\right)^2 S_{\zeta_a}(\omega)\mathrm{d}\omega, \tag{11}$$

where ζ_a is the wave amplitude of the regular wave components, and $S_{\zeta_a}(\omega)$ is the spectral density of the defined unidirectional wave spectrum. In this work, JONSWAP spectrum, together with the peakedness factor of 3.3, is used to represent the irregular waves for the North Sea [26].

It must be acknowledged that frequency domain modeling has limited applicability. Firstly, it is restricted to the linear theory. The accuracy of this approach around the resonance of WECs is limited where the motion amplitude is too high and the linear assumption is violated [27]. However, the displacement limit is considered in this paper, which could ease this problem [11]. Secondly, frequency domain modeling does not allow the implementation of real-time control strategies by which PTO parameters can be adjusted instantaneously with the PTO force saturation and buoy displacement constraints [19,28]. Although there are limitations in frequency domain modeling, it is considered reasonable given the purpose of this paper to get insight into the influence of sizing on the techno-economic performance. Frequency domain models are more computationally efficient compared to time domain approaches, which makes it highly suitable in the optimization studies that requires a large number of iterations. In addition, the energy production of WECs in different buoy and PTO sizes is calculated based on the same frequency domain model, which is fair for the size determination and techno-economic analysis.

2.3. Size Optimization Method

A proposed size optimization method for improving the techno-economic performance of WECs is presented in the following part, and the methods to conduct PTO sizing and buoy sizing are explained, respectively. An economic model is established to calculate the corresponding costs. The flowchart of this size optimization method is shown in the Figure 2. The cost function for the size optimization adopted in this paper is LCOE, which is introduced in more detail in Section 2.3.3. An exhaustive search algorithm is used in the optimization. The buoy scale factor λ and a normalized factor for PTO sizing, namely

PTO sizing ratio, are treated as the optimization variables. Before defining the PTO sizing ratio, it is necessary to introduce the unconstrained PTO force and the maximum required PTO force. The unconstrained PTO force is defined based on the sea state, and it represents the PTO forces required to maximize the power absorption without any force constraint for the particular sea state. The maximum required PTO force is defined based on the sea site and is the largest value of unconstrained PTO forces for all operational sea states in a particular sea site. This largest value occurs at the operational sea state with largest wave power density. Then, the PTO sizing ratio is equal to the PTO force limit divided by the maximum required PTO force at the corresponding sea site, and the PTO force limit is the force constraint for the PTO system with the particular size. The maximum required PTO force varies with the wave resource, the buoy size, and the control strategy. So, in each case, the maximum required PTO force is recalculated for each sea site and buoy scale factor λ. The initial bounds of the buoy scale factor λ and PTO sizing ratio are set as 0.3,2.0 and 0.1,1.0, respectively. If the the optimal solution is not found within these ranges during iterations, the bounds would be automatically extended until a solution is obtained. A discrete iteration step of 0.1 is used in the exhaustive searching algorithm for both buoy scale factors λ and PTO sizing ratios. The proposed size optimization method is also compatible with other optimization algorithms, which may provide more precise solutions or save computational costs. However, it is beyond the scope of this paper to discuss the relative impacts of optimization algorithms in detail.
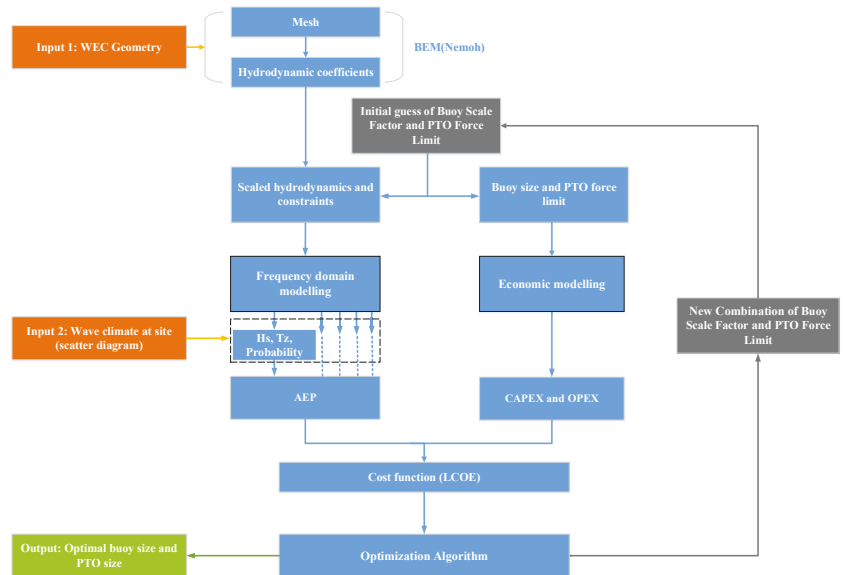
Figure 2. Flowchart of the size optimization method of Wave Energy Converters (WECs).

2.3.1. PTO Sizing

Here, the PTO sizing implies the implementation of determining the optimal PTO size for different sea sites. The PTO size is directly related to the rated power, PTO force limits, displacement limits, and PTO peak power constraints of WECs [29]. In this work, the PTO force limit is used to represent the PTO size. According to (5) and (8), the PTO force amplitude can be expressed as

$$\left|\hat{F}_{pto}\right| = \left|\hat{u}Z_{pto}\right| = \frac{\left|Z_{pto}\right|}{\left|Z_i + Z_{pto}\right|}\left|\hat{F}_e\right| = \left|\hat{F}_e\right|\frac{\sqrt{R_{pto}^2 + X_{pto}^2}}{\sqrt{(R_{pto} + R_i)^2 + (X_i + X_{pto})^2}}. \tag{12}$$

As is shown in (12), the PTO force amplitude is a function of R_{pto} and X_{pto}. Therefore, one approach to restrict the PTO force amplitude is to adjust PTO parameters. Reactive control and passive control are typical control strategies in WECs. In the reactive control, both the PTO reactance and the PTO damping coefficient could be varied to tune the device. However, in the passive control, only the PTO resistance load (damping force) is provided. Next, the methods to determine the PTO parameters for limiting the PTO force amplitude in the passive control strategy and the reactive control strategy are explained, respectively.

- The determination of PTO parameters in passive control:
  Here, the PTO force amplitude is constrained by means of adjusting the PTO parameters. Besides, the PTO parameters are also expected to be determined to limit the stroke and maximize the absorbed power.
  First, let us discuss the PTO force constraints. In the passive control strategy, only PTO damping can be varied and the PTO reactance equals zero. Therefore, the PTO force amplitude expressed in (12) can be simplified as

$$\left|\hat{F}_{pto}\right| = \left|\hat{F}_e\right| \frac{R_{pto}}{\sqrt{(R_{pto} + R_i)^2 + X_i^2}}. \tag{13}$$

To reveal the relationship between $\left|\hat{F}_{pto}\right|$ and R_{pto}, the derivation of (13) with respect to R_{pto} is calculated and gives

$$\frac{d(\left|\hat{F}_{pto}\right|)}{dR_{pto}} = \left|\hat{F}_e\right| \frac{R_{pto}R_i + X_i^2 + R_{pto}^2}{\left[(R_{pto} + R_i)^2 + X_i^2\right]^{\frac{3}{2}}}. \tag{14}$$

It can be deduced that (14) is always positive as R_{pto} and R_i are greater than 0, which also implies that $\left|\hat{F}_{pto}\right|$ is a monotonic function of R_{pto}. In other words, limiting the PTO damping can directly constrain the PTO force amplitude. During size optimization, the PTO sizing ratio and buoy scale factor λ are used as optimization variables. However, to determine PTO parameters with the force limit, the PTO force limit should be derived to be explicit. According to the definition of the PTO sizing ratio, the PTO force limit can be calculated by multiplying the given PTO sizing ratio with the maximum required PTO force for the particular buoy scale factor and considered sea site. Therefore, the PTO force limit is directly related to each set of optimization variables. Here, the PTO force limit is represented by F_{pto_limit}, and the maximum allowed PTO damping R_{pto_force} can be obtained by solving (15), in which only the positive solution should be retained.

$$\left|\hat{F}_e\right| \frac{R_{pto\_force}}{\sqrt{(R_{pto\_force} + R_i)^2 + X_i^2}} = F_{pto\_limit}. \tag{15}$$

Therefore, for constraining the PTO force amplitude, R_{pto} should satisfy

$$R_{pto} \le R_{pto\_force}. \tag{16}$$

Secondly, except PTO force constraints, the displacement limit should be considered during the selection of PTO parameters. It can be deduced from (8) that the $\hat{u}$ decreases with R_{pto} increasing. If the stroke constraint of the buoy, S_m, comes to play, the PTO resistance should be increased to limit the velocity amplitude, which is shown as

$$\left|\hat{u}\right| = \frac{\left|\hat{F}_e\right|}{\left|R_{pto} + Z_i\right|} \le \left|u_m\right|. \tag{17}$$

In this way, for constraining the stroke amplitude, R_{pto} should satisfy

$$R_{pto} \geq \sqrt{(\frac{\hat{F}_e}{u_m})^2 - X_i^2)} - R_i = R_{pto\_stroke}, \tag{18}$$

where u_m is the velocity limit, which is equal to ωS_m. Therefore, it can be seen from (16) and (18) that the upper bound and the lower bound of the available PTO damping are decided by the PTO force limit and the stoke limit, respectively, which could also be expressed as

$$R_{pto\_stroke} \leq R_{pto} \leq R_{pto\_force}. \tag{19}$$

Thus, the PTO damping should be selected from the range expressed in (19) to satisfy the constraints.

According to Reference [28], the optimal PTO damping for maximizing the absorbed power without any constraint is expressed as

$$R_{pto\_opt} = |Z_i| = \sqrt{R_i^2 + X_i^2}. \tag{20}$$

To maximize the absorbed power of WECs, R_{pto} should be as close to R_{pto_opt} as possible. So, the principle of PTO damping selection in PTO sizing can be presented as:

- If $R_{pto\_stroke} \leq R_{pto\_opt} \leq R_{pto\_force}$, the optimal R_{pto} should be selected as R_{pto_opt}.
- If $R_{pto\_opt} < R_{pto\_stroke}$ or $R_{pto\_opt} > R_{pto\_force}$, the optimal R_{pto} should be selected as the one of R_{pto_stroke} and R_{pto_force} which is closer to R_{pto_opt}.
- In case $R_{pto\_force} < R_{pto\_stroke}$, there is no feasible PTO damping coefficient satisfying both of the constraints. This case would happen when the PTO force limit is very low or the wave power is very high, which realistically means the device has to be stopped from operation for protecting itself from frequently violating the physical constraints.

- The determination of PTO parameters in reactive control:
  Unlike PTO sizing in passive control, both R_{pto} and X_{pto} can be varied to meet the requirement of motion and PTO force constraints. Given the complexity of the multivariable optimization with nonlinear constraints, a numerical optimization tool is used to select the optimal combination of R_{pto} and X_{pto}, and it can be expressed in the form as

$$maximize f = P_{absorbed}(R_{pto}, X_{pto})$$

$$subject\ to \begin{cases} |\hat{F}_{pto}(R_{pto}, X_{pto})| \leq F_{pto\_limit} \\ |\hat{u}(R_{pto}, X_{pto})| \leq u_m \\ R_{pto} \geq 0 \\ X_{pto} \in \mathbb{R}. \end{cases} \tag{21}$$

The optimization is performed based on the "interior point" algorithm in MATLAB environment, and the tolerance of the function is set as 1e-4. To avoid the local optimal solution, the 'MultiStart' solver is adopted. In this solver, iterations start with multiple random points, in which the global optimal solution is expected to be found [30]. In this work, the number of multiple starting points is set as 20, and the bounds of the PTO damping and PTO reactance are set as [0,10 $R_i(\omega)$] and [-10$X_i(\omega)$, 10$X_i(\omega)$] for each sea state. In case that no feasible solution is found in the optimization, the PTO absorbed power would be treated as 0.

Based on the above method, PTO parameters for different PTO force constraints can be obtained for each wave condition. Then, the corresponding power performance of WECs can be calculated. Hence, this method takes into account the effects of PTO sizing on the power performance of WECs. However, it has to be clarified that the above PTO

sizing method is established based on regular wave conditions. To constrain the buoy displacement and PTO force in irregular wave conditions, it is necessary to calculate their instantaneous solutions, in which time domain modeling is required. However, the inefficiency of time domain simulation would make the iteration process much more time consuming, which is not preferable for the optimization problem. To simplify this problem, in this paper PTO parameters are selected only to suit the typical characteristics of irregular wave conditions, referring to Reference [18]. According to Reference [10], the time-averaged power transport per unit length of wave front of incoming waves at regular wave conditions and irregular wave conditions can be calculated as

$$P_{wave\_re} = \frac{1}{32\pi}\rho g^2 H^2 T,$$ (22)

$$P_{wave\_irr} = \frac{1}{64\pi}\rho g^2 H_s^2 T_e.$$ (23)

By equaling (22) to (23) at the case of the same energy period, namely T equaling T_e, the corresponding wave height in regular wave condition is solved as $H_s/\sqrt{2}$. To transfer the T_z in scatter diagrams to T_e, the wave period ratio between T_e and T_z is selected as 1.18 given the JONSWAP spectrum and the peakedness factor of 3.3 [31]. Then, PTO parameters for irregular wave conditions can be selected to suit regular wave conditions whose period and height correspond to T_e and $H_s/\sqrt{2}$, respectively [18]. The purpose of the transfer between irregular wave conditions and regular wave conditions is to simplify the determination of PTO parameters for PTO sizing. However, the selected PTO parameters based on regular wave condition cannot strictly guarantee that the PTO force and stroke constraints would not be violated at the corresponding irregular wave conditions. Considering the purpose of this paper to investigate the impacts of sizing on the techno-economic performance, it is considered to be acceptable. In this paper, all the power absorption of WECs are calculated based on irregular wave conditions, and the PTO parameters are optimized for each sea state. As an example, the optimized PTO parameters of WEC in the original buoy size for different sea states are shown in Figures 3 and 4.
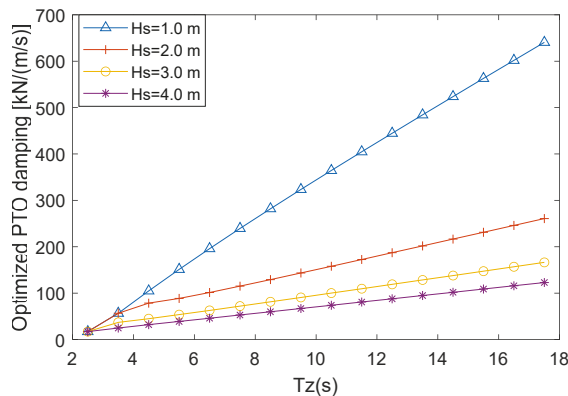
Figure 3. Optimized Power Take-Off (PTO) damping of the WEC with passive control for various sea states ($\lambda = 1$ and PTO force limit = 50 kN).

(**a**) PTO damping   (**b**) PTO reactance
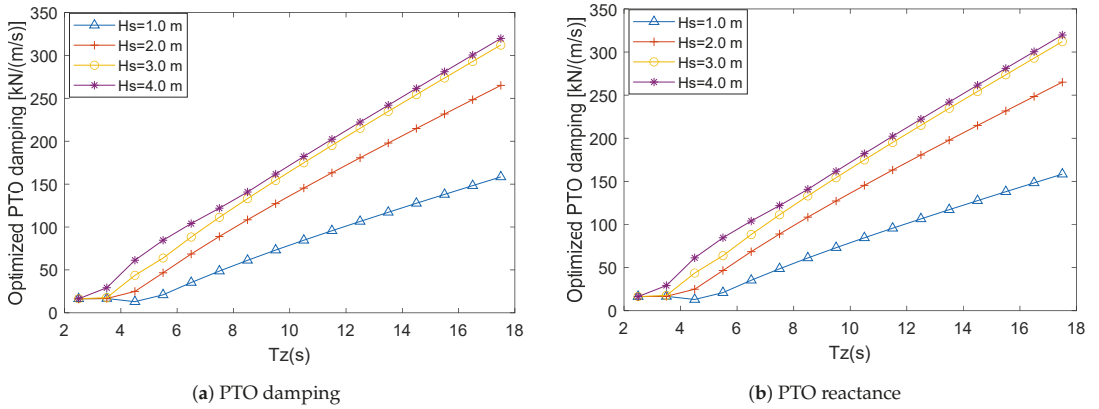
Figure 4. Optimized PTO parameters of the WEC with reactive control for various sea states ($\lambda = 1$ and PTO force limit = 250 kN).

Therefore, as the PTO parameters are determined, the absorbed power of WECs at each sea state can be obtained and the AEP (Annual Energy Production) at the specific sea site is calculated as

$$AEP = A \cdot \eta \cdot \sum_{x=1}^{x=n} P_{absorbed}(x) \cdot T(x), \qquad (24)$$

where η is the overall conversion efficiency from the annual absorbed energy to the AEP and is assumed 70% [32]; A is the availability of WECs to work, and it is set as 90% due to the necessary operation and maintenance [23]; T represents the total hours of the appearance of a certain sea state, which is presented in the scatter diagram in Tables 1–3; x represents the sea state in scatter diagrams.

2.3.2. Buoy Sizing

During the iterations of the size optimization, the buoy size of WECs are scaled following geometrical similarity. Therefore, the hydrodynamic coefficients of buoys in different sizes can be obtained by means of Froude scaling law [33],

$$
\begin{aligned}
\lambda &= \frac{L_s}{L_o} = \frac{H_s}{H_o} \\
\omega_s &= \omega_o \lambda^{-0.5} \\
F_{e\_s} &= F_{e\_o} \lambda^3, \\
B_{r\_s} &= B_{r\_o} \lambda^{2.5} \\
M_{r\_s} &= M_{r\_o} \lambda^3
\end{aligned}
\qquad (25)
$$

where λ is the buoy scale factor; L is the geometrical length of the buoy; ω is the wave frequency; F_e, B_r, and M_r are the excitation force, the radiation damping, and the added mass coefficients, respectively; and the subscript s and o represent the "scaled device" and the "original device", respectively. Hence, this allows the hydrodynamic coefficients of the original buoy to be transferred to the scaled buoy instead of using BEM method to calculate the hydrodynamic coefficients in each iteration. In this way, the computing efficiency can be significantly improved. The density of the buoy structure in different sizes are assumed to be same. The maximum operation wave height and the displacement limit of WECs are scaled with the buoy scale factor λ.

2.3.3. Economic Modeling for Cost Estimation

LCOE is an important techno-economic metric of WECs. For evaluating the LCOE, it is essential to establish an economic model to estimate the CAPEX and OPEX of WECs.

Following Reference [34], the steel price is selected as 1.6 GBP (British Pounds)/kg and the structure cost is calculated by assuming that all the structure cost comes from the steel cost. Based on the inflation calculator tool [35], the cumulative inflation rate of GBP from 2017 to 2020 is 5.89% and the exchange rate of Euros to GBP is set as 0.87. Referring to Reference [34], the statistical percentages of CAPEX-related components in total LCOE can be found. The percentage values are recalculated as the average percentage in total CAPEX, shown in Table 4. According to Table 4, the cost of "Foundation and Mooring" and "Installation" accounts for 19.1% and 10.2% averagely of CAPEX, respectively. Comparatively, the cost of the structure accounts for 38.2% of CAPEX in average. Therefore, mass-related capital cost can be calculated as

$$C_{Mass} = C_S + C_F + C_I = (\frac{P_{F\&M}}{P_S} + \frac{P_I}{P_S} + 1)C_S, \tag{26}$$

where C_{Mass} represents the Mass-related-capital-cost; C_S, C_F, and C_I are the cost of the structure, foundation, and the installation, respectively, and P_s, $P_{F\&M}$, and P_I are their corresponding percentages in the total LCOE . It can be seen from Table 4 that the cost of "Connection" and "PTO" averagely accounts for 8.3% and 24.2% of CAPEX, respectively. Similarly, power-related capital cost can be calculated as

$$C_{Power} = C_P + C_C = (\frac{P_C}{P_P} + 1)C_{PTO}, \tag{27}$$

where C_{Power} represents the power-related capital cost; C_P and C_C are the cost of the PTO and the connection, respectively; and P_P and P_C are their corresponding percentages in the total LCOE. Therefore, the CAPEX is calculated as

$$CAPEX = C_{Mass} + C_{Power}. \tag{28}$$

Table 4. Percentages of Capital Expenditure (CAPEX)-related components of WECs in total CAPEX.

CAPEX	Categories	Average Percentage
Mass-related capital cost	Structure Foundation and mooring Installation	P_S = 38.2% $P_{F\&M}$ = 19.1% P_I = 10.2%
Power-related capital cost	PTO component Connection	P_P = 24.2% P_C = 8.3%

In this paper, PTO is assumed to be a direct drive generator and all PTO costs come from the generator. The generator cost is divided into the cost of active material and the cost of manufacturing. The amount of active material required is approximately related to the PTO force limit and the force density of generators. Referring to Reference [36], the maximum force density in this work is assumed as 44 kN/m^2, which generally ranges from 30 to 60 kN/m^2 depending on the design. The cost of active material of this generator in series production is estimated as 12,000 Euros/m^2 based on the currency value in 2006. The cumulative inflation rate from 2006 to 2020 is 22.1% [35]. Taking the inflation into account, the active material of this generator in this paper is estimated as 14,655.31 Euros/m^2. Regarding the manufacturing cost, it is approximately assumed as half of the total cost of the generator [37]. So, the cost of PTO can be expressed as

$$C_{PTO} = Cost_{Material} + Cost_{Manufacturing}. \tag{29}$$

In this paper, the annual OPEX is assumed as 8% of the CAPEX, and the discount rate *r* is assumed as 8% with the lifespan of 20 years, referring to Reference [8]. Then, the LCOE of WECs is calculated as

$$LCOE = \frac{CAPEX + \sum_{t=1}^{n} \frac{OPEX_t}{(1+r)^t}}{\sum_{t=1}^{n} \frac{AEP_t}{(1+r)^t}}, \tag{30}$$

where *n* represents the total years of the lifespan, and *t* represents the evaluated year.

It has to be clarified that it is a preliminary economic model, and the parameters in the model differ from one to another project in practice. For instance, reactive control is associated with negative power flow, which could lead to larger losses and related wear. Therefore, control strategies in practice is able to affect the OPEX and conversion efficiency. However, the specific effects are related to the PTO design and maintenance strategy, which is outside the scope of this paper. Given the purpose of this paper to identify the influence of sizing on the techno-economic performance, the assumption on the constant OPEX percentage and conversion efficiency for both control strategies is considered reasonable. Furthermore, survivability of WECs in practice is complex and related to many affecting factors. For instance, the increase of the buoy size results in the larger exerted force and input power flow, which could make the WEC more vulnerable. However, it is also dependent on the mooring design, material and even control strategies of WECs. For simplicity, the lifespan for WECs in all sizes is assumed to be constant. Nevertheless, our aim based on the economic analysis is not to give a final judgement of the optimal size of the WEC but to use the LCOE as an indication for providing an insight about the effects of sizing on the techno-economic performance. Overall, the proposed size optimization method has pure theoretical characteristics, and a more complex size optimization study is required in practical applications.

3. Results and Discussion

This section starts with the discussion about the effects of buoy sizing and PTO sizing on the performance of the WEC. Next, the size optimization results for the sea sites are presented. The interaction between PTO sizing and buoy sizing and the benefits of downsizing PTO size for decreasing LCOE are analyzed. Finally, a comparison between this proposed method and other existing methods for size optimization is performed.

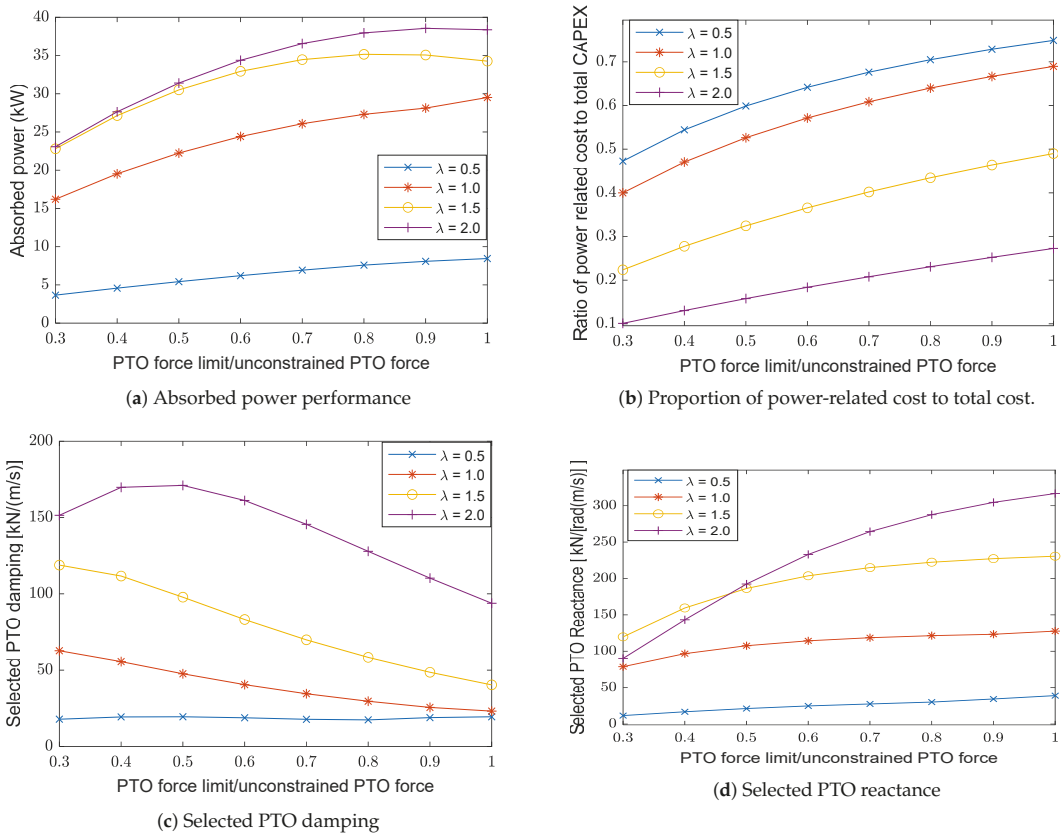### 3.1. The Effects of Sizing on the Performance of the Wec

Taking one single sea state ($H_s = 1.5$ m, $T_z = 5$ s) as an example, the effects of PTO sizing and buoy sizing on the performance of the WEC are investigated. In Figures 5 and 6, the effects on the absorbed power, economic performance and PTO parameters of the WEC with passive control and reactive control are presented, respectively. The horizontal axis in Figures 5 and 6 is expressed as "PTO force limit/unconstrained PTO force". Here, the unconstrained PTO force corresponds to the PTO force required to maximize the power absorption for the considered sea state ($H_s = 1.5$ m, $T_z = 5$ s). The PTO parameters corresponding to each PTO size and buoy size were calculated following the method described in Section 2.3.1. From Figures 5 and 6, it is noted that both the power performance and the economic performance are highly related to the sizing of the WEC. In Figures 5a and 6a, it can be seen that the absorbed power of the WEC increases with the PTO size and the buoy size. In Figures 5b and 6b, the proportion of the power-related capital cost to the total CAPEX increases with the PTO size, but it decreases with the rise of the buoy scale factor λ. Therefore, at a certain PTO sizing ratio, the CAPEX would be more dominated by the mass-related capital cost than power-related capital cost with the increase of the buoy scale factor λ. Comparing Figures 5 and 6, it can be found that the effects of sizing on the WEC are also related to the control strategy. Firstly, the absorbed power of the WEC with reactive control is significantly higher than that in passive control. Secondly, the proportion of power-related capital cost to the total CAPEX in the WEC with reactive

control is much higher than that with passive control. This phenomenon can be explained by that the reactive control strategy is associated with higher PTO force limits than the passive control strategy. The higher PTO force then leads to the increase of the proportion. Thirdly, the trends of PTO parameters changing with the force limit depend on the control strategy. In Figure 5c, the PTO damping coefficient increases with the ratio "PTO force limit/unconstrained PTO force" when the passive control strategy is used. This is logical as the PTO force monotonically increases with the PTO damping, which has been explained in (14). Comparatively, it can be seen from Figure 6c,d, with the increase of "PTO force limit/unconstrained PTO force", the PTO damping coefficient tends to decrease, while the PTO reactance increases. The reason is that the PTO in reactive control would act more like a pure damper to reduce its required force, when the force constraint becomes tighter.

(**a**) PTO absorbed power

(**b**) Proportion of power-related cost to total cost

(**c**) Selected PTO damping
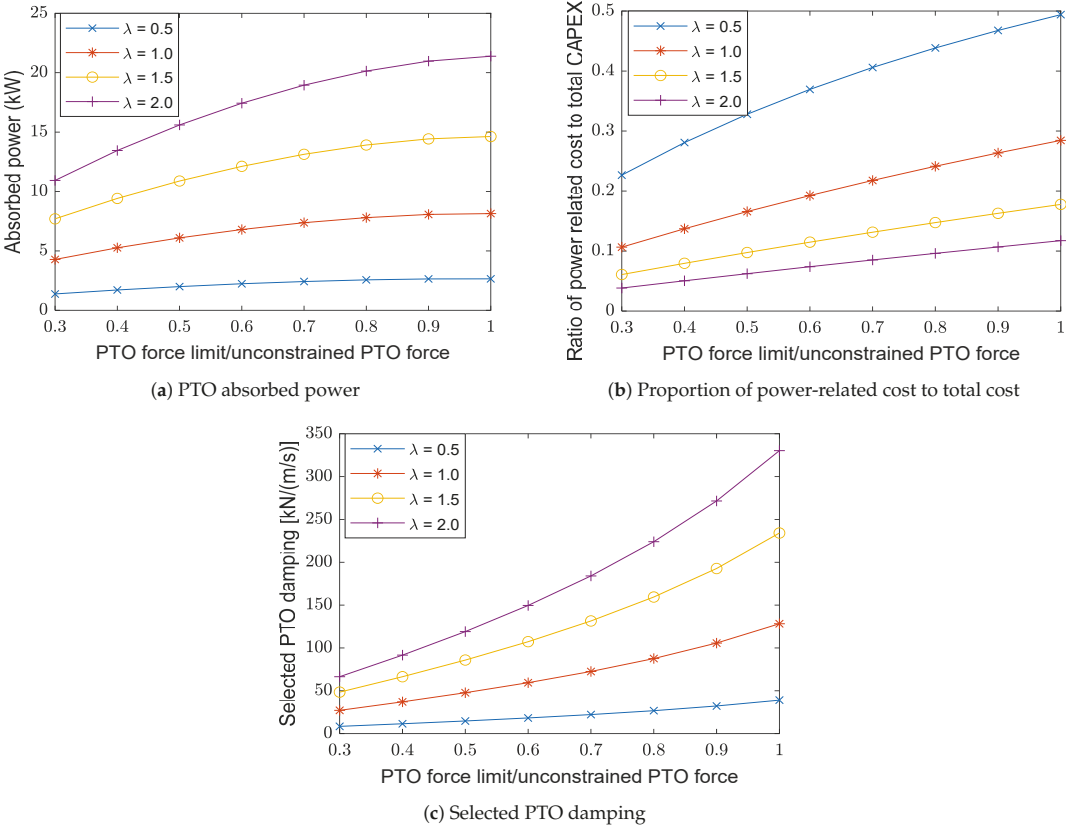
Figure 5. Performance of the WEC with passive control under different PTO sizes and buoy scale factor λ, at $H_s = 1.5$ m and $T_z = 5$ s.

(**a**) Absorbed power performance

(**b**) Proportion of power-related cost to total cost.

(**c**) Selected PTO damping

(**d**) Selected PTO reactance

Figure 6. Performance of the WEC with reactive control under different PTO sizes and buoy scale factor λ, at $H_s = 1.5$ m and $T_z = 5$ s.

3.2. Size Optimization for Typical Realistic Sea Sites

3.2.1. Results of Size Optimization

Based on the proposed method, the size optimization of the WEC for three sea sites is performed. First, to define the PTO sizing ratio, it is necessary to obtain the maximum required PTO forces corresponding to each buoy size. They are calculated by (12), and the results are shown in Figure 7. Figure 7a shows the relation of unconstrained PTO forces of the WEC in original buoy size to sea states, and the maximum required PTO forces for different sea sites are picked. It can be found from Figure 7b that the maximum required PTO force increases dramatically with the increase of the buoy size. In addition, the maximum required PTO forces in the WEC with reactive control are much higher than those with passive control. This is to be expected as PTO forces in reactive control consist of PTO damping-induced forces and PTO reactance-induced forces, while there are only PTO damping-induced forces in the case of passive control.
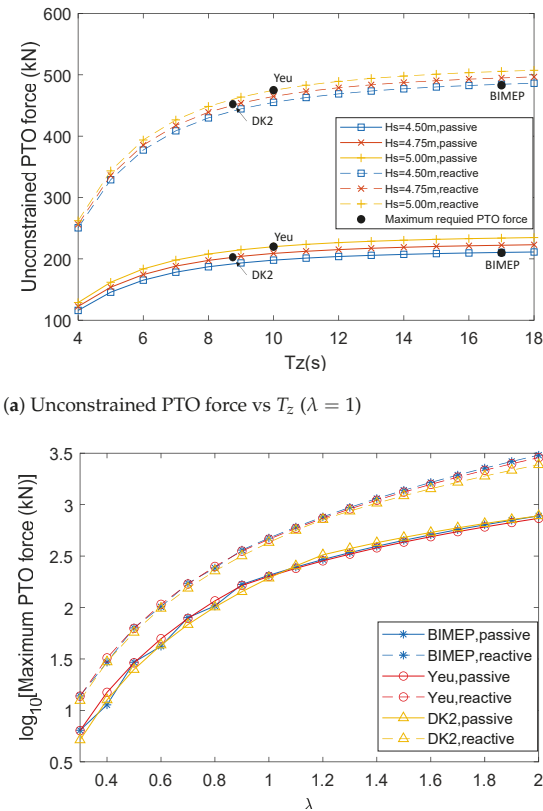
(**a**) Unconstrained PTO force vs T_z ($\lambda = 1$)

(**b**) Maximum required PTO force vs buoy scale factor λ

Figure 7. Maximum required PTO forces for various sea sites and buoy scale scale factor λ.

The size optimization results of the WEC using passive and reactive control for the three sea sites are depicted in Figures 8 and 9, respectively. It can be clearly seen from these figures that both the LCOE and the AEP can be significantly influenced by sizing of the WEC, no matter in which sea site or with what kind of control strategies. Therefore, for improving the viability of the WEC, it is highly suggested to conduct size optimization of the WEC for the considered wave resources. Next, it can be noted that upscaling buoy size is able to improve the AEP, while it cannot necessarily reduce the LCOE of the WEC. Similarly, the AEP is highly sensitive to the PTO sizing ratio, and the increase of the PTO size can make a significant contribution to the improvement of the AEP. However, from the techno-economic point of view, enlarging PTO size does not necessarily result in a lower LCOE. In this case, it can be noted that downsizing the PTO size to a suitable level is beneficial for reducing the LCOE. Hence, to improve the techno-economic performance, it is significant to conduct PTO sizing for compromising the AEP and the cost.
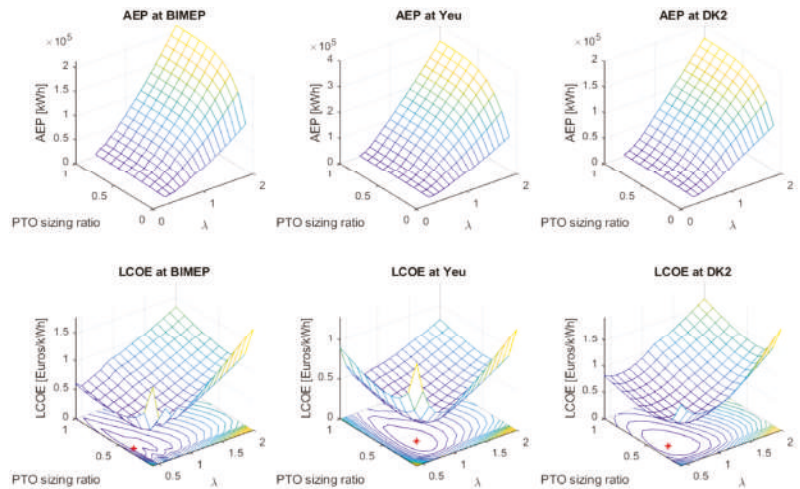
Figure 8. Size optimization of the WEC with passive control.
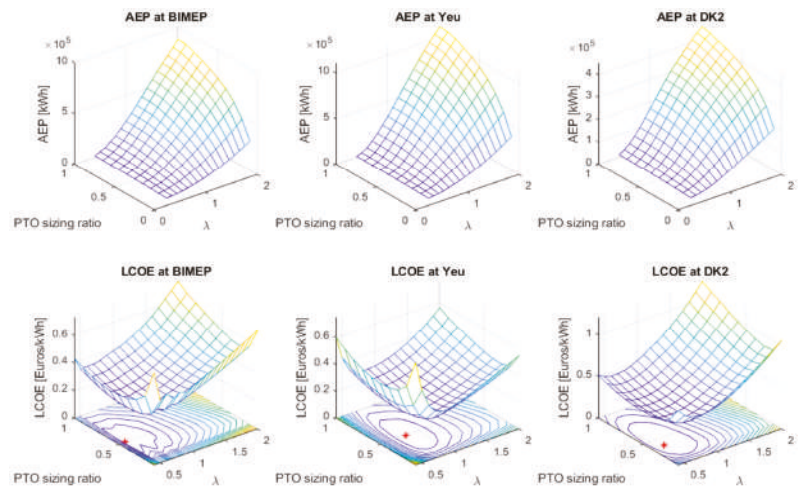
Figure 9. Size optimization of the WEC with reactive control.

In Figure 10, the dependence of size optimization of the WEC on wave resources and control strategies is shown. From Figure 10a,d, it can be found that there is not a direct relationship between the buoy size determination and the mean wave power density of wave resources. In other words, the optimal buoy size cannot be indicated by the mean wave power density. For instance, the mean wave power density in BIMEP is almost twice as much as that in DK2, but DK2 corresponds to a higher optimal buoy scale factor λ. As is seen in Figure 10a, control strategies do not have a notable influence on the buoy size determination for a given sea site. The reason is that the trends of the AEP changing with the buoy scale factor λ are comparable in both cases of reactive and passive control. Though control strategies lead to an notable difference in the absolute values of the

AEP. Regarding PTO sizing, it can be found from Figure 10b that the optimal PTO sizing ratios in the WEC with the reactive control are slightly higher than those with passive control in BIMEP and Yeu. The only exception occurs in DK2 where the reactive and the passive control are associated with the same optimal PTO sizing ratio. In addition, it is noteworthy that the optimal PTO sizing ratio is relatively independent of wave resources, and it converges at around 0.4 to 0.5.

Different from the size determination, the optimized LCOE is highly related to wave resources and control strategies. It can be found from Figure 10c that the LCOE of the WEC with reactive control is much lower than the WEC with passive control, and the reduction can reach at 35 % in average for these sea sites. The optimized LCOE of the WEC with reactive control ranges around 0.2 to 0.35 Euros/kWh, while this value ranges around 0.35 to 0.55 Euros/kWh in the case of passive control. This is to be expected since the WEC with reactive control produces much more power than the WEC with passive control at the same sea state. From Figure 10c,d, it can be found that the higher the mean wave power density, the lower the optimal LCOE.

(**a**) Optimal buoy size

(**b**) Optimal PTO size

(**c**) Lowest LCOE

(**d**) Mean wave power density
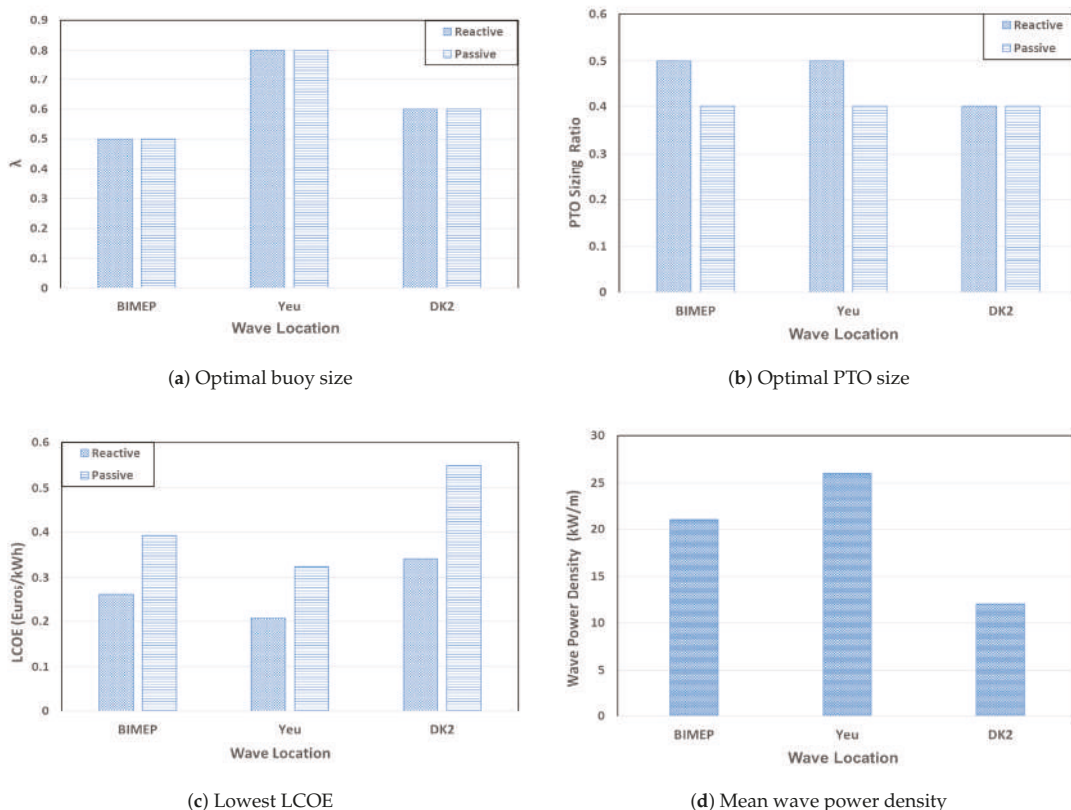
Figure 10. The dependence of size optimization on wave resources and control strategies.

After the optimal buoy and PTO size have been determined for each sea site, the optimal cost proportion of the WEC can be obtained. The proportion of the PTO cost to the total CAPEX at the optimal sizing condition is shown in Figure 11. It can be seen that this cost proportion tends to be relatively independent of wave resources, while it is highly related to the control strategy of the WEC. In this case, the PTO cost of the WEC with reactive control accounts for 45% to 50% of the total CAPEX. Comparatively, for the WEC with passive

control, this proportion decreases dramatically to around 30%. This can be explained by that the required PTO forces in the WEC with reactive control are much higher than those with passive control. It also implies that the PTO size in the WEC with reactive control should be designed larger than that with passive control. Besides, it is noticed that the optimized cost proportion of PTO is much higher than the statistic value of 24.2% depicted in Table 4. The reason is that the WECs investigated in the literature [34] are generally in large scales, and the costs of the structure are dominating. However, the optimized buoy size of the WEC in this case is relatively small, with the diameter ranging around 2.5 m to 4 m ($\lambda = 0.5 - 0.8$). As a consequence, the PTO cost is more weighted compared with the structure cost. This phenomenon has also been explained in Section 3.1 as the proportion of power-related capital cost decreases with the buoy scale factor λ.
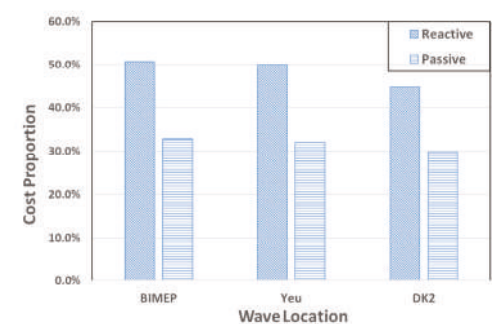
Figure 11. The proportion of cost on PTO to total CAPEX at the optimal buoy size and PTO size.

3.2.2. The Benefits of PTO Downsizing for the Techno-Economic Performance

The benefits of PTO sizing for reducing the LCOE of the WEC at the optimal buoy sizes are presented in Figure 12. It can be seen that the LCOE can be significantly reduced by downsizing the PTO size even though the buoy sizes have been optimized. In this case, downsizing the PTO sizing ratio to around 0.4 to 0.5 is preferable to minimize the LCOE. For the WEC with the passive control, downsizing the PTO size is able to reduce the LCOE by 24% to 31%, and it could reduce the LCOE by 24% to 25% in the case of reactive control. Hence, it is essential to take PTO size optimization into account when conducting sizing of the WEC. It also indicates that the techno-economic performance of WECs are generally underestimated due to the absence of PTO sizing in evaluation studies.

(**a**) The WEC with passive control　　　　　　　(**b**) The WEC with reactive control
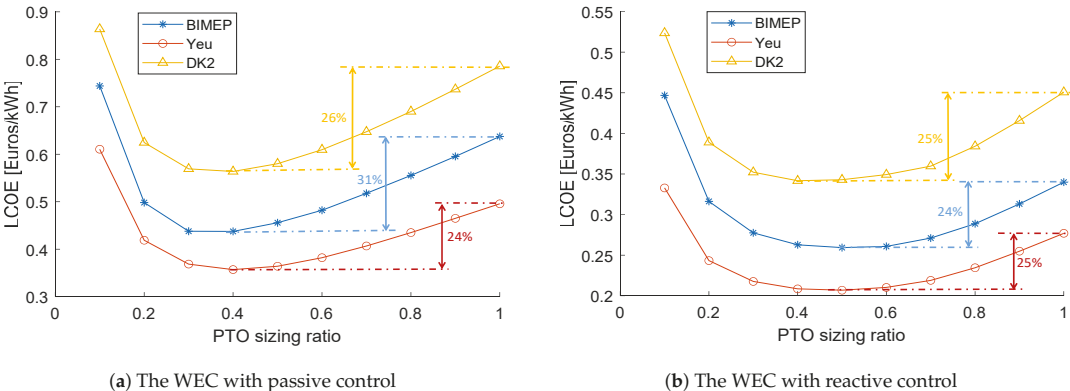
Figure 12. The effects of PTO downsizing on Levelized Cost Of Energy (LCOE) of the WEC at the optimal buoy size.

3.2.3. The Interaction between PTO Sizing and Buoy Sizing

The interaction between PTO sizing and buoy sizing is shown in Figure 13. It can be seen that the optimal buoy size generally declines with the corresponding PTO sizing ratio. However, this effect is limited and the optimal buoy size tends to be constant as the PTO sizing ratio is higher than 0.3 or 0.4. Hence, in this case, it can be noted that the buoy size optimization can be influenced by PTO sizing, but only to a limited extent. However, it should be pointed out that the interaction between PTO sizing and buoy sizing is related to wave resources, WEC principles, and economic parameters. Therefore, for avoiding the misestimate of the optimal buoy size, it is suggested to conduct PTO sizing simultaneously with buoy sizing. Besides, comparing Figure 13a,b, it is observed that there is no notable difference between the WEC with passive control and reactive control regarding the impact of PTO sizing on the buoy size determination.

(**a**) The WEC with passive control (**b**) The WEC with reactive control
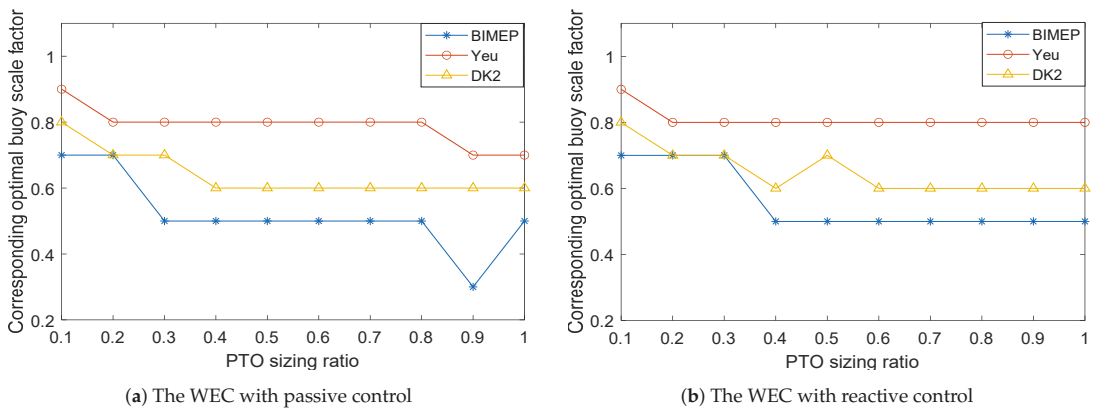
Figure 13. The interaction between PTO and buoy sizing.

3.3. The Proposed Method Versus Other Size Optimization Methods

3.3.1. Budal Diagram

Budal diagram is a useful tool to estimate the theoretical absorbed power of the WEC. According to Budal diagram, there are two upper absorbed power bounds in regular wave conditions, namely P_A and P_B. P_A bound is related to the maximum amount of power that could be extracted from incoming waves, while P_B reflects the bound of power that could be absorbed by the realistically sized WEC [9,11]. P_A corresponds to the maximum absorbed power at the high wave frequency limit and is expressed as

$$P_A = J/k = \frac{\rho g^3 H^2 T^3}{128\pi^3};$$ (31)

here, ρ is the water density; g is the gravity acceleration; H is the wave height; ω is the wave frequency of incoming waves; k is the wave number; and J is the wave-energy transport per unit frontage of the incident wave and deep water condition. Another power bound P_B corresponds to the maximum absorbed power at the low wave frequency limit and is expressed as

$$P_B = \frac{\pi\rho g H V}{4T},$$ (32)

where V is the volume of the buoy. The size of the WEC should match the wave resource to enable the WEC viable. Therefore, combined with the information of wave resources, Budal diagram could be used to select the suitable size of the WEC [9,11]. However, for calculating V in (32), the designed working condition (H and T) should be explicit. In Reference [11], the WEC is assumed to be commercially viable if the amount of working

time at full capacity exceeds one third of the annual time. Thus, the size of the WEC should match "one third wave power threshold" of the wave resource. Based on the power threshold, the wave height H_D and wave period T_D in the designed wave condition can be calculated. The selection of suitable size of the WEC is conducted following these steps [9]:

1. calculate the wave power threshold $J_T(W/m)$ which is being exceeded one third of the annual time in the concerned wave climate;
2. choose the most frequent wave period in scatter diagrams as the designed wave period T_D which corresponds to T in (31) and (32);
3. since T_D and J_T are already known from step 1 and 2, in harmonic waves, the wave height H_D can be calculated;
4. the suitable volume V can be calculated by solving $P_A = P_B$; and
5. finally, as the buoy volume is determined, the optimal PTO force limit is selected as the value which is required to maximize the absorbed power of the WEC at the designed wave condition (H_D and T_D).

Therefore, the suitable size of the WEC could be estimated by Budal diagram without calculating the power performance of the WEC in different sizes. However, in this method, the volume V depends on the assumption of viable conditions, such as "working at full capacity over one third of the annual time" [11]. In addition, Budal diagram is derived as the theoretical power bounds without considering the influence of PTO control strategies. So, the dependence of buoy size determination on the control strategies of the WEC cannot be reflected in this method. The size selection of the WEC is shown in Table 5.

Table 5. Size selection based on Budal diagram.

Sea Site	Wave Power Density Threshold	T_D	H_D	Buoy Volume	PTO Force Limit Reactive	Passive
Yeu Island	30.4 kW/m	7.8 s	2.00 m	224 m^3	985 kN	216 kN
BIMEP	14.6 kW/m	8.4 s	1.33 m	206 m^3	946 kN	145 kN
DK2	8.2 kW/m	5.4 s	1.24 m	33 m^3	142 kN	36 kN

3.3.2. The Size Optimization without PTO Downsizing

As is introduced in Section 1, existing literature regarding size optimization of WECs focused only on buoy sizing without considering PTO sizing. In those studies, the buoy size was optimized for the chosen sea sites, but the PTO size was simply scaled with the buoy scale factor λ [8,13]. This kind of buoy size optimization is conducted based on Froude scaling. With the aim to compare different size optimization methods, the size optimization without PTO sizing is conducted as a reference in this paper. The original buoy diameter is still defined as 5 m, the original PTO size is selected to sustain the maximum required force for the considered sea site, namely without PTO downsizing. Then, PTO force limits of the WEC in other buoy scale factors λ are scaled following Froude law, as (33).

$$F_{PTO\_limit\_scaled} = F_{PTO\_limit\_original}\lambda^3. \tag{33}$$

The power performance and the cost of the WEC at each buoy size are calculated by frequency domain modeling and the economic modeling, respectively. Therefore, the LCOE of the WEC at each buoy scale factor λ can be obtained. The optimization results are shown in Figure 14.
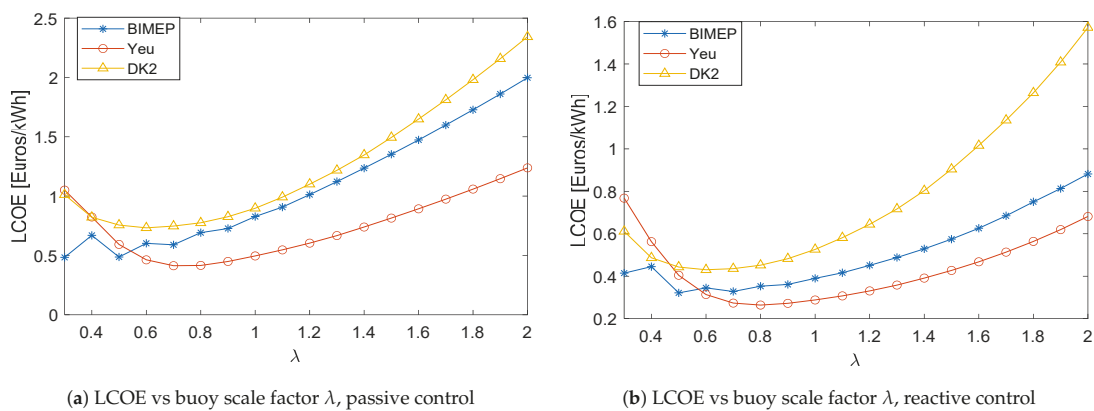
(**a**) LCOE vs buoy scale factor λ, passive control   (**b**) LCOE vs buoy scale factor λ, reactive control

Figure 14. The size optimization of the WEC without PTO sizing.

3.3.3. Comparison of Size Optimization Methods

As is explained above, there are several methods available to conduct the size optimization for improving techno-economic performance of the WEC. A comparison among these methods is performed and the results are shown in Figure 15. Firstly, from Figure 15a,b, it can be observed that Budal diagram is not capable of determining the suitable sizes of the WEC. The deviation of the selected size between Budal diagram and the proposed method differs with wave resources, and this deviation tends to be random. For instance, the selected buoy scale factor λ for BIMEP is three times as much as that estimated by this proposed method, while the difference of selected sizes for DK2 is relatively small. However, as a theoretical and efficient approach, Budal diagram can be used to narrow the scope of size selection for potential sea sites. Secondly, compared with Budal diagram, size optimization without PTO downsizing shows a better ability to estimate the suitable buoy size of the WEC. Generally, without PTO sizing, the buoy size optimization can still acquire the suitable buoy size. This phenomenon also verifies the finding in Section 3.2.3. Thirdly, it can be seen from Figure 15c,d that the LCOE of the WEC optimized by this proposed method is clearly lower than those by the other two methods, no matter which control strategy is adopted. Hence, it can be concluded that this proposed method is able to result in a further improvement on the techno-economic performance of the WEC.

(**a**) Buoy size determination, passive control   (**b**) Buoy size determination, reactive control

Figure 15. *Cont.*

(**c**) Lowest LCOE, passive control   (**d**) Lowest LCOE, reactive control
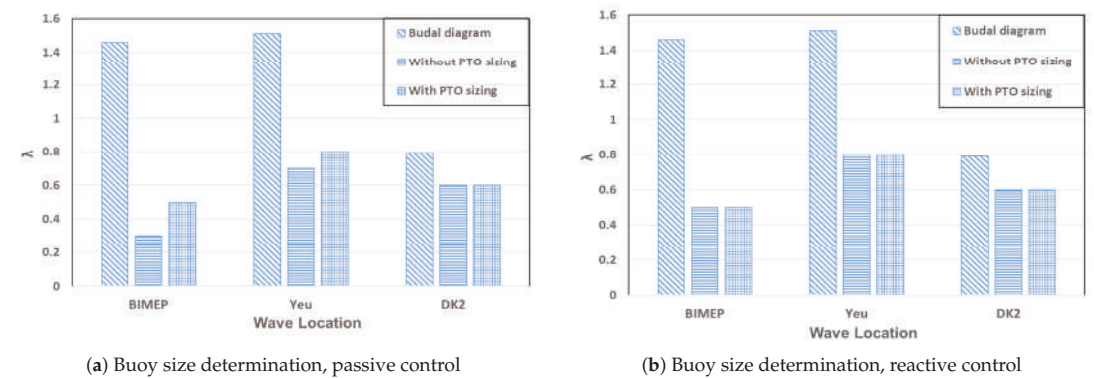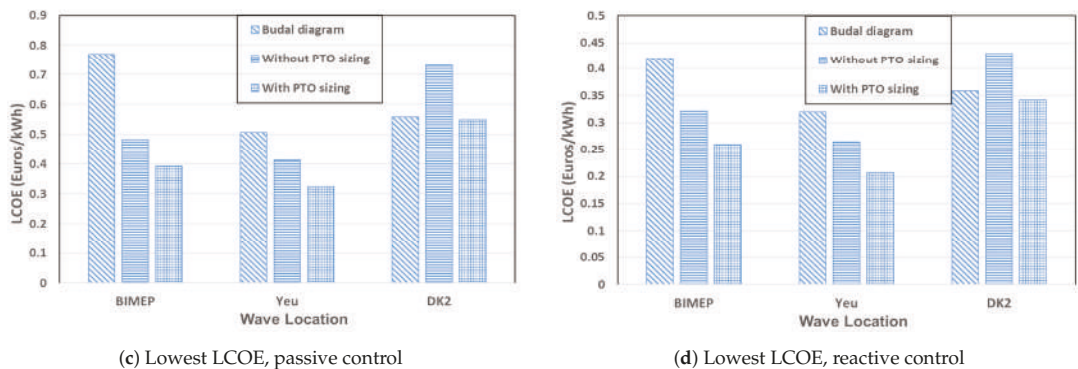
Figure 15. Comparison among different size optimization methods.

4. Conclusions

In this paper, a size optimization method of the WEC is proposed for improving the techno-economic performance and applied to a spherical heaving point absorber. Both buoy sizing and PTO sizing are taken into account. A frequency domain model and a preliminary economic model are established to calculate the power performance and economic performance of the WEC in various sizes, respectively. Besides, PTO force limits are used to represent different PTO sizes. For the determination of PTO parameters, a theoretical method is derived to maximize the power absorption under certain force constraints. The reactive control strategy and the passive control strategy are considered, respectively. Based on the proposed method, the size optimization is carried out for three typical sea sites. Furthermore, a comparison between the proposed method and other size optimization methods is performed. The following conclusions are drawn:

Firstly, as expected, both buoy sizing and PTO sizing are able to affect the techno-economic performance of the WEC. To improve the techno-economic performance, it is highly suggested to perform the buoy size optimization and PTO size optimization collectively.

Secondly, the optimal buoy size differs with wave resources, but it is not necessarily proportional to the mean wave power density. In this case, the optimal buoy scale factor λ ranges from 0.5 to 0.8. Besides, in most sea sites, the optimal PTO sizing ratios in the WEC with reactive control are slightly higher than those with passive control. The optimal PTO sizing ratios converge at around 0.4 to 0.5 for different sea sites. Furthermore, the higher mean wave power density and reactive control can clearly contribute to the reduction of the LCOE.

Thirdly, downsizing the PTO size would penalize the AEP, but it is beneficial for reducing the LCOE. In this case, the LCOE can be reduced by 24% to 31% through downsizing the PTO sizing ratio from 1 to around 0.4 to 0.5.

Fourthly, the corresponding optimal buoy size tends to slightly decrease with the PTO sizing ratio, but the influence of PTO sizing on the buoy size determination is limited.

Finally, Budal diagram is not able to estimate the suitable buoy size, but size optimization without PTO sizing can make the approximate estimate. Compared with other methods, a further reduction in the LCOE can be achieved by this proposed method.

Author Contributions: Conceptualization, J.T. and H.P.; methodology, J.T., H.P., and A.J.L.; software, J.T.; validation, J.T.; formal analysis, J.T., H.P., and A.J.L.; investigation, J.T.; resources, S.A.M.; data curation, J.T.; writing—original draft preparation, J.T.; writing—review and editing, J.T., H.P., and A.J.L.; visualization, J.T.; supervision, H.P., P.W., and S.A.M.; project administration, S.A.M.; funding acquisition, S.A.M. and H.P. All authors have read and agreed to the published version of the manuscript.

Institutional Review Board Statement: Not applicable.

Informed Consent Statement: Not applicable.

Data Availability Statement: The data presented in this study are available on request from the corresponding author.

Conflicts of Interest: The authors declare no conflict of interest. The funders had no role in the design of the study; in the collection, analyses, or interpretation of data; in the writing of the manuscript; or in the decision to publish the results.

References

1. Aderinto, T.; Li, H. Ocean Wave energy converters: Status and challenges. *Energies* **2018**, *11*, 1–26. [CrossRef]
2. Lehmann, M.; Karimpour, F.; Goudey, C.A.; Jacobson, P.T.; Alam, M.R. Ocean wave energy in the United States: Current status and future perspectives. *Renew. Sustain. Energy Rev.* **2017**, *74*, 1300–1313. [CrossRef]
3. De Andrés, A.; Macgillivray, A.; Guanche, R.; Jeffrey, H. Factors affecting LCOE of Ocean energy technologies: A study of technology and deployment attractiveness. In Proceedings of the 5th International Conference on Ocean Energy, Halifax, Nova Scotia, 4–6 November 2014; pp. 1–11.
4. Pecher, A. *Handbook of Ocean Wave Energy*; Springer: Berlin/Heidelberg, Germany, 2017; Volume 7. [CrossRef]
5. Babarit, A.; Hals, J.; Muliawan, M.J.; Kurniawan, A.; Moan, T.; Krokstad, J. Numerical benchmarking study of a selection of wave energy converters. *Renew. Energy* **2012**, *41*, 44–63. [CrossRef]
6. Chang, G.; Jones, C.A.; Roberts, J.D.; Neary, V.S. A comprehensive evaluation of factors affecting the levelized cost of wave energy conversion projects. *Renew. Energy* **2018**, *127*, 344–354. [CrossRef]
7. Babarit, A. A database of capture width ratio of wave energy converters. *Renew. Energy* **2015**, *80*, 610–628. doi:10.1016/j.renene. 2015.02.049. [CrossRef]
8. De Andres, A.; Maillet, J.; Todalshaug, J.H.; Möller, P.; Bould, D.; Jeffrey, H. Techno-economic related metrics for a wave energy converters feasibility assessment. *Sustainability* **2016**, *8*, 1109. [CrossRef]
9. Sergiienko, N.Y.; Cazzolato, B.S.; Ding, B.; Hardy, P.; Arjomandi, M. Performance comparison of the floating and fully submerged quasi-point absorber wave energy converters. *Renew. Energy* **2017**, *108*, 425–437. [CrossRef]
10. Falnes, J. *Ocean Waves and Oscillating Systems*; Cambridge University Press: Cambridge, UK, 2003; Volume 30, p. 953. [CrossRef]
11. Falnes, J.; Hals, J. Heaving buoys, point absorbers and arrays. *Philos. Trans. R. Soc. Math. Phys. Eng. Sci.* **2012**, *370*, 246–277. [CrossRef]
12. Pecher, A. *Performance Evaluation of Wave Energy Converters*; River Publishers: Hakodate, Denmark, 2014; pp. 1–107. [CrossRef]
13. O'Connor, M.; Lewis, T.; Dalton, G. Techno-economic performance of the Pelamis P1 and Wavestar at different ratings and various locations in Europe. *Renew. Energy* **2013**, *50*, 889–900. [CrossRef]
14. Tai, V.C.; See, P.C.; Merle, S.; Molinas, M. Sizing and control of the electric power take off for a buoy type point absorber wave energy converter. *Renew. Energy Power Qual. J.* **2012**, *1*, 1614–1619. [CrossRef]
15. Tokat, P. *Performance Evaluation and Life Cycle Cost Analysis of the Electrical Generation Unit of a Wave Energy Converter*; Chalmers Tekniska Hogskola: Gothenburg, Sweden, 2018.
16. Shek, J.; Macpherson, D.; Mueller, M. Phase and amplitude control of a linear generator for wave energy conversion. In Proceedings of the 4th IET International Conference on Power Electronics, Machines and Drives (PEMD 2008), York, UK, 2–4 April 2008; pp. 66–70. [CrossRef]
17. Shek, J.; Macpherson, D.; Mueller, M. Experimental verification of linear generator control for direct drive wave energy conversion. *IET Renew. Power Gener.* **2010**, *4*, 395–403. [CrossRef]
18. Tedeschi, E.; Carraro, M.; Molinas, M.; Mattavelli, P. Effect of control strategies and power take-off efficiency on the power capture from sea waves. *IEEE Trans. Energy Convers.* **2011**, *26*, 1088–1098. [CrossRef]
19. Garcia-Rosa, P.; Bacelli, G.; Ringwood, J. Control-informed geometric optimization of wave energy converters: The impact of device motion and force constraints. *Energies* **2015**, *8*, 13672–13687. [CrossRef]
20. Astariz, S.; Iglesias, G. The economics of wave energy: A review. *Renew. Sustain. Energy Rev.* **2015**, *45*, 397–408. [CrossRef]
21. Hals, J.; Bjarte-Larsson, T.; Falnes, J. Optimum Reactive Control and Control by Latching of a Wave-Absorbing Semisubmerged Heaving Sphere. In Proceedings of the 21st International Conference on Offshore Mechanics and Arctic Engineering, Oslo, Norway, 23–28 June 2002; pp. 415–423. [CrossRef]
22. Tedeschi, E.; Molinas, M. Tunable control strategy for wave energy converters with limited power takeoff rating. *IEEE Trans. Ind. Electron.* **2012**, *59*, 3838–3846. [CrossRef]

23.   Kramer, M.M.; Marquis, L.; Frigaard, P. Performance Evaluation of the Wavestar Prototype. In Proceedings of the 9th European Wave and Tidal Conference, Southampton, UK, 5–9 September 2011; pp. 5–9.
24.   Penalba, M.; Kelly, T.; Ringwood, J. Using NEMOH for Modelling Wave Energy Converters : A Comparative Study with WAMIT. In Proceedings of the 12th European Wave and Tidal Energy Conference, Cork, Ireland, 27 Auguest–1 September 2017; p. 10.
25.   Pastor, J.; Liu, Y. Frequency and time domain modeling and power output for a heaving point absorber wave energy converter. *Int. J. Energy Environ. Eng.* **2014**, *5*, 1–13. [CrossRef]
26.   Journée, J.M.J.; Massie, W.W.; Huijsmans, R.H.M. *Offshore Hydrodynamics*; Delft University of Technology: Delft, The Netherlands, 2015.
27.   Penalba, M.; Giorgi, G.; Ringwood, J.V. Mathematical modelling of wave energy converters: A review of nonlinear approaches. *Renew. Sustain. Energy Rev.* **2017**, *78*, 1188–1207. [CrossRef]
28.   Hals, J.; Falnes, J.; Moan, T. Constrained Optimal Control of a Heaving Buoy Wave-Energy Converter. *J. Offshore Mech. Arct. Eng.* **2010**, *133*, 011401. [CrossRef]
29.   Prado, M.; Polinder, H. *Direct Drive Wave Energy Conversion Systems: An Introduction*; Woodhead Publishing Limited: Sawston, Cambridge, 2013; pp. 175–194.10.1533/9780857097491.2.175. [CrossRef]
30.   Ugray, Z.; Lasdon, L.; Plummer, J.; Glover, F.; Kelly, J.; Martí, R. Scatter Search and Local NLP Solvers : A Multistart Framework for Global Optimization. *Informs J. Comput.* **2007**.10.2139/ssrn.886559. [CrossRef]
31.   Cahill, B.; Lewis, A.W. Wave period ratios and the calculation of wave power. In Proceedings of the 2nd Marine Energy Technology Symposium, Seattle, WA, USA, 15–18 April 2014; pp. 1–10.
32.   Chozas, J.; Kofoed, J.; Helstrup, N. *The COE Calculation Tool for Wave Energy Converters*; Version 1.6; DCE Technical Reports; No. 161; Aalborg University: Aalborg, Denmark, 2014.
33.   Payne, G. Guidance for the experimental tank testing of wave energy converters. *SuperGen Mar.* **2008**, *254*.
34.   De Andres, A.; Medina-Lopez, E.; Crooks, D.; Roberts, O.; Jeffrey, H. On the reversed LCOE calculation: Design constraints for wave energy commercialization. *Int. J. Mar. Energy* **2017**, *18*, 88–108. [CrossRef]
35.   Bank of England. Inflation Calculator-Bank of England [EB/OL]. Available online: https://www.bankofengland.co.uk/monetary-policy/inflation/inflation-calculator (accessed on 4 October 2020).
36.   Polinder, H. *Principles of Electrical Design of Permanent Magnet Generators for Direct Drive Renewable Energy Systems*; Woodhead Publishing Limited: Cambridge, UK, 2013; pp. 30–50. [CrossRef]
37.   Tokat, P.; Thiringer, T. Sizing of IPM Generator for a Single Point Absorber Type Wave Energy Converter. *IEEE Trans. Energy Convers.* **2018**, *33*, 10–19. [CrossRef]

Article

A Comparative Study of Model Predictive Control and Optimal Causal Control for Heaving Point Absorbers

Mirko Previsic [1,*], Anantha Karthikeyan [1] and Jeff Scruggs [2]

[1] RE Vision Consulting, LLC., 1104 Corporate Way, Sacramento, CA 95831, USA; anantha@re-vision.net
[2] Civil & Environmental Engineering, University of Michigan, Ann Arbor, MI 48109, USA; jscruggs@umich.edu
[*] Correspondence: mirko@re-vision.net

Abstract: Efforts by various researchers in recent years to design simple causal control laws that can be applied to WEC devices suggest that these controllers can yield similar levels of energy output as those of more complex non-causal controllers. However, most studies were established without adequately considering device and power conversion system constraints which are relevant design drivers from a cost and economic point of view. It is therefore imperative to understand the benefits of MPC compared to causal control from a performance and constraint handling perspective. In this paper, we compare linear MPC to a casual controller that incorporates constraint handling to benchmark its performance on a one DoF heaving point absorber in a range of wave conditions. Our analysis demonstrates that MPC provides significant performance advantages compared to an optimized causal controller, particularly if significant constraints on device motion and/or forces are imposed. We further demonstrate that distinct control performance regions can be established that correlate well with classical point absorber and volumetric limits of the wave energy conversion device.

Keywords: causal control; Model Predictive Control; point absorber; wave-energy converter; absorbed power

1. Introduction

As the field of wave energy conversion transitions from traditional passive control techniques to advanced optimal control strategies for power maximization, it becomes increasingly important to understand the requirements, capabilities, limitations, and benefits of each method to choose the best optimization strategy for a given application.

The control system affects power capture, structural loads, and power-takeoff (PTO) design. To achieve true economic optimality in a wave energy conversion system design, the control system needs to be able to optimize performance given the constraints imposed by the wave energy converter (WEC) system. This is due to the fact that economic outcomes are optimized if a given component or sub-system is continually utilized at its rated operational condition during a majority of its operational life. These rated operational conditions provide constraints within which the device needs to operate, and the WEC control system is responsible for enforcing these constraints because exceeding them will result in mechanical breakdown. As such, the constraint handling of a controller is incredibly important to maximize the economic competitiveness of a WEC device. Constrained optimal control as offered by a Model Predictive Control (MPC) algorithm framework, which is also referred to as non-causal control, is a key tool in this optimization process.

Control systems for wave energy conversion are broadly classified as either causal or non-causal controllers. A causal controller uses information from sensors that monitor the outputs of a dynamical system, in our case the WEC. The sensor information is used as feedback by the controller to follow a desired command signal. Non-causal controllers such as MPC leverage wave prediction to generate control commands in a feed-forward manner rather than using feedback from sensors that measure system output variables. Combination of non-causal (feed-forward) and causal (feedback) control is also possible in

201

a hybrid manner and can be used to correct for modeling and/or wave prediction errors in non-causal controllers.

Within the literature there are two well-published methods for implementing causal control that incorporate constraint handling. The first approach tries to approximate complex conjugate control (CCC) ([1–4]) with a causal feedback law [5]. This approach does well in the unconstrained case where no motion limits are imposed. To allow for constraints, these methods were subsequently augmented to incorporate an MPC controller that works for the sole purpose of enforcing constraints [5]. Performance of the CCC approximating causal control methods is sub-optimal when constraints are imposed, because the impedance matching value obtained from the CCC approximation provides in-sufficient damping for the constrained case.

The second approach for designing a causal controller comes from recognizing that the causal WEC control problems fall into the Linear Quadratic Gaussian (LQG) paradigm ([6–8]). A non-standard LQG optimization problem is established with the objective of maximizing power. The problem treats the input wave excitation force as a stationary stochastic disturbance with a known spectrum. A wave-shaping filter is designed to model the spectrum and this filter model is incorporated in the optimization along with the system dynamics model of the WEC. The LQG optimal controller derived in this manner does not rely on approximations to CCC and will therefore achieve optimality in a broader set of sea states. Stroke protection techniques can be explicitly designed to protect against end-stop violations [7,9]. The control parameters are optimized offline and implemented using a gain schedule to adapt to changing wave conditions. A block-diagram of a casual controller with non-linear stroke protection is shown in Figure 1.
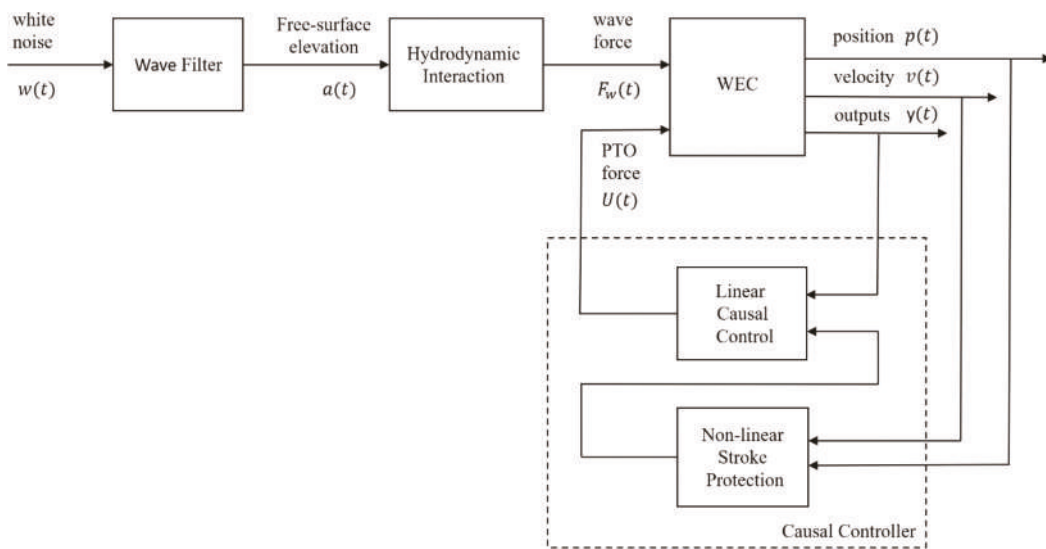
Figure 1. Architecture of causal controller.

Non-causal performance optimization of WECs is typically implemented using a receding horizon MPC framework. To guarantee optimality, MPC needs a forecast of oncoming waves 20 to 30 s into the future to plan optimal control commands. Wave forecasting can be conducted by placing probes up-wave, measuring the free-surface elevation in the wave field [10], or using a wave-sensing radar [11,12] to characterize the wave-field propagation. These up-wave measurements are marched forward in space and time to predict the wave elevation at the target WEC location. The predicted wave excitation force input, in addition to the states of a system dynamics model, are used to

solve a quadratic optimization problem to find the optimal control trajectory. The states of the device are marched forward in time and the optimization process is repeated at each step with new prediction information. Figure 2 shows the basic MPC control architecture.
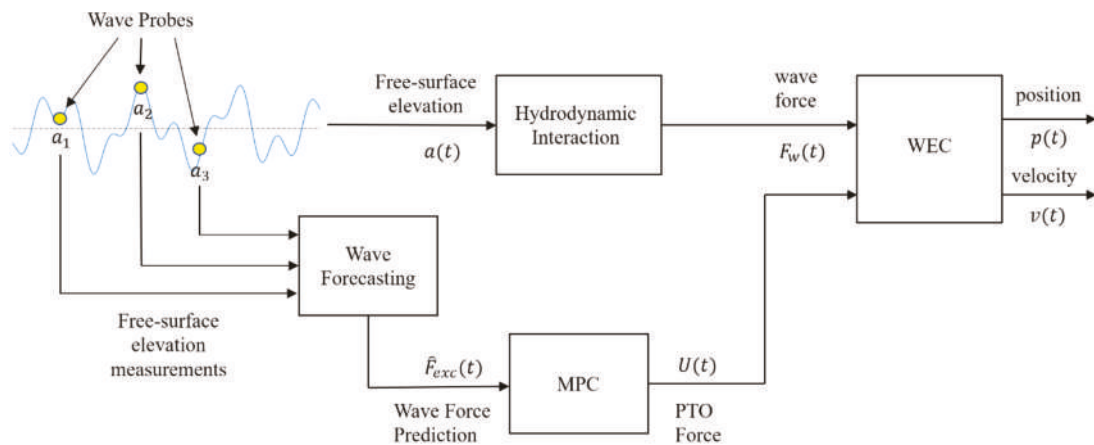

Figure 2. Architecture of Model Predictive Control.

Considerable research has been undertaken on expanding the capabilities of MPC to meet the requirements of an entire range of device topologies and PTO configurations ([13–19]). Some of the common constraints that can be handled effectively within the MPC optimization include: (1) PTO force constraints; (2) WEC position, velocity, and acceleration constraints; (3) discrete (ON/OFF) control of PTO forces; and (4) power-flow constraints. MPC can accommodate non-linear device dynamics, such as viscous drag and non-linear models of powertrain losses, which need to be considered in the optimization problem to guarantee optimality [14].

2. Glossary

Variable	Description	Units
g	Acceleration due to gravity	m/s^2
ρ	Density of sea water	kg/m^3
m	Mass of the buoy	kg
m_∞	Infinite Added Mass	kg
z	Displacement of the buoy in heave	m
$\dot{z}$	Velocity of the buoy in heave	m/s
$\ddot{z}$	Acceleration of the buoy in heave	m/s^2
F_R	Radiation damping force	N
F_m	PTO Force	N
F_s	Hydrostatic spring stiffness	N
F_d	Drag force related to viscous effects	N
F_e	Wave excitation force	N
k	Buoyancy stiffness coefficient	N/m

Variable	Description	Units
S	Water plane area of the buoy	m^2
B_{vis}	Viscous damping coefficient	Ns/m
C_d	Drag coefficient	-
A_r	A matrix of state space model of the radiation damping sub-system	
B_r	B matrix of state space model of the radiation damping sub-system	
C_r	C matrix of state space model of the radiation damping sub-system	
D_r	D matrix of state space model of the radiation damping sub-system	
X_r	State vector comprising of all states used to model the radiation damping sub-system in state space form	
$\dot{X}_r$	Vector comprising of the derivatives of all states used to model the radiation damping sub-system in state space form	
n_r	Number of states used to model the radiation damping sub-system. This is equal to the length of the state vector X_r	
0_r	Row vector of zeros with length n_r	
A	A matrix of WEC state space model	
B	B matrix of WEC state space model	
C	C matrix of WEC state space model	
D	D matrix of WEC state space model	
T_h	Prediction horizon	s
H	Wave height of a monochromatic wave	m
T	Wave period of a monochromatic wave	s
H_s	Significant wave height of a polychromatic wave	m
T_p	Peak period of a polychromatic wave	s
λ	Wavelength	m
k_w	Wavenumber	
$\overline{P}_a$	Average absorbed power	W
v	Buoy heave velocity	m/s
h_r	Radiation impulse-response function	Ns/m
h_e	Excitation impulse-response function	N/m
t	Time instant	s
$u(t)$	Control input at time instant t	N
$f_e(t)$	Wave excitation force at time instant t	N
$x(t)$	State vector at time instant t comprising of all states used to model the device dynamics	
$\dot{x}(t)$	Derivative of the state vector at time instant t that is used to model the device dynamics	

3. The Device Model

We consider a one degree-of-freedom heaving point absorber as an example for our comparison study. A general schematic of the heaving buoy WEC is shown in Figure 3 and key dimensions are provided in Table 1. This device has well-established theoretical limits on power absorption which can be used to identify the design trade-off space for controls optimization.
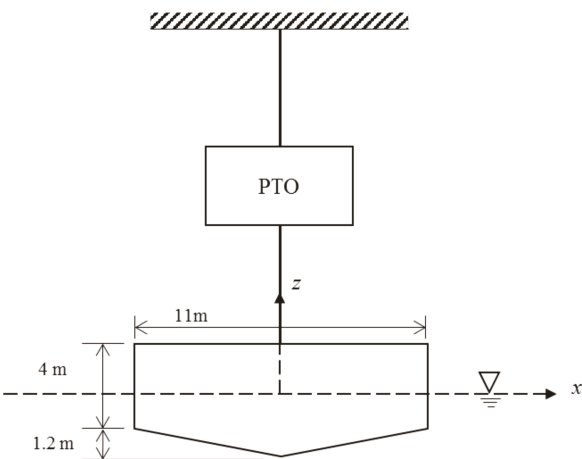
Figure 3. Schematic of the heaving wave-energy converter.

Table 1. Dimensions and physical parameters of the heaving wave energy converter.

Quantity	Value	Units
Buoy diameter	11	m
Buoy cylinder height	4	m
Reaction diameter	11	m
Buoy conical height	1.2	m
Motion limits	±2	m
Buoy mass	228,080	kg
Water Plane Area (S)	95	m²
Coefficient of Drag (Cd)	0.5	

The device geometry was modeled using a commercially available Boundary Element code called WAMIT [20]. The added mass, radiation damping, and excitation force kernels were obtained as a function of frequency by post-processing the WAMIT outputs. Figure 4 shows the frequency dependent parameters plotted against the wave period.
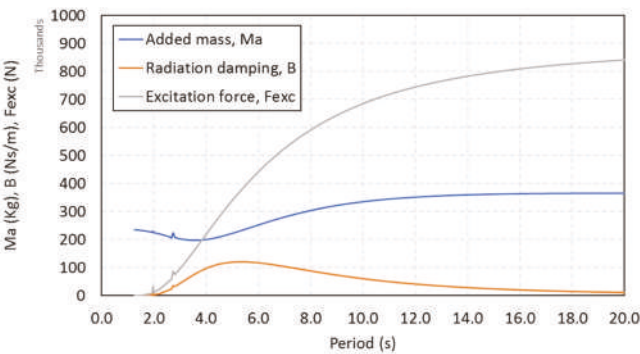
Figure 4. Frequency-dependent parameters of the heaving buoy WEC obtained from WAMIT.

Because this floating body is constrained to move in heave, the equation of motion in the vertical direction is given by:

$$m\,\ddot{z}(t) = F_R(t) + F_e\,(t) + F_m(t) + F_s\,(t) + F_d(t) \tag{1}$$

where z is the displacement, $\dot{z}$ is the velocity, and $\ddot{z}$ is the acceleration of the buoy in heave. m is the displaced mass of the buoy, F_R is the radiation force, F_e is the wave-excitation force, F_m is the PTO force, F_s is the hydrostatic restoring force given by $F_s = -k\,z$, where k is the buoyancy stiffness, defined as $k = \rho g S$, where ρ is the water density, g the gravitational constant, and S the water-plane area. F_d is the drag force related to viscous effects in real fluid. The viscous damping coefficient was assumed to be linear according to the relationship $F_d = -B_{vis}\,v$, where $B_{vis} = 0.5\,C_d\rho S$. C_d is the drag coefficient and ρ is the water density. The radiation force $f_R(t)$, can be expressed as:

$$F_R(t) = -m_\infty \ddot{z}(t) - \int_{-\infty}^{t} h_r(t-\tau)\dot{z}(\tau)d\tau \tag{2}$$

where m_∞ is the infinite frequency added mass and $h_r(t)$ is the impulse response function of the radiation force. The excitation force $F_e(t)$ is expressed as:

$$F_e(t) = \int_{-\infty}^{+\infty} h_e(t-\tau)\overline{\eta}(\tau)d\tau \tag{3}$$

where $h_e(t)$ is the excitation force impulse response function and $\overline{\eta}(t)$ is the wave elevation at the device location. The impulse response function relating the wave elevation to the excitation force affecting the device is non-causal. The main reason is that the chosen input, i.e., the wave elevation at the device location, is not the direct cause of the output, i.e., the interaction force between the wavefield and the device.

To recast the system dynamics into state-space form, the radiation term can be modelled as an embedded sub-system through the following state-space realization:

$$\dot{X}_r(t) = A_r X_r(t) + B_r \dot{z}(t) \tag{4}$$

$$f_r(t) = C_r X_r(t) + D_r \dot{z}(t) \tag{5}$$

This leads to the following state-space model:

$$\dot{x}(t) = Ax(t) + Bu(t) + Bf_e(t) \\ y(t) = Cx(t) + Du(t) \tag{6}$$

with

$$A = \begin{bmatrix} A_r & 0 & B_r \\ 0 & 0 & 1 \\ -\frac{C_r}{m+m_\infty} & -\frac{k}{m+m_\infty} & -\frac{B_{vis}+D_r}{m+m_\infty} \end{bmatrix}, B = \begin{bmatrix} 0 \\ 0 \\ \frac{1}{m+m_\infty} \end{bmatrix} C = \begin{bmatrix} 0_r & 1 & 0 \\ 0_r & 0 & 1 \end{bmatrix}, D = \begin{bmatrix} 0 \\ 0 \end{bmatrix} \tag{7}$$

4. Control Methods

4.1. Model Predictive Control (MPC)

A wave energy converter with a linearized device dynamics model can be optimized using a linear MPC framework. In this type of problem, the non-linearities such as viscous drag are approximated using linear relationships. Under the assumption of no loss in the power generation process, optimizing the device average power absorbed $\overline{P}_a$ at a given

instant t_0 over a defined control horizon T_h can be achieved by determining the optimal control trajectory $u^*(t)$ that maximizes the following cost function:

$$\overline{P}_a = -\frac{1}{T_h} \int_{t_0}^{t_0+T_h} v(t)u(t)dt \tag{8}$$

where $v(t)$ is the instantaneous device velocity. The minus sign is due to the convention of considering absorbed energy with a negative sign. Assuming a fixed time step, we discretize the integral and set up the optimization problem as a minimization by changing the sign in Equation (9). The new optimization objective, therefore, is given by:

$$J = \frac{1}{N} \sum_{k=0}^{N-1} x_{k+1}^T S_v^T u_k \tag{9}$$

where N is the number of time intervals over the control horizon T_h and S_v is a linear operator extracting the WEC velocity from the state-space vector. The control force and state vector, however, are not independent variables, and are constrained by the system dynamics equation of the WEC, which in discrete time is defined as:

$$x_{k+1} = A_d x_k + B_d u_k + B_d f_{e_k}, \ k = 0, \ \dots, \ N-1 \tag{10}$$

with initial condition $x_0 = \overline{x}_0$.

To preserve mechanical and structural integrity, motion constraints and force limits are imposed. These constraints limit the maximum actuation force and the WEC device velocity and vertical displacement, i.e.,

$$u_{min} \leq u_k \leq u_{max}, \ k = 0, \ \dots, \ N-1 \tag{11}$$

$$p_{min} \leq S_p x_k \leq p_{max}, \ k = 0, \ \dots, \ N \tag{12}$$

$$v_{min} \leq S_v x_k \leq v_{max}, \ k = 0, \ \dots, \ N \tag{13}$$

where S_p is a linear operator extracting the WEC displacement from the state vector. The cost function, together with the constraints, represents a linear MPC problem in its standard formulation.

Let us define the following consolidated vectors based on the sequence of states and control commands. This will help in simplifying the notation and problem setup:

$$X = \begin{bmatrix} x_1^T & x_2^T & \dots & x_N^T \end{bmatrix}^T \tag{14}$$

$$U = \begin{bmatrix} u_1^T & u_2^T & \dots & u_N^T \end{bmatrix}^T \tag{15}$$

Let us define Λ_v, Λ_p as block diagonal matrices having the velocity extraction matrix S_v and the position extraction matrix Λ_p, repeated N times respectively on the main block diagonal. Furthermore, let I be the $N \times N$ identity matrix and let ξ be a $N \times 1$ vector of ones. In this manner, the cost function can then be expressed as follows:

$$J = \frac{1}{N} X^T \Lambda_v^T U \tag{16}$$

The inequality constraints can be reformulated using this vector notation as follows:

$$D_u U \leq d_u \tag{17}$$

$$D_x X \leq d_x \tag{18}$$

where

$$D_u = \begin{bmatrix} I \\ -I \end{bmatrix} d_u = \begin{bmatrix} u_{max} * \xi \\ -u_{min} * \xi \end{bmatrix} \tag{19}$$

$$D_x = \begin{bmatrix} \Lambda_p \\ -\Lambda_p \\ \Lambda_v \\ -\Lambda_v \end{bmatrix} \quad d_x = \begin{bmatrix} p_{max} * \xi \\ -p_{min} * \xi \\ v_{max} * \xi \\ -v_{min} * \xi \end{bmatrix} \tag{20}$$

By recursively applying the discrete-time dynamics equations, it is possible to express X as a function of the control vector U, the excitation force vector F_e, and the initial condition $\bar{x}_0$:

$$X = Y_d \bar{x}_0 + \Gamma_d U + \Gamma_d F_e \tag{21}$$

where

$$Y_d = \begin{bmatrix} A_d \\ A_d^2 \\ \vdots \\ A_d^N \end{bmatrix} \tag{22}$$

$$\Gamma_d = \begin{bmatrix} B_d & 0 & 0 & 0 \\ A_d B_d & B_d & 0 & 0 \\ \vdots & \vdots & \ddots & 0 \\ A_d^{N-1} B_d & A_d^{N-2} B_d & \cdots & B_d \end{bmatrix} \tag{23}$$

$$F_e = \begin{bmatrix} f_{e_0}^T & f_{e_1}^T & \cdots & f_{e_{N-1}}^T \end{bmatrix}^T \tag{24}$$

This allows us to rewrite the MPC problem as the following cost function and constraint equations:

$$\min_U U^T \Gamma_d^T \Lambda_v^T U + (\Lambda_v Y_d \bar{x}_0 + \Lambda_v \Gamma_d F_e)^T U \tag{25}$$

$$\begin{bmatrix} D_u \\ D_x \Gamma_d \end{bmatrix} U \leq \begin{bmatrix} d_u \\ d_x - D_x Y_d \bar{x}_0 - D_x \Gamma_d F_e \end{bmatrix} \tag{26}$$

The maximization of absorbed power requires the solution of a constrained convex optimization problem, for which well-consolidated routines, such as interior-point-convex or active-set methods, are available in literature [21,22]. Positive definiteness of the Hessian is, in general, guaranteed for the optimization of a point absorber device, unless the time step chosen for the conversion of the continuous time model into discrete time is too large to represent the actual behavior of the WEC device. At each timestep, an MPC problem needs to be solved, and the first value of the optimal solution vector U^* is applied to the system. The system is marched forward in time by integrating the system dynamics using a standard Runge–Kutta (RK) scheme. The above MPC formulation also assumes that a perfect excitation force prediction is available 20 to 30 s into the future using up-wave measurement probes.

4.2. Causal Feedback Control

The first step in optimal causal feedback control design is to determine an analytically tractable stochastic disturbance model to represent the incident wave force $f_e(t)$. This step is nontrivial for two reasons. Firstly, the power spectral density typically used to characterize the free surface elevation $\bar{\eta}(t)$, denoted $S_\eta(\omega)$, does not constitute a rational spectrum (i.e., it is not a ratio of rational polynomials of frequency ω). Secondly, the transfer function from the free surface elevation to the incident wave force, equal to

$$H_e(s) = \int_{-\infty}^{\infty} e^{-st} h_e(t) dt$$

involves the solution to a partial differential equation (due to fluid–structure interaction), and consequently it also does not evaluate to a rational transfer function. Consequently, the resultant power spectral density of the incident wave force, denoted as

$$S_e(\omega) = S_\eta(\omega)|H_e(j\omega)|^2$$

is an irrational function of frequency. To make the causal control design problem tractable, this spectrum must be approximated, as

$$S_e(\omega) \approx |G(j\omega)|^2$$

where the transfer function $G(s)$ is a stable, minimum-phase, strictly-proper, rational transfer function. Equivalently, we seek to find matrices A_e, B_e, and C_e such that in the above equation,

$$G(s) = C_e[sI - A_e]^{-1}B_e$$

With such a formulation for $G(s)$, we may equivalently represent the incident wave force as filtered white noise; i.e.,

$$\dot{x}_e(t) = A_e x_e(t) + B_e w(t)$$

$$f_e(t) = C_e x_e(t)$$

where $w(t)$ is a white noise process with unit spectral intensity.

There are a number of ways to find appropriate matrices A_e, B_e, and C_e for the noise filter model described above. Here, we make use of the subspace-based spectral factorization approach. Because this approach is applied exactly as described in [23], we will forgo the details here in the interest of brevity.

With the accomplishment of the finite-dimensional approximation of the incident wave force, we then append the internal states $x_e(t)$ to the state $x(t)$ of the physical system; i.e., we define $x_a(t) = \begin{bmatrix} x^T(t) & x_e^T(t) \end{bmatrix}^T$ to arrive at an augmented state space model:

$$\dot{x}_a(t) = A_a x_a(t) + B_a u(t) + E_a w(t)$$
$$y(t) = C_a x_a(t) + D_a u(t)$$

where matrices A_a, B_a, E_a, C_a, and D_a are appropriately defined. Our objective is to design a causal feedback law that maps y into u, to maximize the objective

$$\overline{P}_a = -E\left\{vu + Ru^2\right\}$$

where $E\{.\}$ denotes the expectation in stationarity, and R is a nonnegative parameter. For the case in which $R = 0$, the above expression is simply the mean power absorption. In design, R is typically chosen to be greater than zero, for two reasons. Firstly, it can be used to (approximately) quantify the power dissipation in the power train of the WEC, thus changing the performance objective from absorbed power to generated power. Secondly, it can be used as a tuning parameter to balance the power generation objective against the need to keep the mean-square control force magnitude below a desired threshold.

If there were no constraints on the response of the WEC, the above problem could be solved in closed form. More specifically, it distills to a sign-indefinite Linear Quadratic Gaussian (LQG) control problem, which is guaranteed to have a unique, stabilizing solution assuming that the open-loop mapping from u to $\dot{z}$ is passive [6]. However, for the WEC under consideration here, there are constraints on both the displacement z and the control force u. In the presence of these constraints, the closed-form LQG control solution cannot be used without modification. To address these constraints, in this paper we implement the methodology outlined in detail in [9]. Because the methodology used here is identical

to that one, we only provide an overview here of the basic steps in the nonlinear control design procedure.

The first step is to design a linear feedback controller of the form

$$\dot{\xi} = A_c \xi + B_c y$$
$$u = C_c \xi$$

in which A_c, B_c, and C_c are optimized to maximize $\overline{P}_a$, subject to two constraints. The first of these constraints is a relaxed version of the WEC displacement constraint, in which we require only that the mean-square displacement be below a bound related to p_{max}, i.e.,

$$E\left\{ z^2 \right\} \leq \sigma p_{max}^2$$

where $\sigma < 1$ is a design parameter, chosen here to be 0.25. The second constraint is the restriction that the open-loop controller must be stable; i.e., that A_c be a Hurwitz matrix. Convex techniques for accomplishing this constrained optimization are covered extensively in [9]. The resultant linear controller is guaranteed to result in positive power generation, be robust to saturations in the input u, and maintain mean-square displacements below p_{max}^2. However, it does not guarantee that the displacement limit is satisfied at all times.

The second step is to augment the above linear control design with a nonlinear stroke-protection feedback loop that ensures that the displacement limit is satisfied at all times (rather than just in the mean-square sense). This stroke protection loop, and its relationship to the linear control design, is illustrated in Figure 1. It accepts as inputs the position and velocity, and outputs a supplemental nonlinear force q. This quantity q is sent back to the linear controller through an augmented input matrix, i.e., via the equations:

$$\dot{\xi} = A_c \xi + B_c y + E_c q$$
$$u = C_c \xi + q$$

where E_c is a matrix of design parameters. The design of the feedback function that maps $\{z, \dot{z}\}$ into q, and the design of E_c, are described fully in [9]. Here it suffices to say that q can be viewed as being similar to the restoring force of a "virtual hardening spring," providing no force when the displacement is far from its limit, but increasing to infinity when the displacement approaches its limit. The participation of velocity $\dot{z}$ in the function can be thought of as providing damping. Meanwhile, the matrix E_c is designed such that the open-loop transfer function from q to $\dot{z}$ is passive, which guarantees unconditional stability of the closed-loop system.

The controller resulting from the above design framework is guaranteed to protect the displacement from reaching its limit for the case in which the force u is unbounded. When saturation limits are imposed on u, of the form

$$u = \begin{cases} u_{min} : & C_c \xi + q < u_{min} \\ C_c \xi + q : & u_{min} \leq C_c \xi + q \leq u_{max} \\ u_{max} : & C_c \xi + q > u_{max} \end{cases}$$

then the displacement protection is not strictly guaranteed. Indeed, when both the force and displacement are constrained, there may not exist a controller that can honor both. However, proper tuning of the various design parameters in the control design can be undertaken to assure that displacement constraints are satisfied in all but extremely rare cases in stationary response.

5. Theoretical Limits on the Average Absorbed Power

5.1. Point Absorber Limit

Consider a heaving axisymmetric body oscillating without constraints in resonance with an incoming regular wave of period T (s) and height H (m). Let J_E (W/m) denote the wave power level, $k_w(1/m)$ denote the wavenumber, and λ (m) the wavelength. In this case, the point absorber effect in wave-energy extraction [24] imposes a fundamental limit on the average absorbed power $\overline{P}_a$. As described in [24,25], this limit can be derived from the relationship between absorption width $d_a = \overline{P}_a / J_E (m)$ and wavelength λ, as shown below:

$$d_a \leq \frac{1}{k_w} = \frac{\lambda}{2\pi} \tag{27}$$

Or equivalently:

$$\overline{P}_a \leq \frac{1}{k} J_E = \frac{\rho}{128} \left(\frac{g}{\pi}\right)^3 T^3 H^2 \tag{28}$$

The last equality in Equation (28) is valid for deep water conditions. This is referred to as the Point Absorber Limit. The theoretical limit may be reached if the average absorbed power equals half the average excitation power, which happens when the radiated power is equal to the absorbed power. Furthermore, it is known that the Point Absorber Limit can only be reached up to a certain wave period and height. This depends on the motion amplitude constraints on the absorber. Beyond, only a lower relative power absorption can be realized, as defined by a device's volumetric limit.

5.2. Volumetric Limit

The heaving body sweeps a finite volume during its oscillation cycle based on physical limits. This volumetric constraint imposes a limit on the average power absorbed from each oscillation cycle. As shown in [25], the average power P_a in the motion-constrained case is limited by the expression:

$$\overline{P}_a < (\pi \rho g H V / 4T) \tag{29}$$

This is referred to as the volumetric limit. With advanced control, we expect to achieve the active theoretical limit based on the device's operational region.

5.3. Controller Design Trade-Off Space

The controller design trade-off space for a WEC is defined by the Point Absorber and Volumetric Limit. For any given wave period, we will call the lesser of the two the "active theoretical limit" or the "theoretical limit" for simplicity. The controller performance cannot exceed the theoretical limit, and this defines the design trade-off space for controller optimization. As shown in Figure 5, the Point Absorber Limit is "active" for shorter wave periods. We will call this set of wave periods Region I. The Volumetric Limit is "active" for longer wave periods and we will call this set of wave periods Region II. The cross-over period, where the Point Absorber and Volumetric Limits are equal, demarcates the two regions.

Equations (28) and (29) show that both upper limits are wave height dependent and describe the WEC device performance in sinusoidal waves. To understand theoretical upper limits for an irregular wave train, we compute the wave height for a sinusoidal wave with the equivalent average power density of the irregular wave train as follows. The power in a monochromatic wave of height H and period T is given by:

$$P_{mono} = H^2 T \tag{30}$$

The equivalent wave height (H) of a monochromatic wave with the same power as the polychromatic wave can be found by equating the two. Assuming the period of the

monochromatic wave to be the same as the peak period of the polychromatic sea state, we obtain the wave height of the equivalent sinusoidal wave as:

$$H = 0.64 \, H_s \tag{31}$$

This approach allows us to classify regions in the scatter diagram based on point absorber theory, and to draw meaningful conclusions regarding the importance of MPC-based control. For this purpose, we divided the entire set of input wave conditions into three distinct regions based on theoretical limits. Figure 6 illustrates the partitioning of sea states, where Region I corresponds to wave conditions where performance is dominated by the Point Absorber Limit. Region II corresponds to wave conditions where performance is dominated by the Volumetric Limit. Finally, Region III is associated with large waves where controllers are expected to maintain rated power production and minimize structural loads on the system. Region III is not important from a performance optimization perspective, but it is important that a control law active in this region will continue to produce power at the rated capacity, while minimizing structural loads. Although slightly counter-intuitive, structural loads in Region III can be smaller than those in Regions I and II because we are effectively de-tuning the system to the incident wave conditions.
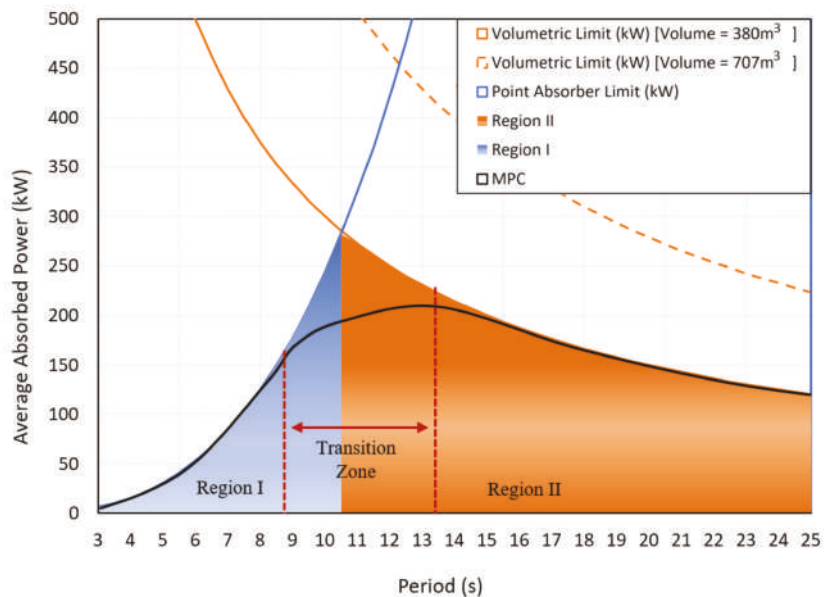
Figure 5. Controller design trade-off space based on theoretical limits for sinusoidal wave inputs of height H = 1 m.

Applying the above region-based approach to a small and a large heaving point absorber provides the following regions. To understand their significance in context, we simply superimposed the regions onto the frequency distribution of the DoE's reference resource in Humboldt Bay, California. As shown in Figure 7, the reference geometry used for this paper has only a few sea states, where causal control has the potential to provide similar performance as that of the MPC-based controller. This is in stark contrast to the SANDIA Wavebot, which has a much larger volumetric displacement and as a result performs well in most sea-states using causal control (see Figure 8).
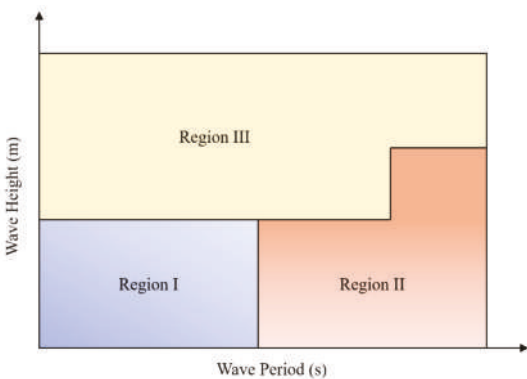
Figure 6. Partitioning of sea states based on fundamental limits.

% of Total Occurrence Hm0 (m),	Peak Period - Tp (s), center of bin																				
	0.6	1.7	2.9	4.1	5.2	6.4	7.5	8.7	9.9	11.0	12.2	13.3	14.5	15.7	16.8	18.0	19.1	20.3	21.5	22.6	23.8
0.25							0.0	0.0													
0.75					0.0	0.5	1.5	2.7	1.9	1.1	0.5	0.2	0.0								
1.25					0.0	0.6	4.1	5.6	4.5	2.7	1.3	0.7	0.3	0.1	0.0	0.0					
1.75						0.1	3.3	5.1	4.6	3.9	2.1	1.2	0.8	0.3	0.1	0.0					
2.25						0.9	5.3	3.7	4.1	2.9	1.3	0.8	0.4	0.2	0.1	0.0					
2.75						0.1	2.4	2.6	2.8	2.8	1.6	0.8	0.3	0.1	0.1	0.0					
3.25							0.4	1.5	1.5	2.0	1.4	0.8	0.3	0.1	0.0	0.0	0.0	0.0			
3.75							0.0	0.5	0.6	1.1	1.0	0.6	0.3	0.1	0.0	0.0					
4.25								0.1	0.2	0.4	0.6	0.4	0.2	0.1	0.0	0.0					
4.75								0.0	0.1	0.1	0.3	0.3	0.2	0.1	0.0	0.0					
5.25										0.0	0.0	0.1	0.2	0.1	0.1	0.0					
5.75												0.0	0.1	0.1	0.0	0.0					
6.25													0.0	0.0	0.0	0.0					
6.75														0.0	0.0						
7.25																					

(Region I is indicated on the left; Region II on the right.)

Figure 7. % of Total Occurrences at DOE reference site overlaid on Operating Region for the Heaving Buoy.

% of Total Occurrence Hm0 (m),	Peak Period - Tp (s), center of bin																				
	0.6	1.7	2.9	4.1	5.2	6.4	7.5	8.7	9.9	11.0	12.2	13.3	14.5	15.7	16.8	18.0	19.1	20.3	21.5	22.6	23.8
0.25							0.0	0.0													
0.75					0.0	0.5	1.5	2.7	1.9	1.1	0.5	0.2	0.0								
1.25					0.0	0.6	4.1	5.6	4.5	2.7	1.3	0.7	0.3	0.1	0.0	0.0					
1.75						0.1	3.3	5.1	4.6	3.9	2.1	1.2	0.8	0.3	0.1	0.0					
2.25						0.9	5.3	3.7	4.1	2.9	1.3	0.8	0.4	0.2	0.1	0.0					
2.75						0.1	2.4	2.6	2.8	2.8	1.6	0.8	0.3	0.1	0.1	0.0					
3.25							0.4	1.5	1.5	2.0	1.4	0.8	0.3	0.1	0.0	0.0	0.0	0.0			
3.75							0.0	0.5	0.6	1.1	1.0	0.6	0.3	0.1	0.0	0.0					
4.25								0.1	0.2	0.4	0.6	0.4	0.2	0.1	0.0	0.0					
4.75								0.0	0.1	0.1	0.3	0.3	0.2	0.1	0.0	0.0					
5.25										0.0	0.0	0.1	0.2	0.1	0.1	0.0					
5.75												0.0	0.1	0.1	0.0	0.0					
6.25													0.0	0.0	0.0	0.0					
6.75																					
7.25																					

(Region I is indicated on the left; Region II on the right.)

Figure 8. Percentage of total occurrences overlaid on operating region-SANDIA WaveBot.

The comparison in Table 2 shows a buoy with a much larger volumetric displacement, similar to that tested by SANDIA [26]. It shows that fewer regions are present where volumetric limits dominate and, therefore, MPC becomes less important.

Table 2. Percentage of total sea state occurrence in Regions I and II for the heaving buoy and SANDIA WaveBot.

| % of Total Occurrence	Heaving Buoy (Swept Volume = 380 m³)	SANDIA WaveBot (Swept Volume = 4303 m³)
Region I	32%	94%
Region II	68%	6%

6. Results

6.1. Benchmarking Performance of Causal Control Design Methods

To provide a fundamental understanding of the unconstrained controls' performance, we compared Optimal Causal Control, which is based on the LQG paradigm [7], with SANDIA's causal controller designed based on the CCC approximation principle–Proportional Integral (PI) and Feedback Resonator (MPC-FBR). A set of MATLAB and Simulink files containing methods for implementing PI and FBR controllers is available online through the Marine Hydro-Kinetic Data Repository [26]. Both controllers were simulated to compare performance in different wave conditions using no wave prediction information. MPC was also simulated with the same inputs to serve as an upper limit for benchmarking performance of the two causal controller design methods.

The results of this initial trade-off study demonstrated that the algorithm provided by SANDIA provided significantly lower power capture across all sea states, but especially in longer-period waves, where the impedance-matching condition of the underlying controls law is physically impossible due to the device's volumetric constraints. Because we found the LQG method outperformed the CCC controller, the remainder of comparisons in this paper were carried out between the LQG causal control method and a linear MPC controller. Time-domain simulations were carried out using Optimal Causal Control using the LQG method outlined in [9] and linear Model Predictive Control for a complete set of wave conditions. A discrete time-step of 0.01 s and a simulation length of 3600 s was utilized. A Pierson–Moskowitz (PM) wave spectrum with the following formulation was chosen to generate the wave train using the WAFO Toolbox [27]. A plot of the input PM spectrum is shown in Figure 9

$$S(\omega) = \frac{5H_{m0}^2}{\omega_p \omega_n^5} e^{-\frac{5}{4} \omega_n^{-4}} \tag{32}$$

where $\omega_p = \frac{2\pi}{T_p}$ and $\omega_n = \frac{\omega}{\omega_p}$.
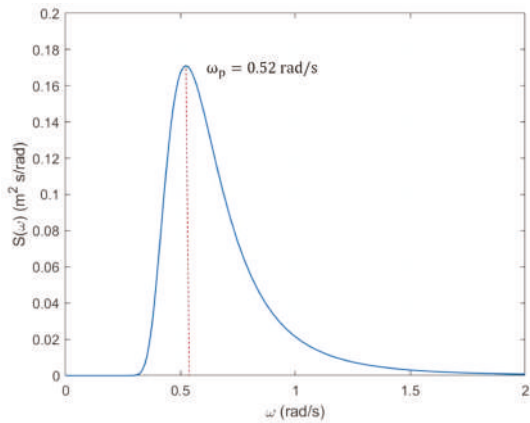
Figure 9. Spectral density computed using a PM spectrum for Hm0 = 1 m, Tp = 12 s.

6.2. Controller Performance with Unconstrained PTO Force

First, let us look at the unconstrained case where no PTO force limits are imposed on the controller. Motion constraints are still enforced because the displacement of the device relative to the equilibrium is limited to ±2 m. Figure 10 shows a plot of the ratio of average absorbed power using causal control normalized to the average absorbed power using MPC. For short period waves, the ratio of causal controller response closely follows that of MPC and the performance ratio is within 90%. This corresponds to Region I, where power absorption is dominated by the Point Absorber Limit. In long-period waves, the performance ratio starts to deteriorate for wave periods >10 s. This corresponds to Region II, where power absorption is dominated by the volumetric constraint. The results show that, unlike in the case of MPC, the stroke-limited power absorption capability of causal controllers is sub-optimal.

Causal Control / MPC		Peak Period - Tp (s), center of bin																		
		0.6	1.7	2.9	4.1	5.2	6.4	7.5	8.7	9.9	11.0	12.2	13.3	14.5	15.7	16.8	18.0	19.1	20.3	21.5
	0.25																			
	0.75																			
	1.25						100%	100%	96%	60%	59%	59%	57%	55%	58%	64%	66%	67%		
	1.75						100%	100%	82%	71%	61%	72%	77%	74%	76%	76%	75%	76%		
Hm0 (m),	2.25							100%	99%	82%	80%	80%	77%	82%	79%	79%	78%	77%	77%	
center of	2.75							100%	93%	82%	83%	81%	82%	82%	81%	80%	78%	77%	76%	
bin	3.25							100%	92%	83%	83%	82%	83%	81%	81%	79%	77%	77%	73%	
	3.75																			
	4.25		Region I							Region II										
	4.75																			
	5.25																			
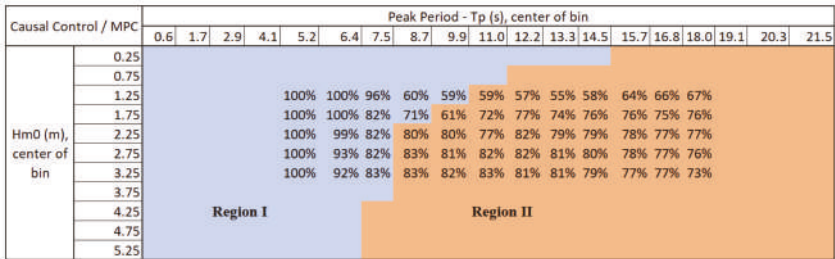
Figure 10. Avg. power (causal control)/avg. power (MPC) for a set of power-producing sea states.

Figures 11–14 show the time domain comparison of the device response with MPC and causal control for a significant wave height of 1.0 m and Tp = 15 s. The comparison is shown for a wave input in Region II where the volumetric constraint is active. Note that the MPC motion profile often covers the full stroke as opposed to causal control (Figure 13). MPC's "latching" behavior can also be seen in the velocity response profile.
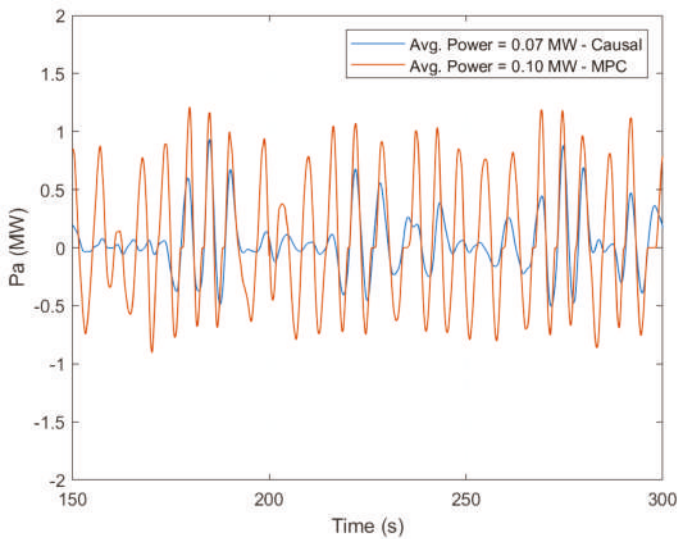
Figure 11. Comparison of average power using causal control vs. MPC for an input wave with Hs = 1.0 m, Tp = 15 s.
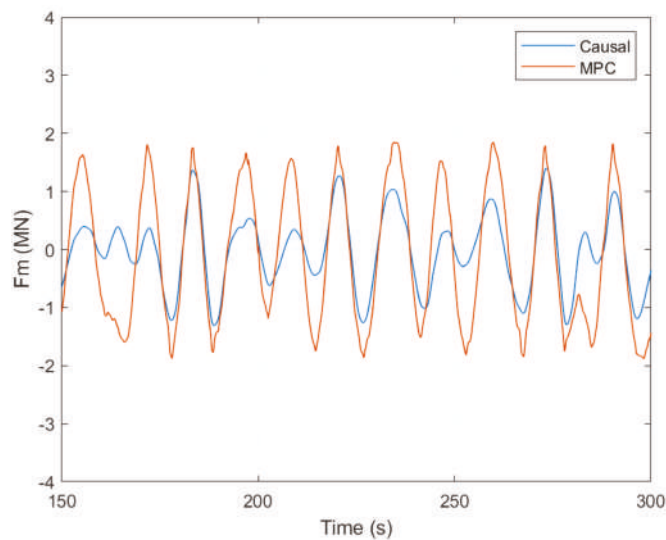
Figure 12. Comparison of PTO force using causal control vs. MPC for an input wave with Hs = 1.0 m, Tp = 15 s.
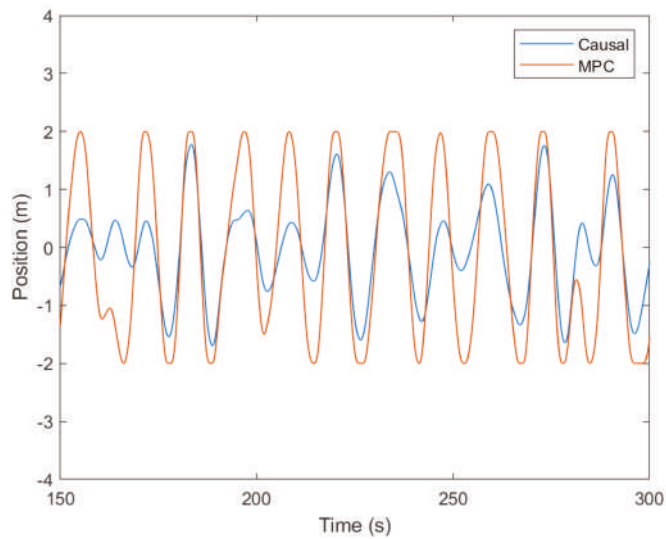
Figure 13. Comparison of position response using causal control vs. MPC for an input wave with Hs = 1.0 m, Tp = 15 s.
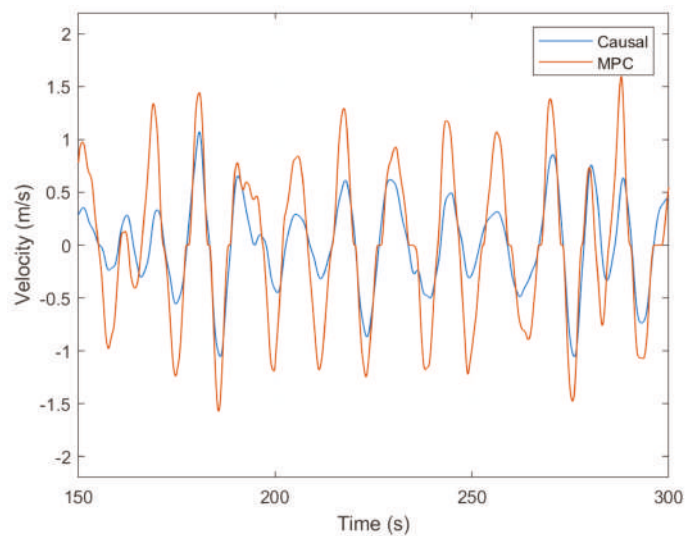
Figure 14. Comparison of velocity response using causal control vs. MPC for an input wave with Hs = 1.0 m, Tp = 15 s.

6.3. Comparison of Annual Average Energy Capture for Reference Site

A simulation study was carried out to benchmark performance of the two control approaches by calculating the overall annual average energy capture for a deep-water reference site. The heaving buoy WEC was simulated for all of the wave conditions in the scatter diagram shown in Figure 7 for the reference site at Humboldt Bay, CA. Both controllers were simulated with a stroke limit of ±2 m, and no limits on the peak PTO force were imposed.

Assuming a plant capacity factor of 30%, we obtained rated power of 473 kW using MPC and 375 kW with causal control (see Table 3). At this site, the causal controller captures only 79% of the MPC-based controller.

Table 3. Performance comparison of MPC and causal control for the DoE reference site at Humboldt Bay, CA, USA.

		MPC	Causal Control
Rated Power (kW)		473	375
Average Power (kW)		142	113
Capacity Factor		30%	30%
% Annual Energy Captured	Region I	19%	18%
	Region II	81%	82%

Figure 10 shows the ratio of average absorbed power between causal control and MPC at each sea state. Note that in the regions which are point absorber limited (Region I), the two controllers perform equally well. For long-period waves where performance is upper bound by the Volumetric Limit (Region II), as expected, MPC outperforms causal control. Overall, we note that the percentage of sea state occurrences in Region II is 67.8% and is responsible for close to 81% of the respective annual energy captured from all sea states.

6.4. Controller Performance with Constrained PTO Force

Controllers must often operate with limits imposed on the maximum PTO force due to hardware limitations. Therefore, it is important to determine how well the two control approaches handle force constraints. In this situation, the controller must attempt to maximize power absorption while simultaneously limiting the maximum forces used on the PTO. Not all controllers can achieve this dual objective effectively, which typically results in sub-optimal performance for causal controllers. Figure 15 shows a plot of average power capture vs. force constraint for both control approaches. Note that for the same choice of PTO force limit, the average power capture with MPC significantly exceeds causal control. Another way of interpreting these results is that MPC requires less PTO force to achieve the same power capture performance as that of causal control. Figures 16–19 show time domain comparison of the device response with causal control and MPC when the PTO force is limited to 0.5 MN.
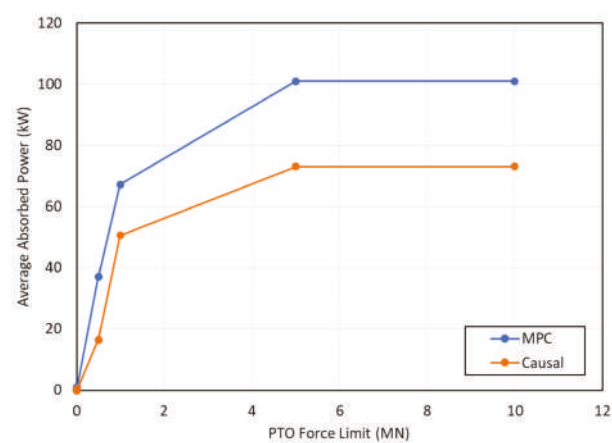
Figure 15. Average absorbed power vs. PTO force limit for wave input with Hs = 1 m, Tp = 16 s.
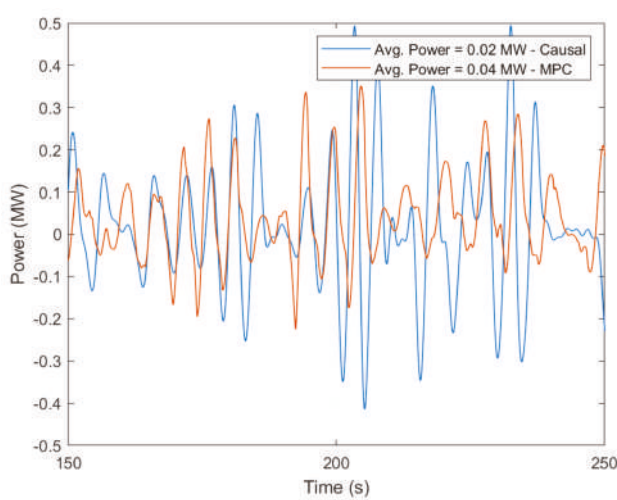
Figure 16. Time domain response comparison for absorbed power with PTO force limit = 0.5 MN. Significant wave height Hs = 1.0 m, peak period Tp = 16 s.
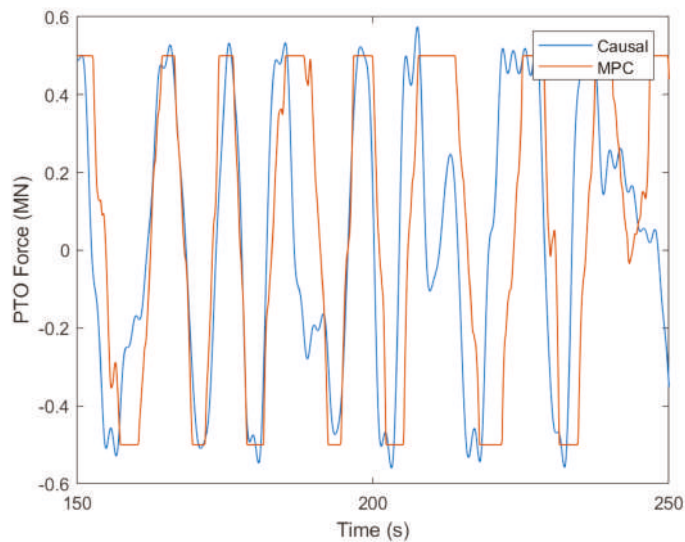
Figure 17. Time domain response comparison of PTO force with force limit = 0.5 MN. Significant wave height Hs = 1.0 m, peak period Tp = 16 s.
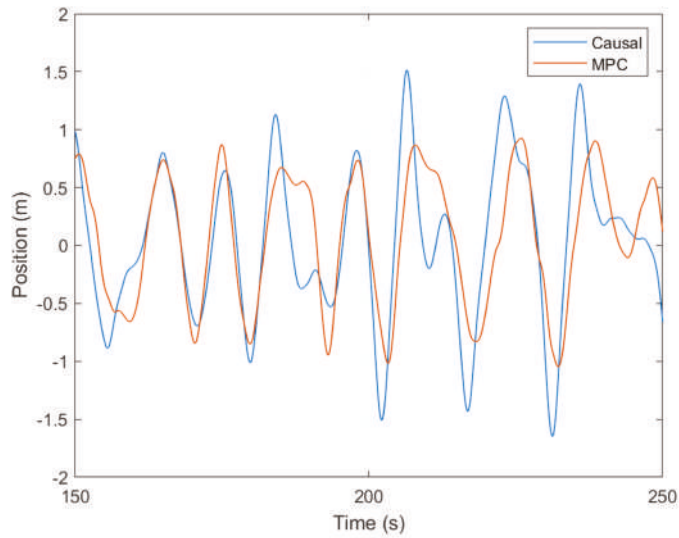
Figure 18. Time domain response comparison of WEC position with PTO force limit = 0.5 MN. Significant wave height Hs = 1.0 m, peak period Tp = 16 s.
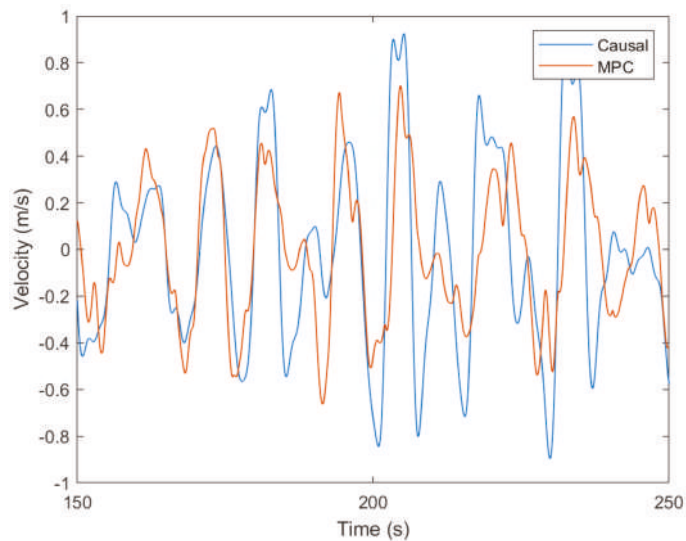
Figure 19. Time domain response comparison of WEC velocity with PTO force limit = 0.5 MN. Significant wave height Hs = 1.0 m, peak period Tp = 16 s.

In addition to the control commands issued by the linear causal controller, the causal controller also has a non-linear stroke protection block which adds to the requirements of the PTO machinery force. Causal controllers require careful tuning of the non-linear control parameters to reduce spikes in PTO machinery force. Tuning the stroke protection parameters helps to smooth the PTO force response but it comes at the cost of sacrificing the amount of power that is absorbed. Figure 17 shows a comparison of the PTO force response with causal control and MPC. Note that MPC is able to limit the PTO force effectively, and does not violate the force limit. In contrast, causal control occasionally violates the force limit.

7. Conclusions

In this paper, we presented results of a performance comparison study between causal and non-causal methods in a design trade-off space formed by theoretical upper limits on power absorption. While exploring this design trade-off space, we show that identification of operating regions based on device displaced volume and site-specific annual spectrum data are key drivers in identifying suitable control methods for a given WEC application. MPC and causal control performance is similar for Region I, where performance is constrained by Point Absorber Limits and assuming that the PTO is capable of full four-quadrant control. For operating Region II, where performance is limited by Volumetric Limits, MPC shows a significant performance advantage compared to the causal control method.

It should be noted that the cost of most in-ocean systems is directly proportional to their displaced volume. This means that the ratio of average power to volume (P/V) is a key indicator of structural efficiency of a WEC device. Small point absorbers tend to have better P/V ratios, which drives economically viable solutions towards smaller devices. As shown in this study, these smaller point absorbers will produce power predominantly in Region II, where volumetric constraints dominate and MPC provides significant performance advantages. Furthermore, constrained optimal control offered by MPC provides benefits beyond pure performance gains. The ability to directly handle a wide range of constraints as part of the optimization problem ensures constraints can be gently applied, thus reducing transient loads that are harmful to the PTO and device structural components, while maximizing power production.

References

1. Nebel, P. Maximizing the Efficiency of Wave-Energy Plant Using Complex-Conjugate Control. *J. Syst. Control Eng.* **1992**, *206*, 225–236. [CrossRef]
2. Budal, K.; Falnes, J. Interacting Point Absorbers with Controlled Motion. In *Power from Sea Waves*; Count, B., Ed.; Academic: London, UK, 1980; pp. 381–399.
3. Evans, D.V. A theory for wave-power absorption by oscillating bodies. *J. Fluid Mech.* **1976**, *77*, 1–25. [CrossRef]
4. Falnes, J.; Kurniawan, A. *Ocean. Waves and Oscillating Systems: Linear Interactions Including Wave Energy Extraction*; Cambridge University Press: Cambridge, UK, 2002.
5. Coe, R.; Bacelli, G.; Nevarez, V.; Cho, H.; Wilches-Bernal, F. *A Comparative Study on Wave Prediction for WECs. SANDIA REPORT SAND2018-8602*; Sandia National Lab.(SNL-NM): Albuquerque, NM, USA, 2018.
6. Scruggs, J.; Lattanzio, S.; Taflanidis, A.; Cassidy, I. Optimal causal control of a wave energy converter in a random sea. *Appl. Ocean Res.* **2013**, *42*, 1–15. [CrossRef]
7. Scruggs, J. Causal control design for wave energy converters with finite stroke. *IFAC-PapersOnLine* **2017**, *50*, 15678–15685. [CrossRef]
8. Nie, R.; Scruggs, J.; Chertok, A.; Clabby, D.; Previsic, M.; Karthikeyan, A. Optimal causal control of wave energy converters in stochastic waves—Accommodating nonlinear dynamic and loss models. *Int. J. Mar. Energy* **2016**, *15*, 41–55. [CrossRef]
9. Lao, Y.; Scruggs, J.; Karthikeyan, A.; Previsic, M. Discrete-time causal control of WECs with finite stroke in stochastic waves. In Proceedings of the 13th European Wave and Tidal Energy Conference, Napoli, Italy, 1–6 September 2019.
10. Blondel, E.; Bonnefoy, F.; Ferrant, P. Deterministic non-linear wave prediction using probe data. *Ocean Eng.* **2010**, *37*, 913–926. [CrossRef]
11. Lyzenga, D.; Nwogu, O.; Trizna, D.; Hathaway, K. Ocean wave field measurements using X-band Doppler radars at low grazing angles. In Proceedings of the 2010 IEEE International Geoscience and Remote Sensing Symposium, Honolulu, HI, USA, 25–30 July 2010.
12. Lyzenga, D.R.; Walker, D.T. A Simple Model for Marine Radar Images of the Ocean Surface. *IEEE Geosci. Remote Sens. Lett.* **2015**, *12*, 2389–2392. [CrossRef]
13. Gieske, P. Model Predictive Control of a Wave Energy Converter: Archimedes Wave Swing. Master's Thesis, Delft University of Technology, Delft, The Netherlands, 2007.
14. Karthikeyan, A.; Previsic, M.; Scruggs, J.; Chertok, A. Non-linear Model Predictive Control of Wave Energy Converters with Realistic Power Take-off Configurations and Loss Model. In Proceedings of the 2019 IEEE Conference on Control Technology and Applications (CCTA), Hong Kong, China, 19–21 August 2019.
15. Eriksson, C. Model Predictive Control of CorPower Ocean Wave Energy Converter. Ph.D. Thesis, KTH, Stockholm, Sweden, 2016.
16. Cretel, J.; Lewis, A.; Lightbody, G.; Thomas, G. An application of model predictive control to a wave energy point absorber. In Proceedings of the IFAC Conference on Control Methodologies and Technology for Energy Efficiency, Vilamoura, Portugal, 29–31 March 2010.
17. Nathan, T.; Yeoung, R. Nonlinear model predicitve control applied to a generic ocean-wave energy extractor. *J. Offshore Mech. Arct. Eng.* **2014**, *135*, 41901.
18. Richter, M.; Magana, M.E.; Sawodny, O.; Brekken, T.K.A. Nonlinear Model Predictive Control of a Point Absorber Wave Energy Converter. *IEEE Trans. Sustain. Energy* **2013**, *4*, 118–126. [CrossRef]
19. Faedo, N.; Olaya, S.; Ringwood, J.V. Optimal control, MPC and MPC-like algorithms for wave energy systems: An overview. *IFAC J. Syst. Control* **2017**, *1*, 37–56. [CrossRef]
20. WAMIT. Available online: https://www.wamit.com/ (accessed on 20 June 2020).
21. Coleman, T.F.; Li, Y. A Reflective Newton Method for Minimizing a Quadratic Function Subject to Bounds on Some of the Variables. *SIAM J. Optim.* **1996**, *6*, 1040–1058. [CrossRef]
22. Gill, P.E.; Murray, W.; Wright, M.H. *Practical Optimization*; Academic Press: London, UK, 1981.

23. Lao, Y.; Scruggs, J.T. A Modified Technique for Spectral Factorization of Infinite-Dimensional Systems Using Subspace Techniques. In Proceedings of the 2019 IEEE 58th Conference on Decision and Control (CDC), Nice, France, 11–13 December 2019.

24. Budal, K.; Falnes, J. A Resonant Point Absorber of Ocean Waves. *Nature* **1975**, *256*, 478–479.

25. Hals, J.; Falnes, J.; Moan, T. Constrained Optimal Control of a Heaving Buoy Wave-Energy Converter. *J. Offshore Mech. Arct. Eng.* **2010**, *133*, 011401. [CrossRef]

26. Laboratories, S.N. MASK3 for Advanced WEC Dynamics and Controls [Data Set]. Available online: https://dx.doi.org/10.15473/1581762 (accessed on 20 May 2020).

27. WAFO-Group. *WAFO—A Matlab Toolbox for Analysis of Random Waves and Loads—A Tutorial*; Center for Mathematical Sciences, Lund University: Lund, Sweden, 2000.

Article

Real-Time Nonlinear Model Predictive Controller for Multiple Degrees of Freedom Wave Energy Converters with Non-Ideal Power Take-Off

Ali S. Haider [1,*], Ted K. A. Brekken [1] and Alan McCall [2]

1   Electrical Engineering and Computer Science, Oregon State University, Corvallis, OR 97331, USA; brekken@eecs.oregonstate.edu
2   Dehlsen Associates, LLC., Santa Barbara, CA 93101, USA; amccall@ecomerittech.com
*   Correspondence: haidera@oregonstate.edu

Abstract: An increase in wave energy converter (WEC) efficiency requires not only consideration of the nonlinear effects in the WEC dynamics and the power take-off (PTO) mechanisms, but also more integrated treatment of the whole system, i.e., the buoy dynamics, the PTO system, and the control strategy. It results in an optimization formulation that has a nonquadratic and nonstandard cost functional. This article presents the application of real-time nonlinear model predictive controller (NMPC) to two degrees of freedom point absorber type WEC with highly nonlinear PTO characteristics. The nonlinear effects, such as the fluid viscous drag, are also included in the plant dynamics. The controller is implemented on a real-time target machine, and the WEC device is emulated in real-time using the WECSIM toolbox. The results for the successful performance of the design are presented for irregular waves under linear and nonlinear hydrodynamic conditions.

Keywords: nonlinear model predictive control; two degrees of freedom wave energy converter; nonlinear hydrodynamics; nonlinear power take-off

1. Introduction

Renewable energy technologies present a viable and sustainable contribution to the world's growing energy demands, and the ocean provides potential for an enormous untapped energy resource for the world's energy portfolio [1,2]. The prospect of ocean wave energy has triggered research in optimal power capture techniques for wave energy converters, including non-ideal operating conditions, such as the non-ideal PTO system constraints [3] and nonlinear sea conditions. Achieving optimal power capture by a WEC in practice is a multifaceted objective. It depends on various factors, such as the physical design of the WEC, the design of the PTO system, the ocean conditions, and the control techniques.

Model predictive control (MPC) is a promising control approach for wave energy converters' relatively slow plant dynamics because it maximizes energy capture while respecting the system's mechanical limits. MPC is a look-ahead control strategy that predicts future system behavior to solve a constrained optimization problem and determines the best control action to maximize the output power of WEC. MPC and other optimal control schemes, such as pseudospectral methods and MPC-like algorithms, have been comprehensively studied in the literature for a single WEC device and an array of wave energy converters [4–9]. An MPC algorithm uses an internal model of the plant to predict the system's future states [10]. Nonlinear control algorithms can consider the non-ideal operating conditions and nonlinear effects, including but not limited to non-ideal power take-off mechanism [11], nonlinear viscous drag terms [12,13], and nonlinear mooring dynamics [2]. The non-ideality of PTO systems in most literature is limited to the efficiency of the PTO mechanism [13–16]. One of the motivations for this research is to consider

223

higher-order nonlinear PTO characteristics as an optimization objective for the NMPC problem. The economic MPC techniques consider a general economic cost function directly in real time [17–19]. However, we have deployed a real-time iterative (RTI) algorithm [20,21] to optimize a more general class of non-ideal PTO mechanisms using pseudo-quadratic formulations [3]; this method also supports nonlinearities in the plant dynamics, such as mooring and fluid viscous drag. Another motivation for this work is investigating nonlinear multiple degrees of freedom WEC coupled to non-ideal PTO.

Lots of work has been focused on studying multiple degrees of freedom WEC devices that prove a significant improvement of power capture by the WEC device. Multi-resonant feedback control of a three degree of freedom WEC is presented [22], where a linear hydrodynamic model is considered, and multi-resonant proportional-derivative control law is proposed where the focus is linear plant dynamics under unconstrained control. An analysis of a multi-degree-of-freedom point absorber WEC in the surge, heave, and pitch directions is presented in [23], and frequency and time-domain formulations are presented for the linear plant dynamics. A time-domain model for a point absorber WEC in six degrees of freedom is developed in [24] with an optimal resistive loading. The three degrees of a freedom model of a WEC is presented in [25], where the capture performance of various PTO systems is investigated for a linear plant model. An active control strategy based on the optimal velocity trajectory tracking for a multi-DoF submerged point absorber WEC is presented in [26], where a linearized dynamic system model is considered along with an ideal PTO mechanism. A nonlinear MPC design and implementation based on differential flatness parameterization has been proposed in [27]. Given that most of the work focused on linear plant dynamics for multiple degrees of freedom WEC or ideal PTO mechanisms, and the lack of application of NMPC for such class or problems, we have investigated the application of NMPC to nonlinear multiple DoF WEC plant with a non-ideal PTO mechanism, and focus on the real-time implementation of the control algorithm on a real-time target machine.

This research presents the maximization of power extraction by a 2-DoF WEC device, a WECSIM [28] model of the full-scale version of the Dehlsen Associates, LLC multi-pod CENTIPOD [29]. Although the CENTIPOD device is an array device, the cross-coupling between pods is ignored for this study, which is negligible for the sea conditions of interest in this work and will be investigated in the future. The goal is to optimize the power extracted by the heave and pitch PTOs subject to actuation and velocity constraints. The objective function is a nonstandard and nonquadratic functional of PTO force and velocity, resulting from a practical PTO generator power loss characteristic. The WEC model includes nonlinear viscous drag terms; hence, the resulting plant model is a nonlinear dynamic system. We have implemented an NMPC for the problem. To tackle a free-formed objective function subjected to nonlinear system dynamics, we have used the extended version of the NMPC design from [30], based on pseudo-quadratization using an ACADO toolkit [21]. No prior knowledge of wave excitation is assumed. The WEC model is simulated on a real-time emulator machine, while control is deployed on a Speedgoat real-time performance machine [31], which is interfaced with the WEC emulator machine through an ethernet port. The simulation results for real-time NMPC are presented for the linear and nonlinear hydrodynamics conditions simulated in WECSIM.

2. Time Domain Model of a Multiple Degree of Freedom WEC

The WEC device is a full-scale version of the Dehlsen Associates, LLC multi-pod CENTIPOD [29,32]. A 1:35-scale version of the device is shown in Figure 1. This CENTIPOD device has three floating pods and three spars fixed to a backbone structure. The backbone is anchored using mooring lines, as shown in Figure 2. In its 2-DoF version, each pod is attached to a PTO mechanism in the heave and pitch degrees of freedom. All pods in Figure 2 are assumed identical, and since the CENTIPOD device is an array device, the array effect [33] could become prominent as the significant height of the waves increases and the incident angle of the waves is not parallel to the *x*-axis in Figure 2. For this study,

incident waves are assumed parallel to the *x*-axis, and for the sea state of interest in this work, the cross-coupling between the pods is very small and is neglected, although it will be investigated in future work.
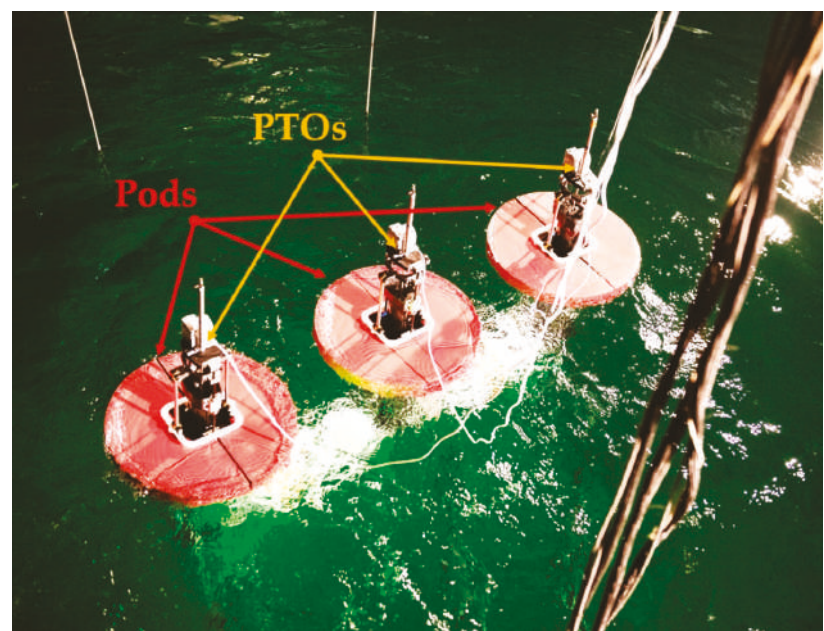

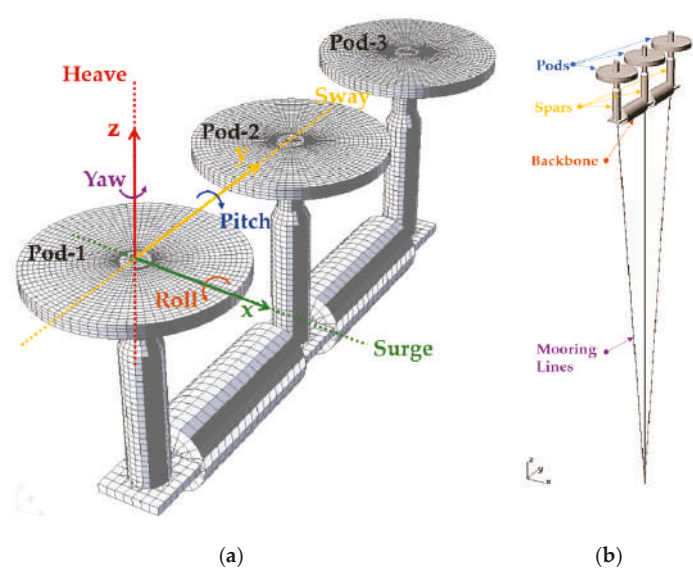**Figure 1.** Image of the Dehlsen Associates, LLC, 1:35-scale CENTIPOD WEC.

(**a**)   (**b**)

Figure 2. Degrees of freedom for dynamic modeling of CENTIPOD WEC: (**a**) baseline configuration; (**b**) model with mooring lines.

We will follow the subscript notation of the WEC-Sim toolbox [28] for the degrees of freedom for WEC, in which the integers from 1, 2, ... 6 correspond to surge, sway, heave, roll, pitch, and yaw, respectively. Some other notations and symbols for WEC modeling are given in Table 1.

Table 1. Notations and symbols for WEC modeling.

Variable	Description
v_i	Velocity (Linear or Angular) in i^{th} DoF
x_i	Displacement (Linear or Angular) in i^{th} DoF
ξ_i	Intermediate State variables for radiation force State-Space approximation
$F_{r,pq}$	Radiation force in p^{th} DoF due to velocity in q^{th} DoF
$F_{hs,i}$	Hydrostatic force in i^{th} DoF
$F_{v,i}$	Viscous drag force in i^{th} DoF
$F_{e,i}$	Wave excitation force in i^{th} DoF
$F_{p,i}$	PTO force in i^{th} DoF
m	Mass of the float
$A_{pq}(\infty)$	Added mass at the infinite frequency in p^{th} DoF due to acceleration in q^{th} DoF
C_i	The hydrostatic restoring coefficient in i^{th} DoF
$C_{vd,i}$	Viscous drag coefficient in i^{th} DoF
A_{qp}	Frequency-dependent added mass in p^{th} DoF due to acceleration in q^{th} DoF
B_{qp}	Frequency-dependent damping in p^{th} DoF due to velocity in q^{th} DoF
K_{pq}	Radiation force impulse response without infinite frequency added mass
Z_{qp}	WEC Intrinsic impedance response in p^{th} DoF due to velocity in q^{th} DoF
a_i	Polynomial coefficients
$c_{i,j}$	Polynomial coefficients for cost functional
$I_{p,i}$	i^{th} PTO current
η_{Conv}	PTO converter efficiency
K_{Cu}	PTO generator copper loss constant
R_Ω	PTO generator winding resistance

2.1. Surge-Pitch-Heave Model of WEC Modeling in State-Space Form

Each pod in Figure 2 is modeling as a wave point absorber device. The Cummins equation for the coupled surge and pitch dynamics for a point absorber pod (assuming a local reference frame) is given by,

$$(m + A_{11}(\infty))\dot{v}_1 + A_{15}(\infty)\dot{v}_5 = -F_{r,11}(t) - F_{r,15}(t) - F_{v,1}(t) + F_{e,1}(t), \tag{1}$$

$$(m + A_{55}(\infty))\dot{v}_5 + A_{51}(\infty)\dot{v}_1 = -F_{r,55}(t) - F_{r,51}(t) - F_{v,5}(t) - F_{hs,5}(t) - F_{p,5}(t) + F_{e,5}(t). \tag{2}$$

The Cummins equation for the heave dynamics of a point absorber pod is given by,

$$(m + A_{33}(\infty))\dot{v}_3(t) = -F_{r,33}(t) - F_{hs,3}(t) - F_{v,3}(t) - F_{p,3}(t) + F_{e,3}(t), \tag{3}$$

The hydrostatic, viscous damping, and radiation force terms in (1) through (3) are given by,

$$F_{r,ij}(t) = \int_{-\infty}^{t} K_{ij}(t - \tau)v_j d\tau, \tag{4}$$

$$F_{hs,i}(t) = C_i x_i, \tag{5}$$

$$F_{v,i}(t) = C_{d,i}v_i|v_i|. \tag{6}$$

A transfer function expression can approximate the convolution integral term in (4),

$$F_{r,pq}(t) = \int_{-\infty}^{t} K_{pq}(t - \tau)v_q d\tau \Leftrightarrow F_{r,pq}(j\omega) = Z_{pq}(j\omega)V_q(j\omega), \tag{7}$$

Using the device data from WAMIT [34], we can approximate the intrinsic impedance $Z_{pq}(j\omega)$ in (7) by a second order transfer function using system identification techniques,

$$Z_{pq}(j\omega) = \left[j\omega \left(A_{pq}(j\omega) - A_{pq}(\infty) \right) + B_{qp}(j\omega) \right] \approx \left. \frac{\alpha_{pq,1}s + \alpha_{pq,0}}{s^2 + \beta_{pq,1}s + \beta_{pq,0}} \right|_{s=j\omega}, \qquad (8)$$

Using (8) in (7) enables us to express the radiation force as a second-order transfer function,

$$F_{r,pq}(s) \approx \frac{\alpha_{pq,1}s + \alpha_{pq,0}}{s^2 + \beta_{pq,1}s + \beta_{pq,0}} V_q(s), \qquad (9)$$

The transfer function expression in (9) can be converted to the state-space expressions in the observer canonical forms for each of the radiation force terms,

$$\begin{bmatrix} \dot{\xi}_k(t) \\ \dot{\xi}_{k+1}(t) \end{bmatrix} = \begin{bmatrix} 0 & 1 \\ a_k & a_{k+1} \end{bmatrix} \begin{bmatrix} \xi_k(t) \\ \xi_{k+1}(t) \end{bmatrix} + \begin{bmatrix} b_k \\ b_{k+1} \end{bmatrix} v_q(t), \qquad (10)$$

$$y_{pq}(t) = \begin{bmatrix} 1 & 0 \end{bmatrix} \begin{bmatrix} \xi_k(t) \\ \xi_{k+1}(t) \end{bmatrix} \approx F_{r,pq}(t). \qquad (11)$$

By the comparison of (9)–(11), we have, $\alpha_{pq,1} = b_k$, $\beta_{pq,1} = -a_{k+1}$, $\beta_{pq,0} = -a_k$, and $\alpha_{pq,0} = b_{k+1} - b_k a_{k+1}$. Making a change of variables in (1),

$$M_{ii} = (m + A_{ii}(\infty)), \qquad (12)$$

$$F_{1,net} = -F_{r,11}(t) - F_{r,15}(t) - F_{v,1}(t) + F_{e,1}(t), \qquad (13)$$

$$F_{5,net} = -F_{r,55}(t) - F_{r,51}(t) - C_5 x_5 - F_{v,5}(t) - F_{p,5}(t) + F_{e,5}(t). \qquad (14)$$

Using (12)–(14) in (1), we get the pitch-surge coupled model of a pod as,

$$\begin{bmatrix} \dot{v}_1 \\ \dot{v}_5 \end{bmatrix} = \begin{bmatrix} M_{11} & A_{15}(\infty) \\ A_{51}(\infty) & M_{55} \end{bmatrix}^{-1} \begin{bmatrix} F_{1,net} \\ F_{5,net} \end{bmatrix} \qquad (15)$$

The viscous drag force term $v_i|v_i|$ in (6) is a hard nonlinearity that may lead to convergence issues for the optimization solvers. One solution is to approximate this term with a soft nonlinearity by replacing it with a smooth higher-order polynomial. A third-order polynomial approximation for $v_i|v_i|$ is used in the surge and heave direction, where the range of interest of velocity is $v_i \in (-1.5, 1.5)$ m/sec, and a fifth-order polynomial approximation is used for pitch direction, where the range of interest of velocity is $v_i \in (-0.5, 0.5)$ rad/sec. With, $p_{i,j}$ being the jth polynomial coefficient for i^{th} degree polynomial curve fit

$$F_{v,i} = C_{d,i} v_i |v_i| \approx C_{d,i} \left(p_{3,3} v_i^3 + p_{3,1} v_i \right), \quad i = 1, 3, \qquad (16)$$

$$F_{v,5} = C_{d,5} v_5 |v_5| \approx C_{d,5} \left(p_{5,5} v_5^5 + p_{5,3} v_5^3 + p_{5,1} v_5 \right). \qquad (17)$$

The curve fits (16) and (17) are shown in Figure 3a,b, respectively. Using (15) and (3), we get a Surge-Heave-Pitch model of a pod as,

$$\dot{\mathbf{X}} = \mathbf{A}\mathbf{X} + \mathbf{B_p}\mathbf{F_p} + \mathbf{B_v}\mathbf{F_v} + \mathbf{B_e}\mathbf{F_e}, \qquad (18)$$

where,

$$\mathbf{F_p} = \begin{bmatrix} F_{p,5} & F_{p,3} \end{bmatrix}^T, \qquad (19)$$

$$\mathbf{F_v} = \begin{bmatrix} F_{v,1} & F_{v,5} & F_{v,3} \end{bmatrix}^T, \qquad (20)$$

$$\mathbf{F_e} = \begin{bmatrix} F_{e,1} & F_{e,5} & F_{e,3} \end{bmatrix}^T, \qquad (21)$$

$$\mathbf{X} = \begin{bmatrix} v_1 & v_5 & x_5 & \tilde{\zeta}_3 & \tilde{\zeta}_4 & \tilde{\zeta}_5 & \tilde{\zeta}_6 & \tilde{\zeta}_7 & \tilde{\zeta}_8 & \tilde{\zeta}_9 & \tilde{\zeta}_{10} & v_3 & x_3 & \tilde{\zeta}_1 & \tilde{\zeta}_2 \end{bmatrix}^T. \tag{22}$$

and the radiation force terms are approximated by following state variables using (10),

$$F_{r,11} = \tilde{\zeta}_3, F_{r,15} = \tilde{\zeta}_5, F_{r,51} = \tilde{\zeta}_7, F_{r,55} = \tilde{\zeta}_9, F_{r,33} = \tilde{\zeta}_1. \tag{23}$$

and,

$$\mathbf{A} = \left[\begin{array}{ccccccccccc|cccc}
0 & 0 & -m_{15}C_5 & -m_{11} & 0 & -m_{11} & 0 & -m_{15} & 0 & -m_{15} & 0 & & & & \\
0 & 0 & -m_{55}C_5 & -m_{51} & 0 & -m_{51} & 0 & -m_{55} & 0 & -m_{55} & 0 & & & & \\
0 & 1 & 0 & 0 & 0 & 0 & 0 & 0 & 0 & 0 & 0 & & & & \\
b_3 & 0 & 0 & 0 & 1 & 0 & 0 & 0 & 0 & 0 & 0 & & & & \\
b_4 & 0 & 0 & a_3 & a_4 & 0 & 0 & 0 & 0 & 0 & 0 & & & & \\
0 & b_5 & 0 & 0 & 0 & 0 & 1 & 0 & 0 & 0 & 0 & & \mathbf{0}_{11\times 4} & & \\
0 & b_6 & 0 & 0 & 0 & a_5 & a_6 & 0 & 0 & 0 & 0 & & & & \\
0 & b_7 & 0 & 0 & 0 & 0 & 0 & 0 & 1 & 0 & 0 & & & & \\
0 & b_8 & 0 & 0 & 0 & 0 & 0 & a_7 & a_8 & 0 & 0 & & & & \\
b_9 & 0 & 0 & 0 & 0 & 0 & 0 & 0 & 0 & 0 & 1 & & & & \\
b_{10} & 0 & 0 & 0 & 0 & 0 & 0 & 0 & 0 & a_9 & a_{10} & & & & \\
\hline
& & & & & & & & & & & 0 & \frac{-C_3}{M_{33}} & \frac{-1}{M_{33}} & 0 \\
& & & \mathbf{0}_{4\times 11} & & & & & & & & 1 & 0 & 0 & 0 \\
& & & & & & & & & & & b_1 & 0 & 0 & 1 \\
& & & & & & & & & & & b_2 & 0 & a_1 & a_2
\end{array}\right], \tag{24}$$

$$\mathbf{B_p} = \begin{bmatrix} -m_{15} & 0 \\ -m_{55} & 0 \\ 0 & 0 \\ 0 & 0 \\ 0 & 0 \\ 0 & 0 \\ 0 & 0 \\ 0 & 0 \\ 0 & 0 \\ 0 & 0 \\ 0 & \frac{-1}{M_{33}} \\ 0 & 0 \\ 0 & 0 \\ 0 & 0 \end{bmatrix}, \mathbf{B_v} = \begin{bmatrix} -m_{11} & -m_{15} & 0 \\ -m_{51} & -m_{55} & 0 \\ 0 & 0 & 0 \\ 0 & 0 & 0 \\ 0 & 0 & 0 \\ 0 & 0 & 0 \\ 0 & 0 & 0 \\ 0 & 0 & 0 \\ 0 & 0 & 0 \\ 0 & 0 & 0 \\ 0 & 0 & \frac{-1}{M_{33}} \\ 0 & 0 & 0 \\ 0 & 0 & 0 \\ 0 & 0 & 0 \end{bmatrix}, \mathbf{B_e} = \begin{bmatrix} m_{11} & m_{15} & 0 \\ m_{51} & m_{55} & 0 \\ 0 & 0 & 0 \\ 0 & 0 & 0 \\ 0 & 0 & 0 \\ 0 & 0 & 0 \\ 0 & 0 & 0 \\ 0 & 0 & 0 \\ 0 & 0 & 0 \\ 0 & 0 & 0 \\ 0 & 0 & \frac{1}{M_{33}} \\ 0 & 0 & 0 \\ 0 & 0 & 0 \\ 0 & 0 & 0 \end{bmatrix}, \tag{25}$$

Putting (16) and (17) in (18) gives us a 2-DoF (heave and pitch) WEC nonlinear plant model, where the surge is coupled with the pitch and heave is a decoupled DoF. We can use this plant model as a prediction model in NMPC.

2.2. Nonquadratic WEC-PTO Model

The electrical power output from the PTO mechanism of the WEC is the difference between the mechanical power input from the waves and the losses in the PTO system. For a given PTO generator, the electrical PTO power cost functional to be maximized, including the electrical losses, is given by,

$$\max_{F_{p,i}} P_{E,i} = \eta_{Conv}\left(P_{Mechanical,i} - P_{Loss,i} \right) = \eta_{Conv}\left(F_{p,i}v_i - K_{Cu}\left[I_{p,i}(F_{p,i})\right]^2 R_\Omega \right), \tag{26}$$

The case study scenario is taken from McCleer Power's Linear PTO generator [3] with the PTO force–current characteristics given by Figure 4. We can approximate the experimental data in Figure 4 with a mathematical relation, such as a piecewise linear function or a nonlinear function. We have used polynomial approximation which is a

smooth function. This relation is described by a third-order curve fit between the PTO current and the PTO force,

$$I_{p,i}(F_{p,i}) = a_{3,i}F_{p,i}^3 + a_{2,i}F_{p,i}^2 + a_{1,i}F_{p,i} + a_{0,i}, \tag{27}$$

Putting (27) in (16), we get,

$$P_{E,i} = c_{0,i}F_{p,i}v_i - \left(c_{1,i}F_{p,i}^6 + c_{2,i}F_{p,i}^5 + c_{3,i}F_{p,i}^4 + c_{4,i}F_{p,i}^3 + c_{5,i}F_{p,i}^2 + c_{6,i}F_{p,i} + c_{7,i} \right) , \tag{28}$$

The PTO cost functional surface in (28) is plotted in the PTO velocity–force plane, as shown in Figure 5. The surface plot of the mechanical PTO power, $P_{Mechanical,i} = F_{p,i}v_i$ is non-convex, as shown in Figure 5. However, the electrical PTO power surface, $P_{E,i}$ in (26) has a quadratic power loss term, and it gives convexity to the electrical power surface along the PTO force axis in Figure 5.
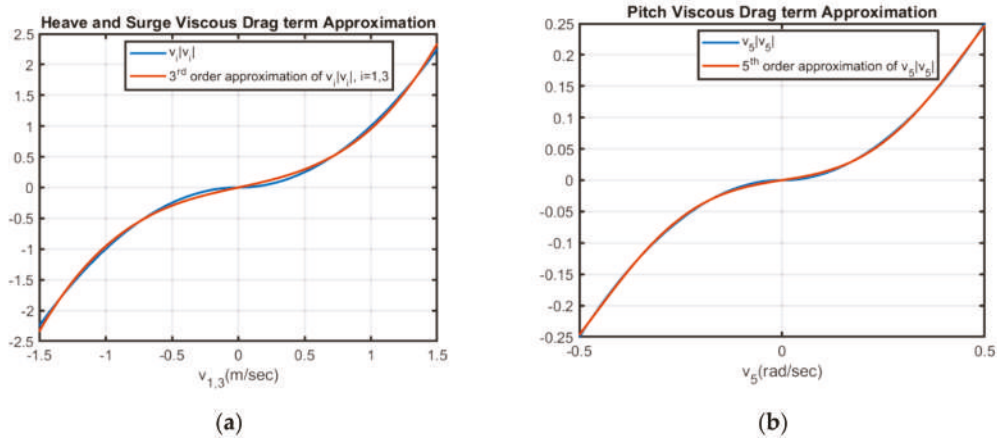
Figure 3. Polynomial approximations of the quadratic drag term $v_i|v_i|$: (**a**) 3rd order curve fit for heave and surge axes; (**b**) 5th order curve fit for pitch axis.
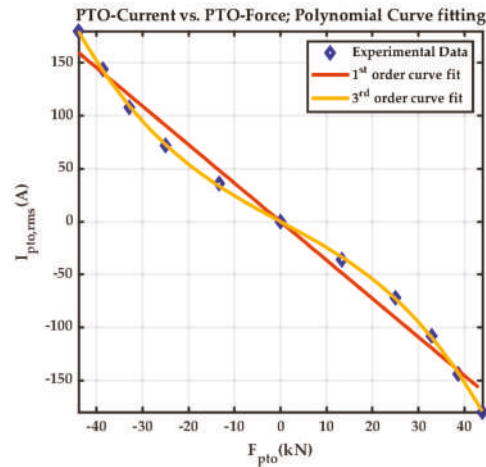
Figure 4. Polynomial curve fitting to the PTO force-current experimental data for a PTO generator.
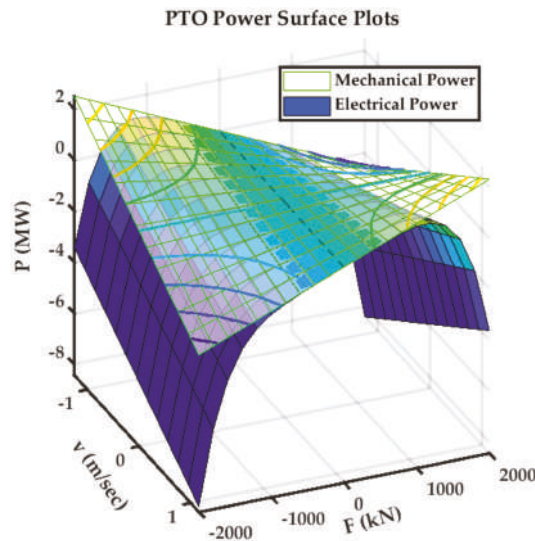
Figure 5. Mechanical and electrical PTO power surface plot in PTO velocity-force plane.

3. Implementation of NMPC for 2-DoF Heave-Pitch WEC

The optimal control problem of a WEC involves manipulating the PTO force/torque to maximize the power capture while respecting some system constraints. Various optimal control approaches have been developed, and a comprehensive review can be found in [34]. MPC is a model-based online optimal control solution, and a given NMPC problem optimizes a manipulated variable $u(t)$ to maximize some cost functional $P(\cdot)$ while respecting the system constraints. A special class of NMPC problems has been formulated in [30], in which the cost functional takes on a nonlinear piecewise polynomial form. Considering the case of finite horizon optimization control, we can mathematically describe the NMPC problem of such a class as,

$$\underset{\mathbf{u}(t)}{maximize}\ \mathbf{P}\Big[t,\dot{\mathbf{X}}(t),\mathbf{X}(t),\mathbf{U}(t),\mathbf{p}(t)\Big] \tag{29}$$

$$\text{Where}:\ \mathbf{P}(\cdot) = \begin{cases} P_1(\cdot) + \rho_{N,1}(\cdot), & q_k(t) < R_1 \\ P_2(\cdot) + \rho_{N,2}(\cdot), & R_1 \leq q_k(t) \leq R_2 \\ \quad\vdots & \quad\vdots \\ P_j(\cdot) + \rho_{N,j}(\cdot), & R_{j-1} \leq q_k(t) \leq R_j \end{cases}, \tag{30}$$

subject to,

$$\text{Dynamic Constraints}:\ \mathbf{0} = \mathbf{g}\Big(t,\dot{\mathbf{X}}(t),\mathbf{X}(t),\mathbf{U}(t),\mathbf{d}(t),\mathbf{p}(t),N\Big), \tag{31}$$

$$\text{Boundary Constraint Function}:\ \mathbf{0} = \mathbf{r}(N,\mathbf{X}(0),\mathbf{U}(0),\mathbf{X}(N),\mathbf{U}(N),\mathbf{p}), \tag{32}$$

$$\text{Path Constraints Function}:\ 0 \geq \mathbf{s}(t,\mathbf{X}(t),\mathbf{U}(t),\mathbf{p}(t)). \tag{33}$$

The description of various variables and constants in (298) through (33) is given in Table 2. The wave excitation force $\mathbf{F_e}$ acting on the hull is considered an unmeasured system disturbance, and based on the available measurements, the controller internally estimates $\mathbf{F_e}$.

Table 2. Symbols and notations for NMPC formulation.

Variable	Description
N	Prediction horizon
$\mathbf{X}$	State vector
$\rho_{N,i}$	Finite horizon terminal cost penalty or Mayer terms
$P_i(\cdot)$	Some Nonlinear functions or Lagrange terms
$\mathbf{p}$	A column vector of time-varying parameters
$\mathbf{U}$	PTO Force manipulated variable vector, $\mathbf{F_p}(N)$
$\mathbf{d}$	Excitation force disturbance vector, $\mathbf{F_e}(N)$
$q_k(t)$	Cost functional scheduling variable
R_i	Some real numbers, such that $R_{k+1} > R_k$

For the 2-DoF (heave-pitch) WEC problem, the objective function to be maximized in (28) will be the sum of electrical PTO power output in the heave and pitch DoFs for each pod,

$$P_E = P_{E,3} + P_{E,5} \; , \tag{34}$$

Using the technique developed in [30], we can put (34) into the pseudo-quadratic form by defining a suitable $\mathbf{h_i}$ vector for heave and pitch as,

$$\mathbf{h}_i = \begin{bmatrix} F_{p,i}^3 & F_{p,i}^2 & F_{p,i} & v_i & 1 \end{bmatrix}^T, \; i = 3, 5 \tag{35}$$

with,

$$\mathbf{h} = \begin{bmatrix} \mathbf{h_3} \\ \mathbf{h_5} \end{bmatrix}, \tag{36}$$

we can reformulate (34) as,

$$P_E = \frac{1}{2}\mathbf{h}^T \left(2 \begin{bmatrix} \mathbf{W_3} & \mathbf{0} \\ \mathbf{0} & \mathbf{W_5} \end{bmatrix} \right) \mathbf{h} = \frac{1}{2}\mathbf{h}^T (2\mathbf{W})\mathbf{h}, \tag{37}$$

By using (28) in (34), the weighting matrix $\mathbf{W}$ can be obtained by polynomial decomposition of (34) by the vector $\mathbf{h}$ in (36) as the basis vector,

$$\mathbf{W_i} = \frac{1}{2} \begin{bmatrix} -2c_{1,i} & -c_{2,i} & 0 & 0 & 0 \\ -c_{2,i} & -2c_{3,i} & -c_{4,i} & 0 & 0 \\ 0 & -c_{4,i} & -2c_{5,i} & c_{0,i} & -c_{6,i} \\ 0 & 0 & c_{0,i} & 0 & 0 \\ 0 & 0 & -c_{6,i} & 0 & -2c_{7,i} \end{bmatrix}, \; i = 3, 5 \tag{38}$$

The controller is implemented using an ACADO toolkit [21] following the approach developed in [3].

4. Results

The schematic diagram of the test setup is shown in Figure 6. The corresponding hardware setup is shown in Figure 7. NMPC is designed in the host machine, which generated code and deployed the controller to the Speedgoat performance real-time target machine [31], model-109100 with Intel Core i3 3.3 GHz, two cores, and 2048 MB DDR3 RAM. The Speedgoat machine is interfaced with a real-time WEC emulator machine through an Ethernet universal data port (UDP) channel. The three WEC pods in Figure 1 are assumed identical, and the same controller is implemented for each pod as shown in Figure 8, while the cross-coupling between pods is ignored for this work. The physical velocity and force constraints of the PTO mechanisms imposed as $|v_3| \leq 2 \; m/sec$, $|v_5| \leq 0.5 \; rad/sec$ and $|F_{p,i}| \leq 400 \; kN$. The emulated WEC-Sim model of CENTIPOD device is shown in Figure 9.
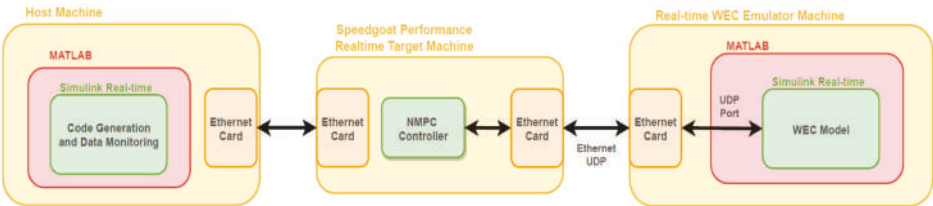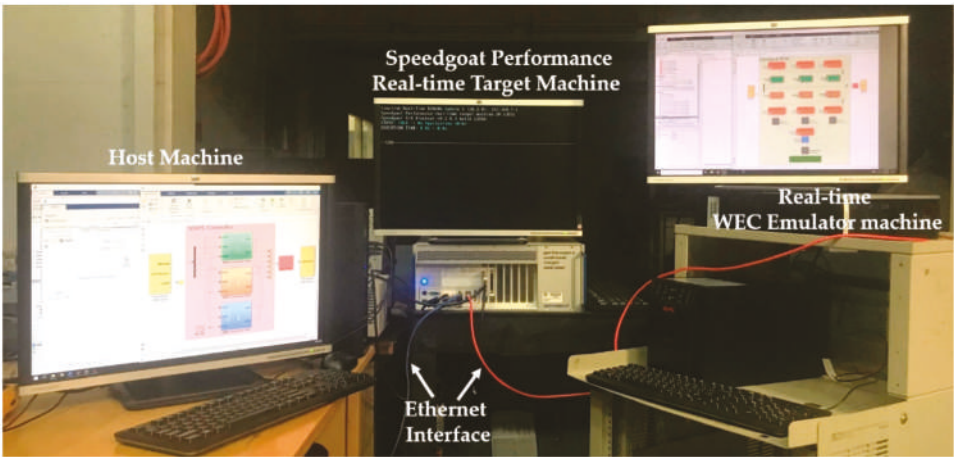
Figure 6. Schematic diagram of the test setup.

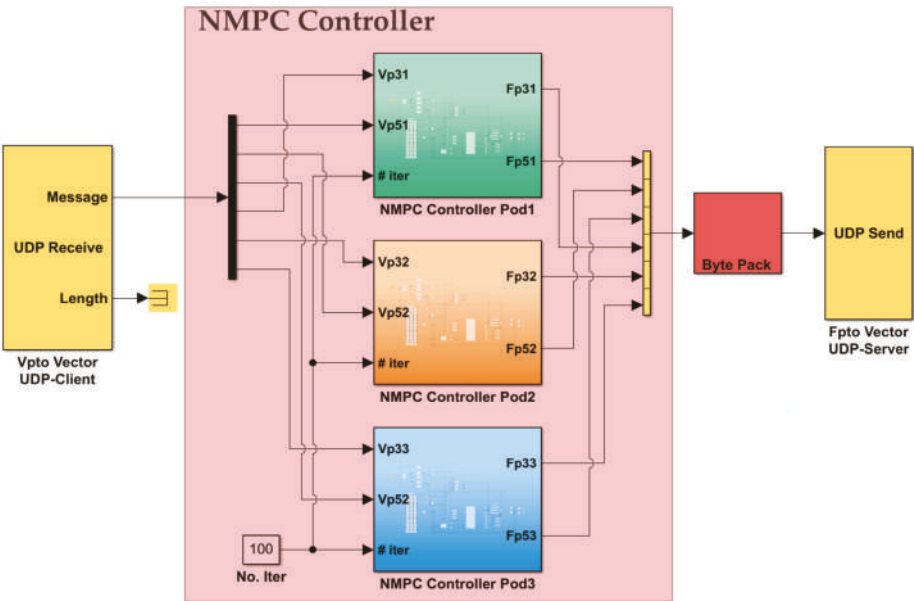
Figure 7. Hardware test setup.

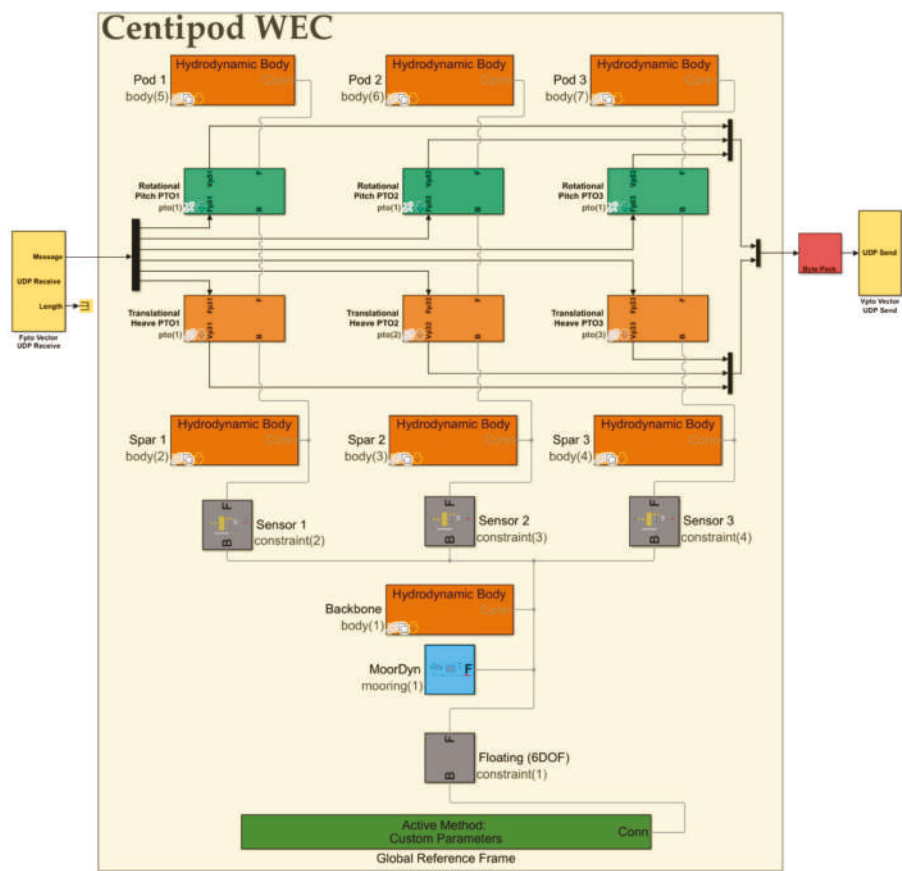**Figure 8.** NMPC controller for 2-DoF 3-pod CENTIPOD WEC.

Figure 9. WEC-Sim model of Dehlsen's 2-DoF CENTIPOD device with heave and pitch PTOs for each pod.

Since the WEC pods are assumed identical with no cross-coupling, results are presented only for a single pod. The sea state of interest for WEC-Sim is given in Table 3. This particular sea state's selection is based on the future testing site of interest for the WEC device, although the hardware testing and a more elaborated study involving other sea states are planned for the future. A step time of 0.1 *sec* is used for MPC formulation, close to one-tenth of the peak wave period. The performance of NMPC is compared against the linear MPC, and the analysis is performed for the linear and nonlinear hydrodynamics sea conditions.

Table 3. Sea states for WEC-Sim simulation.

WEC-Sim Simulation Parameter	Value
Significant Wave Height [m]	2.5
Peak Period [s]	8
Wave Spectrum Type	Pierson Moskowitz (PM)
Wave Class	Irregular

The average electrical power output results for the heave and pitch PTOs for 2-DoF pod-1 are shown in Figures 10a and 10b, respectively, for linear MPC and NMPC subjected to linear hydrodynamic conditions. Here, we consider the exponentially weighted moving average (EWMA) with the forgetting factor set to unity. The instantaneous electrical power output results corresponding to Figure 10 are shown in Figure 11. The PTO force and wave excitation force profiles for 2-DoF Pod-1 with linear and nonlinear MPC under linear hydrodynamic conditions are shown in Figure 12. The PTO velocity and displacement plots for 2-DoF Pod-1 with linear and nonlinear MPC under linear hydrodynamic conditions are shown in Figure 13.
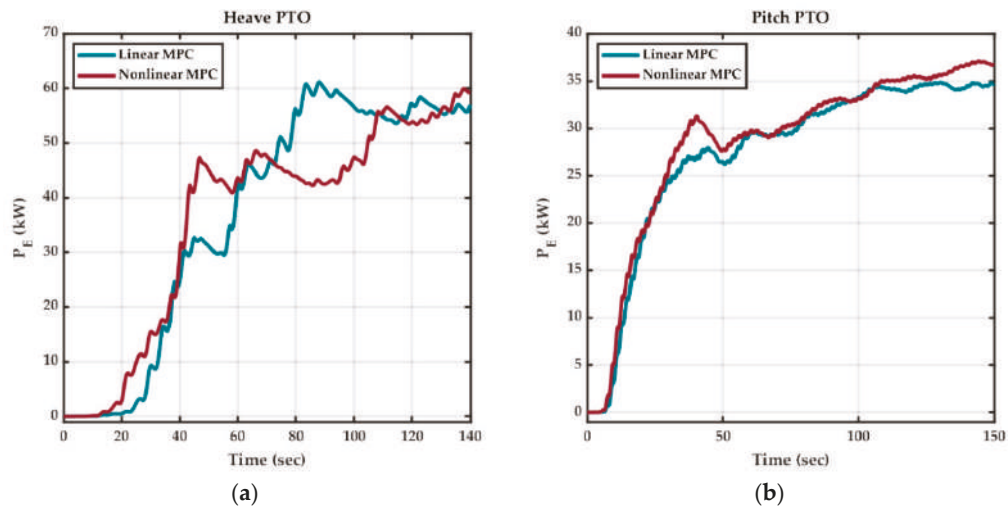
Figure 10. Average electrical PTO power output for 2-DoF Pod-1 with linear and nonlinear MPC under linear hydrodynamic conditions in WEC-Sim and $|F_{pto}| \leq 400 \ kN$: (**a**) Pod-1 Heave PTO; (**b**) Pod-1 Pitch PTO.
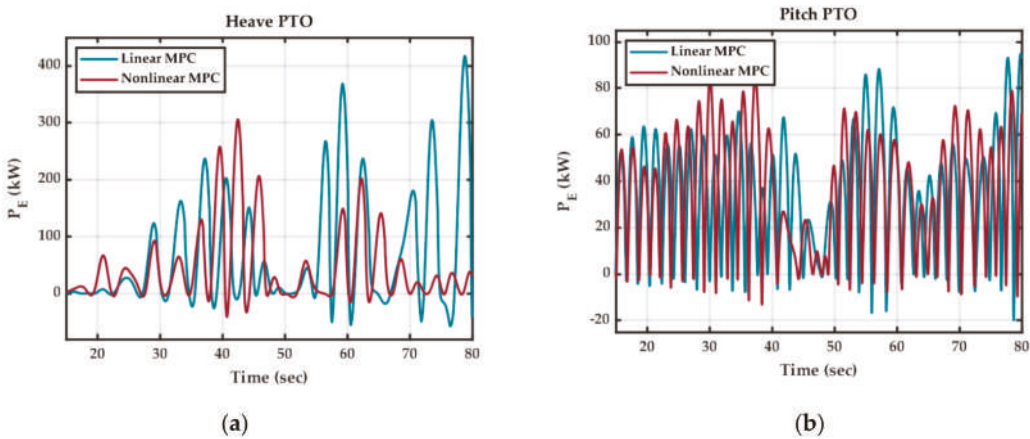
Figure 11. Instantaneous electrical PTO power output for 2-DoF Pod-1 with linear and nonlinear MPC under linear hydrodynamic conditions in WEC-Sim and $|F_{pto}| \leq 400 \ kN$: (**a**) Pod-1 Heave PTO; (**b**) Pod-1 Pitch PTO.
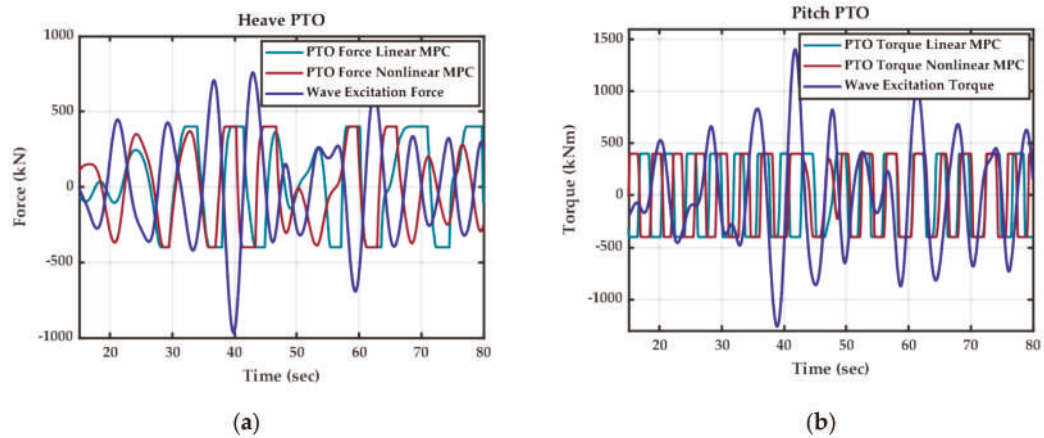
Figure 12. The PTO force and wave excitation force profiles for 2-DoF Pod-1 with linear and nonlinear MPC under linear hydrodynamic conditions in WEC-Sim and $|F_{pto}| \leq 400\ kN$: (**a**) Pod-1 Heave PTO; (**b**) Pod-1 Pitch PTO.
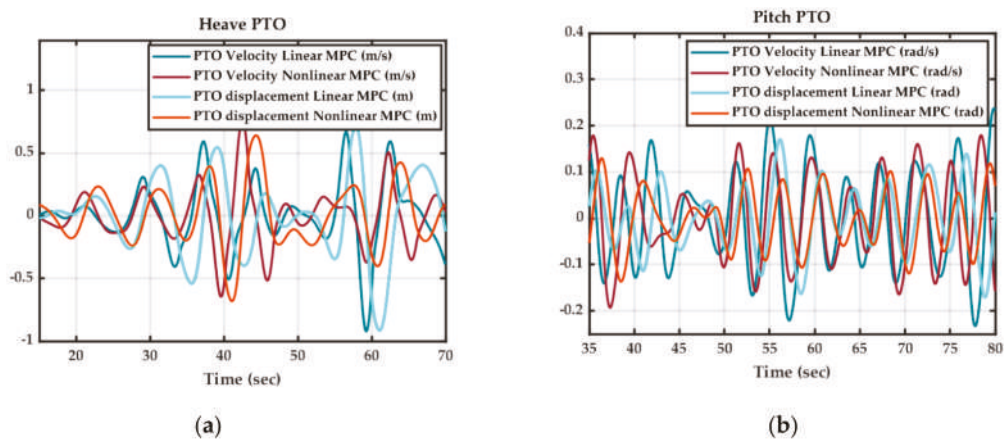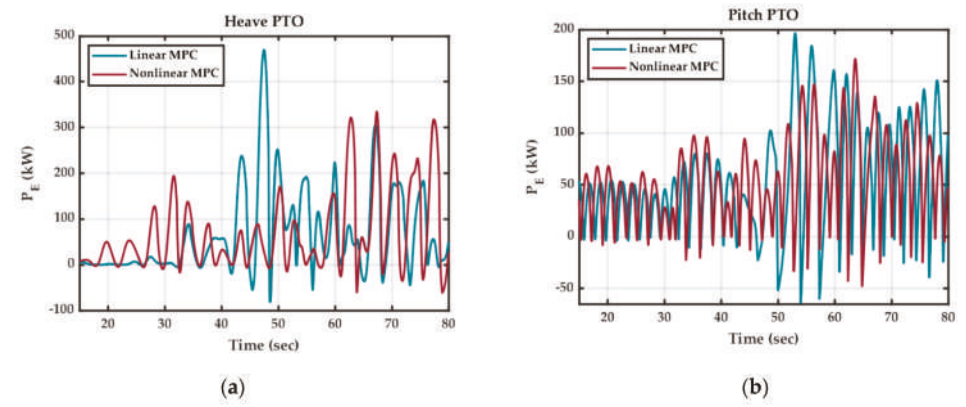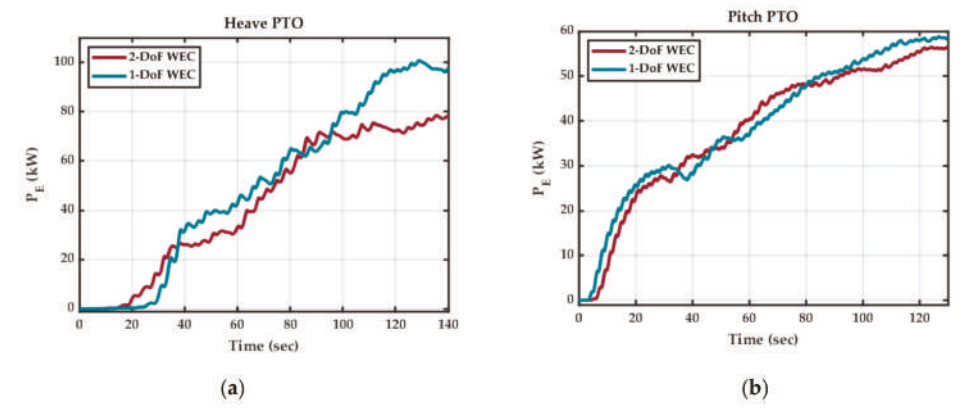

Figure 13. The PTO velocity and displacement plots for 2-DoF Pod-1 with linear and nonlinear MPC under linear hydrodynamic conditions in WEC-Sim and $|F_{pto}| \leq 400\ kN$: (**a**) Pod-1 Heave PTO; (**b**) Pod-1 Pitch PTO.

The average and instantaneous electrical power output results under nonlinear hydrodynamics for 2-DoF Pod-1 with linear and nonlinear MPC are shown in Figures 14 and 15, respectively. The comparison of average electrical PTO power output with NMPC for 1-DoF and 2-DoF Pod-1 is shown in Figure 16 under nonlinear hydrodynamic conditions.
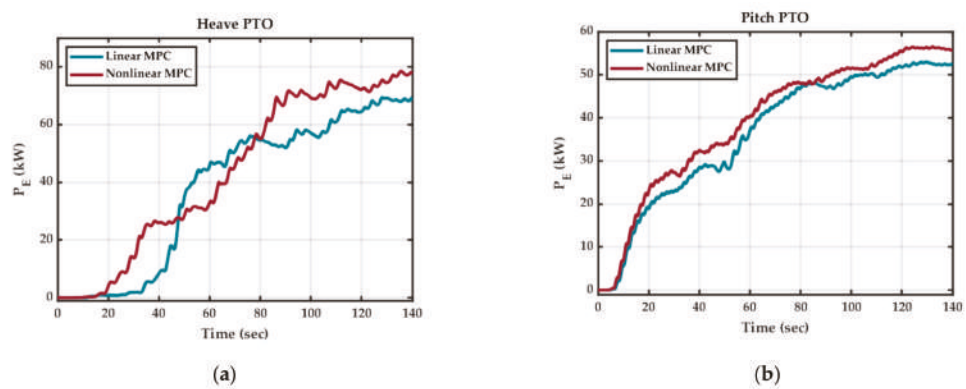
Figure 14. Average electrical PTO power output for 2-DoF Pod-1 with linear and nonlinear MPC under Nonlinear hydrodynamic conditions in WEC-Sim and $|F_{pto}| \leq 400\ kN$: (**a**) Pod-1 Heave PTO; (**b**) Pod-1 Pitch PTO.

Figure 15. Instantaneous electrical PTO power output for 2-DoF Pod-1 with linear and nonlinear MPC under nonlinear hydrodynamic conditions in WEC-Sim and $|F_{pto}| \leq 400\ kN$: (**a**) Pod-1 Heave PTO; (**b**) Pod-1 Pitch PTO.

Figure 16. Average electrical PTO power output for 1-DoF and 2-DoF Pod-1 with nonlinear MPC under nonlinear hydrodynamic conditions in WEC-Sim and $|F_{pto}| \leq 400\ kN$: (**a**) Pod-1 Heave PTO; (**b**) Pod-1 Pitch PTO.

5. Discussion

The average electrical power output results in Figures 10 and 14 are summarized in Table 4. NMPC shows a better performance in terms of increased power output when compared to linear MPC. This increase in the output power becomes more prominent under nonlinear hydrodynamic conditions, which are not accounted for by the linear MPC. An overall 5% increase in power by NMPC compared to linear MPC is obtained under linear hydrodynamic conditions. NMPC obtains an overall 5% increase in total power output by pod-1 than linear MPC under linear hydrodynamic conditions and 10.6% under nonlinear hydrodynamic conditions. The corresponding task execution time (TET) stats for the real-time implementations of linear MPC and NMPC in a Speedgoat real-time machine are given in Table 5. Given the controller step time of 0.1 sec, the increase in TET for NMPC compared to linear MPC is not very significant.

Table 4. Average electrical power output per PTO for 2-DoF Pod1 with linear MPC and NMPC.

	Average Electrical Power [kW]					
Control Algorithm	**Linear Hydrodynamic Conditions**			**Nonlinear Hydrodynamic Conditions**		
	Heave	**Pitch**	**Total**	**Heave**	**Pitch**	**Total**
Linear MPC	57	35	92	70	52	122
Nonlinear MPC	60	37	97	79	56	135

Table 5. Real-time timings stats for Linear MPC vs. Nonlinear MPC.

	Task Execution Time (TET) [sec]		
Control Algorithm	**1-DoF Heave**	**1-DoF Pitch**	**2-DoF Heave and Pitch**
Linear MPC	2.12×10^{-4}	2.67×10^{-4}	5.21×10^{-4}
Nonlinear MPC	3.05×10^{-4}	3.21×10^{-4}	6.14×10^{-4}

The average electrical power output results per PTO for 1-DoF and 2-DoF Pod1 with NMPC from Figure 16 are summarized in Table 6. In moving from 1-DoF WEC to 2-DoF WEC, a 35% increase in output power is obtained compared to heave only, and 129% increase compared to pitch only.

Table 6. Average electrical power output per PTO for 1-DoF and 2-DoF Pod1 with NMPC.

	Average Electrical Power [kW]		
	1-DoF WEC		**2-DoF WEC**
Axis	**Heave**	**Pitch**	**Heave and Pitch**
Heave	98	0	78
Pitch	0	58	55
Net Power	98	58	133

The locus of electrical PTO power for linear MPC and NMPC under nonlinear hydrodynamic conditions in WEC-Sim, along with the electrical power cost functional surface from Figure 5, are shown in Figure 17.

The locus of electrical PTO power in Figure 17 traverses a trajectory on the cost manifolds and satisfies the cost objective. The cost index formulation in (15) includes a convexifying quadratic term of PTO current, making the resultant electrical PTO surface convex in Figure 5, and with a smooth PTO current profile, the close loop system tends to maintain a stable operation. If the QP problem formulated at a given sample interval is infeasible, the controller will not find a solution. This issue can be handled by monitoring the status of the QP solver during each sampling interval and selecting a suboptimal

solution when the QP solver fails. An average of 35% processor load was observed per sampling interval during testing.
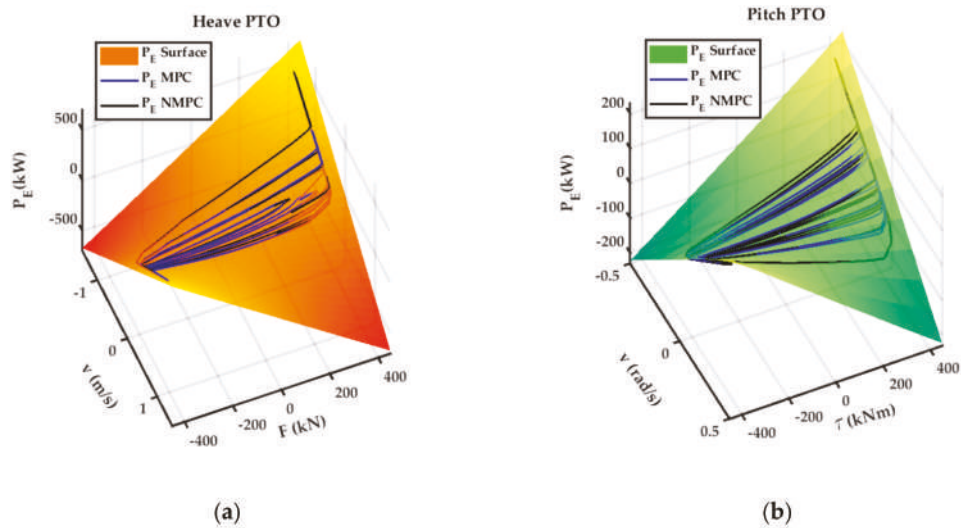
Figure 17. The locus of electrical PTO power on the electrical power cost functional surface for linear MPC and NMPC under nonlinear hydrodynamic conditions in WEC-Sim and $|F_{pto}| \leq 400\ kN$: (**a**) Pod-1 Heave PTO; (**b**) Pod-1 Pitch PTO.

6. Conclusions

This article presents a real-time implementation of NMPC for a nonlinear 2-DoF WEC based on Dehlsen Associates' CENTIPOD multi-pod WEC device, with non-ideal PTOs in the heave and pitch axes. The three pods of the WEC device are assumed identical, and a nonlinear state-space model of a single pod is developed. An NMPC controller is implemented for a 2-DoF WEC device with the cost functional based on a PTO model case study with a highly nonlinear PTO current–force characteristic. The results of the linear MPC are compared with NMPC for the sea states of interest (irregular waves with Pierson Moskowitz spectrum) under linear and nonlinear hydrodynamic conditions in WEC-Sim. The proposed methodology successfully maintained an overall feasible operation of the real-time NMPC problem in simulation as indicated by the status port of the NMPC QP-solver.

An average of 35% processor load was observed per sampling interval during testing. An overall 5% increase in total power output by a single pod is obtained by NMPC compared to linear MPC under linear hydrodynamic conditions and 10.6% under nonlinear hydrodynamic conditions. Moreover, a 35% increase in net output power is obtained by the 2-DoF WEC device compared to the 1-DoF heave only, and a 129% increase compared to the 1-DoF pitch only. While the result reflects only a single sea state, the improvement is likely to be reflected similarly in annual energy production (AEP). The AEP would have a substantive impact on the levelized cost of energy (LCOE). The present work did not consider the cross-coupling between the three pods of the CENTIPOD device. The cross-coupling would be investigated in future work with anticipation of a further increase in the captured power for the sea conditions where the cross-coupling effect is no longer negligible.

References

1. Muetze, A.; Vining, J.G. Ocean Wave Energy Conversion—A Survey. In Proceedings of the Conference Record of the 2006 IEEE Industry Applications Conference Forty-First IAS Annual Meeting, Tampa, Fl, USA, 8–12 October 2006; Volume 3, pp. 1410–1417.
2. Richter, M.; Magana, M.E.; Sawodny, O.; Brekken, T.K.A. Nonlinear Model Predictive Control of a Point Absorber Wave Energy Converter. *IEEE Trans. Sustain. Energy* **2013**, *4*, 118–126. [CrossRef]
3. Haider, A.S.; Brekken, T.K.A.; McCall, A. A State-of-the-Art Strategy to Implement Nonlinear Model Predictive Controller with Non-Quadratic Piecewise Discontinuous Cost Index for Ocean Wave Energy Systems. In Proceedings of the 2020 IEEE Energy Conversion Congress and Exposition (ECCE), Detroit, MI, USA, 11–15 October 2020; pp. 1873–1878.
4. Brekken, T.K.A. On Model Predictive Control for a Point Absorber Wave Energy Converter. In Proceedings of the 2011 IEEE Trondheim PowerTech, Trondheim, Norway, 19–23 June 2011; pp. 1–8.
5. Faedo, N.; Olaya, S.; Ringwood, J.V. Optimal Control, MPC and MPC-like Algorithms for Wave Energy Systems: An Overview. *IFAC J. Syst. Control* **2017**, *1*, 37–56. [CrossRef]
6. Zhong, Q.; Yeung, R.W. Model-Predictive Control Strategy for an Array of Wave-Energy Converters. *J. Mar. Sci. Appl.* **2019**, *18*, 26–37. [CrossRef]
7. Genest, R.; Ringwood, J.V. A Critical Comparison of Model-Predictive and Pseudospectral Control for Wave Energy Devices. *J. Ocean Eng. Mar. Energy* **2016**, *2*, 485–499. [CrossRef]
8. Li, G.; Belmont, M.R. Model Predictive Control of Sea Wave Energy Converters—Part I: A Convex Approach for the Case of a Single Device. *Renew. Energy* **2014**, *69*, 453–463. [CrossRef]
9. Li, G.; Belmont, M.R. Model Predictive Control of Sea Wave Energy Converters—Part II: The Case of an Array of Devices. *Renew. Energy* **2014**, *68*, 540–549. [CrossRef]
10. Starrett, M.; So, R.; Brekken, T.K.A.; McCall, A. Increasing Power Capture from Multibody Wave Energy Conversion Systems Using Model Predictive Control. In Proceedings of the 2015 IEEE Conference on Technologies for Sustainability (SusTech), Ogden, UT, USA, 30 July–1 August 2015; pp. 20–26.
11. Falcão, A.F.O.; Henriques, J.C.C. Effect of Non-Ideal Power Take-off Efficiency on Performance of Single- and Two-Body Reactively Controlled Wave Energy Converters. *J. Ocean Eng. Mar. Energy* **2015**, *1*, 273–286. [CrossRef]
12. Davis, A.F.; Thomson, J.; Mundon, T.R.; Fabien, B.C. Modeling and Analysis of a Multi Degree of Freedom Point Absorber Wave Energy Converter. In Proceedings of the OMAE 2014, San Francisco, CA, USA, 8 June 2014; Volume 8A: Ocean Engineering.
13. Al Shami, E.; Wang, X.; Ji, X. A Study of the Effects of Increasing the Degrees of Freedom of a Point-Absorber Wave Energy Converter on Its Harvesting Performance. *Mech. Syst. Signal Process.* **2019**, *133*, 106281. [CrossRef]
14. Strager, T.; Martin dit Neuville, A.; Fernández López, P.; Giorgio, G.; Mureşan, T.; Andersen, P.; Nielsen, K.M.; Pedersen, T.S.; Vidal Sánchez, E. Optimising Reactive Control in Non-Ideal Efficiency Wave Energy Converters. In Proceedings of the OMAE 2014, San Francisco, CA, USA, 8 June 2014; Volume 9A: Ocean Renewable Energy.
15. Perdigão, J.; Sarmento, A. Overall-Efficiency Optimisation in OWC Devices. *Appl. Ocean Res.* **2003**, *25*, 157–166. [CrossRef]
16. Tedeschi, E.; Carraro, M.; Molinas, M.; Mattavelli, P. Effect of Control Strategies and Power Take-Off Efficiency on the Power Capture From Sea Waves. *IEEE Trans. Energy Convers.* **2011**, *26*, 1088–1098. [CrossRef]
17. Jia, Y.; Meng, K.; Dong, L.; Liu, T.; Sun, C.; Dong, Z.Y. Economic Model Predictive Control of a Point Absorber Wave Energy Converter. *IEEE Trans. Sustain. Energy* **2021**, *12*, 578–586. [CrossRef]
18. Ellis, M.; Durand, H.; Christofides, P.D. A Tutorial Review of Economic Model Predictive Control Methods. *J. Process Control* **2014**, *24*, 1156–1178. [CrossRef]
19. Rawlings, J.B.; Angeli, D.; Bates, C.N. Fundamentals of Economic Model Predictive Control. In Proceedings of the 2012 IEEE 51st IEEE Conference on Decision and Control (CDC), Maui, HI, USA, 10–13 December 2012; pp. 3851–3861.

20. Houska, B.; Ferreau, H.J.; Diehl, M. An Auto-Generated Real-Time Iteration Algorithm for Nonlinear MPC in the Microsecond Range. *Automatica* **2011**, *47*, 2279–2285. [CrossRef]
21. Houska, B.; Ferreau, H.J.; Diehl, M. ACADO Toolkit—An Open-Source Framework for Automatic Control and Dynamic Optimization. *Optim. Control. Appl. Methods* **2011**, *32*, 298–312. [CrossRef]
22. Abdelkhalik, O.; Zou, S.; Robinett, R.D.; Bacelli, G.; Wilson, D.G.; Coe, R.; Korde, U. Multiresonant Feedback Control of a Three-Degree-of-Freedom Wave Energy Converter. *IEEE Trans. Sustain. Energy* **2017**, *8*, 1518–1527. [CrossRef]
23. Frequency- and Time-Domain Analysis of a Multi-Degree-of-Freedom Point Absorber Wave Energy Converter–Yizhi Ye, Weidong Chen, 2017. Available online: https://journals.sagepub.com/doi/full/10.1177/1687814017722081 (accessed on 20 July 2021).
24. Coe, R.G.; Bull, D.L. Nonlinear Time-Domain Performance Model for a Wave Energy Converter in Three Dimensions. In Proceedings of the 2014 Oceans, St. John's, NL, Canada, 14–19 September 2014; pp. 1–10.
25. Huang, S.; Shi, H.; Dong, X. Capture Performance of A Multi-Freedom Wave Energy Converter with Different Power Take-off Systems. *China Ocean Eng.* **2019**, *33*, 288–296. [CrossRef]
26. Hillis, A.J.; Whitlam, C.; Brask, A.; Chapman, J.; Plummer, A.R. Active Control for Multi-Degree-of-Freedom Wave Energy Converters with Load Limiting. *Renew. Energy* **2020**, *159*, 1177–1187. [CrossRef]
27. Li, G. Nonlinear Model Predictive Control of a Wave Energy Converter Based on Differential Flatness Parameterisation. *Int. J. Control* **2017**, *90*, 68–77. [CrossRef]
28. WEC-Sim (Wave Energy Converter SIMulator)—WEC-Sim Documentation. Available online: https://wec-sim.github.io/WEC-Sim/ (accessed on 27 March 2021).
29. van Rij, J.; Yu, Y.-H.; McCall, A.; Coe, R.G. Extreme Load Computational Fluid Dynamics Analysis and Verification for a Multibody Wave Energy Converter. In Proceedings of the OMAE 2019, Glasgow, UK, 9–14 June 2019; Volume 10: Ocean Renewable Energy.
30. Haider, A.S.; Brekken, T.K.A.; McCall, A. Application of Real-Time Nonlinear Model Predictive Control for Wave Energy Conversion. *IET Renew. Power Gener.* **2021**. [CrossRef]
31. Speedgoat—The Quickest Path to Real-Time Simulation and Testing. Available online: https://www.speedgoat.com/ (accessed on 23 February 2021).
32. Ecomerit Technologies. Available online: http://www.ecomerittech.com/centipod.php (accessed on 14 August 2021).
33. Wamit, Inc. The State of the Art in Wave Interaction Analysis. Available online: https://www.wamit.com/ (accessed on 28 March 2021).
34. Ringwood, J.V. Wave Energy Control: Status and Perspectives 2020 ∗∗This Paper Is Based upon Work Supported by Science Foundation Ireland under Grant No. 13/IA/1886 and Grant No. 12/RC/2302 for the Marine Renewable Ireland (MaREI) Centre. *IFAC-PapersOnLine* **2020**, *53*, 12271–12282. [CrossRef]

Article

Sliding Mode Control of a Nonlinear Wave Energy Converter Model

Tania Demonte Gonzalez [1,*]**, Gordon G. Parker** [1]**, Enrico Anderlini** [2] **and Wayne W. Weaver** [1]

[1] Department of Mechanical-Engineering-Engineering Mechanics, Michigan Technological University, Houghton, MI 49931, USA; ggparker@mtu.edu (G.G.P.); wwweaver@mtu.edu (W.W.W.)

[2] Department of Mechanical Engineering, University College London, London WC1E 6BT, UK; e.anderlini@ucl.ac.uk

[*] Correspondence: tsdemont@mtu.edu

Abstract: The most accurate wave energy converter models for heaving point absorbers include nonlinearities, which increase as resonance is achieved to maximize the energy capture. Over the power production spectrum and within the physical limits of the devices, the efficiency of wave energy converters can be enhanced by employing a control scheme that accounts for these nonlinearities. This paper proposes a sliding mode control for a heaving point absorber that includes the nonlinear effects of the dynamic and static Froude-Krylov forces. The sliding mode controller tracks a reference velocity that matches the phase of the excitation force to ensure higher energy absorption. This control algorithm is tested in regular linear waves and is compared to a complex-conjugate control and a nonlinear variation of the complex-conjugate control. The results show that the sliding mode control successfully tracks the reference and keeps the device displacement bounded while absorbing more energy than the other control strategies. Furthermore, due to the robustness of the control law, it can also accommodate disturbances and uncertainties in the dynamic model of the wave energy converter.

Keywords: wave energy; nonlinear model; Froude-Krylov force; sliding mode control

1. Introduction

Recently, the generation of electricity from ocean waves has gained special attention. Studies of the potential global market for wave power showed that the world's wave power resource is estimated to be two TW [1]. Additionally, waves have a very high power density, requiring smaller devices to capture the energy carried by the incoming waves. Wave energy can also improve energy security by complementing the output of other renewable energy sources, thus reducing the storage needs. However, although phased development has helped reduce risks, the wave energy sector is still in its infancy, with recent prototype wave energy converters (WECs) having a Levelized Cost of Energy (LCoE) in the range of $120–$470/MWh [2]. Hence, technological advances are required to reduce the LCoE 50–75% to enable the industry to leap from government-funded research to sustainable industrial competition within the energy market. Optimizing the control of WECs has been identified as one of the critical areas with the highest potential to improve the viability of wave energy [3], as the latest control methods can enhance power absorption by up to 20% while reducing structural loads.

Researchers have used well-established control methods in WECs that include Complex-Conjugate Control (CCC), Latching, and Model Predictive Control (MPC) [4]. In complex-conjugate control, optimal energy absorption is sought by tuning the power take-off (PTO) resistance and reactance to cancel the system's inherent hydrodynamic resistance and reactance [5]. This control strategy is conceptually simple and presents a low computational cost; however, it leads to excessive motions and loads of the WEC. This can be avoided by implementing alternative suboptimal control schemes that include

physical constraints on the motions and power of the device. Latching control is based on locking the device through dedicated mechanisms during a certain period of time of the wave oscillation cycle to achieve resonance of the WEC [6,7]. Resonance is achieved when the system is being excited at its natural frequency. While latching control solves the PTO limitation problem of CCC, it is prone to failure of the mechanical clamping pieces generating extra costs and reducing its reliability. MPC strategies maximize the energy absorbed by applying the optimal control force to achieve resonance at each time step over a future time horizon [8]. However, a prediction of the wave motion is required, and its complexity of implementation in real-time demands high computational requirements.

Most of these control techniques use the linear model developed by Cummins [9] with hydrodynamic parameters obtained from boundary element methods (BEM) due to their simplicity and high computational efficiency. Although linear models are effective for most ocean engineering applications where the aim is typically to stabilize the structure, linear models are inadequate for WEC control, where the primary objective is to amplify the device's motions to maximize the power absorption [10]. As a result, control strategies based on linear models are often suboptimal and lead to higher LCoE.

Nonlinear models often include the quadratic term of the pressure from the incident flow, the integration of the pressure forces over the instantaneous wetted surface of the device called Froude-Krylov (FK) forces, and the nonlinear incident flow potential [11]. Each of these nonlinearities adds an extra level of complexity and computational load. However, it is understood that nonlinear models are more accurate than linear models, particularly for buoy geometries with varying cross-sectional areas. A previous study [12] that compared different modeling options showed that the dominant sources of nonlinearities are likely to be the nonlinear Froude-Krylov forces for devices with a varying cross-sectional area.

While, in linear modeling, the FK forces are calculated over a constant wetted area of the device, in nonlinear models, the pressure is integrated over the instantaneous wetted surface area. This is generally done by implementing a very fine mesh or a remeshing routine of the surface, which requires more computational effort. As a result, the nonlinear model is more accurate but is very computationally expensive. However, in Reference [13], Giorgi et al. developed a computationally efficient analytical method to compute the nonlinear dynamic and static Froude-Krylov forces based on the instantaneous wetted surface area of the buoy. This analytical method presents only a 2% error compared to the more computationally expensive methods. Therefore, in this study, the nonlinear FK forces are incorporated using a variation of the algebraic solution proposed by Giorgi et al.

This paper proposes a second-order Sliding Mode Control (SMC) strategy that incorporates the nonlinear Froude-Krylov forces to reduce the discrepancies between the mathematical model and the actual system. In addition, this SMC is designed to track the desired reference signals using low computational efforts and rejecting disturbances encountered by the WEC or parametric errors presented in the model. The controller will be investigated in a simulation environment using a standard spherical WEC and regular waves.

Many researchers have studied SMC in oscillating water columns (OWC). A popular SMC for a nonlinear OWC is the super-twisting algorithm presented in [14]. This control strategy has been used in different configurations of OWCs, where it noticeably improved the electric power conversion compared to other strategies [15]. Sliding mode control has also been used to track underwater vehicles' positions [16] due to its robustness characteristics that allow for model uncertainties or environmental disturbances. In this paper, SMC is applied to a heaving point absorber. An SMC strategy for heaving WECs was proposed in Reference [17], where it was shown to provide a viable solution to increase energy extraction. The SMC was designed to track a reference velocity without violating the physical constraints of the device. The results showed that the SMC successfully tracked the reference signal even when system perturbations were present. However, this work was done using a linear approximation of the WEC's dynamic model. This study aims to

improve the energy extraction performance of WECs where its SMC can exploit the WEC's nonlinear model terms.

The main contributions of this study consist of first, the derivation of algebraic nonlinear Froude-Krylov forces based on the work of Giorgi et al., second, the application of an SMC to the nonlinear WEC model; and third, the design of a nonlinear variant of complex-conjugate control.

This paper is organized into six sections. First, the following section describes the general dynamics of a heaving WEC and the derivation of the nonlinear algebraic Froude-Krylov forces showing the first contribution mentioned above. Then, the second and third contributions are in Section 3, where the SMC strategy is designed and compared to a complex-conjugate control and a nonlinear variant of complex-conjugate control. In Section 4, the simulation used to evaluate closed-loop performance is described. Section 5 shows the results, and Section 6 provides conclusions and area for further study.

2. Model Description

Mathematical models for WECs are essential for the design of model-based control. These models are typically linear because of their low computational requirements, in which they assume small motions. However, there are situations in which the movement is not small while still producing power, and the nonlinearities of the device become significant.

The incoming waves are classified as linear and nonlinear depending on the wave steepness S, which is the ratio between the wave height h and the wavelength λ [18]. Waves are also classified as regular and irregular, where regular waves are characterized by a specific amplitude A, frequency ω_0, and wavelength, whereas irregular waves are composed of multiple frequency waves. In this paper, linear and regular waves are used, representing the wave free surface elevation $\eta(t)$ as a function of time only:

$$\eta(t) = A\cos(\omega_0 t) \tag{1}$$

A floating single degree of freedom (SDOF) buoy is shown in Figure 1, where the lower part of the sphere is attached to a linear generator for power take-off (PTO), which is fixed to the seabed. The PTO subsystem converts the wave energy into electrical energy and energizes the system to track the reference profile. The excitation force is shown as $F_{exc}(t)$, and is composed of the hydrodynamic Froude-Krylov force and the diffraction force, the buoy's displacement from its equilibrium position is denoted $z(t)$, and the control force implemented by the PTO system is $F_c(t)$.
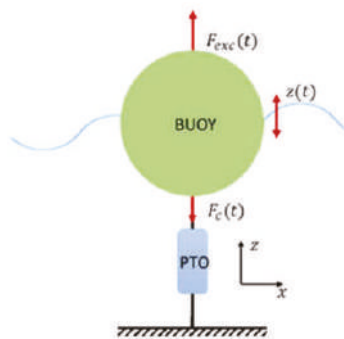

Figure 1. Heaving buoy with power take-off (PTO) fixed to the sea bed.

The general heaving WEC hydrodynamic model used in this paper is described as:

$$m\ddot{z}(t) = F_{FK} + F_d + F_R - F_c \tag{2}$$

where:

> m: Mass of the buoy in the air
> F_{FK}: Froude-Krylov Forces
> F_d: Diffraction Force
> F_R: Radiation Force
> F_c: Control Force

2.1. Diffraction Force

The diffraction force is the force the incoming waves apply on the buoy as it is held fixed in the water [5]. It can be is represented as the convolution of the product of the wave free surface elevation and the diffraction impulse response function (*IRF*):

$$F_d = \int_{-\infty}^{+\infty} K_{d_{IRF}}(t - \tau)\, \eta(t)\, d\tau \tag{3}$$

where $K_{d_{IRF}}$ is the diffraction *IRF*.

When the buoy diameter is much smaller than the wavelength, the disturbance field generated by the body is small enough to be ignored [19]. Therefore, the diffraction force is neglected in the simulation of this paper. This force could also be accounted as a disturbance to the system.

2.2. Radiation Force

The radiation force can be interpreted as the force that the body experiences when it oscillates in calm water. It is common to divide this force into two parts: the added mass force, proportional to the body's acceleration $\ddot{z}(t)$, and the wave damping force, proportional to the body velocity $\dot{z}(t)$ [20]. Thus, the radiation force can be represented as:

$$F_R(t) = -\int_{-\infty}^{+\infty} K_{r_{IRF}}(t - \tau)\, \dot{z}(t)\, d\tau - m_a(\omega_\infty)\ddot{z}(t) \tag{4}$$

where:

> $K_{r_{IRF}}$: Radiation *IRF*
> $m_a(\omega_\infty)$: Added mass

Evaluating the convolution integral in the radiation force is very expensive to compute at every time step of the simulation, and it is not possible on a real-time application. However, when the buoy is exposed to only harmonic waves of frequency ω_0, the convolution in Equation (4) can be represented as:

$$F_R = c(\omega_0)\dot{z}(t) - m_a(\omega_\infty)\ddot{z}(t) \tag{5}$$

where $c(\omega_0)$ is the linear damping constant.

2.3. Froude-Krylov Forces

The Froude-Krylov forces F_{FK} are the hydrostatic force $F_{FK_{st}}$ and the hydrodynamic force $F_{FK_{dy}}$. The hydrostatic force is the difference between the gravity force F_g and the force caused by the hydrostatic pressure over the wetted surface of the buoy, and the hydrodynamic force is the integral of the unsteady pressure field over the wetted surface of the floating buoy caused by the incident waves.

$$F_{FK} = F_g - \iint P(t)\, \mathbf{n}dS \tag{6}$$

In linear models, the integration is done over the constant mean wetted surface, while in the nonlinear approach, the instantaneous wetted surface of the body is considered. This approach typically requires significant computational effort. However, Giorgi et al. proposed an algebraic solution that significantly reduces the computational effort for heaving axisymmetric geometries. The algebraic solution is found by defining the pressure

$P(t)$, the infinitesimal element of the surface $\mathbf{n}\,dS$, and the limits of integration. The total pressure for deep water waves can be found using Airy's wave theory.

$$P(t) = \rho g e^{\chi z} A \cos(\omega t) - \rho g z(t) \tag{7}$$

where:

ρ: Density of water

g: Gravity acceleration constant

χ: Wavenumber

In Giorgi et al.'s work, the surface of the geometry of the buoy was defined in parametric cylindrical coordinates as:

$$\begin{cases} x(\sigma, \theta) = f(\sigma)\cos(\theta) \\ y(\sigma, \theta) = f(\sigma)\sin(\theta), \\ z(\sigma, \theta) = \sigma \end{cases} \qquad \theta \in [0, 2\pi) \wedge \sigma \in [\sigma_1, \sigma_2] \tag{8}$$

where $f(\sigma)$ is the profile of revolution of the point absorber. Using the radial e_σ and tangent e_θ vectors canonical basis, and only the vertical component for heave motion restriction, the infinitesimal surface element, and the pressure becomes:

$$e_\sigma \times e_\theta \, dS = \mathbf{n} \| e_\sigma \times e_\theta \| \, d\sigma d\theta = \mathbf{n}\, f(\sigma) \sqrt{f'(\sigma)^2 + 1} \, d\sigma d\theta$$

$$P_z(t) = P(t) \cdot \langle \mathbf{n}, \mathbf{k} \rangle = P(t) \cdot \frac{f\prime(\sigma)}{\sqrt{f'(\sigma)^2 + 1}} \tag{9}$$

Combining these equations, the Froude-Krylov forces are:

$$F_{FK} = F_g - \iint P(t) f'(\sigma) f(\sigma) d\sigma d\theta \tag{10}$$

The paper continues defining the limits of integration based on the free surface elevation and the draft of the buoy h_0 at equilibrium as:

$$\begin{cases} \sigma_1 = z_d(t) - h_0 \\ \sigma_2 = \eta(t) \end{cases} \tag{11}$$

where $z_d(t)$ is the vertical displacement of the buoy from equilibrium. For a spherical point absorber, the profile of revolution derived in Giorgi et al. paper is $f(\sigma) = \sqrt{R^2 - (\sigma - z_d)^2}$, where R is the radius of the buoy.

In this paper, the limits of integration and the profile of revolution have been redefined using calculus to derive the instantaneous wetted surface area of the sphere. Considering the bottom of the sphere as the lower limit of integration, the profile of revolution of the sphere at still water level (SWL) shown in Figure 2a is $f(\sigma) = \sqrt{R^2 - (-R + h_0 + \sigma)^2}$, where the SWL was used as a reference and the instantaneous wetted surface area is shaded in blue. In this case, the lower limit of integration is $-h_0$ and the upper limit is 0. When the buoy is displaced by $z_d(t)$, and the free surface elevation $\eta(t)$ is not zero as shown in Figure 2b the profile of revolution of the sphere becomes:

$$f(\sigma) = \sqrt{R^2 - (-R + h_0 - z_d(t) + \eta(t) + \sigma)^2} \tag{12}$$
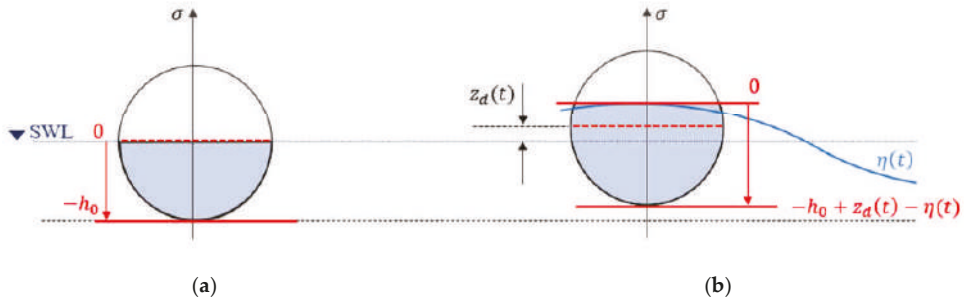
Figure 2. Heaving spherical point absorber at the still water level (SWL) on the left (**a**); to the right (**b**) is shown the displacement from resting position $z_d(t)$ and the wave elevation $\eta(t)$.

The limits of integration are: 0 for the upper limit, and $l_b = -h_0 + z_d(t) - \eta(t)$ for the lower limit. Combining Equations (8)–(12), the integral of the Froude-Krylov forces of a heaving spherical buoy can be expressed as:

$$F_{FK_z} = F_g - 2\pi\rho g \int_{l_b}^{0} (e^{\chi z} A\cos(\omega t) - \sigma)(-R + h_0 - z_d(t) + \eta(t) + \sigma) \, d\sigma \tag{13}$$

Solving the integral and separating the Froude-Krylov forces, the resulting nonlinear hydrostatic, and hydrodynamic forces of the system are:

$$F_{FK_{st}} = F_g + \frac{\pi\rho g}{3}(\eta(t) + h_0 - z_d(t))^2(3R - \eta(t) - h_0 + z_d(t)) \tag{14}$$

$$F_{FK_{dy}} = \frac{2\pi\rho g \eta(t)}{\chi^2}\left(e^{-\chi(\eta(t)+h_0-z_d(t))} + \chi\left(-R + \eta(t) + h_0 - z_d(t) + Re^{-\chi(\eta(t)+h_0-z_d(t))}\right) - 1\right) \tag{15}$$

The complete nonlinear model of a single degree of freedom WEC in heave mode can then be described as:

$$M\ddot{z}(t) = F_d + F_{FK_{st}} + F_{FK_{dy}} - c(\omega_0)\dot{z}(t) - F_c \tag{16}$$

where $M = (m + m_a(\omega_\infty))$.

For the subsequent control design, it will be convenient to write Equation (16) as:

$$\ddot{z}(t) = f_t(z(t), \dot{z}(t), \eta(t)) - \overline{F}_c \tag{17}$$

where f_t is the true model of the system, and $\overline{F}_c = F_c M_t^{-1}$ where M_t is the true mass. In contrast, the model used for control design is approximated as:

$$\ddot{z}(t) = f(z(t), \dot{z}(t), \eta(t)) - \hat{F}_c \tag{18}$$

$$f(z(t), \dot{z}(t), \eta(t)) = \left[F_d + F_{FK_{st}} + F_{FK_{dy}} - c(\omega_0)\dot{z}(t)\right]M^{-1}$$

$$\hat{F}_c = F_c M^{-1}$$

The calculation of the absorbed energy is [21]:

$$W = \int_o^t F_c \, \dot{z}(t) \, dt \tag{19}$$

3. Control Design

This section presents a sliding mode control (SMC) design, illustrated in Figure 3, for a heaving WEC based on the nonlinear differential equation model of Equation (16). Motivated by linear, complex conjugate control, the SMC reference trajectory is selected to match the frequency and phase of the excitation force. Since the WEC model is not linear, as assumed by complex conjugate control, it is recognized that this reference trajectory will not be optimal. Creating a real-time, energy extraction optimal reference trajectory is an open topic and well-suited for MPC applications. The reference velocity is then integrated to produce the reference displacement profile $z_r(t)$.
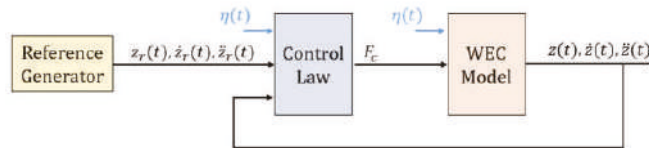

Figure 3. Configuration of proposed control schemes.

The sliding mode control is derived by first defining the sliding surface as:

$$s(z;t) = \dot{e}(t) + w\,e(t) \tag{20}$$

where z is the state vector, $z = [z;\dot{z}]$ and w is a real-positive value that sets the rate at which the system converges to the sliding surface. The problem of tracking a given profile becomes equivalent to maintaining the stationarity conditions:

$$\dot{s}(t) = \ddot{e}(t) + w\,\dot{e}(t) = \ddot{z}_r(t) - \ddot{z}(t) + w\,\dot{e}(t) = 0 \tag{21}$$

Substituting Equation (18) into Equation (21), and solving for $\hat{F}_c$ gives the control law:

$$\hat{F}_c = f\big(z(t), \dot{z}(t), \eta(t)\big) - \big(\ddot{z}_r(t) + w\dot{e}(t)\big) \tag{22}$$

This control law will only work if the assumed form of the model is perfect and there are no disturbances. To account for these inevitable situations, Lyapunov's Direct method is used to augment the control law of Equation (22) to ensure stability.

The Lyapunov candidate function is selected as:

$$V(t) = \frac{1}{2}s^2(t) \tag{23}$$

For stability,

$$\dot{V} = s(t)\dot{s}(t) = s(t)\big(\ddot{z}_r(t) - \ddot{z}(t) + w\dot{e}(t)\big) < 0 \tag{24}$$

Substituting the true model, Equation (17) into Equation (24) gives:

$$\dot{V} = s(t)\big(\ddot{z}_r(t) - f_t\big(z(t), \dot{z}(t), \eta(t)\big) + \overline{F}_c + w\dot{e}(t)\big) < 0 \tag{25}$$

Next, substitute a modified version of the control law of Equation (22) where we have added a new term, $A_c sgn(s(t))$, that does not affect the stationary condition imposed earlier:

$$\hat{F}_c = -\ddot{z}_r(t) + f\big(z(t), \dot{z}(t), \eta(t)\big) - w\dot{e}(t) - A_c sgn(s(t)) \tag{26}$$

Furthermore, note that $\hat{F}_c \neq \overline{F}_c$ are related by $\overline{F}_c = \frac{M}{M_t}\hat{F}_c$. The time-dependency notation will be omitted for the following equations for brevity. We now have the stability condition:

$$\dot{V} = s\left(\ddot{z}_r - f_t(z,\dot{z},\eta) + \frac{M}{M_t}\left(-\ddot{z}_r + f(z,\dot{z},\eta) - w\dot{e} - A_c sgn(s)\right) + w\dot{e}\right) < 0 \quad (27)$$

or

$$A_c|s| > \ddot{z}_r - f(z,\dot{z},\eta) - w\dot{e} + \frac{M_t}{M}\left(-\ddot{z}_r + f_t(z,\dot{z},\eta) - w\dot{e}\right) \quad (28)$$

As long as A_c is sufficiently large to dominate the uncertainties on the right side of Equation (28), the system will be stable.

The discontinuous terms in the control of Equation (26) $A_c\,sgn(s(t))$ can cause chattering. This is eliminated by replacing the signum function with a hyperbolic tangent [22]. Then, the control law is interpolated by replacing $tanh(s(t))$ function by $s(t)/\Phi$ as:

$$F_c = F_d + F_{FK} - c(\omega_0)\dot{z}(t) - (\ddot{z}_r(t) + w\dot{e}(t))M + A_c\,tanh(s(t)/\Phi) \quad (29)$$

where Φ is the boundary layer thickness.

The reference signal generator outputs the desired velocity profile of the WEC plant that is then integrated to obtain the desired displacement profile z_r. The control law takes as inputs the formed error signals, the desired acceleration profile $\ddot{z}_r$, the FK forces and the actual buoy displacement as in Equation (29). The control parameters A_c and Φ were chosen during the simulation process. As aforementioned, the reference velocity profile is designed to match the frequency and phase of the excitation force. As described in Reference [5], the optimum velocity condition requires:

$$\dot{z}_r(t) = \frac{F_{exc}(\omega_0)}{2\,c(\omega_0)} \quad (30)$$

To achieve this condition, phase control is needed so that the oscillation velocity $\dot{z}(t)$ is in phase with the excitation force and amplitude control to get a velocity amplitude of $|\dot{z}_r(t)| = |F_{exc}|/2c(\omega_0)$. However, this optimal condition leads to excessive motions of the device that would be infeasible in real-world applications. Therefore, the reference velocity profile is defined to be in phase with the excitation force with a suboptimal amplitude that varies for each sea state condition. Even though the WEC plant is nonlinear, in this study, the calculation of the reference velocity profile is based on the linear excitation force obtained from WAMIT [23].

To compare the results of the SMC, an approximate CCC [24] is used. Referring to the impedance matching principle [25], the optimal control force may be written as:

$$F_C^{opt}(\omega) = -Z_c^{opt}(\omega)\dot{z}(\omega) = -Z_i^*(\omega)\dot{z}(\omega) \quad (31)$$

where the optimal control impedance $Z_c^{opt}(\omega)$ must equal the complex-conjugate of the intrinsic impedance $Z_i = R_i(\omega) + iX(\omega)$ composed by the intrinsic resistance $R_i(\omega)$ and the intrinsic reactance $X_i(\omega)$. For monochromatic incident waves, this optimal force may be written in the time-domain as:

$$F_C^{opt}(t) = -M_c\ddot{z}(t) + c_c(\omega_0)\,\dot{z}(t) - k_c\,z(t) \quad (32)$$

For the optimal control, the controller values must equal the intrinsic values $M_c = M$, $c_c(\omega_0) = c(\omega_0)$, $k_c = k$, where k is the linear approximation of the static Froude-Krylov force. By cancellation, this control force gives the optimal response velocity shown in Equation (30) when the WEC model is assumed to be linear, and k is used instead of the nonlinear hydrostatic FK force. Since in this paper the WEC model is nonlinear, the

optimal control force using CCC was modified to obtain a perfect cancellation of the $F_{FK_{st}}$ as:

$$F_C^{opt}(t) = -M\ddot{z}(t) + c(\omega_0)\dot{z}(t) + F_{FK_{st}} \tag{33}$$

This control strategy used for comparison will be referred to as nonlinear complex-conjugate control $(NL - CCC)$ from this point on. The configuration of this control scheme is similar to that of the SMC shown in Figure 3. However, this control law only takes as inputs $z(t)$, $\dot{z}(t)$, $\ddot{z}(t)$, and, $\eta(t)$.

4. Simulation

As shown in previous studies [11], the significance of the Froude-Krylov nonlinear forces for a spherical body is great due to its varying cross-sectional area. The buoy parameters used in this simulation are listed in Table 1 and were chosen to resemble the parameters of a real device such as the WAVESTAR [26] device. The density of the body was chosen to be 500 kg/m^3 to make the draft of the buoy h_0 coincident with the center of gravity of the sphere, and the frequency-dependent hydrodynamic parameters were found by solving the radiation problem in WAMIT.

Table 1. Simulation parameters.

Parameter	Values
Buoy radius R	2.5 m
Buoy mass m	32,725 kg
Buoy draft h_d	2.5 m
Added mass $m_a(\omega_\infty)$	14,019 kg
Radiation damping $c(\omega_0)$	11,208 N/(m/s)
Water density ρ	1000 kg/m^3
Gravity constant g	9.81 m/s^2
Wave amplitude $A(\omega_0)$	0.5 m
Wave frequency ω_0	1.05 rad/s
Wavenumber $\chi(\omega_0)$	0.112
SMC convergence rate w	8
SMC coefficient ϕ	1000
SMC coefficient A_c	10 kN

The results showed in the following section correspond to the wave period of $T = 6$ s and $\omega_0 = 1.05$ rad/s. Therefore, the frequency-dependent parameters shown in Table 1 are based on this wave frequency.

Under the deep water assumption, the simulation was run for different monochromatic wave periods ranging from 3 to 9 s. In addition, the steepness of the wave S was kept constant at 0.018, which is the highest wave steepness under the linear waves assumption [18]. To maintain the wave steepness constant, the amplitude of the wave is related to the wavelength as $S = 2A/\lambda = 0.018$.

Table 2 shows the range of wave periods and their corresponding wavelength and wave amplitude.

Table 2. Wave characteristics and control parameters.

Wave Period (s)	3	4	5	6	7	8	9
Wavelength (m)	15	25	39	56	77	100	127
Wave Amplitude (m)	0.13	0.22	0.35	0.50	0.69	0.90	1.14
SMC Reference Amplitude (m)	0.6	1.1	1.8	2.19	2.14	2.05	1.9

The reference velocity profile in Equation (30) has been proven to be the optimum velocity [5] when using a linear approximation of the WEC, enabling maximum energy

absorption for a given buoy shape. However, this is not the case for this nonlinear WEC model where the $F_{FK_{dy}}$ is dependent on the incident wave elevation and the buoy displacement. Additionally, it is well-known that CCC magnifies the buoy's motion, driving the device to be either fully submerged or completely out of the water for certain wave periods. This undesirable behavior can be eliminated with the SMC by keeping the amplitude of the desired displacement bounded:

$$h_0 + S_f R - 2R > z_r > h_0 - S_f R \qquad (34)$$

where S_f is a safety factor used to determine the maximum and minimum buoy height covered by water, as shown in Figure 4. Therefore, the amplitude of the desired displacement of the device was chosen to be a value within those limits. The SMC reference amplitude for each wave period is listed in Table 2.
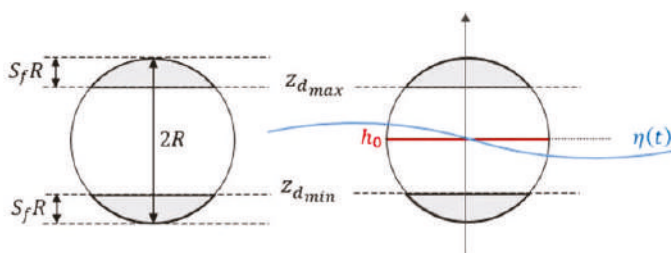

Figure 4. Spherical buoy limits of displacement.

5. Results

As aforementioned in Section 3, this paper compares the performance of the SMC against a complex-conjugate control (CCC) and a complex-conjugate control that includes the nonlinear static FK force in the control law (NL-CCC). The reference velocity used for the SMC is a cosine wave of the same frequency and phase as the linear hydrodynamic Froude-Krylov force obtained from WAMIT. To reduce the risk of driving the buoy completely out of the water or completely submerged into the water, a safety factor of $S_f = 10\%$ was used in the simulation, leaving 25 cm of clearance at the top and bottom of the spherical body.

The case shown in the results corresponds to a case where the CCC leads to a stable steady-state solution within the physical limits of the buoy. For higher wave periods, the solution with CCC would not reach steady-state. The maximum wave period at which the WEC controlled with the complex-conjugate control reached a steady-state solution within the physical limits of the buoy was at $T = 6s$. Therefore, that is the case that is shown in this paper. Figure 5 shows the relative displacement $z_d(t) - \eta(t)$ of the system using the different control strategies and the displacement limits to keep the buoy safe.

The relative displacement is kept within limits for the three control strategies used. The relative displacement when SMC is implemented is very well-behaved, and it takes advantage of the full range of motion available for the WEC. When CCC is implemented, there is a transient part for the first 15 s due to a 20-s ramp used to attenuate the overshoot caused by the control force. The relative displacement then reaches steady-state within the allowable range of motion. Note that the relative displacement with CCC is not in phase with the SMC. If the WEC plant were linear, the CCC and SMC would be in the phase. However, since the plant is nonlinear and the controller is a linear approximation, there is no perfect cancellation of the static FK force leading to a mismatch in relative displacements. Once the nonlinear static FK force is added to the CCC to form the NL-CCC, the relative displacement is in phase with the SMC. However, the amplitude of the relative displacement does not cover the full range of motion available since the minimum point at steady-state is already very close to the lower limit.
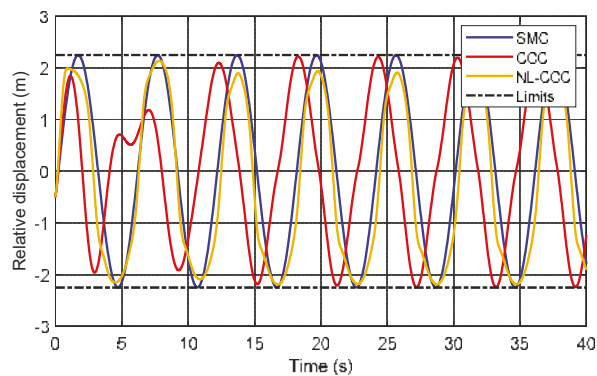
Figure 5. Relative displacement $z_d(t) - \eta(t)$ of the WEC when implementing SMC, CCC, and NL−CCC at $T = 6$ s.

The energy absorbed by the system when using the three control strategies and the control force used is shown in Figure 6. From this figure, it can be observed that the CCC performance is very poor compared to the SMC and the NL-CCC performance. This low energy absorption is caused by the very limited control force needed to maintain the WECs motion bounded. On the contrary, the energy absorbed when using SMC and NL-CCC are similar, with the SMC being slightly higher. However, the NL-CCC required a higher magnitude control force than the SMC to achieve slightly less energy absorption.


(a)

(b)
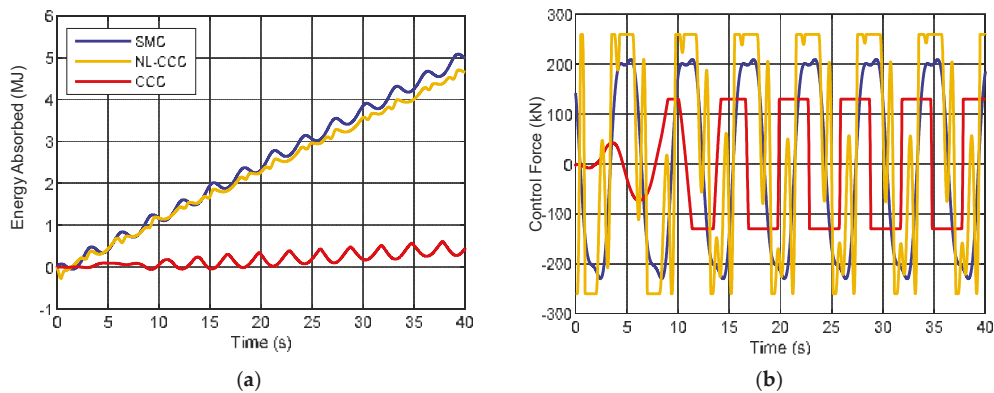
Figure 6. Absorbed energy (**a**) and control force (**b**) when implementing SMC, NL−CCC and CCC at $T = 6$ s.

Additionally, the SMC control force is a continuous function that does not need to be clipped in order to keep the WEC safe. On the other hand, the control force of CCC and NL-CCC are both saturated, causing discontinuities in the force. Furthermore, in order to maintain the WEC bounded in the safe range of motion, the control force of CCC and NL-CCC has to be limited at a different value for each sea state. While, for the SMC, this is not necessary, since the motion of the WEC is determined by the reference signals.

Although, in this case, the difference between the energy absorbed by the SMC and NL-CCC is very close, that is not the case for higher wave periods. The power absorbed by the WEC when using the three control strategies at different wave periods is shown in Figure 7. As the wave period increases, because the wave steepness is kept constant, the wave height increases. With increasing the wave amplitudes, the WECs displacement is significantly different from the wave elevation. Therefore, the mean wetted surface

is significantly different from the instantaneous wetted surface used in this nonlinear approach, making the nonlinear Froude-Krylov forces very significant. Hence, when using a linear control strategy such as the CCC for higher wave periods, the control force must be highly limited in order to keep the WEC safe, reducing the power absorption significantly. Similarly, when using the NL-CCC, even though the nonlinear static FK force is incorporated in the controller, the nonlinear dynamic FK becomes very relevant; therefore, the control force must be limited to keep the WEC bounded. The hydrodynamic parameters used for the wave periods shown in this figure are shown in Appendix A.
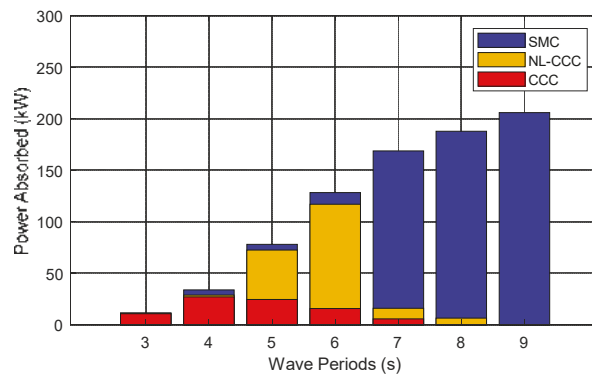

Figure 7. Absorbed Power for the different control strategies with varying wave periods and constant steepness of regular waves.

The difference in power absorption between the three strategies is very small in the shorter wave periods range, particularly between the SMC and the NL-CCC. Except for the WECs natural frequency of $\omega_n = 2.43 \frac{\text{rad}}{\text{s}}$, where, again, the CCC and NL-CCC control strategies need to be very limited to avoid extreme excursions of the WEC. Due to the SMC's ability to track the reference signal and assuming that there are no constraints in the control force for the longer wave periods, the power absorption outperforms that of CCC and NL-CCC.

The sliding mode controller is additionally very robust against modeling uncertainties or disturbances experienced by the system. From the parameters in Equation (29), a source of uncertainty could be the terms in the radiation force ($m_a(\omega_\infty)$, $c(\omega_0)$), and the wavenumber $\chi(\omega_0)$ in the dynamic Froude-Krylov force. These parameters can vary due to an error in the system identification, or the device is biofouled, the system is disturbed, etc.

The exact model assumes 100% certainty of the three parameters mentioned above and the perturbed model assumes 50% uncertainty of the three parameters simultaneously. In Figure 8 is shown a line with slope $-w$ in blue, and the sliding surface $s(t)$ in red for the perturbed model. In Figure 8a, the SMC coefficient A_c of the term $A_c \tan h(s/\phi)$ in Equation (29) was kept the same as the value used in the exact model 10 *k*N. However, as seen from the figure, the initial loop starts at (0;0) due to matching initial conditions between the system states and the reference states, then the sliding surface keeps looping around the blue line, increasing in magnitude. This indicates that the error is not bounded, and therefore, the system could go unstable. Therefore, A_c was increased to 100 *MN* to handle the uncertainty errors. The sliding surface shown in red in Figure 8b forms a closed contour and loops around it, meaning that the error is controlled and will not go unbounded. Hence, when the model is not exact, the A_c needs to be increased. For different wave periods, and depending on the modeling error or disturbances, the SMC coefficient A_c might have to be adjusted to ensure the WEC is tracking the reference signals without much deviation.
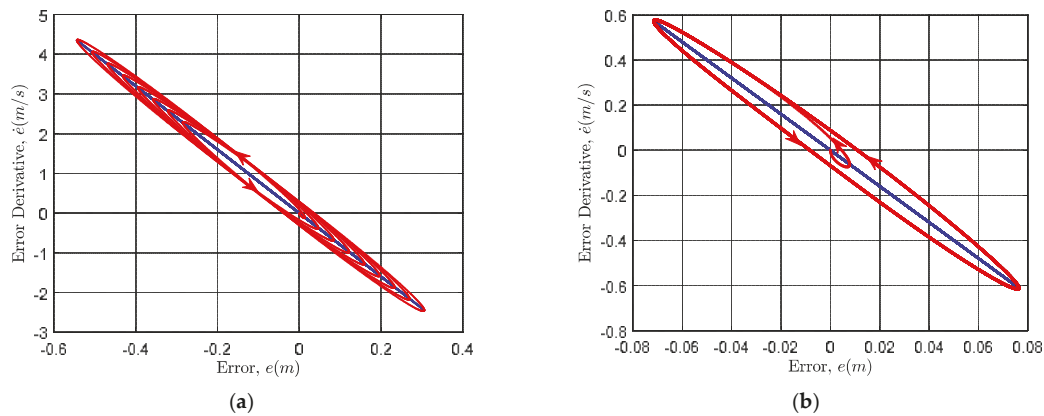
Figure 8. Phase−plane plot of sliding surface $s(t)$ with SMC coefficient of $A_c = 10 \; kN$ on the left (**a**), and $A_c = 100 \; MN$ on the right (**b**).

Figure 9a shows the error between the reference displacement and the WEC displacement for the exact and perturbed model with $A_c = 100 \; MN$. The error for the exact model is close to 0, while, for the perturbed model, it oscillates between $\pm 7.76 10^{-2}$ m which is approximately a 3.5% error. To keep this error between a 5% error margin, the SMC coefficient A_c had to be increased. As mentioned in Section 3, the higher the magnitude of this coefficient, the more robust the SMC is. However, as seen from the control force in Figure 9b, the increase in its magnitude barely affected the control force. This behavior is because the term $A_c \tan h(s(t))$ of the control law offsets the difference in the terms with uncertainties between the exact and perturbed model.
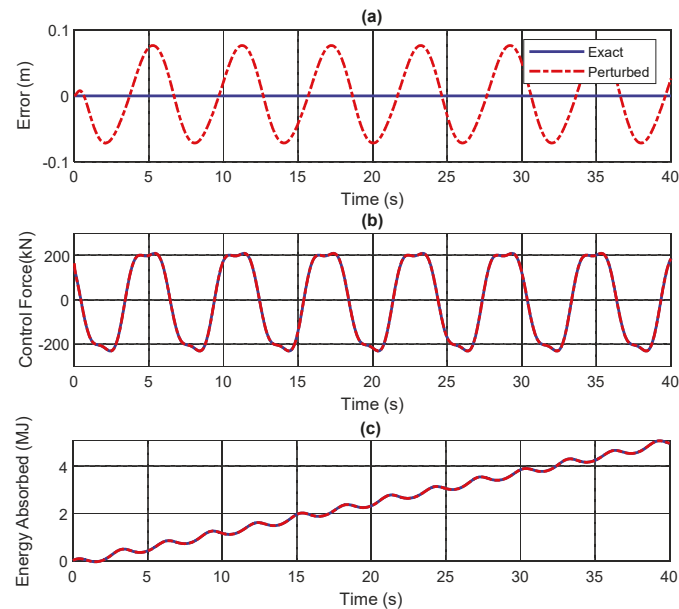
Figure 9. (**a**) Displacement error between reference and WEC displacement, (**b**) Control Force, and (**c**) Energy Absorption of the Exact Model and the Perturbed Model.

The energy absorption shown in Figure 9c does not seem to be influenced by the slight error in the WEC's displacement and the control force. Both the exact and perturbed models needed almost the same control force to deliver equivalent energy absorption. Therefore, the SMC has proven to work very well in systems prone to modeling errors and environmental disturbances such as wave energy converters.

6. Conclusions

Three different control strategies have been presented and applied to a spherical heaving point absorber wave energy converter. These control strategies have shown promising results when used in linear models of WECs. However, it has been shown that linear model approximations lead to inaccurate models when there is a significant difference between WEC displacement and wave elevation. Therefore, this paper presented a sliding mode controller applied to a nonlinear WEC model. This plant incorporates the algebraic nonlinear static and dynamic Froude-Krylov forces.

The SMC was compared to a complex-conjugate control, and a variation of this complex-conjugate control with a nonlinear static FK force term. The controllers aimed to obtain the higher power possible of all control strategies tested while maintaining the WEC within a safe range of motion. The simulation was done using linear and regular waves at a constant wave steepness of 0.018.

It was found that the proposed SMC successfully tracked the reference signals given at all of the wave periods tested. This was achieved by a continuous control force without constraints in magnitude, which would reduce the chance of failure in real-world applications by making the device more reliable. Furthermore, it was shown that the control force does not need to be limited at different values for each sea-state in order to keep the WEC in the safe range of motion, as long as the reference signals fall within those safe bounds.

The sliding mode controller allowed the maximum energy absorption between the control strategies tested at all of the wave periods. At lower wave periods, this was done by requiring less control force than the NL-CCC, and at higher wave periods, where the nonlinearities become very significant, the energy absorbed when using SMC proved to be substantially greater than when using CCC and NL-CCC. In addition, the sliding mode controller allows for the use of any desired reference signal, meaning that if there already exists a path that would deliver the optimal absorbed energy, it could just be used as a reference in the SMC and achieve optimal performance.

Furthermore, the SMC was simulated with modeling errors of 50% in the radiation force, and 50% error in the wavenumber used to calculate the nonlinear dynamic FK force. Despite these uncertainties, the SMC kept the wave energy converter in the tracking reference while using a continuous control force and delivering the same energy absorbed as the exact system. This robustness characteristic of sliding mode controllers is ideal for marine devices where the system parameters may vary over time due to aging, biofouling, corrosion, etc.

Future work includes extending the proposed sliding mode controller to work in irregular waves to test for more real-world scenarios. In addition, the designed controller can be experimentally validated by using a scaled-down point absorber hardware in the wave tank.

This paper used purely heaving point absorbers due to the computationally efficient algebraic nonlinear Froude-Krylov forces derived from Giorgi et al.'s work. However, this could be extended to more degrees of freedom in the future, where numerical approaches need to be used to solve the Froude-Krylov integrals, as explained in Reference [13].

Author Contributions: Methodology, T.D.G. and G.G.P.; Resources, G.G.P. and E.A.; Software, T.D.G.; Supervision, G.G.P.; Validation, T.D.G.; Visualization, T.D.G.; Writing—original draft, T.D.G.; and Writing—review and editing, E.A. and W.W.W. All authors have read and agreed to the published version of the manuscript.

Institutional Review Board Statement: Not applicable.

Informed Consent Statement: Not applicable.

Data Availability Statement: Publicly available datasets were analyzed in this study. This data can be found here: https://github.com/tsdemont/Results_JMSE_1349687 (accessed on 25 August 2021).

Conflicts of Interest: The authors declare no conflict of interest.

Appendix A

The hydrodynamic parameters used in the simulation for each wave period shown in Figure 7 are listed in Table A1. These parameters were obtained from WAMIT [23] for the spherical body with parameters listed in Table 1.

In addition, the amplitude of the SMC displacement reference used for each wave period is shown in Table 2. The energy absorbed by the WEC shown in Figure 7 was obtained using all of these parameters.

Table A1. Hydrodynamic parameters for different wave periods.

Wave Period (s)	3	4	5	6	7	8	9
Wave frequency ω_0 (rad/s)	2	1.57	1.26	1.05	0.89	0.78	0.7
Wavenumber $\chi(\omega_0)$	0.42	0.25	0.16	0.11	0.082	0.063	0.05
Radiation damping $c(\omega_0)$ (N/(m/s))	16.19	16.81	14.35	11.21	8.51	6.64	5.02

References

1. Gunn, K.; Stock-Williams, C. Quantifying the potential global market for wave power. In Proceedings of the 4th International Conference on Ocean Engineering (ICOE 2012), Dublin, Ireland, 17–19 October 2012; pp. 1–7. Available online: https://www.icoe-conference.com/publication/quantifying_the_potential_global_market_for_wave_power/ (accessed on 25 August 2021).
2. LiVecchi, A.; Copping, A.; Jenne, D.; Gorton, A.; Preus, R.; Gill, G.; Robichaud, R.; Green, R.; Geerlofs, S.; Gore, S.; et al. *Powering the Blue Economy: Exploring Opportunities for Marine Renewable Energy in Maritime Markets*; U.S. Department of Energy Office of Energy Efficiency and Renewable Energy: Washington, DC, USA, 2019; pp. 158–163. Available online: https://www.energy.gov/sites/prod/files/2019/03/f61/73355.pdf (accessed on 25 August 2021).
3. Faÿ, F.-X.; Henriques, J.C.; Kelly, J.; Mueller, M.; Abusara, M.; Sheng, W.; Marcos, M. Comparative assessment of control strategies for the biradial turbine in the Mutriku OWC plant. *Renew. Energy* **2020**, *146*, 2766–2784. [CrossRef]
4. Maria-Arenas, A.; Garrido, A.J.; Rusu, E.; Garrido, I. Control Strategies Applied to Wave Energy Converters: State of the Art. *Energies* **2019**, *12*, 3115. [CrossRef]
5. Falnes, J.; Kurniawan, A. *Ocean Waves and Oscillating Systems: Linear Interactions Including Wave-Energy Extraction*; Cambridge University Press: Cambridge, UK, 2020; ISBN 978-1-108-48166-3.
6. Babarit, A.; Clément, A.H. Optimal latching control of a wave energy device in regular and irregular waves. *Appl. Ocean Res.* **2006**, *28*, 77–91. [CrossRef]
7. Todalshaug, J.; Bjarte-Larsson, T.; Falnes, J. Optimum Reactive Control and Control by Latching of a Wave-Absorbing Semisubmerged Heaving Sphere. In Proceedings of the International Conference on Offshore Mechanics and Arctic Engineering, Oslo, Norway, 23–28 June 2002; Volume 4, pp. 415–423. [CrossRef]
8. Cretel, J.; Lewis, A.W.; Lightbody, G.; Thomas, G.P. An Application of Model Predictive Control to a Wave Energy Point Absorber. *IFAC Proc. Vol.* **2010**, *43*, 267–272. [CrossRef]
9. Cummins, W.E. *United States Department of the Navy. The Impulse Response Functions and Ship Motions*; David Taylor Model Basin; United States Department of the Navy: Bethesda, MD, USA, 1962.
10. Windt, C.; Faedo, N.; Penalba, M.; Dias, F.; Ringwood, J.V. Reactive control of wave energy devices—The modelling paradox. *Appl. Ocean Res.* **2021**, *109*, 102574. [CrossRef]
11. Merigaud, A.; Gilloteaux, J.; Ringwood, J. A Nonlinear Extension for Linear Boundary Element Methods in Wave Energy Device Modelling. In Proceedings of the International Conference on Offshore Mechanics and Arctic Engineering, Rio de Janeiro, Brazil, 1–6 July 2012; Volume 4. [CrossRef]
12. Giorgi, G.; Ringwood, J.V. Nonlinear Froude-Krylov and viscous drag representations for wave energy converters in the computation/fidelity continuum. *Ocean Eng.* **2017**, *141*, 164–175. [CrossRef]
13. Giorgi, G.; Ringwood, J.V. Computationally efficient nonlinear Froude–Krylov force calculations for heaving axisymmetric wave energy point absorbers. *J. Ocean Eng. Mar. Energy* **2017**, *3*, 21–33. [CrossRef]

14. Levant, A.; Levantovsky, L. Sliding Order and Sliding Accuracy in Sliding Mode Control. *Int. J. Control NT J CONTR* **1993**, *58*, 1247–1263. [CrossRef]
15. Gaebele, D.T.; Magaña, M.E.; Brekken, T.K.A.; Henriques, J.C.C.; Carrelhas, A.A.D.; Gato, L.M.C. Second Order Sliding Mode Control of Oscillating Water Column Wave Energy Converters for Power Improvement. *IEEE Trans. Sustain. Energy* **2021**, *12*, 1151–1160. [CrossRef]
16. Vu, M.T.; Le, T.-H.; Thanh, H.L.N.N.; Huynh, T.-T.; Van, M.; Hoang, Q.-D.; Do, T.D. Robust Position Control of an Over-actuated Underwater Vehicle under Model Uncertainties and Ocean Current Effects Using Dynamic Sliding Mode Surface and Optimal Allocation Control. *Sensors* **2021**, *21*, 747. [CrossRef] [PubMed]
17. Wahyudie, A.; Jama, M.A.; Assi, A.; Noura, H. Sliding mode and fuzzy logic control for heaving wave energy converter. In Proceedings of the 52nd IEEE Conference on Decision and Control, Firenze, Italy, 10–13 December 2013; pp. 1671–1677.
18. Mehaute, B.L. *An Introduction to Hydrodynamics and Water Waves*; Springer Study Edition; Springer: Berlin/Heidelberg, Germany, 1976; ISBN 978-3-642-85567-2.
19. Korde, U.A.; Ringwood, J. *Hydrodynamic Control of Wave Energy Devices*; Cambridge University Press: Cambridge, UK, 2016.
20. Todalshaug, J.H. Hydrodynamics of WECs. In *Handbook of Ocean Wave Energy*; Pecher, A., Kofoed, J.P., Eds.; Ocean Engineering & Oceanography; Springer International Publishing: Cham, Switzerland, 2017; pp. 139–158; ISBN 978-3-319-39889-1.
21. Falnes, J. A review of wave-energy extraction. *Mar. Struct.* **2007**, *20*, 185–201. [CrossRef]
22. Slotine, J.-J.E.; Li, W. *Applied Nonlinear Control*; Prentice Hall: Englewood Cliffs, NJ, USA, 1991; ISBN 978-0-13-040890-7.
23. Wamit, Inc. The State of the Art in Wave Interaction Analysis. Available online: https://www.wamit.com/ (accessed on 24 July 2021).
24. Todalshaug, J.; Falnes, J.; Moan, T. A Comparison of Selected Strategies for Adaptive Control of Wave Energy Converters. *J. Offshore Mech. Arct. Eng.* **2011**, *133*, 031101.
25. Nebel, P. Maximizing the Efficiency of Wave-Energy Plant Using Complex-Conjugate Control. *Proc. Inst. Mech. Eng. Part J. Syst. Control Eng.* **1992**, *206*, 225–236. [CrossRef]
26. Wavestar. Available online: http://wavestarenergy.com/ (accessed on 24 July 2021).

MDPI